An Experimental Study of the Vortex-Induced Vibration of a Slender Box-Girder Bridge Deck Section

by

Jumana Al-Zubaidi

Department of Aeronautics

Imperial College of Science, Technology and Medicine

Prince Consort Road

London SW7 2AZ

This thesis is submitted for the degree of Doctor of Philosophy of Imperial College London and the Diploma of Imperial College London

2018

Declaration

I herewith certify that all material in this dissertation which is not my own work has been properly acknowledged.

Jumana Al-Zubaidi

The copyright of this thesis rests with the author and is made available under a Creative Attribution Non-Commercial No Derivative licence. Researchers are free to copy, distribute or transmit the thesis on the condition that they attribute it, that they do not use it for commercial purposes and that they do not alter, transform or build upon it. For any reuse or redistribution, researchers must make clear to others the licence terms of this work.

Abstract

This thesis examines the vortex-induced vibration (VIV) of a very slender box-girder bridge deck section. In particular, the dependance of the response and excitation mechanism on the geometry of the bottom knuckles is investigated. This study extends previous research into VIV of bridge decks by considering a very slender box-girder with chord to depth ratio of 11.2. To the best of the author's knowledge, this study is the first to investigate experimentally the VIV of such a slender section.

The behaviour of a slender box-girder in VIV was investigated experimentally, using small-scale physical modelling techniques in a wind tunnel. The excitation mechanisms are studied using pressure taps around a cross-section and several spanwise locations. Accelerometers measure the response. The findings demonstrate that the excitation mechanisms for heave and pitch responses are different (for values of wind speed, divided by frequency and chord, ≤ 1.6). The heave is excited by trailing edge vortices and shows a significant sensitivity to the geometry at the bottom knuckle. For shallow angles $\lesssim 20°$, between the base panel and the lower inclined panels, the trailing edge shedding is sufficiently weakened such that no response is observed. In contrast, the pitch response is excited by a combination of trailing edge vortices and motion-generated impinging vortices, where the frequency of shedding is double, triple and quadruple the oscillation frequency. The mode of the leading edge vortices is sensitive to the bottom knuckle angle and higher modes produce larger vibrations. A critical angle of 20° results in minimum response for the bare deck (only beating angular displacement is observed) and no lock-in.

The difference in excitation mechanisms for the degrees-of-freedom results in different reactions to geometrical and structural modifications, including the bottom knuckle geometry, road furniture and structural damping.

Nomenclature

Acronyms		
VIV	vortex-induced vibration	
LEVS	leading edge vortex-shedding	
ILEV	impinging leading edge vortices	
TEVS	trailing edge vortex-shedding	
Greek Symbols		
α	ratio of vorticity that appears in the wake	
γ	angular displacement	$^\circ$
δ_s	logarithmic decrement of damping	
ζ	damping ratio, relative-to-critical damping	%
ρ	density of fluid	kgm^{-3}
Γ	vortex strength	
υ	kinematic viscosity	$\mathrm{m}^2\mathrm{s}^{-1}$
ϕ	phase angle that force leads displacement	$^\circ$
ϕ_c	damping-altered phase shift	
ω_c	damping-altered natural frequency	rads^{-1}
ω_H	Helmholtz frequency	rads^{-1}
Roman Symbols		
A	amplitude of vertical motion	m
b	half-chord	m
B	maximum deck chord	m
c	speed of sound	ms^{-1}
C	Theodorsen's function	
C_D	drag coefficient	
C_L	lift coefficient	

C'_L	rms lift coefficient	
C_p	coefficient of pressure	
C'_p	coefficient of fluctuating pressure	
C'_{pa}	rms pressure coefficient of acceleration effects	
C_{pb}	coefficient of base pressure	
C_y	coefficient of transverse force	
D	depth of model	m
Fr	Froude number	
$F_{L,circ}$	Theodorsen's circulatory force	N
$F_{L,NC}$	Theodorsen's non-circulatory force	N
f_n	natural frequency in heave	Hz
f_{nt}	natural frequency in torsion	Hz
f_s	vortex-shedding frequency	Hz
F_T	time-dependent fluid force	
f_y	body oscillation frequency	Hz
g	gravitational acceleration	ms^{-2}
h	distance between transducer and pressure tap	
I	mass moment of intertia per unit span	$\mathrm{kgm}^2\mathrm{m}^{-1}$
k	reduced frequency of oscillation	
k_{eff}	stiffness of structure in heave	Nm^{-1}
l	length of pressure tubing	m
L	deck length	m
L_R	correlation length	m
M	mass per unit span	kg
n	frequency ratio of vortex-shedding to oscillation cycle	
p_l	lower surface pressures	
p_u	upper surface pressures	
r	radius of Helmholtz orifice	m^2
Re_D	Reynolds number, based on D	
$R_{p',z}$	spanwise correlation coefficient of fluctuating pressure	
St	Strouhal number	
U	freestream velocity	ms^{-1}

v	volume of Helmoltz cavity	m^3
x	coordinate in chord-wise direction	
y	coordinate perpendicular to the flow direction	

Contents

Abstract **3**

Table of Contents **9**

List of Figures **13**

List of Tables **27**

1 Introduction **29**

1.1 Motivation 29

1.2 Objectives 32

1.3 Layout 33

2 Literature review **35**

2.1 Introduction 35

2.2 Bluff Body Flow Regimes 35

2.3 Vortex-Induced Vibration 41

2.3.1 Lock-in 41

2.3.2 Phase Angle 53

2.3.3 Vorticity 56

2.3.4 Spanwise Correlation 59

2.3.5 The circular cylinder and other low-aspect ratio body shapes 60

2.4 Long-Span Bridges 65

2.4.1 Rectangles and bridge-deck sections 65

2.5 VIV observed in existing bridges 73

2.6 Modifying the response 79
2.7 Synthesis 101

3 Methodology **105**

3.1 Introduction 105
3.2 Small-scale physical models 106
3.3 Wind tunnels 116
3.3.1 $10' \times 5'$ wind tunnel 116
3.3.2 Aeronautical T5 wind tunnel 116
3.3.3 Wind tunnel blockage correction 117
3.4 Experimental set-up 118
3.4.1 Fixed body 118
3.4.2 Free Vibration 118
3.4.3 End Plates 118
3.4.4 Repeatability 119
3.4.5 Flow similarity 123
3.5 General Experimental Procedure 126
3.5.1 Parameter Values 126
3.5.2 Varying the Structural Damping 127
3.5.3 Starting method dependence 131
3.5.4 Runs 132
3.6 Measurements 135
3.6.1 Accelerometers 135
3.6.2 Pressure scanners 135

4 Analyses **137**

4.1 Introduction 137
4.2 Acceleration measurements 137
4.3 Pressure measurements 138
4.3.1 Tubing effects 140
4.3.2 Theodorsen forces 143
4.4 Spanwise Pressure Correlation 146

4.5 Pressure Spectra . . . 146
4.6 Conclusion . . . 147

5 Vortex-induced vibration of a trapezoidal box-girder 149
5.1 Introduction . . . 149
5.2 Results . . . 152
5.3 Heave response: Initial branch and lower branch . . . 170
5.4 Pitch response: leading edge and trailing edge modes . . . 179
5.5 Conclusion . . . 183

6 The effect of the shape of trapezoidal box-girders on vortex-induced vibration 185
6.1 Introduction . . . 185
6.2 Results . . . 187
6.3 Discussion . . . 199
6.3.1 Heave response with different fairings . . . 199
6.3.2 Pitch response with different fairings . . . 202
6.4 Conclusion . . . 208

7 Hysteresis, damping and road furniture 211
7.1 Hysteresis . . . 211
7.1.1 Introduction . . . 211
7.1.2 Results . . . 212
7.1.3 Conclusions . . . 216
7.2 Damping . . . 217
7.2.1 Introduction . . . 217
7.2.2 Results . . . 217
7.2.3 Conclusions . . . 220
7.3 Road Furniture . . . 222
7.3.1 Introduction . . . 222
7.3.2 Results . . . 222
7.3.3 Conclusion . . . 230

8 Conclusions and recommendations for further work **231**

8.1 Conclusions 231

8.2 Limitations and future work 235

Bibliography **237**

List of Figures

2.1 Regimes of fluid flow across a stationary and smooth circular cylinder [13], characterised by Re_D. 37

2.2 The Strouhal number-Reynolds number relationship for stationary circular cylinders [13]. The top line shows the relationship for a smooth cylinder and the bottom line shows the relationship for a rough cylinder. 38

2.3 A numerical simulation of the flow around a trapezoidal bridge deck showing the von Kármán vortex street [14]. The von Kármán vortex street is characterised as the periodic shedding of staggered vortices of opposite sign. 38

2.4 The interpretation of the flow field around a stationary model of the approach span of the Storebælt bridge (B/D=6 where B is the overall chord), [17][18]. 40

2.5 St and drag coefficient, C_D as a function of Re_D, of a stationary model of the Storebælt Bridge approach span (B/D=6), [17]. 41

2.6 Measurements by Feng on a freely vibrating circular cylinder. Here $n = f_s$ and $N = f_n$. The dashed line indicates the linear f_s - U relationship for a stationary cylinder. $\bigcirc$, f_s; +, oscillation frequency; $\square$, ϕ; $\times$, $\frac{\bar{Y}}{D}$ is the dimensionless transverse amplitude, [9]. 43

2.7 Variation with wind speed of the aerodynamic excitation on a rigid circular cylinder undergoing forced excitation at $\frac{y}{D} = 0.011$, $Re_D = 1.2 \times 10^5$, [22]. . 46

2.8 Displacement response exhibiting two branches: an initial branch with a jump down to a lower branch [24]. 47

2.9 Phase shift, ϕ, vortex shedding frequency, $\frac{f_v}{f_n}$ and heave displacement, $\bar{Y}$ phenomena for an elastically-mounted, rigid circular cylinder with increasing wind speed, [9]. Feng's damping levels are those generated by his electromagnetic eddy-current damper, designed by Smith [26]. 48

2.10 Displacement response of an elastically-mounted, rigid circular cylinder at low damping level, exhibiting a branched response and hysteresis, [9]. The arrows indicate the direction of speed increment. 49

2.11 Beating phenomenon at the onset of response of a circular cylinder. Pressure (top) and displacement (bottom) time series, [9]. 50

2.12 Variation of the response of a model circular stack (aspect ratio=10) with logarithmic decrement of damping, δ_s and corresponding Scruton number, $\frac{2m\delta_s}{\rho d^2}$ a measure of the combined effects of body inertia and damping, [27] . 51

2.13 The spectra of velocity fluctuations behind a stationary circular cylinder in smooth and turbulent approaching air streams: (a) $Re_D = 0.26 \times 10^5$ (subcritical and turbulent free-stream); (b) $Re_D = 2.2 \times 10^5$ (subcritical and smooth free-stream); (c) $Re_D = 2.1 \times 10^5$ (supercritical and turbulent free-stream); (d) $Re_D = 7.2 \times 10^5$ (supercritical and smooth free-stream); (e) free-stream turbulence spectrum [27] 52

2.14 Phase angle measurements on a forced and freely oscillating circular cylinder at $A/D = 0.11$, [23]. ◯ forced oscillation, Bearman and Currie [11]; × free oscillation, Feng [9]. 54

2.15 Williamson and Roshko [30] explain the phase jump and hysteresis observed in the displacement response of circular cylinders at low damping as a change in vortex-shedding mode. 55

2.16 Phase angle measurements on a square cylinder undergoing forced oscillations, ◯ $A/D = 0.05$; × $A/D = 0.1$; △ $A/D = 0.25$, [31]. 57

2.17 $|C_y|\, sin\phi$ versus a scaled amplitude ratio $\frac{2|y|I}{D}$. ■ △ ▲, flexible cantilever in water, □ rigid cylinder-forced vibrations in water, •, pivoted rigid cylinder in water and air; +, spring mounted rigid cylinder in air, [32]. 58

2.18 The correlation coefficient of the pressure measured at the centre-line of a side face of a square-section cylinder undergoing forced vibration of amplitude $A/D = 1$, versus spanwise separation, z. $\triangle$, $\frac{U}{f_n D}$ within lock-in range 7.3 - 8.5; $\times$, $\frac{U}{f_n D} = 6.2$; $\bigcirc$, 7.0; $\Diamond$, 8.8; $\square$, 12.0. Results are compared to $\bigtriangledown$, body stationary [31]. 60

2.19 Phase shift, Φ, vortex-shedding frequency, $\frac{f_v}{f_n}$ and heave displacement, $\bar{Y}$ phenomena for a D-section cylinder with the flat face normal to the flow and upstream of the semi-circular afterbody [9]. 62

2.20 Circulation shed per cycle in the range of capture for a circular cylinder ($\bigcirc$, $A/D = 0.1$; $\square$, $A/D = 0.29$) and square section cylinder ($\times$, $A/D = 0.1$; $\triangle$, $A/D = 0.25$) [31]. Here, S is the Strouhal number, $\Delta\Gamma_o$ is the shed vorticity of the oscillating body, $\Delta\Gamma_s$ is the shed vorticity of the stationary body. 63

2.21 Phase angle, ϕ for $\bigcirc$ a circular cylinder, forced to oscillate at $A/D = 0.11$ and $\times$ a square cylinder, forced to oscillate at $A/D = 0.1$ [31]. 64

2.22 Group 1, Group 2 and Group 3 flow patterns [38]. 65

2.23 Response amplitudes for Group 1, Group 2 and Group 3 bluff bodies in vertical and torsional VIV. V_0 is the onset critical velocity in heave, n=1 [38]. 66

2.24 Phase-averaged streamlines and pressure distributions over the upper and lower surfaces of an oscillating rectangular cylinder, B/D=4, at peak amplitude within an oscillation cycle. Flow is from left to right [10]. 67

2.25 Reduced onset critical velocity, $V_{CR,H}$ observed for various bluff bodies. The lines plot equation 2.14 for ILEV excitation, n=1 and n=2. KV denotes von Kármán street excitation [40]. 68

2.26 Response of cylinders undergoing self-excited heave oscillations a) rectangles of varying slenderness, B/D and b) fixed slenderness, $B/D = 10$, different shapes. $\alpha = 0°$, $I_u = 1\% - 5\%$, δ=0.041 at $y = 0.1$mm, L/B=10. Here, Sh is the fixed body Strouhal number and Sh_1 is the ILEV Strouhal number for $n = 1$ [39]. 69

2.27 Strouhal number, St, St^*, for stationary rectangular prisms of different slenderness ratios, B/D in cross-flow $\alpha = 0°$: ——, Nakamura, Ohya and Tsuruta [46] for $I_u = 0.3\%$, $Re_D = 1000$; – – , – · – , Parker and Welsh [44] for $I_u = 0.2\%$, $1.7{\times}10^4 \leq Re_D \leq 3.5 \times 10^4$; – · · – · ·, Nguyen and Naudascher [47] for $I_u = 4.5\%$, $Re_D = 1300$ [39]. 70

2.28 Response diagrams for bending (top) and pitching (bottom) for an elastic H-section ($B/D = 5$) placed in a low turbulence flow, $Re_{D,max} = 1.25{\times}10^6$, at zero incidence [45]. 71

2.29 Observed vertical VIV for the full-scale and wind tunnel tests of the Storebælt bridge, at different damping values and wind speed history, [51]. . . . 72

2.30 View along the deck of the Storebælt bridge during large amplitude VIV at the crest (left) and trough (right) of oscillation. The vehicle in the white circle is a parked van which is partly obscured by the crest of the oscillating deck (left) and reappears in the trough (right), [53]. 73

2.31 Spanwise correlation of fluctuating pressure measured at the centre of the side face of a static and an oscillating rectangular cylinder, $B/D = 4$, in smooth and turbulent flow. $U_r = 8.43$ is the critical wind speed giving maximum amplitudes, other wind speeds are not associated with oscillations. All turbulent cases are measured at the critical wind speed. The base case turbulence: $I_u = 6\%$, L_{11} (streamwise)=2B/3, L_{22} (vertical) = 2B/9, L_{33} (spanwise)=B/3 [10]. 76

2.32 Instantaneous iso-surfaces of the vorticity magnitude at lock-in (a) under smooth flow, and (b) under turbulent flow [10]. 77

2.33 Possible structural deck configuration for long-span bridge decks, [62]. . . . 78

2.34 A typical trapezoidal bridge deck, B/D=4, exhibiting the ILEV excitation mechanism, (a) bare deck, and (b) with the addition of guide vanes at the leading edge and trailing edge corners, [66]. 82

2.35 Schematic of the guide vanes on the Storebælt suspension bridge, [53]. . . . 82

2.36 The flow pattern without guide vanes (top) and with guide vanes (bottom). The guide vanes on the upwind box inject high speed flow into the wake thus preventing the formation and shedding of von Kármán vortices, [65]. . 83

2.37 Cross-section of the main span of the Second Severn Crossing with baffle plates added to reduce the vertical VIV, [?]. 83
2.38 Nine long-span bridges that have experienced VIV and the mitigation methods employed, [71]. 84
2.39 Schematic view of the fairing used in simulations to determine the sensitivity of vortex-shedding to θ_T and θ_B, the top and bottom angles respectively, by Haque *et al.* [72]. 85
2.40 Fluctuating velocity in the near wake, measured at 1D downstream and 1D below the trailing edge of a fixed bridge deck section, B/D=5, with varying triangular fairings, [72]. 86
2.41 rms fluctuating pressure distribution, C'_p on the bottom of a box-girder bridge deck, with varying angles θ_T and θ_B, [72]. 86
2.42 Numerical simulation of the velocity field around a bridge deck with $\theta_T = 40°$ and $\theta_B = 15°$, through one lift cycle, showing the von Kármán vortex street in the near wake. Through shedding cycle, (a) 0°; (b) 90° and (c) 270°. [72] 87
2.43 Numerical simulation of the velocity field around a bridge deck with $\theta_T = 40°$ and $\theta_B = 40°$, through one lift cycle, showing the von Kármán vortex street in the near wake. Through shedding cycle, (a) 0°; (b) 90° and (c) 270°, [72]. 88
2.44 Numerical simulation of the velocity field around a bridge deck with $\theta_T = 40°$ and $\theta_B = 10°$, through one lift cycle, showing the von Kármán vortex street in the near wake. Through shedding cycle, (a) 0°; (b) 90° and (c) 270°. [72] 88
2.45 Fluctuating pressure distribution, C'_p on the bottom of a box-girder bridge deck, with varying angles θ_T and θ_B,[72]. 89
2.46 Numerical simulations at the leading edge of two bridge deck sections (a) without fairings, and (b) with fairings, showing the development of ILEV excitation at the leading edge. The velocity at the leading edge is increased in the presence of a fairing, which intensifies the ILEV mechanism and amplifies response,[74]. 90

2.47 Comparison of VIV response for deck sections A, □ and E, △. (a) bending response and (b) torsion response. [75]. 91
2.48 Lift angle vs. angle of attack for various aerofoils [75]. 91
2.49 Response in heave and torsion for small-scale models of the Storebælt main span, Deck D (left) and Deck E (right), with bare deck and road furniture [75]. 92
2.50 Smoke visualisation of the near wake of a trapezoidal model at $U/(f_nB) \approx 0.4$, (a) Deck A, showing full separation and vortex-formation close to the model and (b) Deck E, showing limited separation with vortex roll-up delayed to further downstream in the wake [75]. 93
2.51 Shedding frequency, f_s measured as velocity fluctuations in the near wake for self-excited heave and torsion VIV of rectangular cylinders belonging to Group 1(LEVS excitation), Group 2 (ILEV excitation) and Group 3 (TEVS excitation), [38]. 94
2.52 Response and f_s for Deck A, with and without road furniture and at $\zeta = 0.1\%$ and 0.2%, [75]. 94
2.53 Response and f_s for a small scale model of the Østeroy bridge, with and without road furniture and at $\zeta = 0.1\%$, [75]. 95
2.54 Octagonal prism model used by Chaix [76] to study the flow in towing tank experiments, undergoing forced oscillations, $\alpha = 0°$. 95
2.55 Savonius-type turbine placed in the leading-edge bottom corner of the Volgograd bridge deck section. Numerical simulations showed that the flow was altered relative to the base case, with lower amplitudes, [48]. 96
2.56 Steady wake flow with base bleed, [81]. 97
2.57 Flow visualisation of an H-section prism, $\alpha = 0°$, $B/D = 5$, $Re_D = 1200$. (a,b) stationary prism with and without a splitter plate; (c,d,e) prisms vibrating transversely with amplitude $y/d = 0.19$; (c) U_{nd}=8.65; (d) U_{nd}=8.65 with splitter plate; (e) U_{nd}=4.3, [82]. 98

2.58 Passive control methods of decorrelating vortex-shedding by three-dimensional geometric modifications: (a) helical strake, (b) segmented trailing edge, (c) wavy trailing edge, (d) wavy stagnation face, (e) sinusoidal axis, (f) hemispherical bumps and (g,h) tabs, [83]. 99

3.1 Two-dimensional bridge deck sections with varying angles between the extension of the bottom plate and the inclined lower plates. All dimensions shown are in mm. 108

3.2 Fairings A to E with pressure tappings shown. Nomenclature relates to a tap number in table 3.2 109

3.3 Top and bottom plate slopes of constructed box-girder bridge decks, compiled by Haque *et al.* [72] 109

3.4 Pressure tap nomenclature on the base model, at a cross section $0.44L$ measured from the end on the model. Indicative leading edge and trailing edge is shown. The co-ordinate origin, referred to in table 3.2 is shown. . . 110

3.5 Road furniture. All dimensions shown are in mm. 111

3.6 Looking downwind at the model mounted within the T5 tunnel at BMT Fluid Mechanics. The view is of the leading edge. The blue sections are foam and the shorter brown sections are made of wood and pressure-tapped. 112

3.7 The view of the dynamic rig in the $10' \times 5'$ tunnel from one end of the model showing 1, the location of the accelerometers; 2, the suspension rig connection to the model. This set-up allows up and down motion in heave and rotational motion in pitch. The variable magnetic eddy-current damper is not shown in this picture. 119

3.8 View of the end plate at one end of the model, mounted in the $10' \times 5'$ wind tunnel. The slots in the wall were made for a previous investigation and were sealed before the current experiments. 120

3.9 Heave response $\bigcirc$, with end plates in the $10' \times 5'$ tunnel; $\bigtriangledown$ with the model flush with the tunnel side walls in the T5 tunnel. These correspond to Run 2B↑ ψ and run 1B↑ φnDF respectively (see section 3.5.4 for nomenclature). 121

3.10 (a) Smoke visualisation at the leading edge and (b) distribution of mean pressure, C_p, measured on the bottom surface. Both at $Re_D = 1.3 \times 10^4$ with $\circ, A/D = 0$; $\bullet$, oscillating. This corresponds to run 1B↑ φnDF (see section 3.5.4 for nomenclature) 125
3.11 General view of the variable magnetic eddy-current (VMEC) damping system at one end of the dynamic rig. Another identical system is at the other end. The copper disc is rigidly connected to the model and moves with it, in between the two electromagnets. 128
3.12 (a) sample of the time-decaying amplitude, measured by perturbing the deck to a position Y_0 and releasing in still air, and (b) the logarithmic amplitude, $\circ$ with a least squares linear curve fit, $-$. 129
3.13 Least-square fit of free-vibration decay for (a) heave and (b) pitch showing the linear relationship between the logarithm of the amplitude and time. $-$, χ;- - -,ψ; ...., φ. 131
3.14 View of one accelerometer (1) in position on the dynamic rig. 135

4.1 Frequency response of the pressure measurement system, with 1.5 m lengths of 1 mm i.d. portex tubing connected to an ESP with a discrete first order filter fit (line), [102]. 141
4.2 Bode plots of frequency response of the pressure measurement system with 750 mm lengths of portex tubing, modified from figure 4.1 and equations 4.6 and 4.7. 142

5.1 Deck B, $B/D = 11.2$, with a 25° angle at the leading and trailing edges. Labels indicate the location of measurements; $\bullet$ base: pressure, C_{pb}; $\circ$, trailing edge: fluctuating pressure, C'_p, shedding frequency, f_s and spanwise correlations, $R_{p',z}$. 150
5.2 Run 1B↑ φnDF: $\bullet$, rms displacement in heave A/D; $\bullet$, torsion γ; $+$, vortex-shedding frequency, f_s of the stationary body; and $\Diamond$, elastically-mounted body; $\cdot$, body frequency, f_y. 153

5.3 Run 2B↑ ψnDF: •, rms displacement in heave A/D; •, torsion γ; ◊, vortex-shedding frequency, f_s of the elastically-mounted body; ·, body frequency, f_y. 154
5.4 Run 1B↑ φnDF: distribution of mean pressure, C_p at $U/(f_nB) = 0.53$ at a cross-section at $0.44L$. ∘, $A/D = 0$, • $A_{max}/D = 2.4\%$. Pressure tap locations are indicated, +. Pressure taps giving erroneous results are circled in red. 157
5.5 Run 1B↑ φnDF: distribution of mean pressure, C_p at $U/(f_nB) = 1.11$ at a cross-section at $0.44L$. ∘, $\gamma = 0°$, • $\gamma_{max} = 0.18°$. Pressure tap locations are indicated, +. Pressure taps giving erroneous results are circled in red. . 158
5.6 Run 2B↑ ψnDF: distribution of mean pressure, C_p at $U/(f_nB) = 0.54$, at a cross-section at $0.44L$. ∘, $A/D = 0$; □ $A_{max}/D = 0.6\%$ $U/(f_nB) = 0.55$, △. Pressure tap locations are indicated, +. Pressure taps giving erroneous results are circled in red. 163
5.7 Run 2B↑ ψnDF: distribution of mean pressure, C_p at $U/(f_nB) = 1.18$ at a cross-section at $0.44L$. ∘, $\gamma = 0°$, • $\gamma_{max} = 0.1°$. Pressure tap locations are indicated, +. Pressure taps giving erroneous results are circled in red. . 164
5.8 Run 1B↑ φnDF: effect of Re_D on mean pressure, C_p for the stationary deck measured at ◯, □, the leading edge; •, trailing edge. 165
5.9 Run 1B↑ φnDF: base pressure, $-C_{pb}$, ◯, $A/D = 0$; •, elastically-mounted. . 165
5.10 Run 1B↑ φnDF: the effect of oscillations on the rms fluctuating pressure, C'_p, bandpass filtered $+/-0.5$Hz f_s, at a cross-section at $0.44L$. +, pressure taps on the cross-section. 166
5.11 Run 1B↑ φnDF: effect of Re_D on r.m.s fluctuating pressure, C'_p for the stationary deck, △, ◊, measured at the leading edge; •, trailing edge. . . . 167
5.12 Run 1B↑ φnDF: rms fluctuating pressure, C'_p measured at (a) the base and (b) trailing edge. ◯, $A/D = 0$; •, elastically-mounted. 168
5.13 Run 1B↑ φnDF: correlation of surface pressures, $R_{p',z}$, measured at the bottom downwind knuckle, versus spanwise separation, z/D for the stationary and oscillating body, with (a) motion-generated component removed; (b) with motion-generated component included. 169

5.14 Run 2B↑ ψnDF: Acceleration measured on the initial branch and lower branch of heave lock-in. 172
5.15 Run 2B↑ ψnDF: Premultiplied spectra at select pressure taps at a cross-section at $0.44L$ at $U/(f_nB)$=0.55 on the lower branch of heave. Peaks at the body frequency are evident, as well as a broadband peak at the stationary body frequency, $St = 0.24$ found at the downwind knuckles. . . 173
5.16 Run 2B↑ ψnDF: correlation of surface pressures on the initial and lower branches of heave lock-in, measured on a line at the trailing edge versus spanwise separation, z/D. 174
5.17 Run 1B↑ φnDF: Premultiplied spectra at select pressure taps at a cross-section $0.44L$ at $U/(f_nB)$=0.69 for the stationary body. Peaks at the downwind knuckles are evident, at $St \approx 0.24$. 175
5.18 Run 2B↑ ψnDF: +, phase angle, ϕ between the lift force generated by VIV and body displacement, through heave lock-in. 176
5.19 Run 2B↑ ψnDF: time series of fluctuating lift at the shedding frequency, f_s for (a) the stationary body; (b)A_{max} for the elastically-mounted body as measured; (c) an estimate of the motion-generated component; (d) with motion-generated component removed. All measurements at $U/(f_nB)$=0.54. Note y-axis scales differ. 177
5.20 Run 2B↑ ψnDF: The variation of the component of rms lift force in phase with the body velocity, $C'_L sin\phi$ through heave lock-in. 178
5.21 Run 1B↑ φnDF: Premultiplied spectra at select pressure taps at a cross-section at $0.44L$ at the onset critical velocity for ptich $U/(f_nB)$=0.79. Three peaks are evident at various locations on the body. 180
5.22 Run 1B↑ φnDF: time series of (a) body displacement displaying beating amplitude modulations and (b) fluctuating pressure measured at the bottom downwind knuckle at $U/f_nB = 0.78$. 182
5.23 Run 1B↑ φnDF: Correlation of surface pressures, measured on a line at the trailing edge (figure 5.1) throughout pitch lock-in, versus spanwise separation, z/D. 183

6.1 Run 2X↑ φnDF (where X = A - E): •, rms displacement in heave A/D; •, torsion γ; 190
6.2 Run 2X↑ φnDF (where X = A - E): +, Body frequency, f_y. $f_{nt} = 2.3f_n$. Deck C did not experience periodic oscillations and has been omitted. . . . 191
6.3 Run 2C↑ φnDF: torsional response, γ° at $U/(f_nB) = 0.79$. The beating is defined as amplitude modulation of the signal, such that peaks vary significantly in amplitude. The peak factor is 3.3. 192
6.4 Run 2C↑ ψnDF: •, rms displacement in heave A/D; •, torsion γ; ◊, vortex-shedding frequency, f_s of the elastically-mounted body; ·, body frequency, f_y. $f_{nt} = 2.3f_n$ 193
6.5 Run 1C↑ φnDF: •, rms displacement in heave A/D; •, torsion γ; ◊, vortex-shedding frequency, f_s of the elastically-mounted body; ·, body frequency, f_y. $f_{nt} = 2.0f_n$ 195
6.6 Run 1A↑ ϖnDF: •, rms displacement in heave A/D; •, torsion γ; ◊, vortex-shedding frequency, f_s of the elastically-mounted body; ·, body frequency, f_y. $f_{nt} = 2.0f_n$ 197
6.7 Run 1D↑ ϖnDF: •, rms displacement in heave A/D; •, torsion γ; ◊, vortex-shedding frequency, f_s of the elastically-mounted body; ·, body frequency, f_y. $f_{nt} = 2.0f_n$ 198
6.8 Run 1B↑ φnDF (left) and Run 1C↑ φnDF (right): Premultiplied spectra at the downwind knuckles, at a cross-section at 0.44L and $U/(f_nB)$=0.38 for the stationary body. The TEVS mode appears stronger and more organised for Deck B. C'_M is calculated as described in chapter 4. 200
6.9 Run 1D↑nDF: Premultiplied spectra at the downwind knuckles, at a cross-section at 0.44L and $U/(f_nB)$=0.45 on the stationary body. No trailing edge shedding mode is apparent. 201
6.10 Distribution of mean pressure, C_p at a cross-section at 0.44L at the resonant wind speed for pitch. ∘, Run 2B↑ ψnDF at $U/(f_nB) = 0.79$; △, Run 2C↑ ψnDF at $U/(f_nB) = 0.70$. Pressure tap locations are indicated, +. Pressure taps giving erroneous results are circled in red. 203

6.11 Run 1C↑ φnDF: Premultiplied spectra at select pressure taps, at a cross-section at 0.44L at $U/(f_nB)$=0.70 the resonant velocity for pitch beating. A peak at the leading edge has frequency $St = 0.13$ and a the strong peak at the trailing edge has frequency $St = 0.24$. 204

6.12 Run 1D↑ φnDF: Premultiplied spectra at select pressure taps, at a cross-section at 0.44L at $U/(f_nB) = 0.65$, the resonant velocity for pitch. A peak at the leading edge has frequency $St = 0.22$, and broadband peaks at the trailing edge (and strongest at the knuckle) have frequency $St = 0.25$. . . . 206

7.1 rms displacement in heave A/D, for • the wind speed increased incrementally (run 1B↑ φnDF), and ▼ from rest (run 1B∧φnDF). 213

7.2 Hysteresis observed for Deck B: Run 1B↑ χnDF ▷, rms displacement in heave A/D; •, torsion γ; Run 1B↓ χnDF ◁, rms displacement in heave A/D; ∘, torsion γ. 214

7.3 Hysteresis observed for Deck C: run 2C↑ φnDF ▷, rms displacement in heave A/D; ∘, torsion γ; run 2C↓ φnDF ◁, rms displacement in heave A/D; •, torsion γ. 215

7.4 Run 1B↑ φnDF and run 1B↑ χnDF: rms displacement in heave A/D, •, $\zeta_{heave} = 0.5\%$; ■, $\zeta_{heave} = 1.0\%$; torsion γ, • ,$\zeta_{heave} = 0.5\%$; □, $\zeta_{pitch} = 1.0\%$. At high wind speeds, $0.60 \leq U/(f_nB) \leq 0.64$ the response seen for Run 1B↑ φnDF is roll. 218

7.5 Run 2B↑ φnDF and run 2B↑ ψnDF: rms displacement in heave A/D, ■, $\zeta_{heave} = 0.5\%$; •, $\zeta_{heave} = 0.7\%$. 219

7.6 Scruton diagram for Deck B. the region of capture: □, minimum wind speed, • maximum wind speed; +, A/D_{max}. The results have been normalised based on the result for $\zeta_{heave} = 0.5\%$. The Scruton number, Sc, varies only with damping, ζ 221

7.7 Run 1B↑ φDF: •, rms displacement in heave A/D; •, torsion γ; ◊, vortex-shedding frequency, f_s of the elastically-mounted body. Comparison should be made to the equivalent run for the bare deck in figure 5.2. 224

7.8 Run 1B↑DF: +, vortex-shedding frequency, f_s, measured on the stationary deck with open railings and a median divider. 225

7.9 Run 1B↑ φDF: Pressure spectra measured at the downwind knuckle for the stationary model with deck furniture. $St = 0.27$ corresponds with the TEVS and $St = 0.20$ with an ILEV mode, n=3. 226

7.10 Run 1B↑ φDF: Pressure spectra measured at the downwind knuckle at $U/(f_n B) = 1.19$ for the stationary model with deck furniture. $St = 0.27$ labels the TEVS, $St = 0.20$ and $St_h = 0.20$ the n=3 ILEV mode and a $\frac{1}{2}$ harmonic respectively. 228

7.11 Run 1C↑ φDF: •, rms displacement in heave A/D; •, torsion γ; ◊, vortex-shedding frequency, f_s of the elastically-mounted body, measured at the downwind knuckle. Comparison should be made to run 1C↑ φnDF in figure 6.5 229

List of Tables

3.1 Dimensions of fairings A to E, all in mm. 110

3.2 Pressure tap locations on the variable leading edge (LE) and trailing edge (TE) fairings. $z_1 = 0.30L$, $z_2 = 0.44L$, $z_3 = 0.51L$, $z_4 = 0.81L$ indicate the four spanwise locations of the pressure taps. Pressure readings are not measured for Deck E. Where pressure measurements at locations on the decks are referenced in the body of this report, they are as follows: upwind top knuckle, n2; upwind bottom knuckle, n10 (fairings A, B) and n11 (fairings C, D and E); body, PT18 and PT6; downwind top knuckle, n3; downwind bottom knuckle, n10 (fairings A and B) and n10 (fairings C, D and E). All measurements to nearest mm. 115

3.3 The parameters of experimental set-up in this investigation. Body frequencies were measured from spectra of free vibrations in still air. *System mass includes contribution from dynamic rig. 126

3.4 Measured system damping in heave and pitch motion for experiments. $\varphi*$ was measured by forcing the model by hand at f_n until harmonic motion was achieved. The natural frequency in pitch was too high to oscillate by hand. 130

3.5 Nomenclature for experimental runs. The run name is based on a combination of numbers, letters and symbols, each referring to a parameter value. 132

3.6 Nomenclature and parameter values for all runs in this investigation. . . . 134

4.1 Acceleration measurement parameters 138

4.2 Pressure measurement parameters 139

5.1 A comparison of the Storebælt main span and the experiments of Larsen and Wall [75] and Terres-Nicoli and Kopp [51] and Deck B in this investigation. 150

6.1 Strouhal numbers, St calculated from the shedding frequency, f_s (measured at the downwind knuckle) relationship with wind speed. ^{em} denotes where St was calculated from measurements of the elastically-mounted deck, when $A/D = \gamma = 0$. 207

Chapter 1

Introduction

1.1 Motivation

Bridges connect two locations of interest, traversing physical obstacles such as waterways, valleys and infrastructure. Humans have built bridges for thousands of years as part of larger road networks. Historically, the Romans built complex arch bridges and aqueducts as part of their network of roads, connecting their empire. This transport network was vital for the expansion and maintenance of the Roman empire, providing an efficient means for the movement of people, communications and goods.

Nowadays, transport infrastructure and the role that bridges play within these networks, is just as vital. The economic benefits of good quality transport infrastructure are widely recognized. In economically developed countries such as the UK and USA, governments have made investment in transport infrastructure a policy focus, despite overall reductions in public spending [1]. In economically developing countries, transport infrastructure is viewed by the UK Government and the European Commission as a key area for aid investment, as a means of providing sustainable economic growth [2].

Bridges are an essential part of a good quality transport network. Where the physical obstacles to be spanned are large in size, long-span bridges are required. These structures have benefits in addition to those of a more typical bridge form. The Storebælt bridge in Denmark has reduced the journey between the Danish islands of Zealand, where the capital city, Copenhagen is, and Funen from 1 hour to 10 minutes [3]. The Storebælt bridge,

along with the Øresund link, consisting of a cable-stayed bridge and tunnel connecting Copenhagen to Malmo, Sweden significantly reduces travel time between mainland Europe and Scandinavia. It has been shown that the role bridges play in the wider transport network can lead to economic benefits, including increased tourism, foreign investment, and attracting business to the region [1]. Long-span bridges are often big-statement projects, resulting in more pronounced economic benefits.

The benefits of a long-span bridge are not just economic. Long-span bridges often provide alternative connections between two urban environments, reducing congestion of local roads. Reduced congestion in urban environments leads to improved air quality and reductions in urban pollution. Often, these bridges are an aesthetic statement, serving to put a region on the map. Long-span bridges often provide a direct crossing of a large, and otherwise difficult to navigate obstacle. The Akashi suspension bridge in Japan connects Kobe, on the mainland to Iwaya, on the Awaji Islands replacing the previous main method of travel between these two points: a ferry. This region is often exposed to extreme storms and in 1955, two ferries sank at this crossing, killing 168 people [4]. The social benefit of the bridge is significant.

By observing trends in long-span bridges over the last century, it is evident that they are becoming even longer. In 1931, the George Washington Bridge in USA, was the first bridge to have a span greater than 1,000 m, with a main span of 1,066 m [5]. In 1981, the Humber suspension bridge, in England, UK was the longest single-span suspension bridge in the world for 16 years [6]. The suspended span was 1,410 m. This century, the Messina Bridge in Italy was developed to detailed design stage before being cancelled by the Italian government. It would have boasted the longest suspended span in the world: 3,330 m; triple that of the Humber Bridge [7].

While bridges are becoming longer, the rate at which this is happening is increasing. Improvements in technology are allowing these longer spans to become physical realities, but as the bridges get longer, structural adequacy is not the only dominant concern. Aerodynamic stability is becoming critical.

In order for super-long-span bridges to be technologically feasible, the spans need to be structurally sufficient under the heavy traffic loads as well as their own self weight. In order to fullfill this requirement, long-span bridges tend to be light. As a bridge

span becomes longer, it also becomes more flexible. These factors in combination lead to flexible, light-weight structures, which if excited at the right conditions are susceptible to large-amplitude oscillations.

Wind-induced oscillations are a common cause of failure or loss of functionality of long-span bridges [8]. Long-span bridges tend to be over large stretches of water or valley, and receive little shelter from the wind. The surrounding topography tends to be relatively flat, with little surface roughness. As a result the oncoming wind to a bridge can have a wide range of speeds and low turbulence. A range of various oscillation regimes exist, excited by the wind under different conditions and speeds. These include flutter, a divergent aerodynamic instability which if not prevented can lead to the destruction of the bridge. Flutter commonly occurs at high wind speeds and is a governing factor in the design of a bridge [8]. The bridge is designed such that the likelihood of a flutter instability is sufficiently low. Flutter is observed as large amplitude torsional oscillations, sometimes coupled with vertical oscillations. Another wind-structure interaction commonly affecting long-span bridges is buffeting, caused by the turbulence in the oncoming wind. This is not usually a destructive phenomenon, but is a long-term fatigue concern in design [8].

Another oscillation regime, is termed vortex-induced vibration (VIV). It is commonly characterised by small and self-limiting oscillations, occurring at the natural frequency of the bridge, and within a small range of wind velocities. Wind speeds tend to be relatively low, and so it is not rare for a long-span bridge to experience VIV several times in a lifetime. Although VIV will not lead to failure of the structure, the high occurrence of oscillations can lead to fatigue damage, requiring refurbishment of parts of the deck and increased maintenance and inspection of the structure. The oscillations can also create a dangerous driving experience and leads to disruption to normal traffic flow. Drivers may be distracted and visibility impaired leading to accidents. A wobbly bridge may be perceived by the public as unsafe leading to reduced use of the structure and a loss in the benefits of having the bridge in the first place.

As technology progresses, allowing longer spans of bridges to become structurally feasible, VIV is limiting the benefits of these bridges. Therefore, there is a need to limit or remove the phenomenon completely. VIV affects bluff bodies in many engineering situations. Much research has been carried out on the VIV of simple sections, such as

rectangles and circular cylinders [9], [10], [11]. Bridge decks tend to be of more complex geometry, and the flow pattern around such sections as well as the aeroelastic response is more complex. Research on the VIV of bridge decks tends to be project specific [12]. Therefore understanding of the fluid-structure interactions for bridge decks is limited and mitigation measures developed in research have been applied to a specific bridge deck section and associated geometry. Only a small number of mitigation methods have been developed and the industry is far from having a mitigation design that suits all or most long-span bridges.

1.2 Objectives

The primary aim of this study is to develop an understanding of the mechanisms of VIV and the associated lock-in of a very slender box-girder deck section. Experiments at small-scale in the wind tunnel were conducted. The small-scale model used to represent a box-girder was a two-dimensional trapezoid of slenderness ratio, $B/D = 11.2$. The wind direction is taken to be perpendicular to the deck axis. Two degrees-of-freedom are investigated; bending and torsion.

The specific objectives are:

- to examine how a slender deck behaves in VIV, in particular the mode of vortex excitation and the response. Slenderness ratio is well established to be a critical factor in the mode of shedding from a rectangle, but the sensitivity for trapezoids remains a question;
- to develop an idea of how the fluid-structure interaction and oscillations develop through lock-in for a slender deck. The interaction is known to modify the shedding strength, frequency, timing and correlation. Here we look at characterising the extent and nature of these modifications for a slender deck;
- to investigate the impact on response of varying the geometry of the bottom knuckles, and to develop an understanding of the mechanisms causing any differences;
- to observe the effect of structural damping on the lock-in. If this slender deck is very sensitive to structural damping, then (a) this may be a useful design tool to

mitigate VIV, and (b) it is critical that a minimum damping is achieved on the prototype - infamously difficult to achieve;

- to use an understanding of the VIV for this slender deck and the sensitivity to damping, road furniture and fairing shape to develop design guidance.

1.3 Layout

The layout of this dissertation is as follows. In chapter 2 literature associated with VIV for a variety of shapes is reviewed. Chapter 3 describes the experimental methodology adopted, including the small-scale physical models and experimental set-up used to represent the full-scale conditions. Chapter 4 describes the analysis methods employed for the experimental data. Chapter 5 presents the VIV response of a typical box-girder section with a 25° angle at the bottom knuckles. Chapter 6 presents the sensitivity of VIV to the geometry of the fairings, looking at five shapes. A critical angle at the bottom knuckles of the trapezoid, for which the response is minimised, is discovered. Chapter 7 describes the impact of starting condition, structural damping and road furniture. The main findings and limitations are discussed in chapter 8, as well as design guidance and recommendations for future work.

Chapter 2

Literature review

2.1 Introduction

This chapter presents a review of the relevant existing research on VIV of various bluff bodies, including bridge decks. The purpose of this literature review is to develop an awareness of the characteristics of VIV for various bluff bodies and an understanding of the physical mechanisms driving the behaviours. This highlights gaps in the current understanding of VIV for slender bridge deck sections and puts the current investigations into context.

2.2 Bluff Body Flow Regimes

The flow regime across a stationary and smooth two-dimensional circular cylinder immersed in a real fluid is well understood. The flow regimes are often categorised by the Reynolds numbers at which they occur. The Reynolds number, Re_D is based on the free stream velocity, U and cylinder diameter, D,

$$Re_D = \frac{UD}{\upsilon} \tag{2.1}$$

where υ is the kinematic viscosity of the fluid.

These flow regimes (figure 2.1) vary in the state of the boundary layers; whether turbulent or laminar, the separation point of the boundary layers, and the wake structures

(Figure 2.1). Above $Re_D \approx 40$ there is a von Kármán vortex street; the periodic and alternating shedding of vortices of opposite sign from the top and bottom of the cylinder. At low Reynolds numbers, $40 < Re_D < 150$, the boundary layer and von Kármán vortex street are laminar. As the Reynolds number is increased to $150 < Re_D < 3 \times 10^5$, the wake becomes turbulent, the laminar boundary layers separate at 80° relative to the front stagnation point on the cylinder and the flow is called *subcritical*. At the onset of the subcritical regime, the wake loses its two-dimensionality. A three-dimensional instability causes large-scale three-dimensionality in the shedding. For the range: $3 \times 10^5 < Re_D < 3.5 \times 10^6$, the laminar boundary layer undergoes turbulent transition, the separation point moves downstream to about 140° relative to the front stagnation point of the cylinder, and the flow is called *supercritical*. The periodic shedding of vortices is disrupted and the wake is disorganised. For $Re_D > 3.5 \times 10^6$, the transition to a turbulent boundary layer moves forward as do the separation points, the wake widens, the periodic shedding of a vortex street wake is re-established at a slightly higher frequency, and the flow is called *transcritical*. To date, the transcritical regime is the final regime to be found in circular cylinder flows and has been observed up to $Re_D = 10^7$.

The frequency of the vortex-shedding, f_s may be expressed as a dimensionless constant, the Strouhal number, St:

$$St = \frac{f_s D}{U} \tag{2.2}$$

where f_s is the shedding frequency of a pair of vortices, in Hz.

Figure 2.2 shows that the Strouhal number of a stationary circular cylinder in a subsonic flow is strongly Reynolds number dependent and as expected follows the flow regimes of Figure 2.1. In the subcritical flow regime the Strouhal number of a fixed cylinder is approximately constant with Reynolds number.

For sharp-edged bluff bodies, the flow separation is fixed at the corners. The dependence on Re_D is much weaker than for circular cylinders. For very low Re_D the flow is dominated by viscosity and is described as creeping and will not separate. With increasing Re_D the flow will begin to separate at the corners. A von Kármán vortex street is formed with alternating vortices being shed from the top and bottom of the body (figure 2.3).

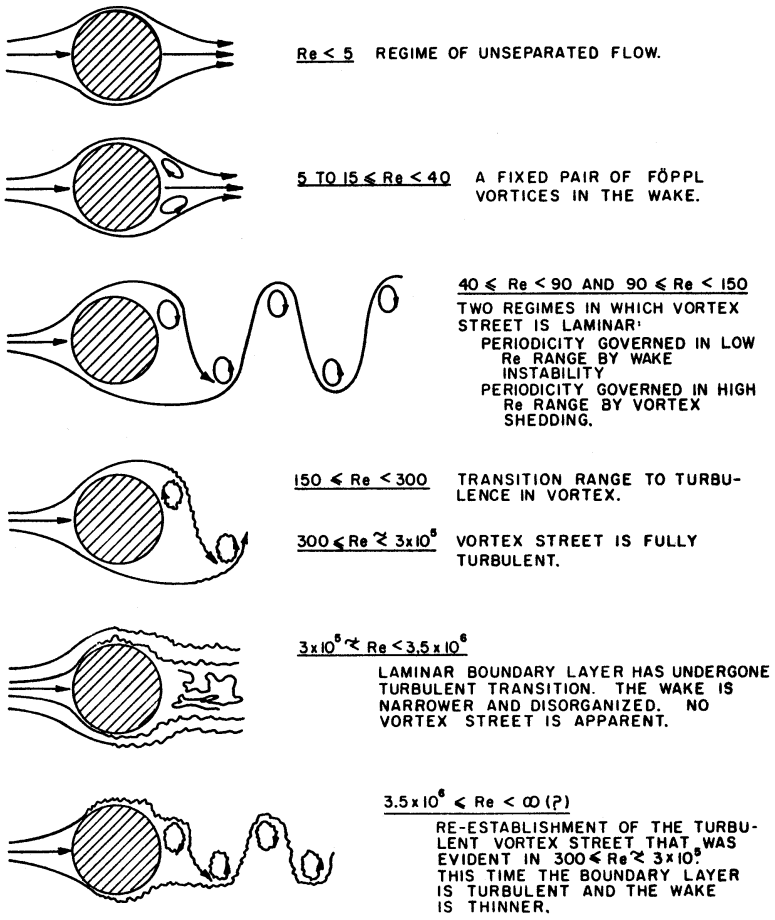


Figure 2.1: Regimes of fluid flow across a stationary and smooth circular cylinder [13], characterised by Re_D.

As for the circular cylinder the flow may be described as subcritical, supercritical or transcritical. The Re_D at which the flow transitions from subcritical to supercritical and supercritical to transcritical are strongly dependent on the shape of the body as well as free-stream turbulence. For a typical full-scale bridge deck section in typical wind conditions, the flow regime will be transcritical - that is the boundary layers and the wake will be fully turbulent. The continuous and alternating formation and shedding of vortices from the top and bottom surfaces of the bridge deck, leads to alternating pressure and velocity distributions over the body and to an alternating force in the cross-wind direction.

In comparison to the flow around circular cylinders, in which the separation point moves with Re_D, widening or narrowing the wake width and modifying f_s, it is a general

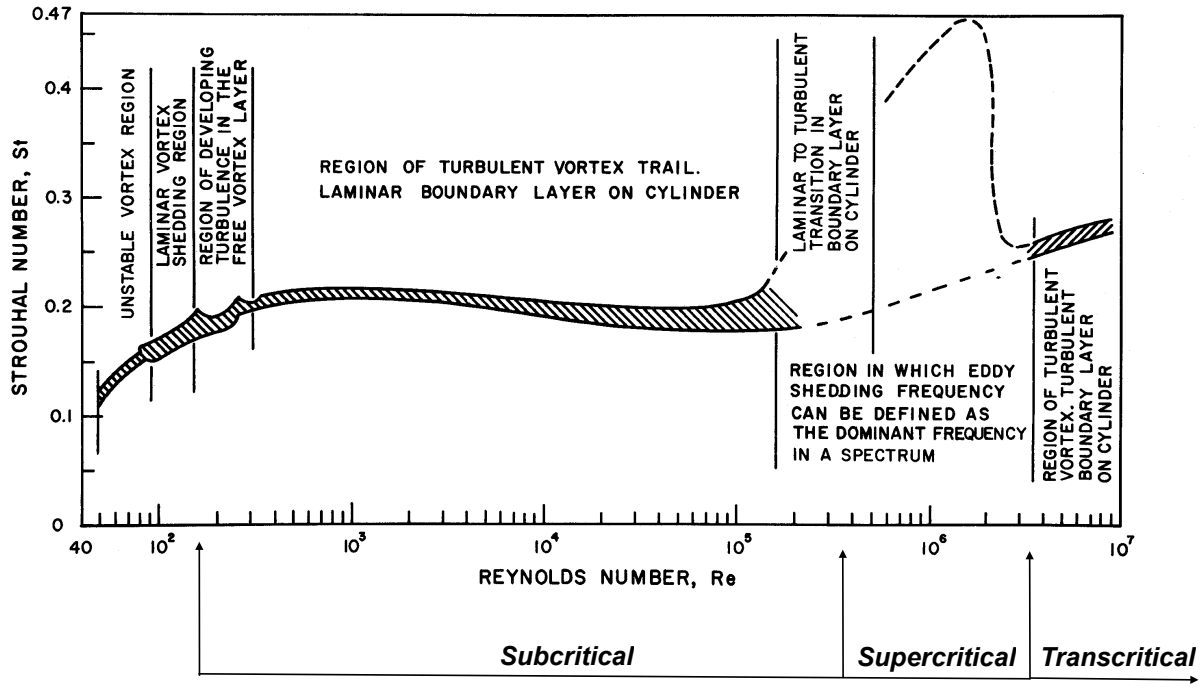


Figure 2.2: The Strouhal number-Reynolds number relationship for stationary circular cylinders [13]. The top line shows the relationship for a smooth cylinder and the bottom line shows the relationship for a rough cylinder.



Figure 2.3: A numerical simulation of the flow around a trapezoidal bridge deck showing the von Kármán vortex street [14]. The von Kármán vortex street is characterised as the periodic shedding of staggered vortices of opposite sign.

belief that the aerodynamics of bluff bodies with sharp edges, such as bridge decks, are insensitive to Re_D as long as a critical value is reached. Larose and Auteuil [15] give this critical $Re_D = 10,000$. Prandtl and Tietjens [16] state that the flow around such bodies is determined by separation at the sharp edges and therefore the flow is insensitive to the Re_D. This assumption of the flow around sharp-edged bluff bodies has formed the justification for relaxing the requirement for similarity of Re_D for small-scale experiments

and full-scale prototypes. This belief has been reinforced by model-scale studies, typically with $Re_D \approx 10^5$, predicting to good accuracy the vortex-induced vibration, VIV of the prototype, typically of Re_D two orders of magnitude greater.

However, a study by Schewe and Larsen [17] has shown significant Re_D dependence of flow around the trapezoidal bridge deck of the approach spans of the Storebælt bridge in Denmark. As part of the design of the bridge, model-scale wind tunnel tests had been carried out to predict the behaviour of the deck in VIV. Once the bridge was built, the vibrations occurred at different wind speeds to those predicted by the model tests. In order to determine the discrepancy between model and prototype behaviour, wind tunnel tests on a stationary model at a large range of Re_D covering those of the original model and the prototype were carried out. The experiments showed there was a significant Re_D effect and three flow regimes were observed in the range $3 \times 10^4 < Re_D < 4 \times 10^6$. Schewe and Larsen describe these flow regimes as the subcritical, supercritical and transcritical.This body appears to be more sensitive to Re_D effects than those studied by Larose and Auteuil [15] and Prandtl and Tietjens [16]. The subcritical flow regime did not have a similar flow field as those of the supercritical or transcritical flow regimes as shown in figure 2.4.

By looking at the flow schematics shown in figure 2.4 and the corresponding St behaviour in figure 2.5, the Re_D effects can be described:

- $3 \times 10^4 < Re_D < 8 \times 10^4$: subcritical flow regime. The flow over the upper panel separates at the upwind knuckle, forming a large separation bubble which is followed by reattachment. At the bottom plate the laminar boundary layer separates at the upwind knuckle. The separated shear layer undergoes transition at some downstream location and remains detached from the deck, resulting in a wide wake with $St \approx 0.18$.

- $8 \times 10^4 < Re_D < 4 \times 10^5$: supercritical flow regime. The separated flow over the upper panel reattaches further upstream, resulting in a smaller separation bubble. At the bottom plate, the separated shear layer undergoes laminar to turbulent transition close to the separation point, resulting in reattachment and the formation of a separation bubble. The flow separates again at the downwind knuckle, forming a narrow wake. Over the supercritical flow regime, St increases gradually with Re_D.

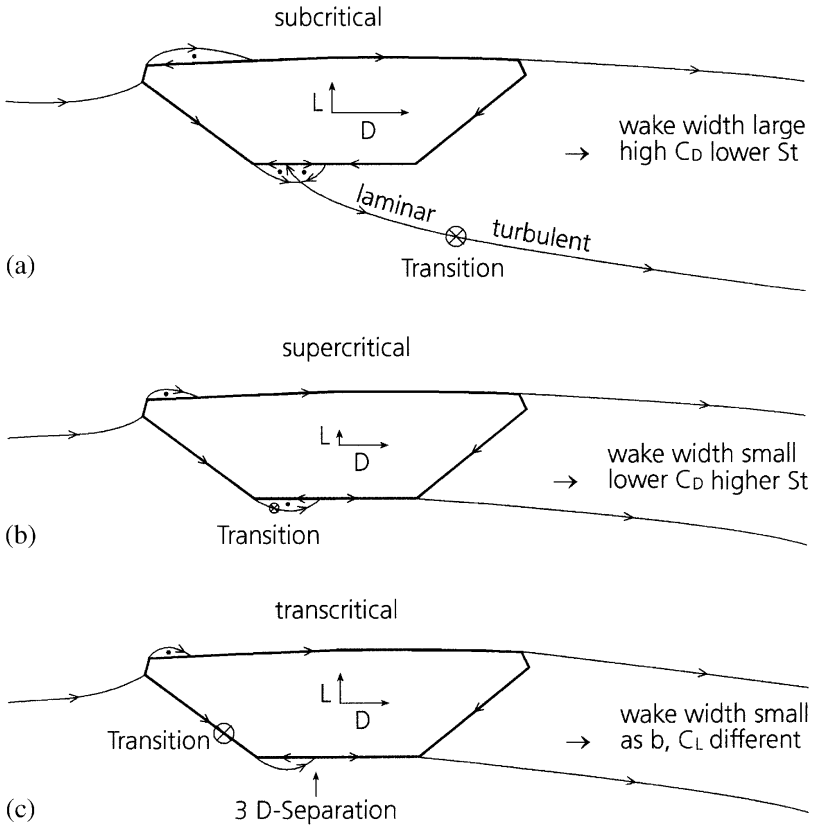


Figure 2.4: The interpretation of the flow field around a stationary model of the approach span of the Storebælt bridge (B/D=6 where B is the overall chord), [17][18].

.

- $4 \times 10^5 < Re_D < 4 \times 10^6$: transcritical flow regime. The transition point over the bottom panels moves ahead of the separation point, resulting in a separation region at the leading edge corner with a high degree of small-scale three-dimensionality in the spanwise direction.

The values of St for the supercritical and transcritical flow regimes are very similar, as in both flows the separation at the trailing edges dominate. Here, it is apparent that the change in the flow over the bottom panels is the cause of the Re_D dependence. There are similarities and difference to the flow around a circular cylinder. For this sharp-edged trapezoid, $B/D = 6$ the subcritical flow is characterised by separation closer to the leading edge for the bottom panel, and an associated wide wake, similar to a circular cylinder.

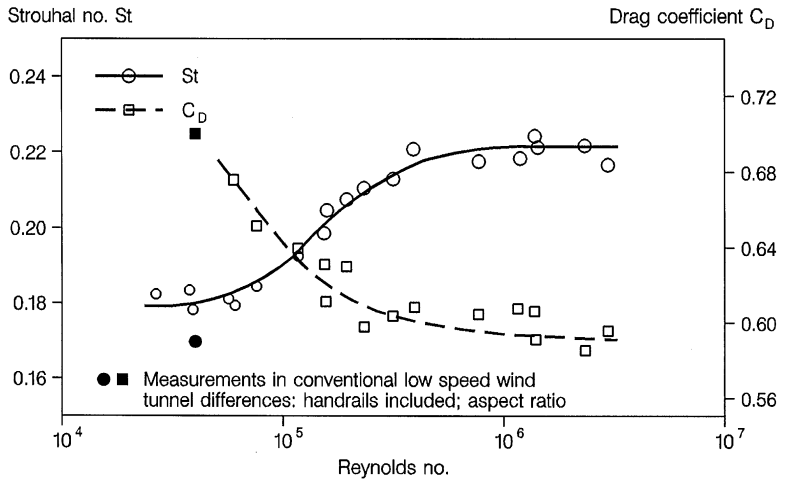


Figure 2.5: St and drag coefficient, C_D as a function of Re_D, of a stationary model of the Storebælt Bridge approach span (B/D=6), [17].

.

The supercritical and transcritical flow regimes are characterised by separation of the shear layers further from the leading edge, with an associated narrow wake, again similar to a circular cylinder. However, here the supercritical regime has a wake with a clear shedding frequency that is not as disorganised as for a circular cylinder.

Experiments on the main span section of the Storebælt bridge, $B/D = 7.8$ by Larose [15], show that for $2.8 \times 10^4 < Re_D < 1.5 \times 10^5$, there was flow similarity with the full-scale flow at $Re_D = 1.7 \times 10^7$. It appears that in order to predict the prototype VIV at full-scale, Re_D similitude is required for some trapezoidal bridge deck shapes, but not for all.

2.3 Vortex-Induced Vibration

2.3.1 Lock-in

If a rigid body is fixed in a uniform flow, and it is shedding vortices, and the conditions are such that St is constant (within a given Re_D), then by observation of equation 2.2, there is a linear relationship between f_s and U; that is f_s increases continuously for increasing

U.

To illustrate the observations of VIV let us consider the experiments of Feng [9]. Feng carried out experiments on stationary and elastically-mounted cylinders in air. The elastically-mounted circular cylinder in figure 2.6 is free to move in a cross-flow direction. The relationship between f_s and U is much the same as for the fixed case, except for a limited range of wind speeds when f_s approaches the natural frequencies, f_n of the body. At these wind speeds the body can take control of the shedding in apparant violation of the St relationship in equation 2.2; f_s is significantly modified relative to the fixed case and the body begins to oscillate (at f_n in air)(figure 2.6). f_s is locked-in by the body motion for a range of wind speeds until f_s of a fixed body at the same wind speed would be significantly different, and f_s jumps back to this fixed body frequency. This phenomenon is known as "lock-in" and is observed as large amplitude, steady-state VIV.

Now let us consider the physics of von Kármán shedding from the trailing edge of a trapezoid. The flow separates at the upwind knuckles, with partial reattachment along the body and small-scale vorticity (for $B/D \gtrsim 2$). At the downwind knuckle, the shear layer has insufficient momentum to remain attached to the inclined panels and separates fully. The free shear layers cause the air in the near wake to rotate, away from the high pressure region in the free-stream and towards the low pressure region directly downwind of the bridge deck.

Trapezoids tend to have shorter bottom panels than top panels, and consequently a larger dead air region can form downwind of the lower inclined panel. A large, coherent vortex can grow here, entraining air from the free stream, often to a much larger size than the corresponding top vortex. The vortex is eventually shed into the far wake, making room for a top vortex to form. There is a cyclic formation and shedding of vortices from the bottom and top of the body, creating a von Kármán vortex street. The location where vortices join the free stream are characterised by local velocities greater than the free stream, as the free stream velocity sums with the vortex velocity. This creates regions of low pressure or suction. As vortices are shed below the tail, this location of suction is created below the tail and exerts a downward force on the body. As a vortex is shed above the tail, the forces pulls the body up. In such a way, there is a cyclic force exerted on the body, at an identical period to the vortex formation and shedding.

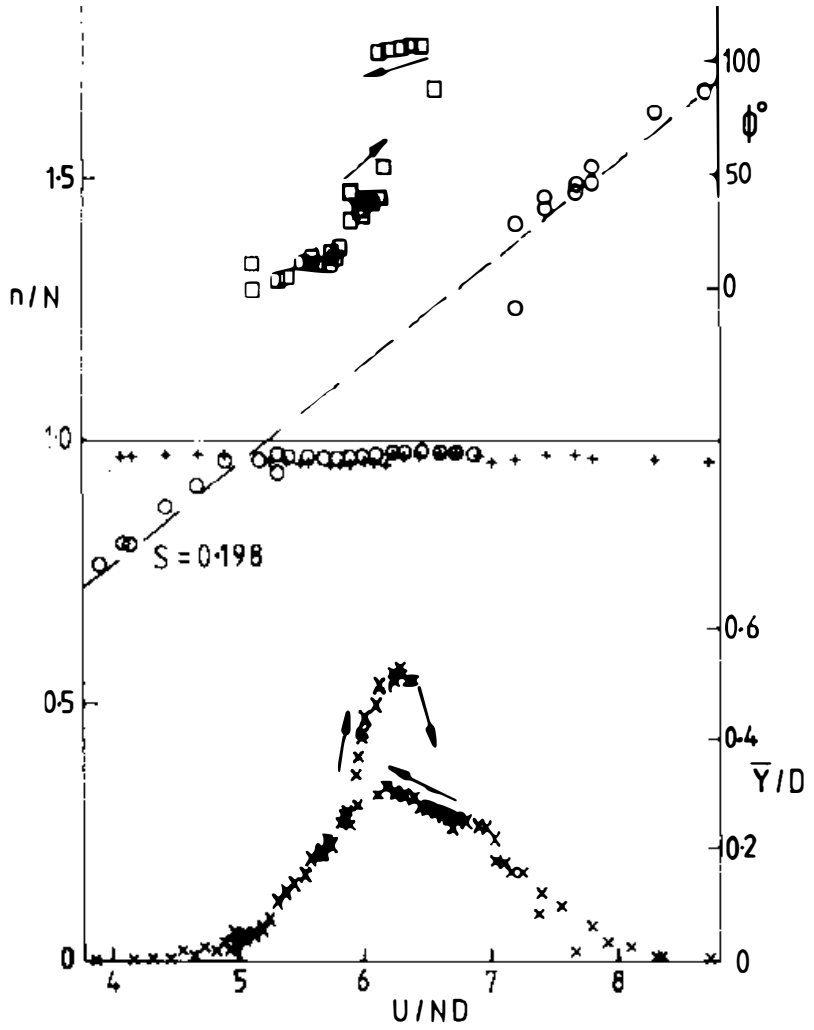


Figure 2.6: Measurements by Feng on a freely vibrating circular cylinder. Here $n = f_s$ and $N = f_n$. The dashed line indicates the linear f_s - U relationship for a stationary cylinder. ◯, f_s; +, oscillation frequency; □, ϕ; ×, $\frac{\bar{Y}}{D}$ is the dimensionless transverse amplitude, [9].

When this cyclic force has frequency close to a structural eigenfrequency of the bridge deck, motion can initiate. The body motion then acts to stabilise the shedding, making it more regular, which enhances the deck motion. VIV occurs as a result of the interaction between the fluid forcing and the body displacement. This interaction significantly modifies the vortex-shedding. Fundamentally, the process is non-linear.

Considering only the transverse degree-of-freedom, the wind-structure interaction can

be modelled as a one-degree-of-freedom oscillator [7]:

$$m(\omega_n y + 2\zeta\omega_y\omega_n y + {\omega_n}^2 y) = \tfrac{1}{2}\rho U^2 B C'_L sin(\omega_s t) \tag{2.3}$$

where y is the displacement of the body, m is the mass of the body, C'_L is a coefficient for the dynamic lift force, ρ is the density of the fluid and ζ is the damping ratio, relative-to-critical damping. Critical damping, $\zeta = 1$ is the quickest approach to zero amplitude body motion. ω are radia frequencies.

At resonance, the shedding frequency is equal to the body frequency. The elastic forces and the inertial forces cancel out, leaving the damping force to balance the excitation force. Assuming the body motion is harmonic, with frequency ω_y:

$$|y| = \frac{\rho U^2 B C'_L}{4m\zeta {\omega_y}^2} \tag{2.4}$$

Equation 2.4 is used in codes of practice, including EN 1991-1-4 [19]. It is a convenient way of understanding the impact of mass and damping on amplitudes. Often the Scruton number is used to describe the combined effects of these parameters:

$$Sc = 4\pi\zeta\frac{m}{\rho B^2} \tag{2.5}$$

For oscillations in air $f_y = f_n$. In denser fluids such as water, the frequency of oscillation may vary significantly from f_n.

Equation 2.4 is a simple tool to view and understand VIV. In reality, the non-linearity of VIV means that the excitation force is also a function of the body motion. Later in this chapter, it will be demonstrated how the body motion changes the magnitude and phase of the excitation force. Equation 2.4 ignores feedback effects such as the self-limiting nature of VIV. As the damping tends to zero, oscillations will not become infinite. Other Van der Pol type models exist [20] that incorporate empirical definitions of the fluid forcing, demonstrating the self-limiting dependance on body motion. These empirical fits are strongly dependant on geometry, incident turbulence and Re_D.

The Vickery-Basu model [21] is a spectral mathematical model that describes the response of a circular cylinder in VIV by superimposing two forces; a vortex-shedding force acting on a static cylinder and a motion-induced force. The motion-induced force,

F_M can be expressed generally in the manner of Scruton [22] as an in-phase and out-of-phase with motion component:

$$F_M = h_a y + k_a \dot{y} \tag{2.6}$$

where h_a and k_a are coefficients that modify the stiffness (or mass) and damping of the structures respectively. The stiffness term in 2.6 has negligible influence on the response of most structures [22].

The damping term can be described in terms of a dimensionless parameter, K_a:

$$k_a = 4\pi f_n \rho D^2 K_a \tag{2.7}$$

Negative K_a is equivalent to negative aerodynamic damping, or aerodynamic excitation. It can be expressed, per unit span, in terms of the logarithmic decrement, δ_a:

$$K_a = \frac{2m\delta_a}{\rho D^2} \tag{2.8}$$

The aerodynamic damping expresses the energy interchange between wind and structure. When K_a is sufficiently negative to cancel out positive structural damping, oscillations can occur. The condition for this occur at the critical wind speed.

K_a is a function of the body amplitude, although at low amplitudes $\lesssim 0.2D$ is it approximately constant, K_{a0}. At larger amplitudes the aerodynamic damping displays a dependancy on amplitude, equation2.9[21] which manifests as the self-limiting nature of VIV.

$$\zeta_a = -\frac{\rho D^2}{m} K_{ao} \frac{1 - y_{rms}}{Y_L/\sqrt{2}} \tag{2.9}$$

where rms denotes root-mean-square and Y_L is the limiting amplitude that would be obtained in the absence of structural damping. ζ is related to the logarithmic decrement of damping by the following relationship:

$$\zeta = \frac{1}{\sqrt{1 + \frac{4\pi^2}{\delta^2}}} \tag{2.10}$$

Figure 2.7 displays the dependance of K_a with wind speed. The plain circular cylinder undergoing forced, small amplitude oscillations, exhibits strong sensitivity to the wind

speed. At a critical wind speed ≈ 5 the aerodynamic damping becomes quickly negative and remains so for a short range of wind speeds, before returning to positive value. The wind speeds characterised by negative K_a indicate unstable conditions, where the wind is doing work on the body to amplify excitation.

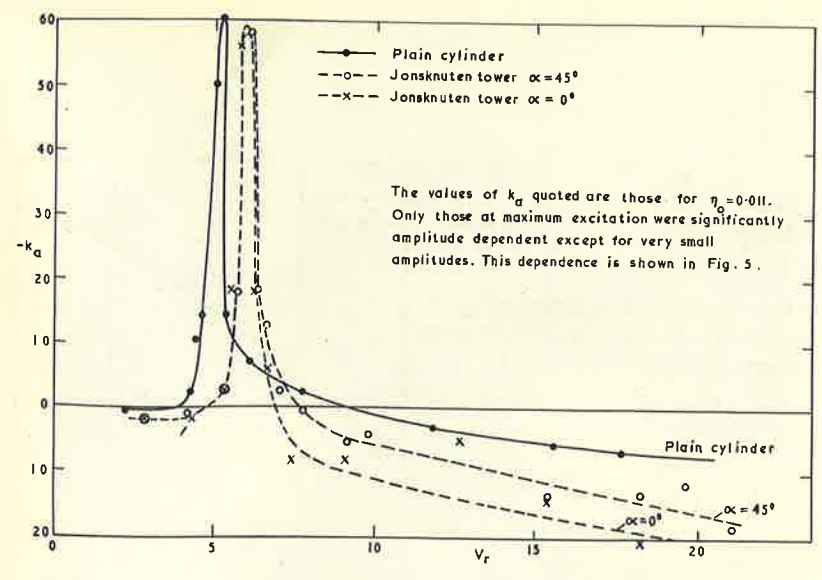


Figure 2.7: Variation with wind speed of the aerodynamic excitation on a rigid circular cylinder undergoing forced excitation at $\frac{y}{D} = 0.011$, $Re_D = 1.2 \times 10^5$, [22].

The Vickery-Basu model, equation 2.11 [21] represents an alternative to equation 2.4 and is well accepted, showing good agreement with wind tunnel tests and field measurements. It has been incorporated in simplified forms into various codes, including EN 1991-1-4 [19].

$$\frac{y_{rms}}{D} = \left(\frac{C'_{L,rms}}{8\pi^2}\right)\left(\frac{U}{f_y D}^2\right)\left(\frac{\rho D^2}{m}\right)\left(\frac{\sqrt{\pi}}{4B_w}\right)\left(\frac{f_y}{f_s}\right) exp\left(\frac{-\left(\frac{1-\frac{f_y}{f_s}}{B_w}\right)^2}{\zeta_s+\zeta_a}\right)^{0.5} \tag{2.11}$$

where B_w is a spectral term; the bandwidth of the vortex-shedding force spectrum.

VIV can also be in-line modes and torsional modes [23]. As each vortex is shed there are force fluctuations in the direction of the flow, which can result in in-line oscillations at double the frequency of the cross-flow oscillations. Generally, the in-line oscillations are at a much smaller amplitude than the cross-flow oscillations. Structures with significant body length in the direction of the flow and low natural torsional frequency are susceptible to vortex-induced torsional oscillations.

Feng [9] investigated the behaviour of a circular cylinder over the range: $1 \times 10^5 < Re < 5 \times 10^5$, at five damping levels. The two cylinders exhibited markedly different behaviours during VIV in heave. The behaviour of the circular cylinder can be seen in figure 2.9. All the damping levels investigated share the same rising side of the displacement response and break off to different maxima, $\bar{Y}_{max}$. Govardhan and Williamson [24] term this discontinuous response as branched (figure 2.8) referring to an "initial" branch corresponding to those displacements from the onset of motion at low wind speed and including $\bar{Y}_{max}$, and a "lower" branch which occurs at higher wind speeds and encompasses the smaller displacements. The lowest two damped cylinders have a branched response with a jump from a large displacement to a much lower displacement at or soon after $\bar{Y}_{max}$. These branches do not exist at higher damping levels, where the displacement response is smooth and continuous. Branched responses have also been observed in experiments on vibrating cables [25] and elastically-mounted rigid circular cylinders [24].

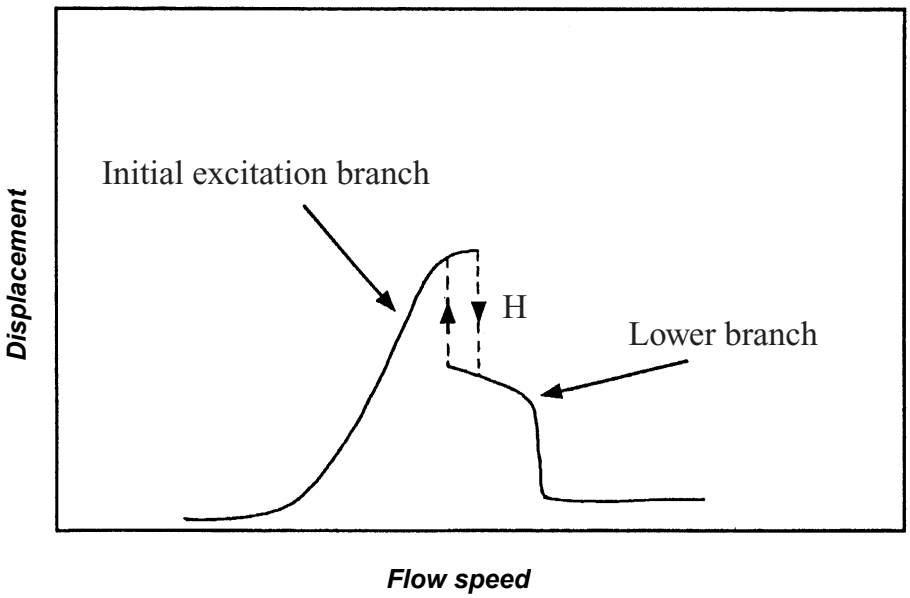


Figure 2.8: Displacement response exhibiting two branches: an initial branch with a jump down to a lower branch [24].

Figure 2.9 shows the vortex-shedding frequency, f_s measured at the transverse diam-

eter of the cylinder during lock-in. f_s smoothly approaches f_n where it is captured for a range of wind speeds, and abruptly jumps back to f_s of a stationary body at higher wind speeds. It should be noted that the jump down to the reduced amplitudes of the lower branch does not coincide with the loss of lock-in. It is something other than a change in lock-in causing the branched behaviour.

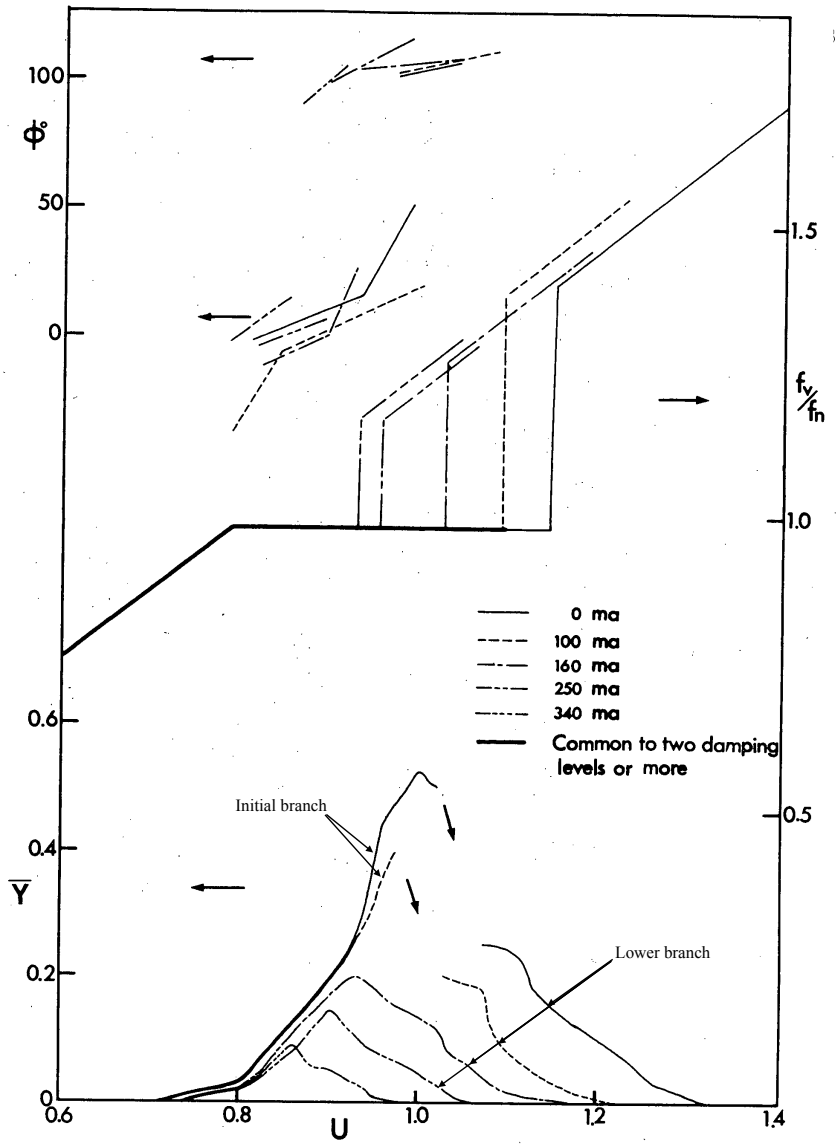


Figure 2.9: Phase shift, ϕ, vortex shedding frequency, $\frac{f_v}{f_n}$ and heave displacement, $\bar{Y}$ phenomena for an elastically-mounted, rigid circular cylinder with increasing wind speed, [9]. Feng's damping levels are those generated by his electromagnetic eddy-current damper, designed by Smith [26].

The displacement response exhibits hysteresis in the transition between the two branches, denoted by H in figure 2.8. Only when the branches exist, is hysteresis in the displacement observed. The higher damping levels shown in figure 2.9, which have smooth displacement responses, do not exhibit hysteresis. Feng [9] measures the displacement of the circular cylinder with increasing wind speed, decreasing wind speed and the body brought to rest before each increment in wind speed (figure 2.10). Decreasing the wind speed and bringing the body to rest significantly affects the displacement. For decreasing the wind speed, the lower branch extends to intersect the initial branch, resulting in a smooth and continuous displacement response, and there is no longer a branched response. The maximum response, $\bar{Y}_{max}$ is significantly reduced by 40%.

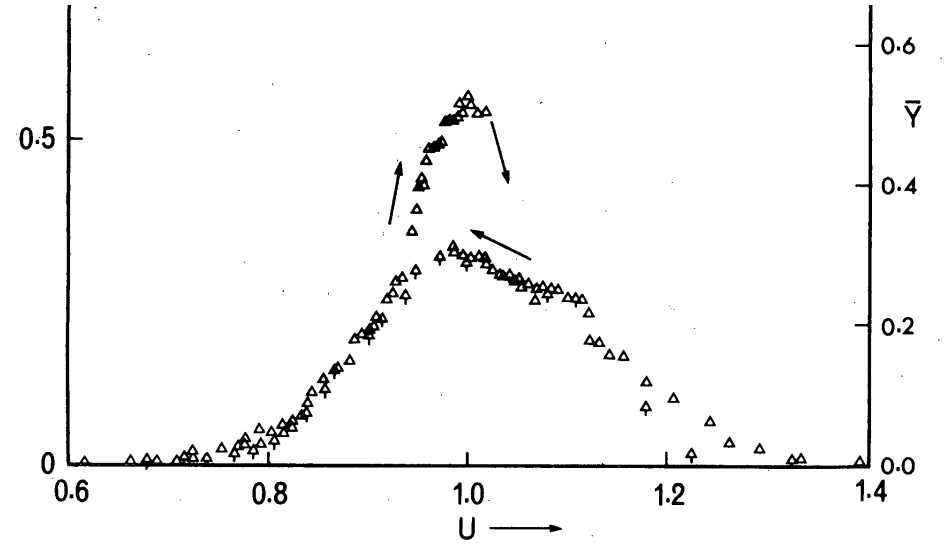


Figure 2.10: Displacement response of an elastically-mounted, rigid circular cylinder at low damping level, exhibiting a branched response and hysteresis, [9]. The arrows indicate the direction of speed increment.

Feng [9] observed a beating phenomenon at the onset of vibration, manifesting as modulated displacement as shown in figure 2.11. The beating was observed for flow speeds at the onset or at the end of VIV. The frequency of the beating was the difference between f_y and f_s, and Feng attributed it to the shedding trying to catch up, and the non-parallel position of the vortex-shedding line along the span of the cylinder resulting in reduced spanwise correlation and associated jumping in and out of resonance.

Structural damping is the dissipation of energy within the structure, often as heat.

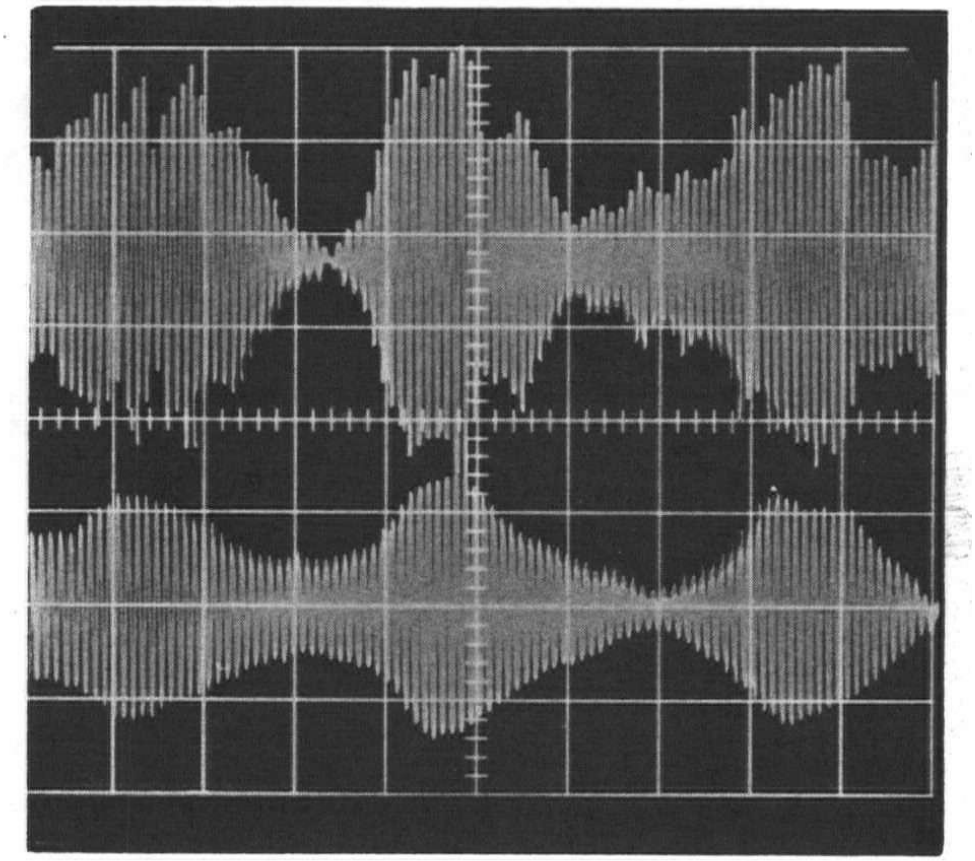


Figure 2.11: Beating phenomenon at the onset of response of a circular cylinder. Pressure (top) and displacement (bottom) time series, [9].

By draining energy from oscillations, damping acts to reduce the amplitude of vibrations and has a significant effect on the response of a structure to VIV. Figure 2.12 shows the response of a model cylindrical stack in wind at different logarithmic decrements of damping, δ_s. It can be seen that at low wind speeds there is little response. As the wind speed increases so that the shedding frequency approaches the natural frequency of the stack, there is an increase in amplitude which remains significant for a range of wind speeds. This response is that of VIV caused by lock-in. Figure 2.12 also shows that, with increasing δ_s, the peak amplitude of response is significantly reduced and the range of wind speeds at which a response is excited also reduces.

In figure 2.9 the damping of the elastically-mounted rigid cylinder has the effect of reducing the range of wind speeds over which the vortex-shedding is locked-in, reducing $\bar{Y}_{max}$ and the speed at which $\bar{Y}_{max}$ occurs: the response to VIV is very sensitive to

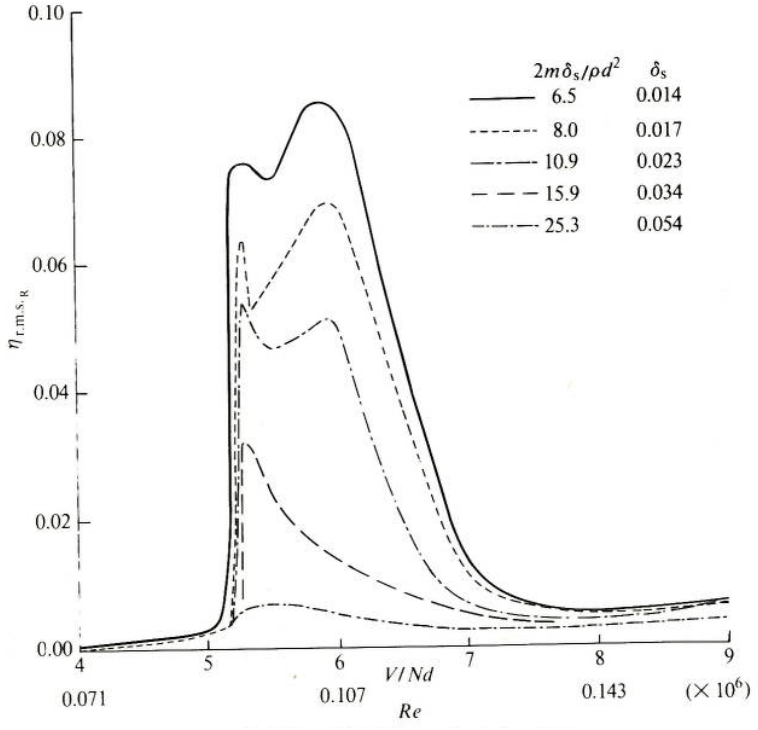


Figure 2.12: Variation of the response of a model circular stack (aspect ratio=10) with logarithmic decrement of damping, δ_s and corresponding Scruton number, $\frac{2m\delta_s}{\rho d^2}$ a measure of the combined effects of body inertia and damping, [27]

.

the level of structural damping. Zradkovich [28] has demonstrated that for large values of mass:damping ratio, expected for bridge decks, the structural response depends on the combined mass and damping, expressed as the Scruton number, 2.5. At lower mass:damping ratios, the mass and damping independently affect the response.

Figure 2.13 shows the spectra of vortex-shedding for stationary cylinders in subcritical and supercritical flows, and smooth and turbulent incident flows. For $Re_D > 150$, the vortex-shedding from a circular cylinder outside of lock-in exhibits large-scale three-dimensionality. It should be noted that although both (a) and (b) in figure 2.13 are subcritical and (c) and (d) are supercritical, there are Re_D differences that may account for some of the different spectra. For the subcritical flow, when the von Kármán vortex street can be observed the spectra exhibit narrowband peaks, whereas for the supercritical flow, when the wake is disorganised, the spectral peaks are spread over a much wider bandwidth with much reduced power. Turbulence appears to have a significant effect on

VIV. It can be seen that shedding occurs over a broader ranger of frequencies for flows with higher levels of incident turbulence, indicative of an increase in three-dimensionality. Large-scale turbulence acts to reduce the spanwise correlation of shedding and causes the wind speed, U to fluctuate in and out of the critical range required to initiate VIV. U needs to remain fairly constant for several minutes for lock-in and for vibrations to build up to large amplitude. Small-scale turbulence reduces excitation by modifying the separation and reattachment of the shear layers on the cross-section.

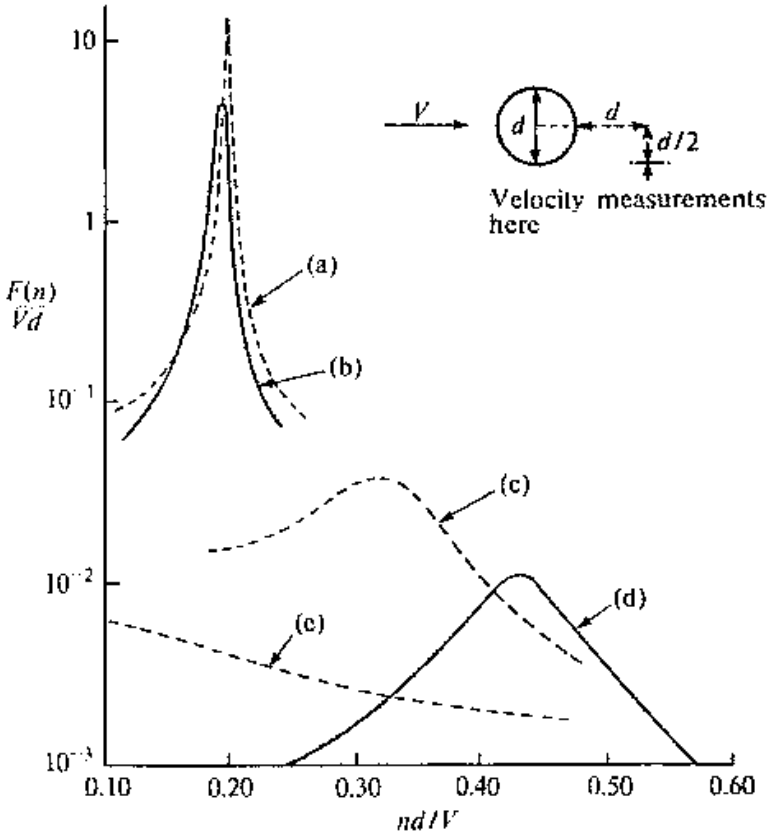


Figure 2.13: The spectra of velocity fluctuations behind a stationary circular cylinder in smooth and turbulent approaching air streams: (a) $Re_D = 0.26 \times 10^5$ (subcritical and turbulent free-stream); (b) $Re_D = 2.2 \times 10^5$ (subcritical and smooth free-stream); (c) $Re_D = 2.1 \times 10^5$ (supercritical and turbulent free-stream); (d) $Re_D = 7.2 \times 10^5$ (supercritical and smooth free-stream); (e) free-stream turbulence spectrum [27]

At the transcritical flow around a circular cylinder, the boundary layers transition to turbulence and separate at more forward positions, resulting in a wider wake than the

subcritical flow, with stronger vortices being shed at a more regular periodicity. There are few studies on the effect of incident turbulence on the response of a body in the trans-critical flow regime at lock-in. However, studies of prototypes and models [12] have shown that VIV diminishes at the turbulence intensities usually experienced by the prototype on site. This suggest experiments in smooth approaching flow at subcritical Re_D will provide a conservative estimate of VIV.

2.3.2 Phase Angle

The phase angle, ϕ is the angle by which the lift force leads the body motion. At lock-in, the interaction between the fluid forcing and the body motion modifies ϕ. ϕ is significant because it gives information on the point in an oscillation cycle during which maximum lift force is generated and it strongly influences the transfer of energy from the fluid to the body motion. The amplitude of oscillation is dependent on the component of the forcing in phase with the velocity of the body, $|C_y|\, sin\phi$.

In figure 2.9, ϕ of an oscillating circular cylinder increases continuously from approximately 0° to 40° and then jumps to 100°. The increase in ϕ during lock-in is important in sustaining vortex-induced motion. In figure 2.14, Bearman [23] plots the data from experiments on forced oscillations of a circular cylinder by Bearman and Currie [11] and shows that, the ϕ jump is actually a progression over a narrow range of non-dimensional wind speeds.

Experiments with forced oscillations allow a more controlled investigation of VIV; the impact of the amplitude of oscillation and the flow speed can be determined by varying each independently. It is widely assumed [29] that the flow patterns in free and forced experiments are the same if Re_D, the non-dimensional flow velocity, (U/f_nD), and the amplitude ratio (A/D) match. This suggests that the previous motion history is not important. Experimental data from free and forced vibration tests, such as the phase angles in figure 2.14 corroborates this assumption.

The jump in ϕ indicates a drastic change in the timing of vortex-shedding. Williamson and Roshko [30] attribute the jump to a transition in the vortex-shedding mode from a 2S to a 2P mode. These modes are shown in figure 2.15. 2S is the classical vortex-shedding

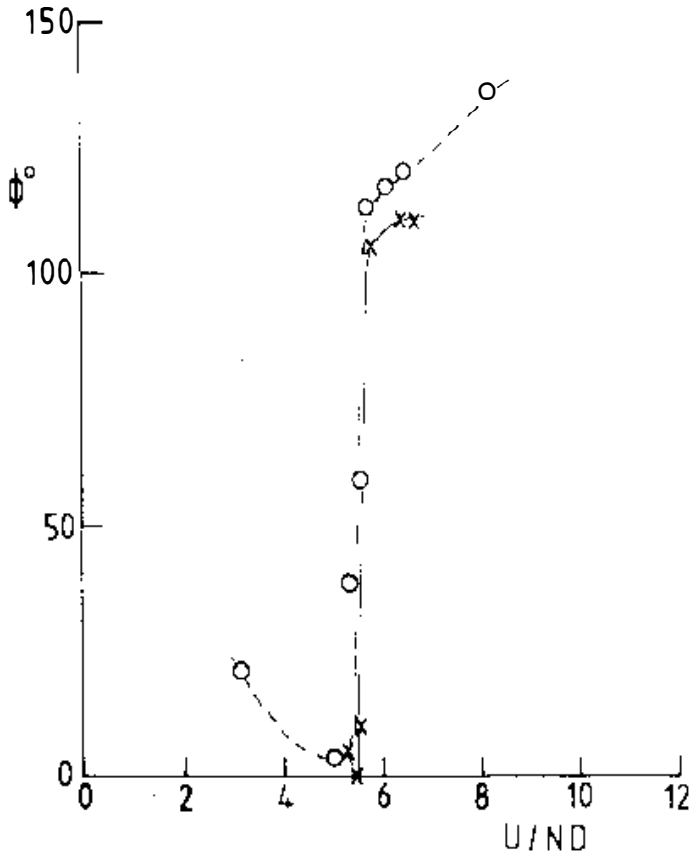


Figure 2.14: Phase angle measurements on a forced and freely oscillating circular cylinder at $A/D = 0.11$, [23]. ◯ forced oscillation, Bearman and Currie [11]; × free oscillation, Feng [9].

mode, with two vortices of opposite sign shed from the top and bottom in each cycle, often described as a von Kármán vortex street (see figure 2.3). The 2P mode is the formation of vortex pairs which convect laterally outwards from the wake centreline. The 2S modes is associated with the initial branch and the 2P mode with the lower branch.

Observations of the forced oscillation of a circular cylinder in water [30] show that during each oscillation cycle, four vortices are formed. As the body accelerates from its equilibrium position one vortex forms, as it decelerates to its maximum upward displacement another vortex forms. As it accelerates downwards towards its maximum downward displacement and then decelerates again, two further vortices are formed. Williamson and Roshko [30] introduce a parameter: wavelength, $\lambda = \frac{U}{f_y}$ that describes the sine wave that the body travels through relative to the fluid. Normalising the wavelength by the

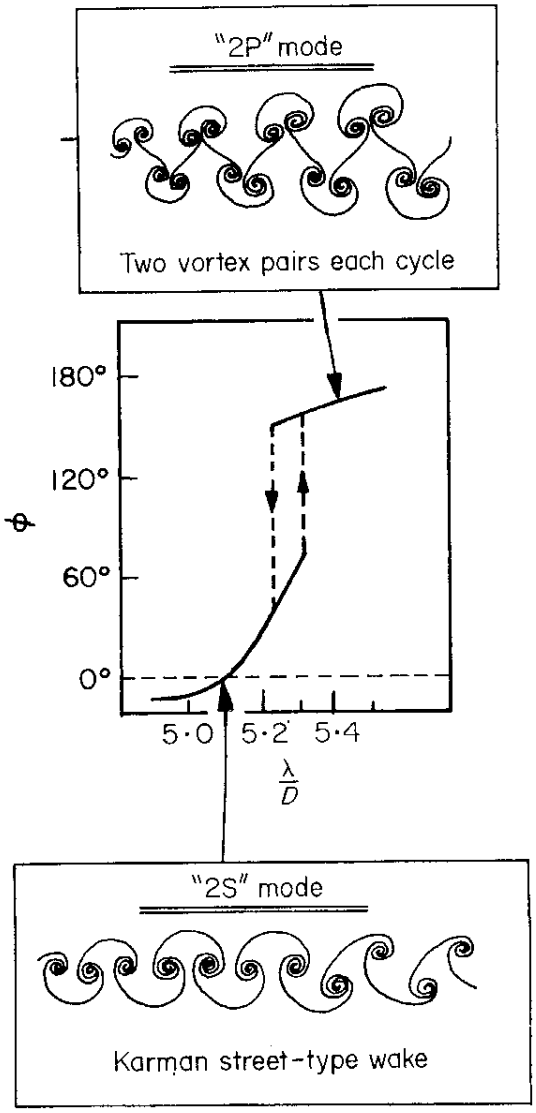


Figure 2.15: Williamson and Roshko [30] explain the phase jump and hysteresis observed in the displacement response of circular cylinders at low damping as a change in vortex-shedding mode.

diameter, D makes it equivalent to the non-dimensional velocity. At low values of λ when the sine wave is "squashed", the four vortices generated in a cycle coalesce to two vortices of opposite sign, forming the classical 2S vortex mode. At high values of λ when the distance between shed vortices is stretched, the four vortices arrange into two vortex pairs and the 2P mode develops.

Figure 2.15 shows the vortex modes on either side of the phase jump. The vortices in the 2S mode are shed when the cylinder is at the extreme points of its motion. In the

2P mode the vortices are shed earlier. It is this change in the timing of shedding that is measured as a phase change. Williamson and Roshko [30] explain that there are a range of wavelengths in which either of the two shedding modes can exist and the prevailing mode is dependent on the history of the flow. Therefore the jump from the 2S to 2P mode occurs at a slightly higher wavelength than the 2P to 2S mode, resulting in the hysteresis observed in the displacement response of a circular cylinder with low damping.

It is clear that the change of phase angle is a key component of increased displacement response, increasing that component of the lift that is in phase with the body motion. How ϕ changes through lock-in is important. Bearman and Obasaju [31] measure the phase angle of a square cylinder, undergoing forced oscillations in air, at different amplitudes and at different wind speeds. When $0 \leq \phi \leq 180$ the fluid forcing excites more motion. Figure 2.16 shows that as amplitude increases, ϕ compensates to limit the excitations to a smaller range of wind speeds.

Griffin and Koopmann [32] have compiled measurements of the component of the lift force in phase with the body velocity, $|C_y|\, sin\phi$ and plotted them against a scaled amplitude ratio $\frac{2|y|I}{D}$ in figure 2.17. The parameter I is a modal response factor, used to compare the data from experiments with different set-ups and bodies with different degrees of freedom.The results show that the component of the fluid force in phase with the velocity increases with oscillation amplitude, up to a maximum limiting value between $0.25D$ and $0.5D$. For increasing amplitudes beyond that, the excitation force decreases until at an amplitude of approximately $1.5D$, there is no excitation. This limits the maximum amplitude for a given body in a given set-up, regardless of how low the damping is. Figure 2.16 and figure 2.17 demonstrate the self-limiting character of VIV.

2.3.3 Vorticity

At lock-in, the interaction between the fluid forcing and the body motion causes an amplification of the fluid force magnitude $|C_y|$ in addition to modifying ϕ. $|C_y|$ is increased due to the combined effect of increasing the strength and spanwise correlation of shed vortices, and a reduction in the vortex-formation region. Davies [33] and Griffin and Ramberg [34] have shown that there is an increase in the wake vortex strength of 36% for an oscillating

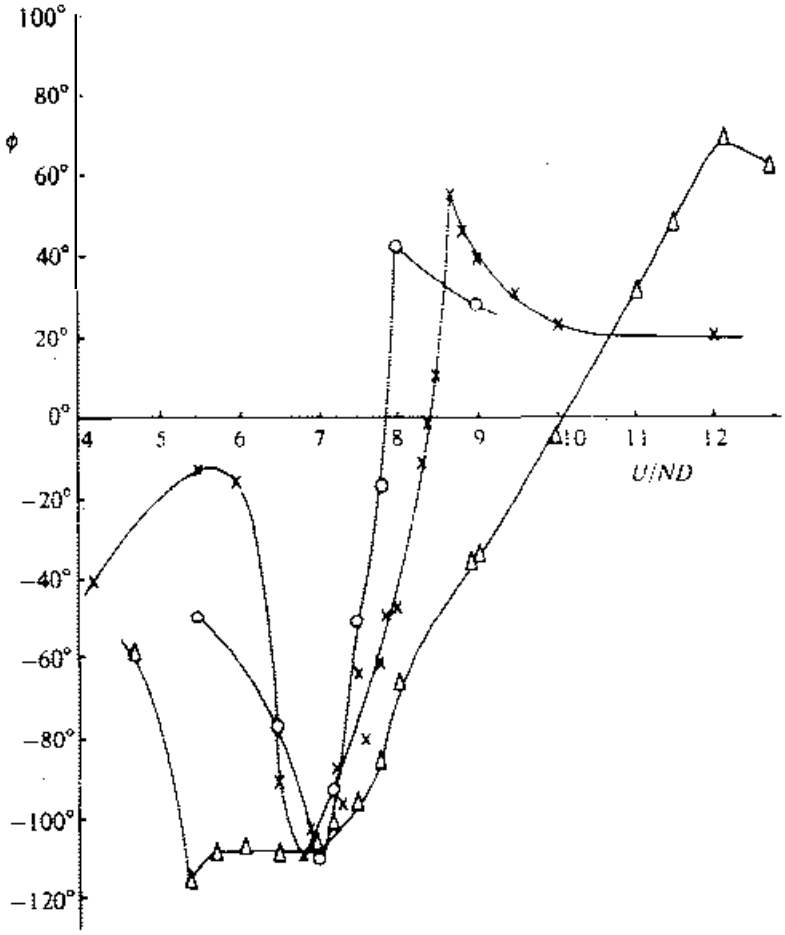


Figure 2.16: Phase angle measurements on a square cylinder undergoing forced oscillations, ◯ $A/D = 0.05$; × $A/D = 0.1$; △ $A/D = 0.25$, [31].

D-section (semi-circular) cylinder and 60% for a circular cylinder respectively, relative to the fixed body case.

Griffin and Ramberg [35] found that the vortex-formation length decreased systematically with increasing amplitude of oscillations. The combination of stronger vortices shed nearer the base of the body and the significant increase in spanwise correlation lead to large increases in $|C_y|$.

Shed vorticity, Γ is often expressed in terms of the base pressure C_{pb}, by rearranging the equation for the rate of circulation shed from a separation point: $(0.5(1 - C_{pb})U^2)$ [36] to give the non-dimensional vortex strength in the wake of an oscillating body:

$$\frac{\Gamma}{UD} = 0.5\alpha(1 - C_{pb})(\frac{U}{f_y D}) \tag{2.12}$$

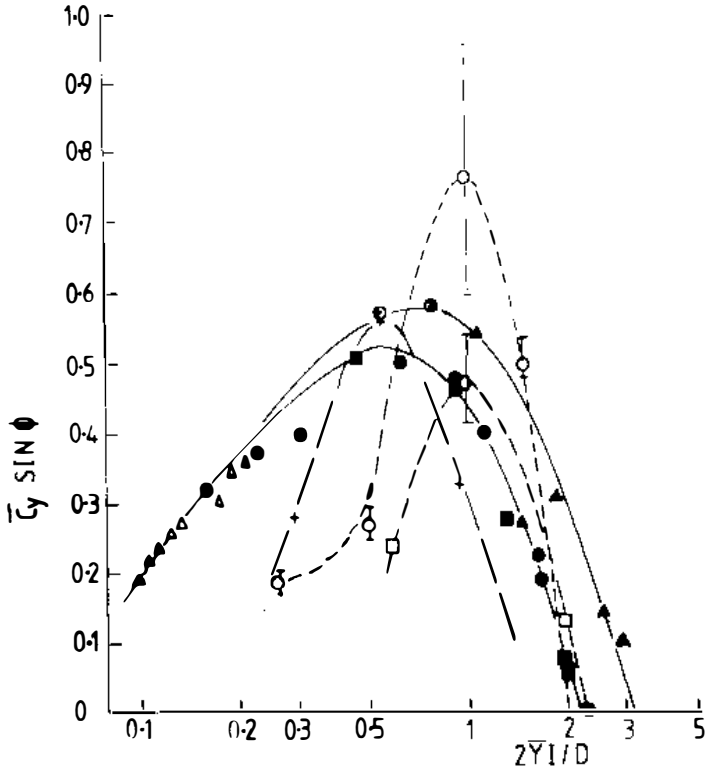


Figure 2.17: $|C_y|\, sin\phi$ versus a scaled amplitude ratio $\frac{2|y|I}{D}$. ■ △ ▲, flexible cantilever in water, □ rigid cylinder-forced vibrations in water, •, pivoted rigid cylinder in water and air; +, spring mounted rigid cylinder in air, [32].

where α is the ratio of vorticity that survives shedding and appears in the wake. This ratio has been shown to be dependent on body shape and Re_D. The resonant point is the flow velocity at which the shedding frequency of the fixed body is equal to the natural frequency in still air. The range of capture is the range of wind speeds for which f_s is locked in and behaves differently to a fixed body. The resonant point always sits within the range of capture for lock-in and its relative position varies with the body shape. Looking at equation 2.12 it can be seen that when the resonant point ($f_s = f_n$) occurs at the beginning of the range of capture, and the shedding is captured for a range of wind speeds, the conditions allow the amplification of Γ during shedding capture, if α and C_{pb} remain constant. Forced oscillations of a circular cylinder by Bearman and Currie [11] agree that the range of capture begins with the resonant point. Therefore the circular section experiences increased vorticity during lock-in because the resonant point falls at

the beginning of lock-in.

When comparing the effect of lock-in on vorticity, it is common to assume α is unaffected by body motion and compare measurements of C_{pb}. Davies [33] has shown that for a D-section cylinder, α varies by 8% from the stationary case. However, other bodies at different Re_D may behave differently.

2.3.4 Spanwise Correlation

For $Re_D > 150$ the vortex-shedding from a circular cylinder outside of lock-in exhibits large-scale three-dimensionality. The increase in two-dimensionality during lock-in is significant. Bearman and Obasaju [23] have shown that a square cylinder undergoing forced vibrations exhibits a large increase in the spanwise correlation of shedding. In figure 2.18, the correlation coefficient, $R(p', z)$ for fluctuating surface pressures, p' measured at the centre of a side face is plotted against separation distance, z. Feng [9] also demonstrates an increase in spanwise correlation of an elastically-mounted circular cylinder at high amplitudes of motion. It is well known that large amplitude oscillations at lock-in increase the spanwise correlation. The motion of the body acts to synchronise the moment and location of shedding along the length. The threshold amplitude of motion required for a significant increase in spanwise correlation depends on the bluff body shape. For a circular cylinder the critical value is about $A/D = 0.05$ [31] and for bodies with sharp-edged separations it is probably lower because the separation point is fixed at the sharp edges. Spanwise correlation is an important parameter with respect to the vulnerability of bodies to large amplitude motion, and many methods of mitigating VIV rely on reducing the correlation, (section 2.5).

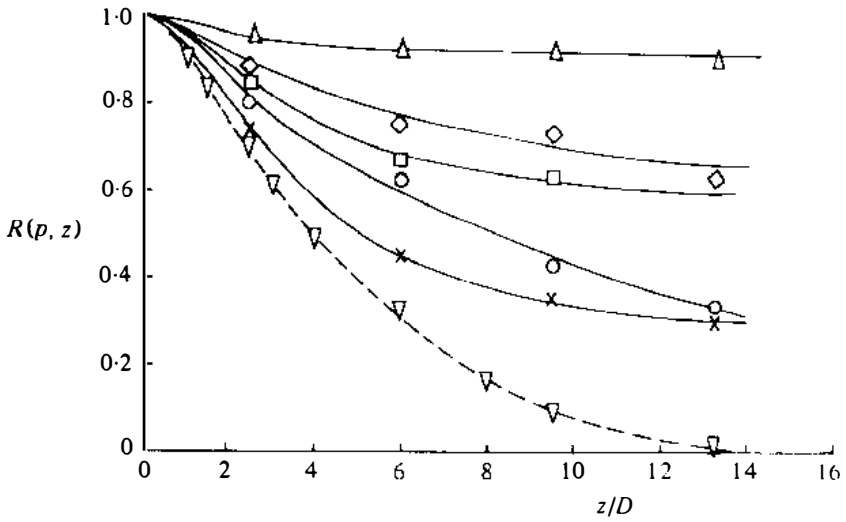


Figure 2.18: The correlation coefficient of the pressure measured at the centre-line of a side face of a square-section cylinder undergoing forced vibration of amplitude $A/D = 1$, versus spanwise separation, z. $\triangle$, $\frac{U}{f_n D}$ within lock-in range 7.3 - 8.5; $\times$, $\frac{U}{f_n D} = 6.2$; $\bigcirc$, 7.0; $\Diamond$, 8.8; $\square$, 12.0. Results are compared to $\bigtriangledown$, body stationary [31].

2.3.5 The circular cylinder and other low-aspect ratio body shapes

Many studies of VIV have looked at the circular cylinder, as the flow is generally well understood and it provides an ideal base case to investigate the fluid-structure interaction. A few studies have looked at the VIV of other two-dimensional shapes, including rectangles, D-sections, triangles, flat plates and trapezoids.

The afterbody is an important physical parameter in the VIV of various body shapes. The afterbody is the cross-section downstream of the separation points and the fluctuating loads act principally on the afterbody surfaces. A D-section cylinder, with the flat face normal to the flow and upstream of its afterbody, can undergo VIV. Vortices are shed off the sharp edges and the resulting forces act on the semi-circle afterbody. The same cylinder positioned with the flat face downstream during lock-in has no afterbody and is not susceptible to VIV.

Feng's experiments [9] on an elastically-mounted D-section cylinder (flat face positioned normal to the flow and upstream) through lock-in (figure 2.19) can be compared

with experiments on a circular cylinder (figure 2.9). For this shape, all damping levels investigated had a branched response, with the initial branch displaying a kinked response and a flatter lower branch. Unlike the circular cylinder, it is the lower branch that is common for all damping levels. The D-section cylinder is much harder to suppress than the circular cylinder [9], and for the higher damping levels, $\bar{Y}_{max}$ is much larger. Increasing the damping moves $\bar{Y}_{max}$ and the median lock-in speed to higher wind speeds. Experiments on circular cylinders displayed hysteresis at low damping levels only [9]. The D-section exhibits hysteresis up to much higher damping levels, and all of those investigated.

The circular cylinders in figure 2.9 begin their range of capture with the resonant point, whereas the D-section cylinder range of capture straddles the resonant point. Forced oscillations of a square cylinder by Bearman and Obasaju [31] show a range of capture that straddles the resonant point, and forced oscillation experiments on on a triangular section with a vertex pointing downstream by Bearman and Davies [37] ends the range of capture on the resonant point. The circular cylinder jumped out of lock-in, whereas the D-section jumps into lock-in (f_s jumps up to f_n) as well as out of lock-in. It is clear that the body shape has a big impact on the range of capture and how the shedding locks-in.

It has been shown that during lock-in of circular cylinders, the shed vorticity is amplified relative to the stationary body case. This is not the case for all body shapes. Square sections [31], flat plates and triangular sections with a vertex pointing downstream [37] have been shown to reduce vorticity during lock-in. Figure 2.20 plots the amplification of vortex strength for oscillating circular and square cylinders compared to the stationary cases throughout lock-in. It is clear that the vortex strength is significantly amplified for the circular cylinder and slightly attenuated for the square cylinder. Examining equation 2.12 and looking at figure 2.9, the position of the resonant point at the very beginning of lock-in serves to amplify vorticity. For a D-section (figure 2.19) the resonant point occurs further through lock-in and will lead to less amplification of vorticity than the circular cylinder where the resonant point occurs at the beginning of lock-in.

Although the vortex strength of a square cylinder does not increase at lock-in, measurements of the r.m.s. of the fluctuating pressure coefficient, C_p' measured at the centre of a side face, show significant increases [31]. The time traces indicates the peak-to-peak amplitude is of a similar magnitude for the oscillating and stationary bodies. The large

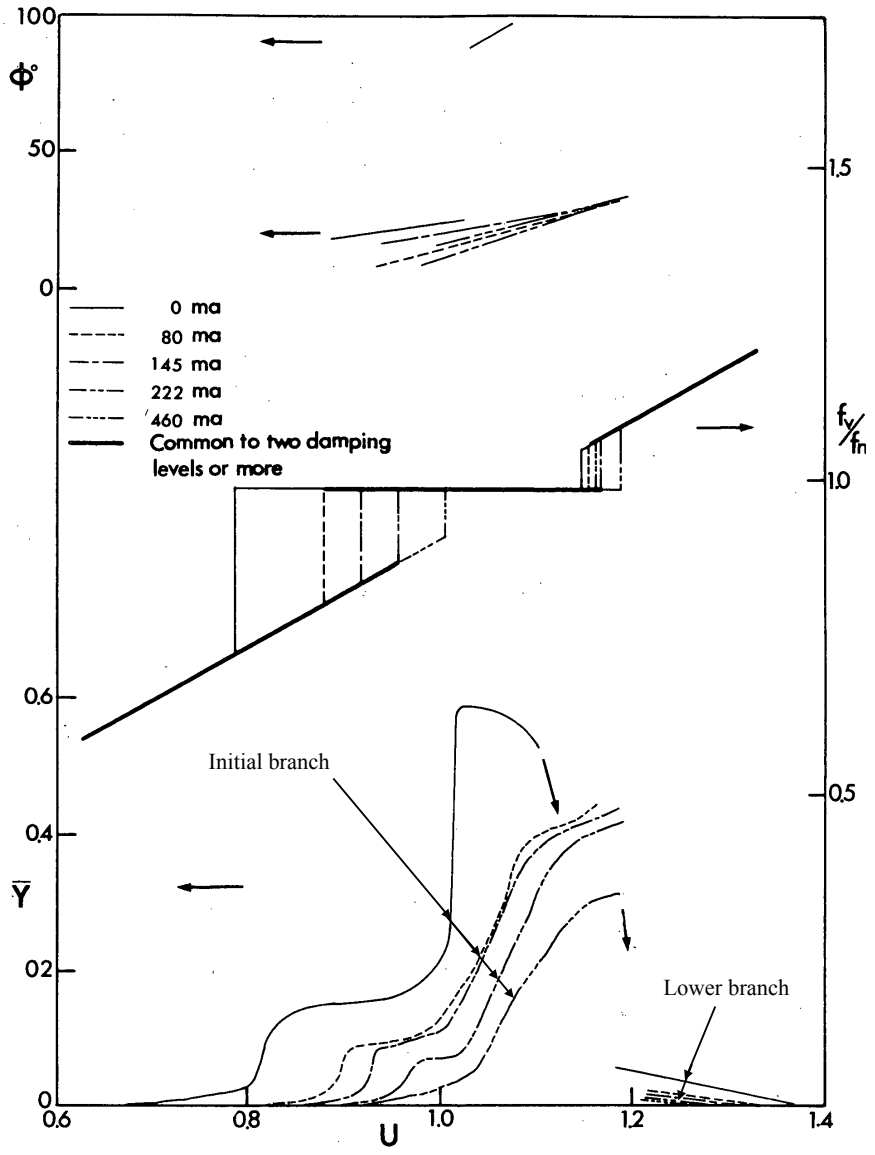


Figure 2.19: Phase shift, Φ, vortex-shedding frequency, $\frac{f_v}{f_n}$ and heave displacement, $\bar{Y}$ phenomena for a D-section cylinder with the flat face normal to the flow and upstream of the semi-circular afterbody [9].

r.m.s. values of C_p' come from the reduced modulation of the oscillating signal, which is more periodic and organised. This implies that lock-in for the square cylinder increases the consistency of shedding but does not increase the vortex strength.

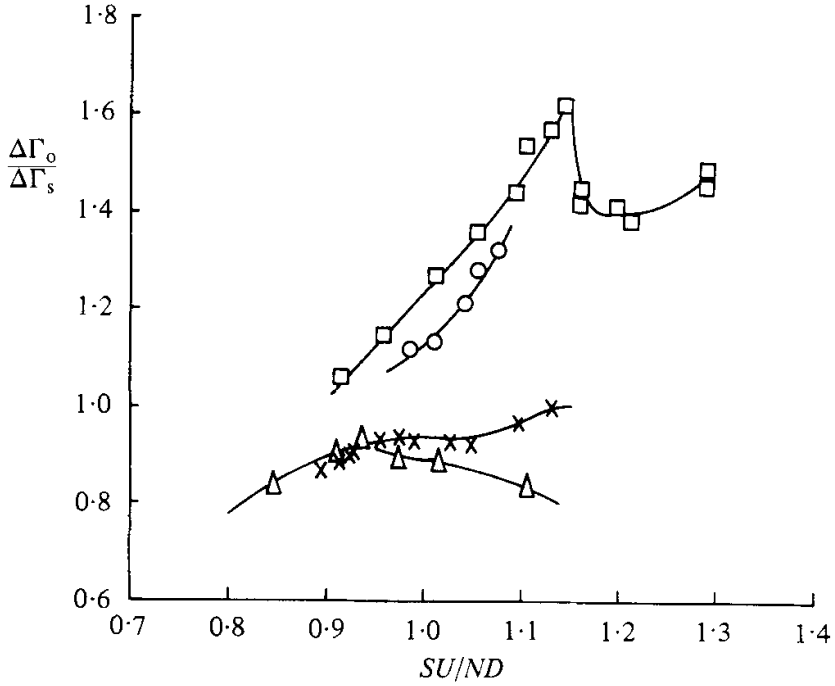


Figure 2.20: Circulation shed per cycle in the range of capture for a circular cylinder (◯, $A/D = 0.1$; □, $A/D = 0.29$) and square section cylinder (×, $A/D = 0.1$; △, $A/D = 0.25$) [31]. Here, S is the Strouhal number, $\Delta\Gamma_o$ is the shed vorticity of the oscillating body, $\Delta\Gamma_s$ is the shed vorticity of the stationary body.

For the D-section cylinder in figure 2.19, ϕ covers a much smaller range of values, with no jumps, except for at the lowest damping level. Figure 2.21 shows a comparison of the phase angles measured at 90° from the front of circular and square cylinders, forced to oscillate at similar amplitudes. As mentioned before, for values $0° \leq \phi \leq 180°$, the fluid force amplifyies oscillations. The circular cylinder is able to sustain oscillations over the whole range of capture whereas the square cylinder is limited to a smaller range at the higher end of the range of capture.

The wake of the circular cylinder is much more three-dimensional than the D-section cylinder throughout lock-in, with lower spanwise correlation of wake velocity [31]. It appears the sharp edges of the D-section act to increase the sensitivity of shedding to motion, and the threshold amplitude for spanwise correlation is reduced.

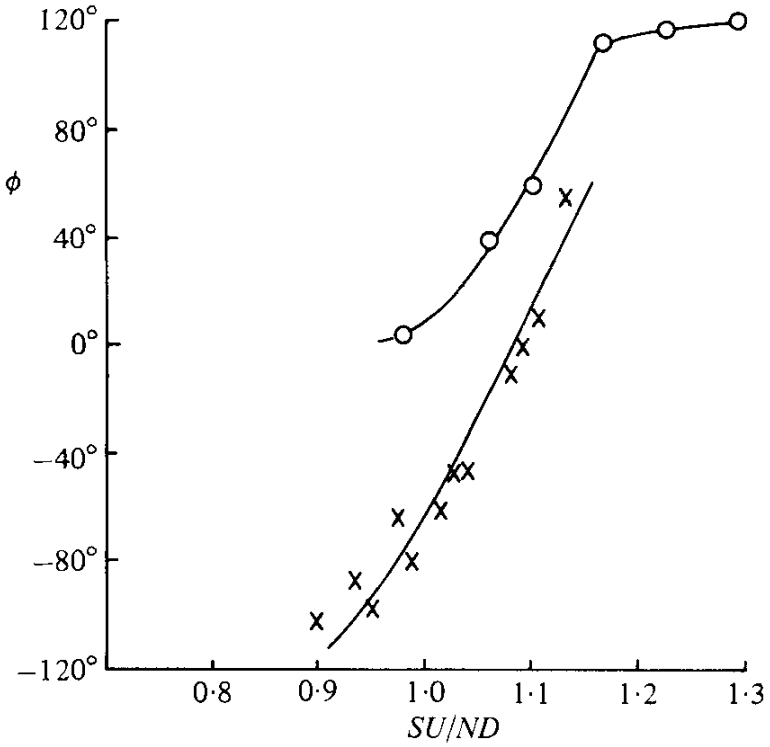


Figure 2.21: Phase angle, ϕ for ◯ a circular cylinder, forced to oscillate at $A/D = 0.11$ and $\times$ a square cylinder, forced to oscillate at $A/D = 0.1$ [31].

The behaviour of some shapes does not follow the circular cylinder, and prediction models devised for the circular sections will not apply well to these shapes. Measurements on the stationary bodies of circular and square cylinders yield higher fluctuating pressures for the square cylinder, which could lead to the assumption that the square cylinder will have larger amplitude VIV when allowed to freely oscillate. However, the fluid-structure interaction for these two shapes is markedly different, amplifying the fluctuating lift on the circular cylinder more than that on a square cylinder. Bearman and Obasaju [31] compare experiments on the forced oscillation of a square cylinder to that of a circular cylinder by Bearman and Currie [11] and find the behaviour during lock-in diverges significantly. A circular cylinder oscillated to $A/D = 0.22$ through lock-in experiences an amplification in C'_p of 3.5 [31]. For a square cylinder at similar amplitudes of motion, the amplification is only 1.6 [11]. Therefore, the mathematical models for a circular cylinder need to be adapted to predict the response of other shapes.

Studies at the National Physics Laboratory by Scruton [22] found that VIV varies with the number of sides of a polygon. Regular polygons with four, six, eight and 12 sides

were tested and at zero angles of wind incidence the strongest excitation was experienced by the square and the weakest by the hexagon.

2.4 Long-Span Bridges

2.4.1 Rectangles and bridge-deck sections

Bodies with appreciable afterbodies experience different and often more complex excitation mechanisms than shorter bodies. The cross-section slenderness ratio, B/D plays an important role in the excitation mechanism of VIV. Shiraishi and Matsumoto [38] classify three groups: Group 1, Group 2 and Group 3, based on increasing slenderness ratio, that exhibit different excitation mechanisms. In smooth flow, Group 1 ($B/D \leq 3$) flow strongly separates at the leading edge with no reattachment over the body. This mechanism is termed Leading Edge Vortex Shedding, LEVS (figure 2.22). Many of the bodies described earlier in this section, including the D-section and square cylinders belong to Group 1. The shed vortices form a von Kármán street, characterised by the Strouhal number. The maximum response occurs at the resonant point, (1/St) (figure 2.23).

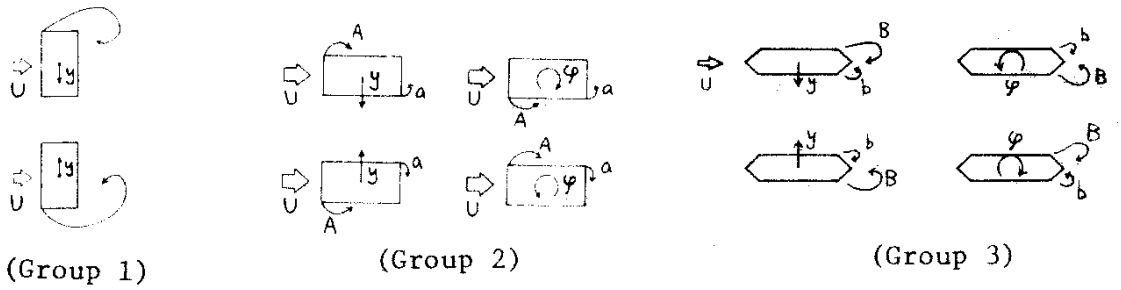


Figure 2.22: Group 1, Group 2 and Group 3 flow patterns [38].

Longer bodies ($3 \leq B/D \leq 7.5$) experience an Impinging Leading Edge Vortex mechanism, ILEV. Unstable shear layers on the top and bottom surface form vortices at the leading edge, that travel down the body, where they coalesce with secondary vortices that form at the trailing edge, and are shed as intense vortices that can excite motion. Figure 2.24 shows the simulation [10] of the flow around an oscillating rectangle, $B/D = 4$,

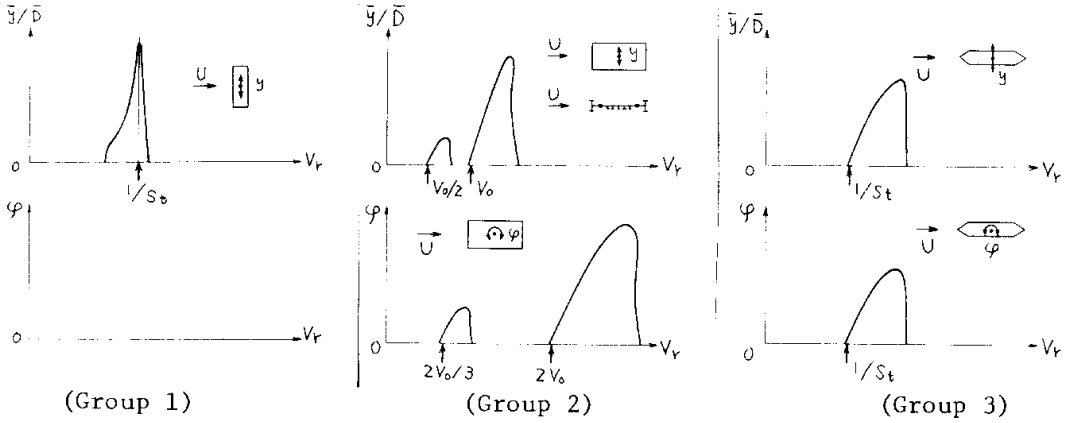


Fig.4 Responsive Amplitude

Figure 2.23: Response amplitudes for Group 1, Group 2 and Group 3 bluff bodies in vertical and torsional VIV. V_0 is the onset critical velocity in heave, n=1 [38].

excited by ILEV. This mechanism is independent of the fixed body shedding and St. Instead, Naudascher and Wang [39] define a modified Strouhal number, St^*:

$$St^* = \frac{f^* D}{U} = (\frac{n-\varepsilon}{\frac{e}{D}}) \times \frac{V_c}{U} \tag{2.13}$$

where f^* is the frequency of impinging vortices, $n = 1, 2, 3, ...$ is the number of vortex pairs shed per oscillation cycle, ε accounts for particular flow conditions (e.g. surface roughness and I_u), e is the distance between the beginning of the shear layer instability (the leading edge of a trapezoid) and the end point (the shedding point), and V_c is the convection velocity of impinging vortices ($\approx 0.6U$). Both ε (= 0 to 0.5) and V_c depend on the vortex mode, n, where $n = 1, 2, 3, ...$ and the particular flow conditions. When $n = 1$, two leading edge vortices convect to the trailing edge, one on the top surface and one on the bottom surface, and a pair of vortices are shed in one oscillation cycle. When $n = 2$, four vortices are shed per oscillation cycle. The addition of fairings to the box girder introduces two additional slenderness ratios, one based on the top surface, e_t and one based on the bottom surface, e_b. For a trapezoid, e_b is often appreciably shorter than e_t. Whereas St is dependant only on the thickness, D, St^* is dependant on the slenderness ratio, B/D, and the onset critical velocity, V_{CR} increases linearly with B/D (figure 2.25).

For ILEV excitation the phase of vorticity differs for heave and pitch motion because

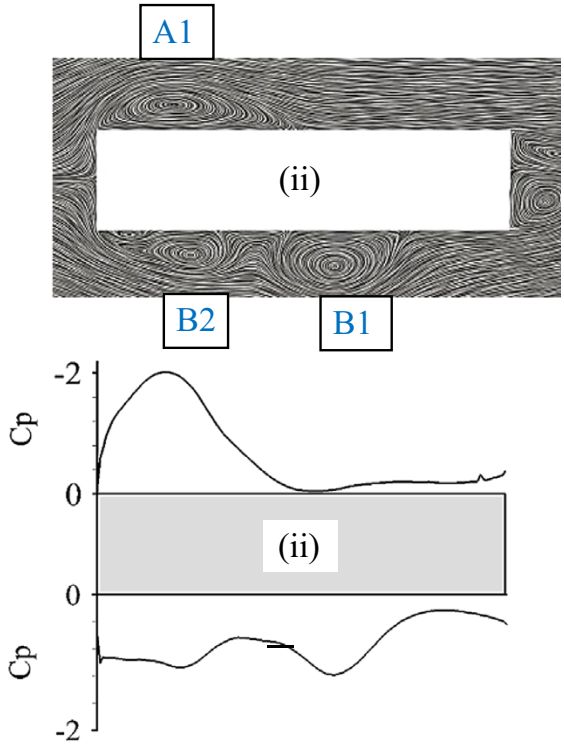


Figure 2.24: Phase-averaged streamlines and pressure distributions over the upper and lower surfaces of an oscillating rectangular cylinder, B/D=4, at peak amplitude within an oscillation cycle. Flow is from left to right [10].

the time it takes the vortices to travel along the body differs: nT_0 in heave and $(n-0.5)T_0$ in pitch, where T_0 is the natural period of motion. This results in differences for the wind speed for the onset of vibrations, V_{CR} and n=1 modes tend to have larger amplitudes than higher modes. Experimental data, shown in figure 2.25 from wind tunnel tests show good agreement for bodies: $2 \lesssim B/D \lesssim 9$ with equation 2.14 for $n = 1$ and $n = 2$. ε is made 0 for simplicity.

$$V_{CR,H} = \frac{e}{D}\frac{1}{0.6n} \tag{2.14}$$

$$V_{CR,T} = \frac{e}{D}\frac{1}{0.6(n-0.5)} \tag{2.15}$$

Multiple oscillation instances can occur, each associated with an n value. In reality

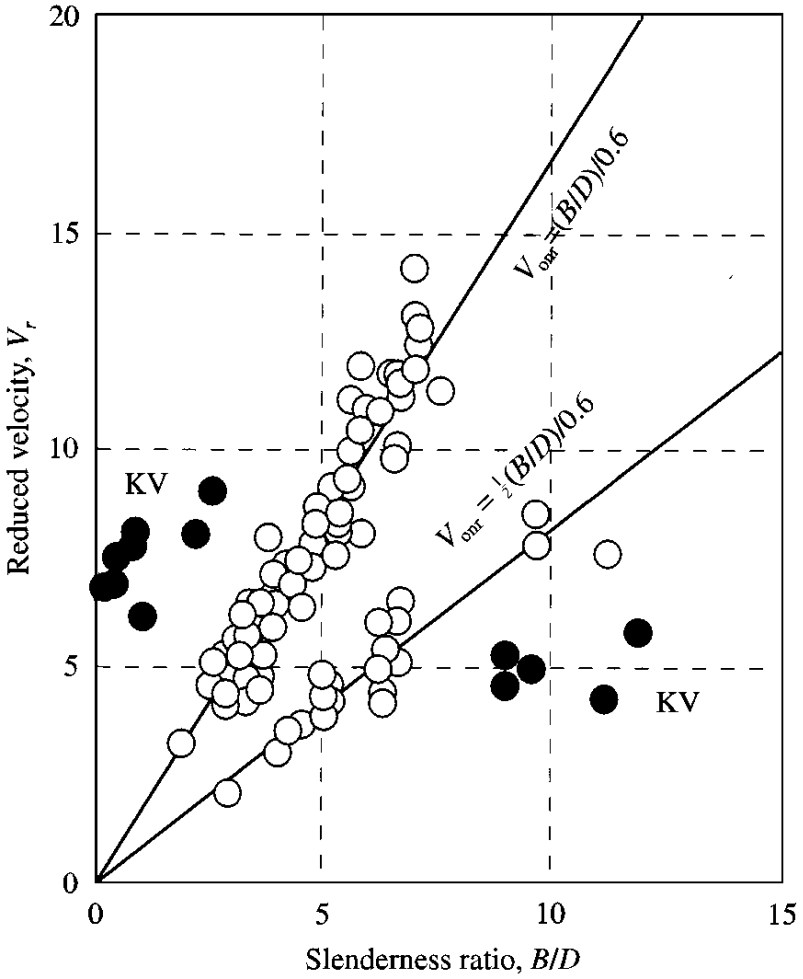


Figure 2.25: Reduced onset critical velocity, $V_{CR,H}$ observed for various bluff bodies. The lines plot equation 2.14 for ILEV excitation, n=1 and n=2. KV denotes von Kármán street excitation [40].

only the lower modes have been observed in experiments and full-scale [39]. Figure 2.23 shows the first and second mode responses for ILEV excitation. There has been variability observed for the onset wind speeds; experiments by Zhang *et al.* [41] on a twin box birdge section shows a small torsional peak at $\approx \frac{V_0}{2}$. Figure 2.26 plots the dependance of amplitude on B/D. The ILEV excitation can generate multiple lock-in instances, as shown in figure 2.23. The secondary mode, n=2 is associated with lower wind speeds and is often smaller amplitude [38]. However, Naudascher and Wang [39] show in figure 2.26 that as the body slenderness increases: a) the n=2 mode appears and then dominates, b)

the oscillations reduce. The cylinders in figure 2.26 can be excited into motion by ILEV and TEVS modes and the response is dependant on the shape of both fairings.

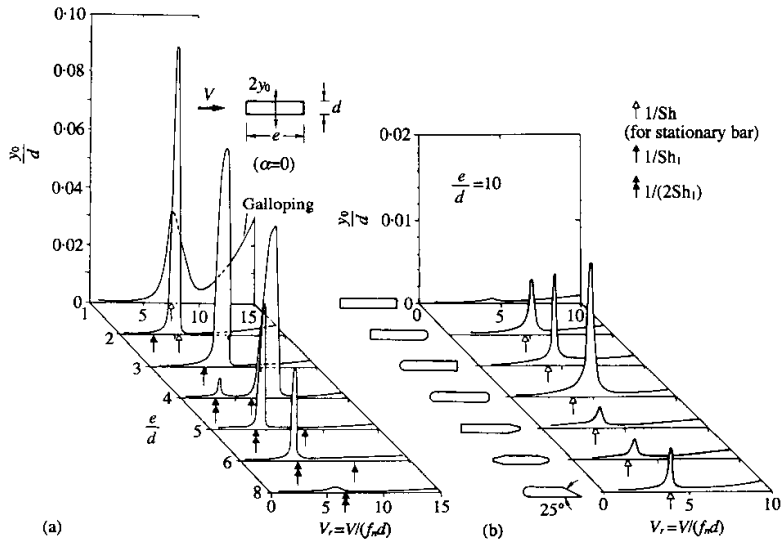


Figure 2.26: Response of cylinders undergoing self-excited heave oscillations a) rectangles of varying slenderness, B/D and b) fixed slenderness, $B/D = 10$, different shapes. $\alpha = 0°$, $I_u = 1\% - 5\%$, δ=0.041 at $y = 0.1$mm, L/B=10. Here, Sh is the fixed body Strouhal number and Sh_1 is the ILEV Strouhal number for $n = 1$ [39].

Nakamura and Mizota [42] agree that increasing the aspect ratio of rectangles reduces the vortex-induced forces. Therefore more slender sections may be expected to experience smaller amplitudes.

Even longer bodies, $B/D \geq 7.5$ fall into Group 3, where the excitation mechanism is trailing edge vortex-shedding, TEVS. Vortices separate at the trailing edge, from the top and bottom of the bluff body alternately and form a von Kármán street. The reduced onset velocity of the first mode is $\approx 1/St$ and is not sensitive to slenderness. This leads to VIV at lower wind velocities than for Group 2, especially at high B/D ratios. Toebes and Eagelson [43] carried out experiments on plates with ratio B/D=8, $\alpha = 0°$, undergoing self-excited torsional vibration. The plates display the TEVS mechanism of vortex formation and a von Kármán street that is dependant on the trailing edge geometry. The control of VIV by the trailing edge geometry and other means is discussed in section 2.5.

Figure 2.27 compiles data from several experiments to show the evolution of shedding with slenderness. Group 2 is split into Group 2a and Group 2b, both ILEV modes, where for the fixed body in Group 2b, the shedding is too weak to be measured on the stationary body. The discontinuities in the shedding indicate transitions between the modes of shedding, LEV to ILEV to TEV. It can be seen that for some slenderness ratios multiple excitation modes can exist. Parker and Welsh [44] found that a rectangle with a semi-circular leading edge transitions from Group 1 straight to Group 3. It should be noted that at low $Re_D \approx 10^3$ that ILEV modes one to four were observed on a stationary rectangle. At higher wind Re_D only $n = 1$ in regime 2a was observed. Schewe [45] observed ILEV modes up to n=5 in bending and n=6 in pitch for an elastic H-section in a wind tunnel (figure 2.28).

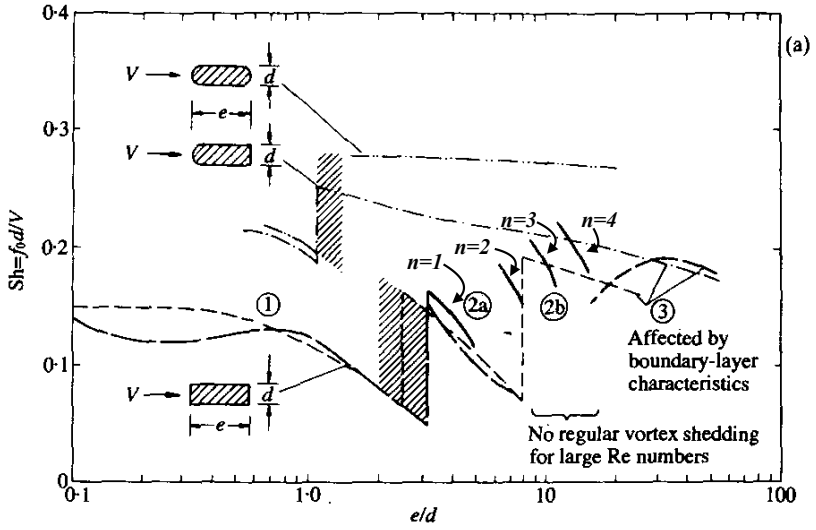


Figure 2.27: Strouhal number, St, St^*, for stationary rectangular prisms of different slenderness ratios, B/D in cross-flow $\alpha = 0°$: ——, Nakamura, Ohya and Tsuruta [46] for $I_u = 0.3\%$, $Re_D = 1000$; – – , – · – , Parker and Welsh [44] for $I_u = 0.2\%$, $1.7{\times}10^4 \leq Re_D \leq 3.5 \times 10^4$; – · · – · ·, Nguyen and Naudascher [47] for $I_u = 4.5\%$, $Re_D = 1300$ [39].

The trapezoid in figure 2.4, $B/D = 6$, exhibits a hybrid excitation mechanism at low Re_D. Trailing edge vortices are observed on the top and separated leading edge vortices on the bottom surface. The Re_D sensitivity for this trapezoid occurs because

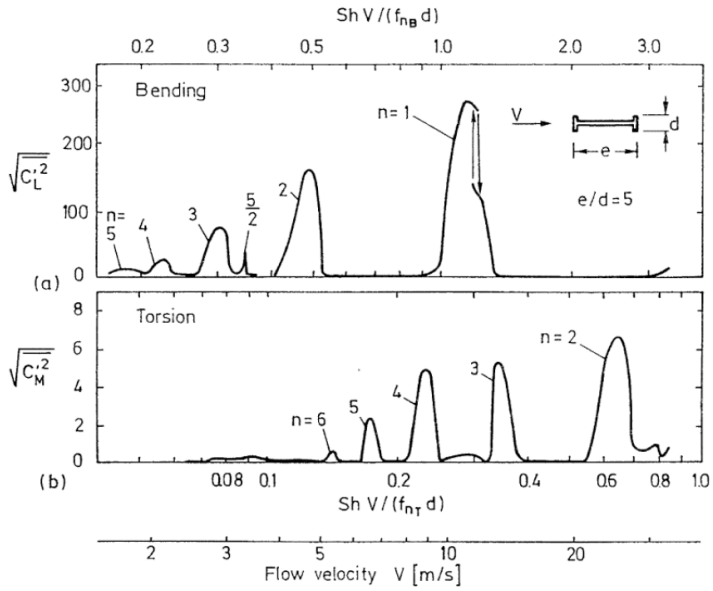


Figure 2.28: Response diagrams for bending (top) and pitching (bottom) for an elastic H-section ($B/D = 5$) placed in a low turbulence flow, $Re_{D,max} = 1.25 \times 10^6$, at zero incidence [45].

several excitation mechanisms exist. Figure 2.27 shows that for a range of slenderness ratios, $2 \lesssim B/D \lesssim 4$ for a rectangle, multiple excitation mechanisms have been observed at different Re_D. It may be that Re_D that plays a significant role in which excitation mechanism manifests. Computational simulations by Corriolis and Morgenthal [48] agree that for static rectangles of $2 \lesssim B/D \lesssim 5$ two flow patterns can exist. The lower values of St are associated with the ILEV mode and higher wind speeds. The higher values of St are associated with a von Kármán-type flow at lower wind speeds. Simulations on the oscillating box-girder deck of the Volgograd Bridge in Russia, $B/D = 2.1$ identified that the von Kármán-type flow is favoured in VIV. At higher slenderness ratios the rectangle exhibits only one mechanism. Therefore Re_D similitude may be required for shorter bodies but not necessarily for more slender bodies.

Some prismatic structures are excited by both Group 2 and Group 3 mechanisms. At high Re_D, ILEV Group 2 is often too weak to be measured on stationary prisms. Although still present, it requires amplification to appear in measurements, either by sound [49] or motion of the leading edge at or close to f^*. Very small vibrations cause sufficient control of the leading edge vortex generation to revive ILEV at high Re_D [50]. Figure

2.27 shows the vortex-generation of stationary rectangles at low Re_D but is applicable to the case of flow-induced vibrations at high Re_D. Terrés and Nícoli [51] found that an elastically-mounted 1:70 scale model of the Storebælt bridge ($B/D = 7.6$) experienced TEVS that triggered low amplitude oscillations and excited motion-induced ILEV. ILEV triggered by the TEVS mode are often referred to as motion-induced vortices [52][10] and can happen when the frequency of shedding of both modes are similar, $St* \approx St$. Measurements of the pressure distribution on the oscillating body confirm the presence of motion-induced components not present in the flow around the stationary body. The fixed body experiences significant pressure fluctuations only at the trailing edge. Significant pressure fluctuations are observed at the leading edge, only when the body is moving.

Hysteresis was observed in full-scale measurements of the Storebælt bridge, with wind-tunnel data [51] showing good agreement, (figure 2.29). With the wind speed increasing, the response curve is ABCDE. With the wind speed decreasing the response curve is ABFDE, with a lower maximum amplitude, a reduced response range, but the same onset critical reduced velocity. Hysteresis for a box-girder is similar to that of a circular cylinder (figure 2.10).

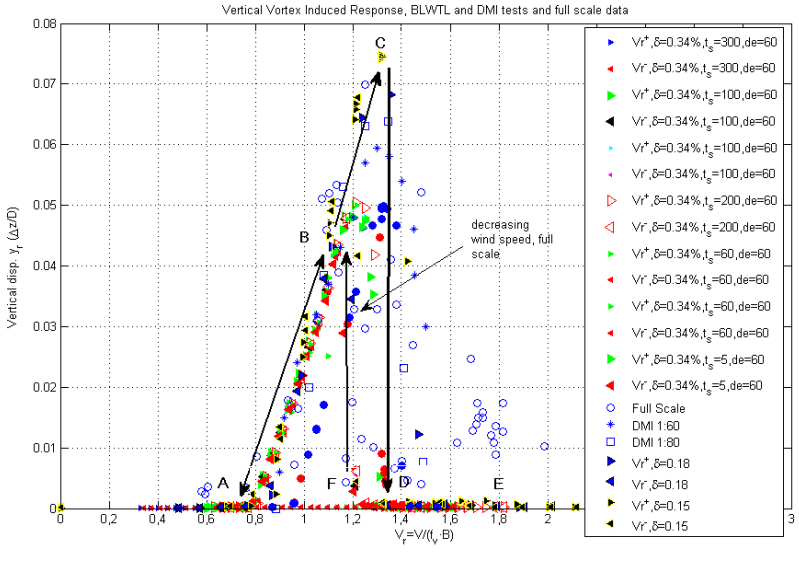


Figure 2.29: Observed vertical VIV for the full-scale and wind tunnel tests of the Storebælt bridge, at different damping values and wind speed history, [51].

2.5 VIV observed in existing bridges

The dynamic effects of the wind on bridges have been investigated and studied with greater interest since the oscillation to collapse of the original suspension bridge over the Tacoma Narrows, near Seattle, USA in 1940. It oscillated to destruction in a torsional mode of flutter. Flutter is a divergent instability caused by the interaction of wind and structure and leading to large amplitude oscillations, often to destruction. Although not the first bridge to be destroyed by wind-induced instabilities, the Tacoma Narrows collapse was a landmark event, changing the approach of structural engineers to wind design of long-span bridges.

The amplitude of VIV in bridges is relatively modest compared to other wind-induced oscillations, such as flutter. However it is present, observable and a design concern. Several bridges of different forms have experienced VIV. Figure 2.30 presents a view along the deck of the Storebælt bridge undergoing VIV.

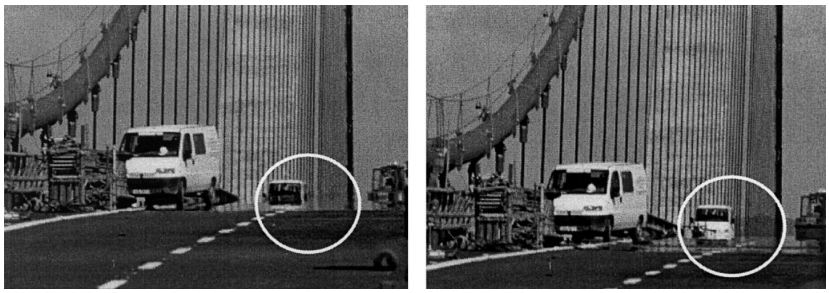


Figure 2.30: View along the deck of the Storebælt bridge during large amplitude VIV at the crest (left) and trough (right) of oscillation. The vehicle in the white circle is a parked van which is partly obscured by the crest of the oscillating deck (left) and reappears in the trough (right), [53].

Although VIV is self-limiting and of modest amplitude, and therefore not considered a destructive phenomenon, they present a serious serviceability concern. Fatigue of moving parts results in an increased inspection and maintenance cost. Frequent oscillations of the deck may require the bridge to be closed to traffic, incurring commercial costs, or may impact on the safety and comfort of the bridge users.

By observation of equation 2.4, it can be seen that low values of mass and damping

will result in large amplitudes of motion. Long-span cable-supported bridges are characterised by their low deck mass and low levels of structural damping, (lower-bound levels are typically 0.2% relative-to-critical). Topography near the bridge can impact the homogeneity of wind conditions, such as wind speed and turbulence, along the span. Li *et al.* [54] found that recorded instances of VIV on a 1650m span suspension bridge in China were higher in amplitude when there was increased spanwise homogeneity. Maximum amplitudes occurred when the wind was perpindicular to the span and with low turbulence, in agreement with full-scale monitoring of the Charilaos Trikoupis Bridge [55]. Long-span bridges usually span waterways or flat land with low surface roughness, leading to low levels of freestream turbulence and ideal flow conditions for large amplitude oscillations.

VIV was observed for Tacoma Narrows, as well as several other bridges. In all these cases the oscillations were observable to the naked eye but did not lead to structural failure. The box-girder deck of the River Wye bridge, U.K., completed in 1966 has oscillated in vertical bending [56], at an amplitude of 18mm, over a small range of wind speeds of 7 - 8 ms^{-1}. In 1967, the cable-stayed road bridge at Long's Creek, Canada oscillated in vertical bending modes within the speed range 11 - 35 ms^{-1} [57]. In 1971 the cable-stayed bridge at Onomichi, Japan [56] exhibited similar vertical oscillations. Figure 2.30 shows images of the vertical oscillations of the deck of the Storebælt bridge [53]. MacDonald *et al.* [**?**] investigated the vertical VIV of the Second Severn Crossing cable-stayed bridge, in the U.K., and discovered that while wind tunnel testing during the design stage had predicted VIV, the amplitudes observed in the full-scale were much larger as structural damping and incidence turbulence values derived from recognised design codes varied significantly to real-life values. The sensitivity of VIV to these parameters emphasises the importance of predicting them well. δ_s cannot be determined analytically and design relies on empirical design codes and measurements on similar structures. The Ishikari Kako bridge in Japan [58] and the Deer Isle Bridge in the USA also have experienced VIV. In 2010 the Volgograd Bridge in Russia was closed to traffic soon after opening, after it experienced large amplitude VIV in bending [48]along seven of the 155m main spans of the steel box girder. Subsequent wind-tunnel tests and computational tests [48] confirmed ILEV as the mechanism. The Kessock Bridge, in the U.K., [59] exhibited large amplitude vertical VIV, in agreement with wind tunnel tests in smooth flow.The

VIV disappeared at $I_u \geq 6\%$ highlights the important role of the wind conditions at the site, and the positioning of the bridge spans relative to the critical wind direction. Monitoring of the Charilaos Trikoupis Bridge in Greece by Flamand *et al.* [55] found that turbulence intensities were below 5% for most VIV events, whereas Eurocode design guidance suggested values of 10% and greater.

As the vortex-excitation mechanisms are more complex for bridge deck geometries than circular cylinders, the effects of turbulence are more complex. Wu and Kareem [60] and Matsumoto *et al.* [61] speculate that turbulence can amplify or reduce responses in VIV depending on the interaction of the vortices in the wake (the von Kármán-type) and the motion-induced ILEV. They suggest that if the von Kármán-type vortices dominate, the turbulence acts to reduce VIV amplitudes and if the motion-induced vortices dominate, the turbulence amplifies amplitude. Daniels *et al.* [10] carried out Large-Eddy numerical simulations of an elastically-mounted rectangle, $B/D = 4$ underginging ILEV-induced VIV in heave and torsion. As the turbulence intensity increased up to 12%, the spanwise correlation and the VIV amplitudes were reduced. With the intensity kept constant, increasing the turbulence length scale, L_u at values approximately equivalent to B reduces the impact of turbulence on the spanwise correlation. It should be noted, L_u in these simulations are not equivalent to the large scales seen in the atmospheric boundary layer. Figure 2.31 shows how the spanwise correlation in heave oscillations vary both with oscillation amplitude and incident turbulence. The correlation coefficient, $R_{p',z}$ is almost 0.9 for all separation distances during lock-in in smooth flow, dominated by the motion magnitude of the structure. Increasing the turbulence intensity diminishes the spanwise correlation; doubling the intensity at the critical wind speed halves $R_{p',z}$ and halving the intensity significantly increases $R_{p',z}$. Figure 2.32 shows the numerical simulations of the ILEV formation and convection in smooth and turbulent incident flows. In the smooth flow, the ILEV rolls up in a two-dimensional sheet and convects downstream across the body. In the turbulent flow the ILEV is broken down, diminishing the spanwise correlation of pressure. No combination of length scale or intensity results in larger correlations than the smooth case at the critical wind speed, but Daniels *et al.* [10] postulate that larger length scales than those tested could lead to larger correlations and amplitudes.

In modern day designs of long-span bridges, the options for the structural form of deck

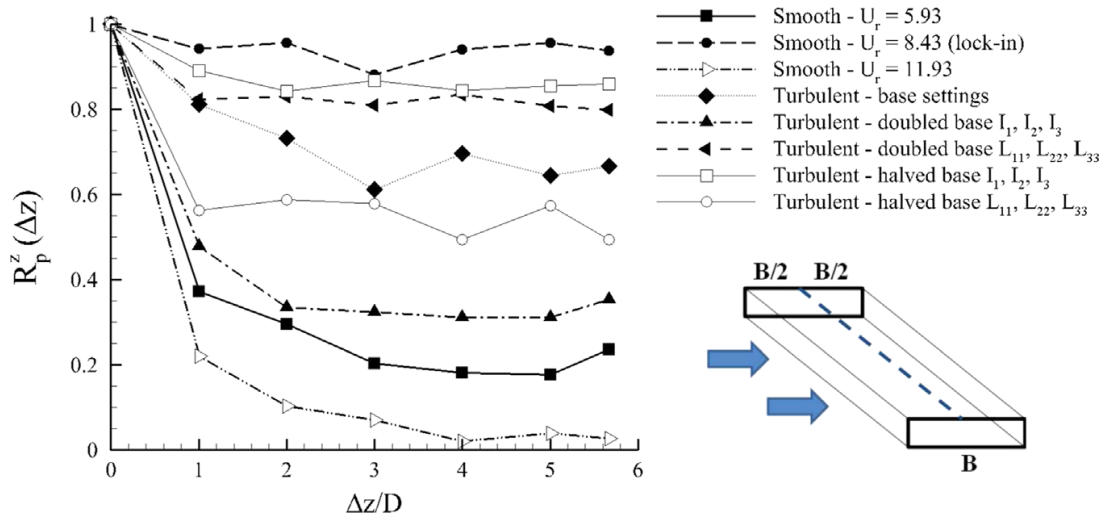


Figure 2.31: Spanwise correlation of fluctuating pressure measured at the centre of the side face of a static and an oscillating rectangular cylinder, $B/D = 4$, in smooth and turbulent flow. $U_r = 8.43$ is the critical wind speed giving maximum amplitudes, other wind speeds are not associated with oscillations. All turbulent cases are measured at the critical wind speed. The base case turbulence: $I_u = 6\%$, L_{11} (streamwise)=2B/3, L_{22} (vertical) = 2B/9, L_{33} (spanwise)=B/3 [10].

may be a plate-girder, a box-girder or a truss-type stiffening girder, as shown in figure 2.33. Additionally, the control and avoidance of unacceptable aerodynamic behaviour is an important factor in the design of these bridges and becomes the dominant concern for very long spans. For cable supported bridges the deck is required to perform a number of functions. Firstly it is a significant element in the global structural system along with the stays and tower, where the primary force is compression and the deck must be sufficiently stiff to resist buckling. Secondly the deck must distribute the applied loading to the global structural system via the stay anchor points. Thirdly, the deck should resist the transverse wind loading and transmit the reactions to the foundations. The shape of the deck has a significant effect on the vortex-shedding. Plate-girder stiffened bridges forming H or channel-sections, such as the Second Severn Crossing are particularly susceptible to vertical bending oscillations.

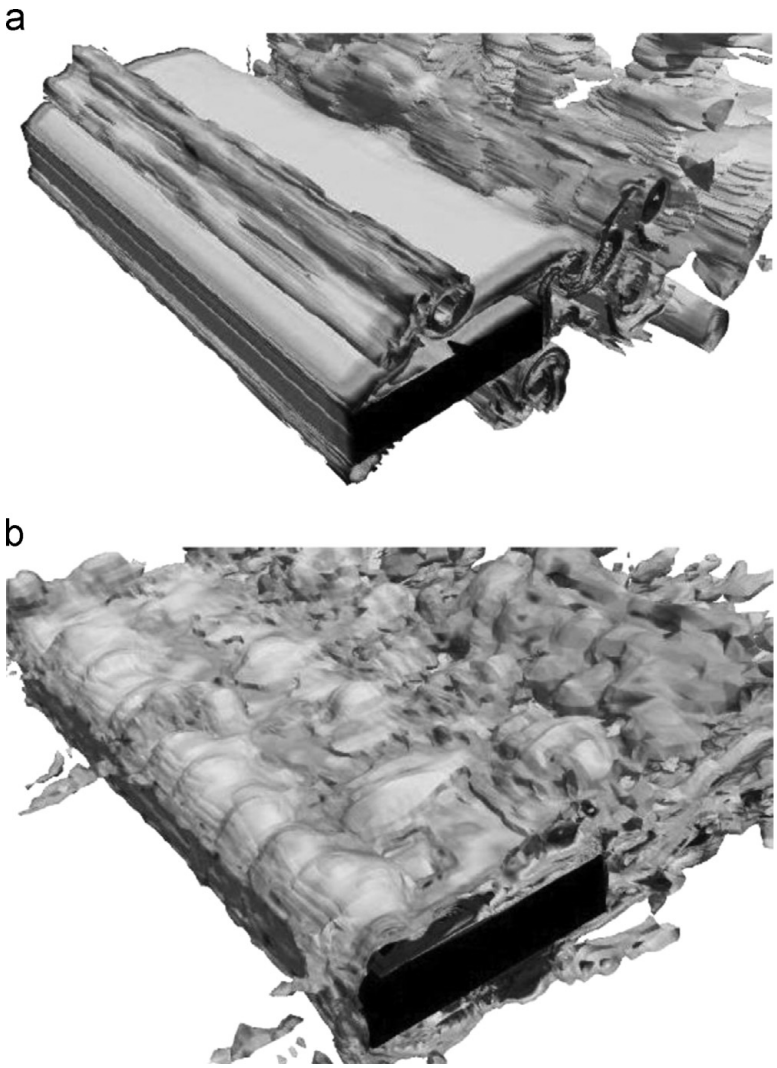


Figure 2.32: Instantaneous iso-surfaces of the vorticity magnitude at lock-in (a) under smooth flow, and (b) under turbulent flow [10].

Most early suspension bridges are truss stiffening girders that do not generate and periodically shed significant vortices and allow the wind to flow more or less undisturbed through the structure. This form of deck, with deep side trusses and bracing is very stiff and continues to be an efficient choice here traffic is required to be carried on two levels and where rail traffic is required to be carried.

The smooth external surface and reduced exposed surface area of the box-girder results in lower maintenance costs than a comparable truss-stiffened deck. The streamlined shape

of the trapezoidal section reduces the drag force from transverse wind loading, leading to savings in the main tower structure compared to plate-girder designs. However, they may suffer VIV at low wind speeds. Most long-span bridge decks constructed now take the form of streamlined box-girders with leading and trailing edge fairings, except for ultra-long spans where flutter limits the aerodynamic stability. As the box-girder is the most common choice of deck construction nowadays, the behaviour in VIV of this shape will be investigated in this study.

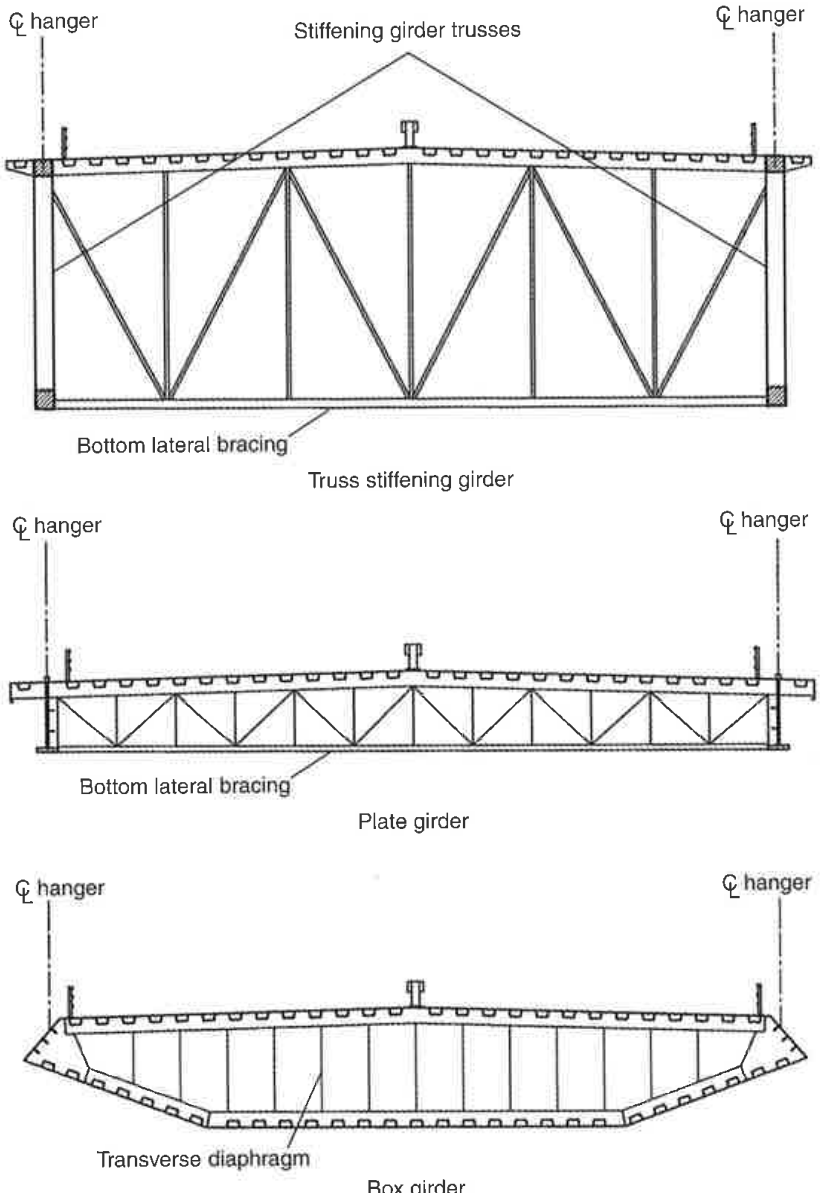


Figure 2.33: Possible structural deck configuration for long-span bridge decks, [62].

The excitation mechanisms are more complex for complex bridge deck geometries. Analytical models are of limited benefit, and more often a combination of computational modelling and wind-tunnel experiments are used to understand the stability of a deck design. Traditionally, wind-tunnel studies have been the most relied on, especially for complex geometries or important structures. Increasingly, as computational resources are more powerful and computational methods more reliable, computational fluid dynamics, CFD, is being used to aid design.

Other components of long-span bridges can exhibit VIV. Towers and cables commonly oscillate due to vortex-shedding and this vibration also needs to be addressed at the design stage. Often, the construction and erection stage of a long-span bridge is when it is most susceptible to aerodynamic loads. During erection the full stiffness of the deck has not been achieved and it is common to temporarily provide mechanical dampers to the bridge during erection to increase the full damping available. The focus of this investigation is the VIV of the deck at completion only.

2.6 Modifying the response

VIV is strongly associated with the natural frequencies of a structure and can occur in any of the modes of bending and torsion and at wind speeds roughly proportional to these frequencies. The simplest mitigation method would be to increase f_n so that resonance occurs at wind speeds which are infrequent. Practically, a box-girder deck may be stiffened in bending by increasing the depth or by the addition of stiffening braces. However, these result in an increase in mass, that somewhat offsets the increase in f_n from stiffness. Heavier decks also have additional material cost in deck and cable. In practice, it is rare that f_n can be increased sufficiently to mitigate VIV.

By observation of equation 2.4, increasing ζ will significantly reduce the amplitude of motion. In practice, long-span bridges tend to have very low structural damping values. ζ can be increased by using materials with a high internal damping such as rubber or viscoelastic materials. However these do not have structural properties that are adequate for the load carrying capacity of bridges. Movement between elements of the bridge can be allowed to increase damping. However moving parts suffer fatigue; increasing

inspection and maintenance costs. A method sometimes used to increase the structural damping is to retrofit bridges with external dampers. The Millennium Bridge in London was retrofitted with tuned mass dampers and viscous dampers [63] after high-amplitude pedestrian-induced oscillations were observed. Generally, tuned mass dampers are more frequently applied, as viscous dampers need two points of relative movement. Tuned mass dampers were added to the Kessock bridge to mitigate the VIV experienced [59]. External dampers are expensive - their addition to the Volgograd Bridge cost an additional $3.8 billion [48], 4.5% of the total budget for the bridge. Aerodynamic passive solutions are better than mechanical dampers as they are cheaper, require less maintenance and are often more aesthetic.

Toebes and Eagelson [43] postulated that the interaction of the top and bottom separated shear layers, on flat plates exhibiting a TEVS excitation, could be annihilated if the shear layers were brought very close to each other, i.e. the trailing edge is faired out to negligible thickness. This is not a practical consideration for a box girder. Many box girders have a single corner trailing edge of negligible thickness, but the separation points of the shear layers move to the adjacent leeward corners of the box, which are separated by $\approx D$ (figure 2.4). Their experiments on plates, $B/D = 8, \alpha = 0°$, with varying trailing edge shapes found that some trailing edges control the VIV over a wider range of wind speeds more readily than others. Rectangular shapes mitigated VIV more effectively than those with triangular fairings and a semi-circular trailing edge.

Experiments by Shiraishi and Matsumoto [38] varyied the leading edge and trailing edge shape independently for rectangular cylinders, B/D =3, 4 and 5, and agreed with the findings of Toebes and Eagelson [43]. They found that heave was more influenced by ILEV mechanism and therefore sensitive to the leading edge shape. A semi-circular edge was more stable than a rectangular edge or a triangular edge. The curved edge suppresses the separation at the leading edge, reducing the strength of vorticity here. Additionally, the amplitudes in the ILEV excitation reduced linearly for increasing B/D, [38]. Parker and Welsh [44] found that the addition of a semi-circular leading edge and trailing edge to rectangles of different slenderness ratios removed the presence of ILEV completely. Instead, as B/D increased, the shedding jumped directly from LEVS to Torsional VIV is found to be more influenced by the TEVS mechanism [43] and therefore sensitive to

the shape of the trailing edge. Fairing shapes at the leading edge that reduce the ILEV instability act to increase the TEV instability when placed at the trailing edge. The rectangular trailing edge was the most stable tested, and the semi-circular trailing edge was the least stable. The sharp trailing edges reduce the generation and intensity of vortices at the trailing edge.

Another way to minimise separations at the leading edge and trailing edge that contribute to the ILEV and TEVS mechanisms respectively, is to place deflectors, or guide vanes at these corners (figure 2.34). Guide vanes are an established and accepted mitigation measure for VIV in long-span bridges today. Section-model tests carried out for the design of the Littlebælt Bridge [64] first demonstrated the effectiveness of guide vanes mounted on the edges of a box-girder to suppress vibrations. An adapted design based on this work was applied to the Storebælt bridge, successfully suppressing the vibration observed during the final stages of construction in 1997 (figure 2.35). The curved steel plates were attached at the joint of the bottom plate and lower inclined plates along the span of the deck.

Further work on VIV mitigation of thin box-girders by guide vanes is found in Larsen *et al.* [65]. Taking detailed measurements from section models in a wind tunnel, he demonstrated how the guide vanes modified the flow regime (figure 2.36) around the asymmetric twin box-girder deck of the Stonecutters Bridge in Hong Kong. The curved plates channel high-speed fluid between the deck plates and the guide vane plates at the leading and trailing edges and into the wake region. The guide vane works to accelerate the fluid around the sharp corners preventing separation of the boundary layer and thus the formation vortices. Guide vanes have been used with success on the Saint. Navaire bridge [66] and the Suehiro Bridge [67]. It is important to note that adding guide vanes to the top corners of a bridge deck may interfere with other road furniture, e.g. solid handrails.

Although guide vanes have been shown to successfully mitigate the VIV of some bridge deck shapes, their applicability to decks of other shapes is unknown. They are a retrofit measure, and modify the aesthetic of the bridge, destroying the otherwise clean lines that a box-girder deck provides. Applying guide vanes along the span of a long-span bridge is an added material cost as well an added inspection and maintenance cost.

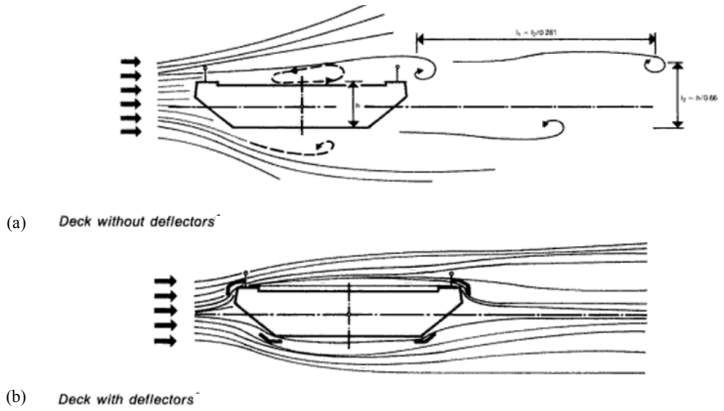


Figure 2.34: A typical trapezoidal bridge deck, B/D=4, exhibiting the ILEV excitation mechanism, (a) bare deck, and (b) with the addition of guide vanes at the leading edge and trailing edge corners, [66].

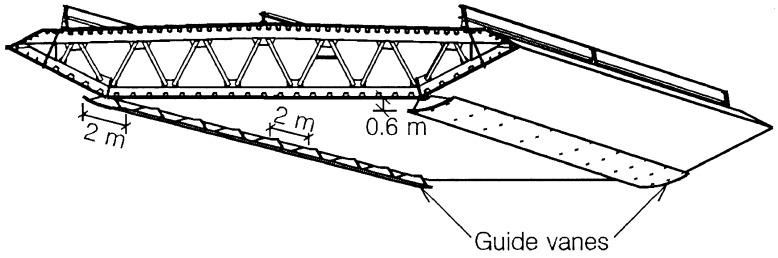


Figure 2.35: Schematic of the guide vanes on the Storebælt suspension bridge, [53].

Another retrofit mitigation are baffle plates. These were used successfully on the Second Severn Crossing [68] (figure 2.37) to reduce the vertical VIV observed shortly after the bridge opened. Two vertical baffle plates were placed beneath the deck, over the central 252m of the main span. Wind tunnel experiments showed a 90% reduction in amplitude of vibration with the addition of baffle plates, and VIV was not observed in the full-scale once they were installed.

The excitation for the deck without baffles was found to be a function primarily of flow on the bottom panels, in the cavity formed between the two main girders. Smoke tests in the wind tunnel identified vortices forming at $\approx B/4$ downwind of the leading edge within this cavity. These vortices convected downwind and navigated around the

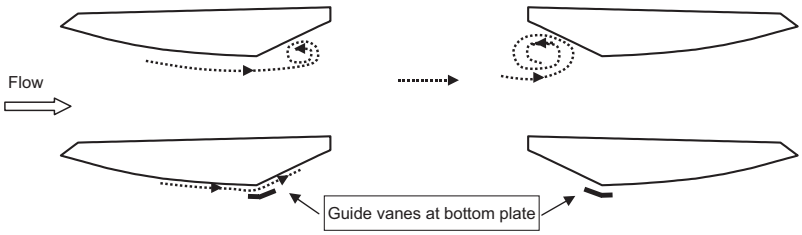


Figure 2.36: The flow pattern without guide vanes (top) and with guide vanes (bottom). The guide vanes on the upwind box inject high speed flow into the wake thus preventing the formation and shedding of von Kármán vortices, [65].

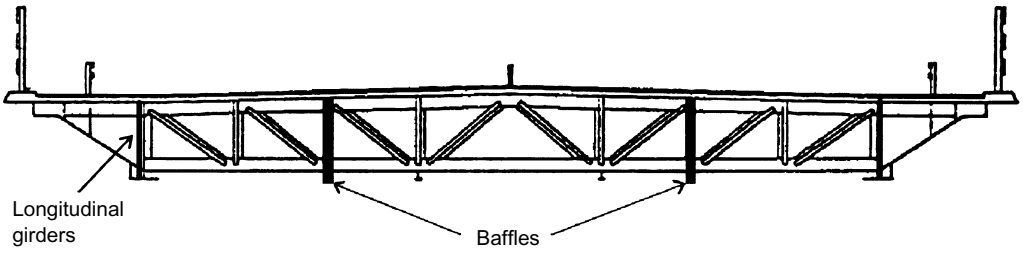


Figure 2.37: Cross-section of the main span of the Second Severn Crossing with baffle plates added to reduce the vertical VIV, [**?**].

trailing girder and into the wake. The positioning of a baffle plate at $B/4$ interfered with the vortex formation [69]. Devices placed on the top face, at or near the leading edge were all ineffective at reducing the VIV, suggesting the flow over the top surface plays a fairly insignificant role. The excitation mechanism of a bottom plate vortex formed near the leading edge and travelling along the body to be shed at the trailing edge is indicative of ILEV, however the bottom vortices appear to dominate.

Underside vortices have been seen for many other plate girder bridges, although sometimes they are not strong enough to cause vibrations, particularly at high incident turbulence. Long's Creek bridge was retrofitted with a soffit plate to mitigate VIV, which closes

off the bottom cavity to the flow and prevents the formation of the ILEV here. Baffles were used to mitigate the VIV of Dames Point bridge, U.S. [70], along with triangular fairings. Figure 2.38 shows nine bridges that have experienced VIV and the mitigation measures employed. The mitigation of the Long's Creek and Dame Point bridges involved triangular fairings at the leading edge and trailing edge.

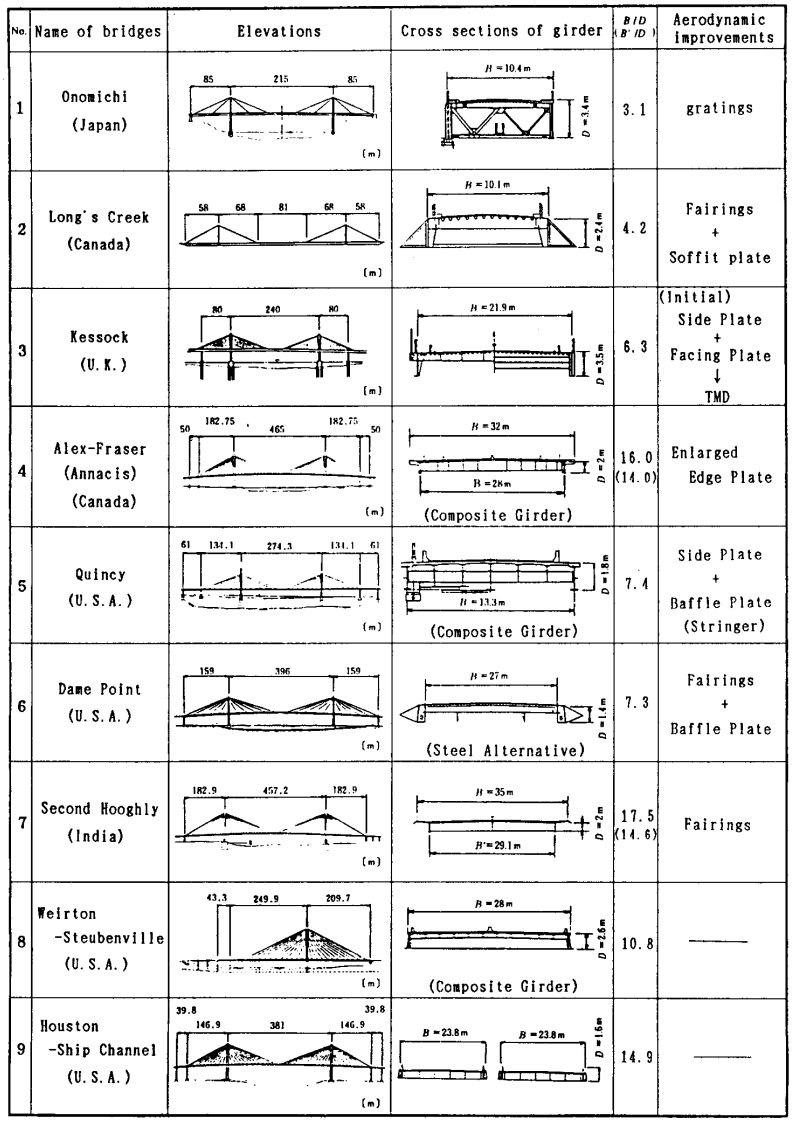


Figure 2.38: Nine long-span bridges that have experienced VIV and the mitigation methods employed, [71].

The rectangles tested by Shiraishi and Matsumoto [38] exhibited both ILEV and TEVS excitation mechanisms and were sensitive to the shape of both the leading edge and trailing

edge. The rectangles tested by Naudascher and Wang [39] in figure 2.26 were excited by either ILEV or TEV depending on the shape of the leading edge and trailing edge. Changing the shape of the leading edge and trailing edge fairings impacts which excitation mechanism, and therefore the amplitude. It can be concluded that VIV mitigation on box-girder bridges needs to look at both the leading and trailing edges.

Haque *et al.* [72] investigated the effect of triangular edge fairings on the aerodynamic response of a rectangular bridge deck using computational fluid dynamics. Their simulations of the stationary deck ($B/D = 5$, $Re_D = 1.2 \times 10^4$) found significant sensitivity of the vortex-shedding to different fairing shapes. The angle at the top of fairings, θ_T, shown in figure 2.39, was varied between 30° and 50° and the angle at the bottom, θ_B was varied between 10° and 40° by moving the nose position and keeping the toe points constant.

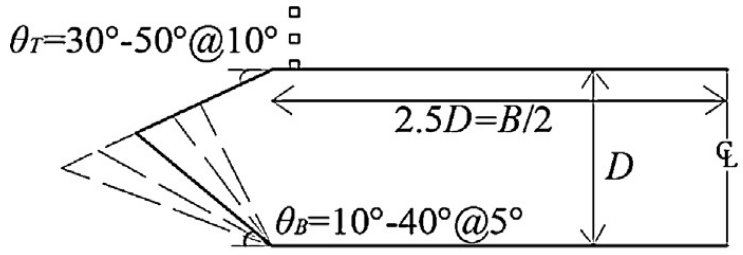


Figure 2.39: Schematic view of the fairing used in simulations to determine the sensitivity of vortex-shedding to θ_T and θ_B, the top and bottom angles respectively, by Haque *et al.* [72].

The simulations included perforated handrails, which are known to have a significant effect on flow and response in VIV. Kobayashi [73] studied the influence of handrails experimentally and found that handrails enhance the vertical VIV, but weaken the torsional VIV. Haque *et al.* [72] found that a critical angle, $\theta_B = 15°$ exists where the fluctuat-

ing velocity in the near wake reduces to almost zero (figure 2.40). The shallower angle, $\theta_B = 10°$ displayed larger velocity fluctuations, indicative of stronger vortices in the near wake. The steeper angle, $\theta_B = 40°$ similarly displayed larger fluctuations in the near wake. Figure 2.41 shows that pressure fluctuations, C_p' are greatest at the trailing edge when $\theta_T = 40°$, $\theta_B = 40°$.

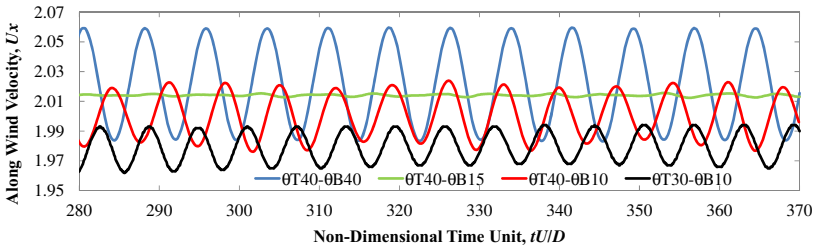


Figure 2.40: Fluctuating velocity in the near wake, measured at 1D downstream and 1D below the trailing edge of a fixed bridge deck section, B/D=5, with varying triangular fairings, [72].

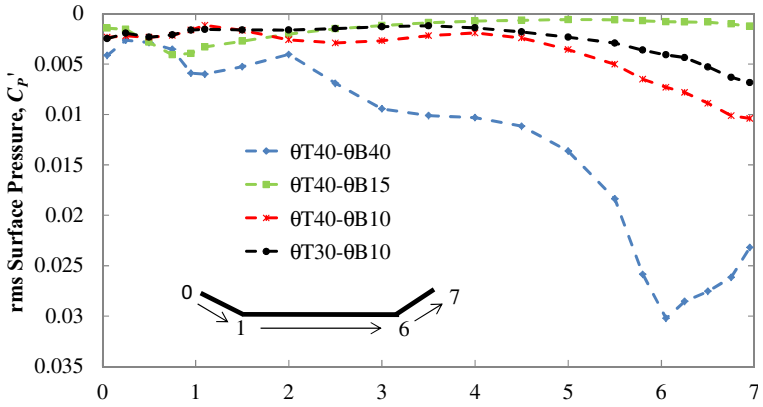


Figure 2.41: rms fluctuating pressure distribution, C_p' on the bottom of a box-girder bridge deck, with varying angles θ_T and θ_B, [72].

Simulations of the velocity fields around the bridge deck (figure 2.43, figure 2.44 and figure 2.42) with different fairings indicate the reason for the differences in pressure and

velocity fluctuations. When θ_B is shallow ($\theta_B \approx 15°$) separation at the corner is reduced. The partially separated shear layer on the bottom surface forms a vortex far downstream, and so the resulting fluctuating forces on the body are weaker. At steeper angles, θ_B, the bottom shear layers separates strongly, and the vortex is formed closer to the body, resulting in larger fluctuating forces (figure 2.45). However, at very shallow angles, $\theta_B = 10°$, the weakly separated bottom shear layer can form a vortex on the top surface if the nose is low enough, i.e. θ_T is high enough, $\approx 40°$. When this happens, the vortex street is formed closer to the body and the fluctuating lift experienced increases. The excitation mechanism here is TEVS, as expected for this stationary body (ILEV are often motion-induced). The angles of the trailing edge fairing strongly influence the forcing felt by the fixed body.

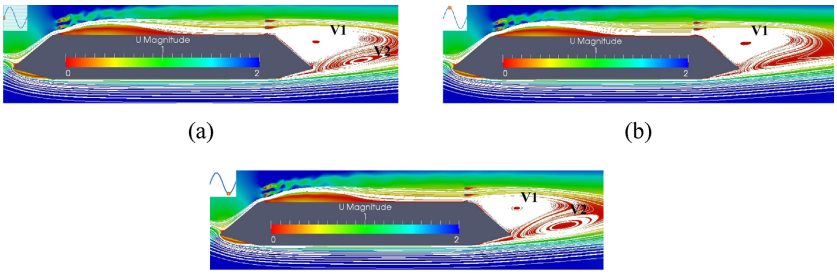


Figure 2.42: Numerical simulation of the velocity field around a bridge deck with $\theta_T = 40°$ and $\theta_B = 15°$, through one lift cycle, showing the von Kármán vortex street in the near wake. Through shedding cycle, (a) 0°; (b) 90° and (c) 270°. [72]

Three-dimensional simulations by Sarwar and Ishihara [74] on the vertical VIV of a rectangular box-girder with outriggers, shown in figure 2.46, in smooth flow, identified sensitivities to geometry. Here, fairings were placed on the outriggers and were found to increase the velocity of the flow at the leading edge, resulting in an intensified shear layer, stronger ILEV vortices, and an amplified response in agreement with experiments in a wind tunnel, and with Shiraishi and Matsumoto [38] who found a triangular fairing positioned at the leading edge of a rectangular body increased the ILEV mechanism.

Larsen and Wall [75] carried out wind tunnel experiments on two-dimensional section models based on the Storebælt bridge, with varying angle between the bottom plate and

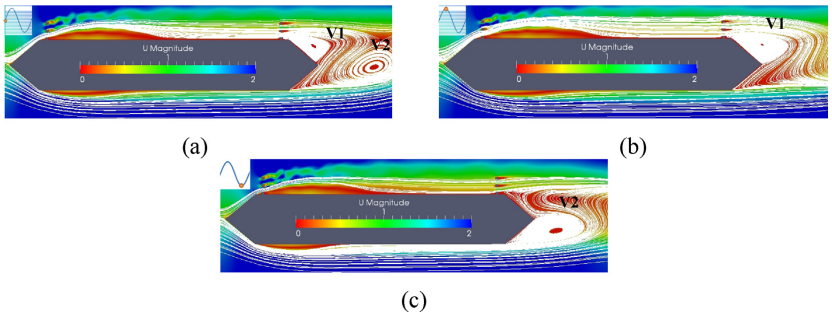


Figure 2.43: Numerical simulation of the velocity field around a bridge deck with $\theta_T = 40°$ and $\theta_B = 40°$, through one lift cycle, showing the von Kármán vortex street in the near wake. Through shedding cycle, (a) 0°; (b) 90° and (c) 270°, [72].

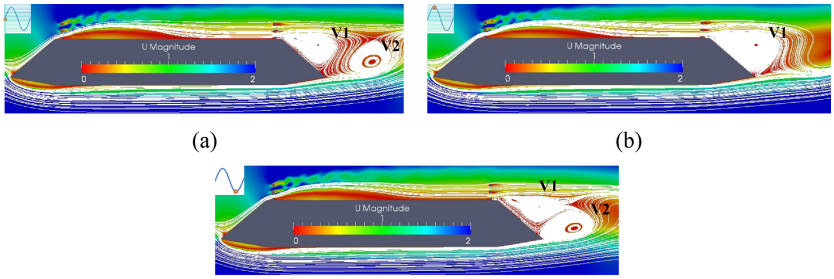


Figure 2.44: Numerical simulation of the velocity field around a bridge deck with $\theta_T = 40°$ and $\theta_B = 10°$, through one lift cycle, showing the von Kármán vortex street in the near wake. Through shedding cycle, (a) 0°; (b) 90° and (c) 270°. [72]

bottom inclined plate. The top knuckle is fixed and road furniture was modelled on the top surface of the deck. It was found that $\theta_B = 14.7°$ inhibited self-excited heave and torsion oscillations at $\zeta = 0.2\%$, (figure 2.47). This is in close agreement with the critically stable angle $\theta_B = 15°$, found in simulations by Haque *et al.* [72]. Larsen and Wall [75] draw a comparison to the flow around aerofoils, which stall at angles of attack $\approx 16°$ (figure 2.48). Shallower angles, $\theta_B \lesssim 14.7°$ were not tested and so it is not known if responses would be greater for these. Experiments on the bare deck in figure 2.49 indicate $\theta_B = 19.7°$ was more stable than the steeper or shallower angles in both heave and pitch. No investigation of the shedding mode, explanation for this critical angle or the sensitivity to road furniture is given by Larsen and Wall.

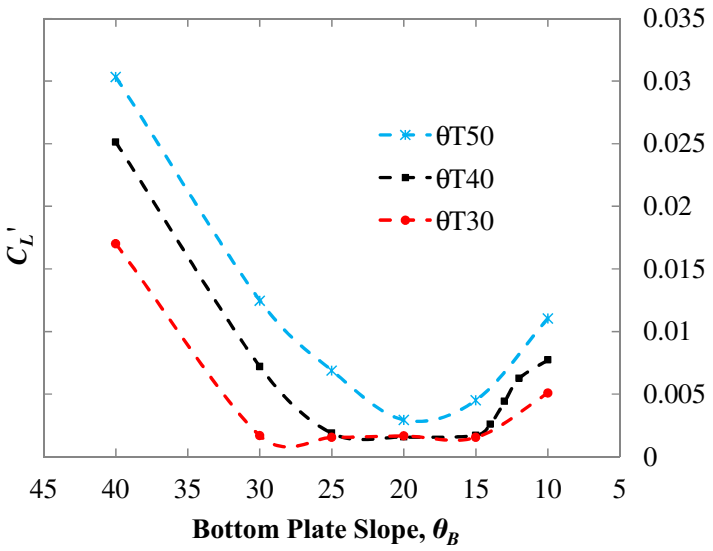


Figure 2.45: Fluctuating pressure distribution, C_p' on the bottom of a box-girder bridge deck, with varying angles θ_T and θ_B,[72].

Larose and Larsen [7] hypothesise that TEVS drives the VIV of most trapezoids and that it is the bottom vortex that is most important. There is more space below the tail for a large coherent vortex to form and be shed. Streamling the trailing edge therefore reduces the strength of this vortex by reducing separation (figure 2.50) and limits TEVS excitation. Flow visualisation of Deck E (figure 2.50) shows that the shallower side plates led to reduced separation of the shear layer. Although there is some circulation in the near wake, the large coherent vortices form at a distance downwind. By comparison, the steeper side slopes of Deck A show strong separation with coherent vortices in the near wake. This is in agreement with the simulations by Haque *et al.* [72].

Over the range of wind speeds investigated: $0.3 \leq \frac{U}{f_n B} \leq 1.6$, the shedding around Deck A locked-in three times, all in heave (figure 2.47). Multiple lock-ins are indicative of the ILEV mode of excitation. However, Larsen and Wall [75] do not investigate the mode of shedding for the response peaks.

Open type railings and median dividers were placed on the models to determine the impact of typical road furniture on the aerodynamics. These significantly impacted on the vortex-shedding (figure 2.52), although no clear pattern was obvious. For the third bending peak, where f_s drops from $2.5f_n$ to lock onto f_n (a phenomenon this author has

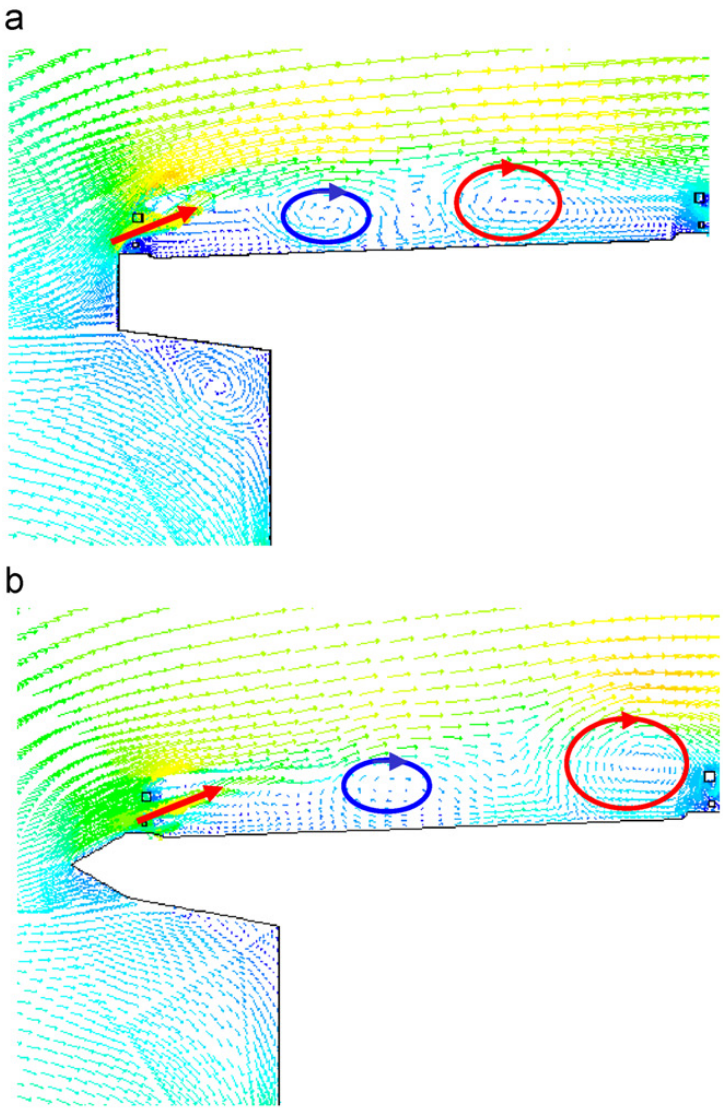


Figure 2.46: Numerical simulations at the leading edge of two bridge deck sections (a) without fairings, and (b) with fairings, showing the development of ILEV excitation at the leading edge. The velocity at the leading edge is increased in the presence of a fairing, which intensifies the ILEV mechanism and amplifies response,[74].

not seen elsewhere in the literature), the railings reinforced the shedding and led to a larger amplitude of response. Where f_s approached f_n at lower wind speeds, the railings served to reduce the oscillation. Wind tunnel experiments by Kobayashi et. al [73] and numerical simulations on the Volgograd Bridge by Coriols and Morgenthal [48] partially agree; they show handrails enhance vertical VIV and reduce torsional VIV. However, in

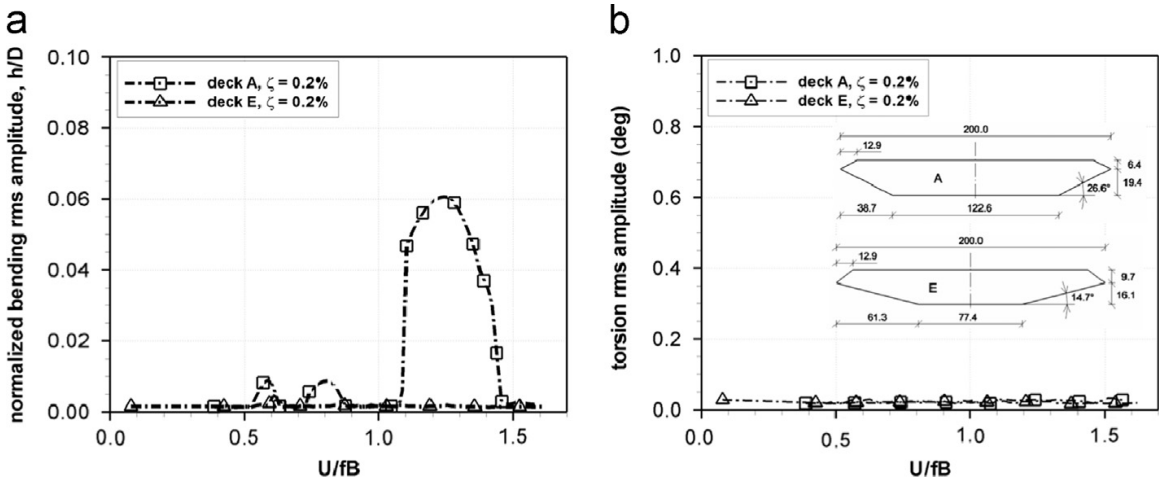


Figure 2.47: Comparison of VIV response for deck sections A, □ and E, △. (a) bending response and (b) torsion response. [75].

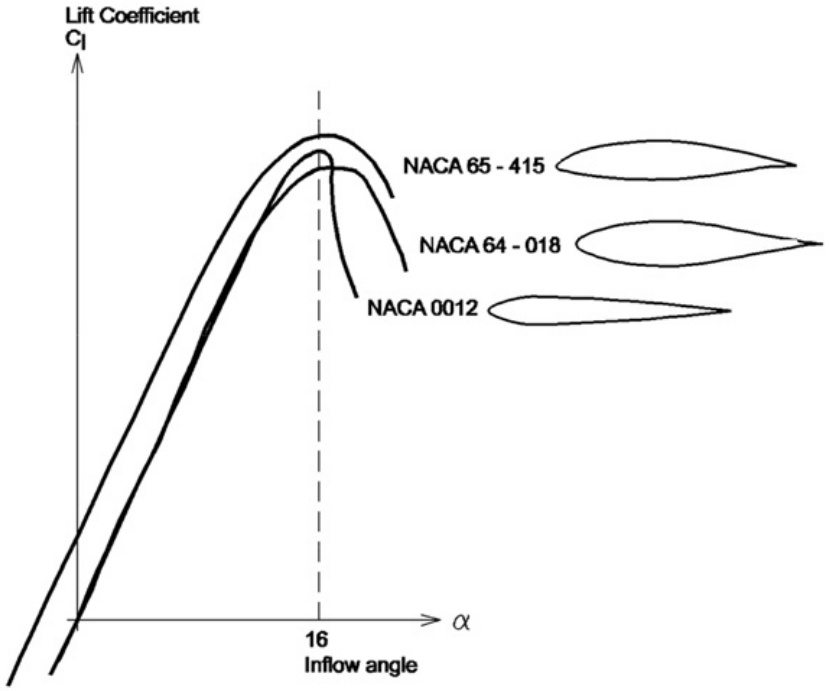


Figure 2.48: Lift angle vs. angle of attack for various aerofoils [75].

figure 2.52 the first and second bending peak were reduced by the presence of hand rails. The model with the shallowest angle remained stable to oscillations with the addition of open railings, although not for solid railings. Solid railings are often created temporarily by snow walls forming beside open railings. Experiments in a wind tunnel on the Østeroy bridge deck [75] show multiple response peaks (figure 2.53), where the third and larget

Deck D Deck E .

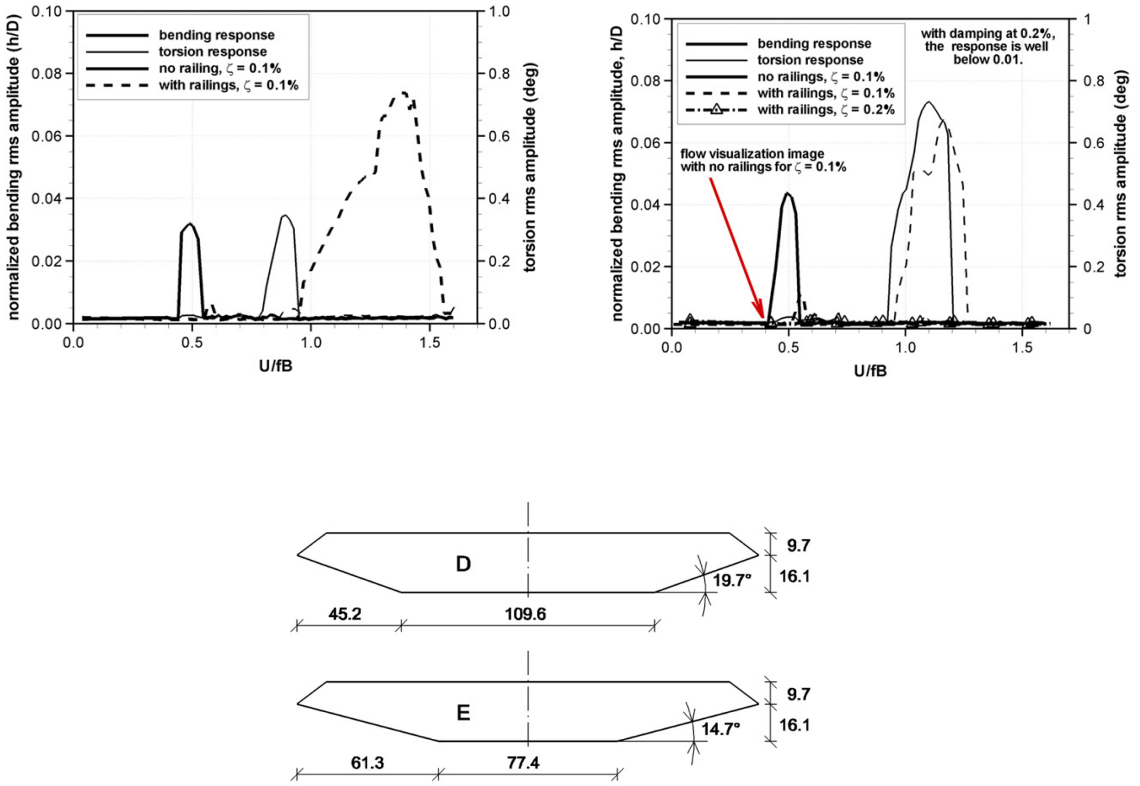


Figure 2.49: Response in heave and torsion for small-scale models of the Storebælt main span, Deck D (left) and Deck E (right), with bare deck and road furniture [75].

bending peak is amplified by railings, whereas the first and second smaller bending peaks are reduced or mitigated at $\zeta = 0.1\%$. There is no explanation by Larsen and Wall for the effects of road furniture on vertical and torsional VIV. However it is clear the barrier configuration has a marked effect on the stability of VIV.

Chaix's experiments [76] on octagonal cylinders found that when the angle β in figure 2.54 is shallow at 10°, the flow did not separate here but further down at the 90° angle at the base. When β was increased to 16°, the flow separated at the corner, leaving more afterbody to experience the lift induced by ILEV and TEVS.

A more unusual suggestion by Coriols and Morgenthal [48] to mitigate VIV is to place a small Savonius-type turbine (in figure 2.55) in the lower leading edge corner of a box-girder. Simulations of the Volgograd Bridge showed reductions in amplitude up to 50%.

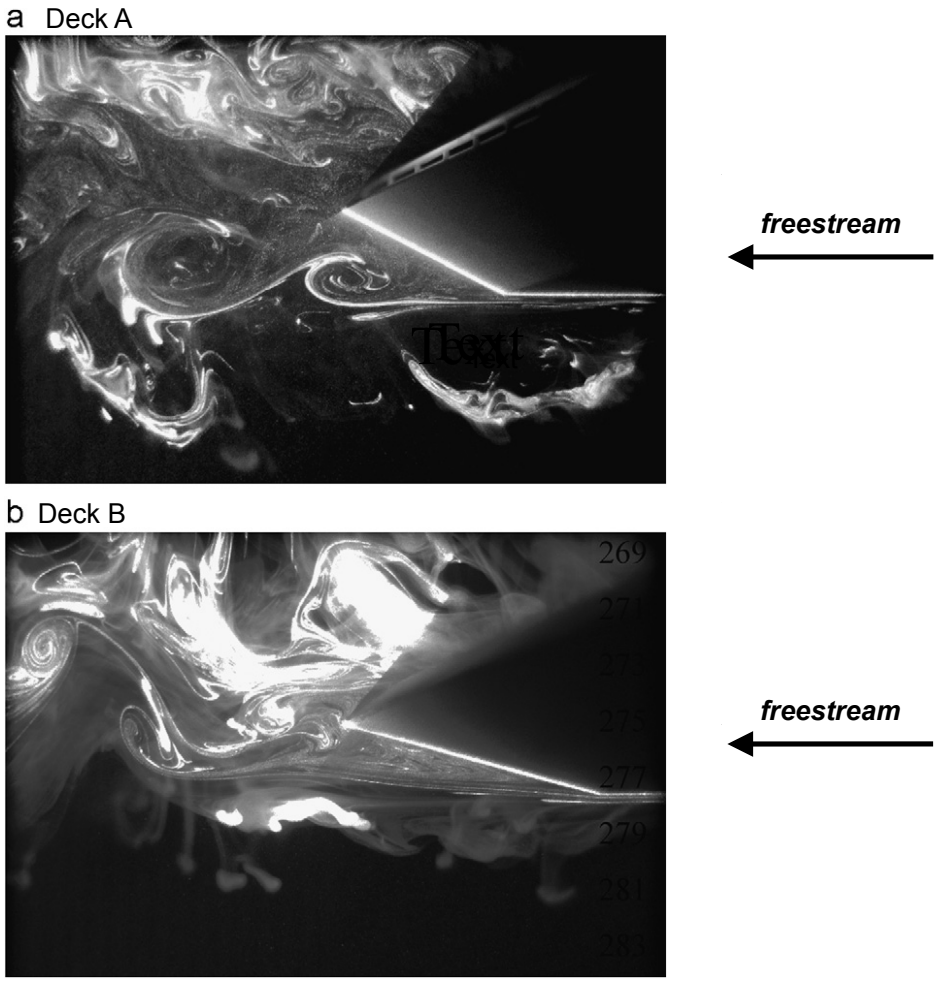


Figure 2.50: Smoke visualisation of the near wake of a trapezoidal model at $U/(f_n B) \approx 0.4$, (a) Deck A, showing full separation and vortex-formation close to the model and (b) Deck E, showing limited separation with vortex roll-up delayed to further downstream in the wake [75].

As well as modifying the flow, the turbine could be used to generate energy for road-side lighting.

The efficiency of aerodynamic countermeasures for bridge decks has tended to be tested on a case-by-case basis and found to be dependant on the deck geometry. Measures found suitable for one cross-section are not suitable for others [77]. Studies of aerodynamic counter-measures have been commercially driven and often lack information of the mechanisms of mitigation and therefore do not provide guidance to select a countermeasure for

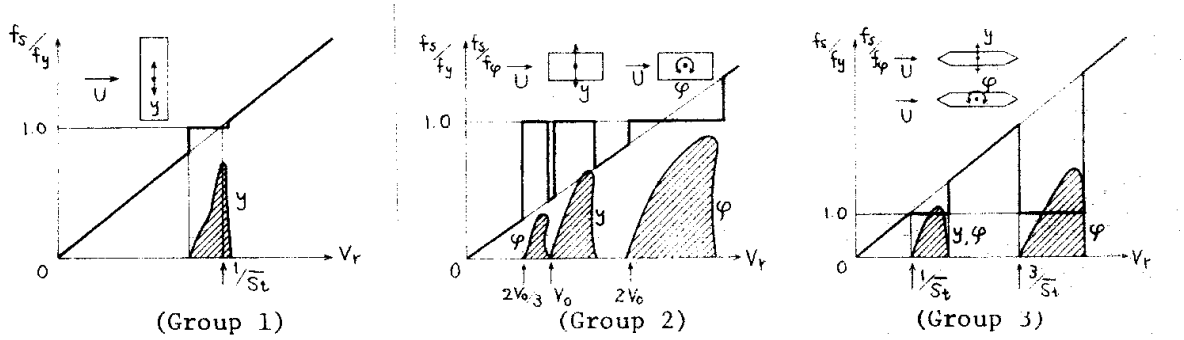


Figure 2.51: Shedding frequency, f_s measured as velocity fluctuations in the near wake for self-excited heave and torsion VIV of rectangular cylinders belonging to Group 1(LEVS excitation), Group 2 (ILEV excitation) and Group 3 (TEVS excitation), [38].

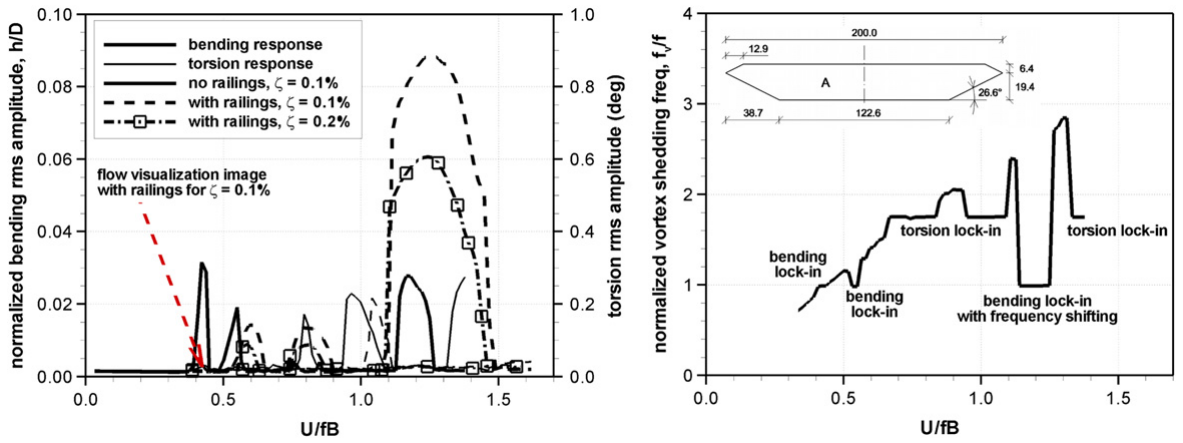


Figure 2.52: Response and f_s for Deck A, with and without road furniture and at $\zeta = 0.1\%$ and 0.2%, [75].

other bridge sections. However mitigation measures for VIV of circular cylinders, rectangular cylinders and blunt-based bodies have been researched more extensively. These mitigation methods can be categorised as two-dimensional devices and three-dimensional devices. Two-dimensional devices mitigate VIV by limiting the interaction of the shear layers in the wake. Three-dimensional devices work by reducing the spanwise correlation of the wake.

Two effective examples of two-dimensional devices to mitigate VIV are splitter plates and base bleed, both of which work by delaying interaction of the shear layers on either

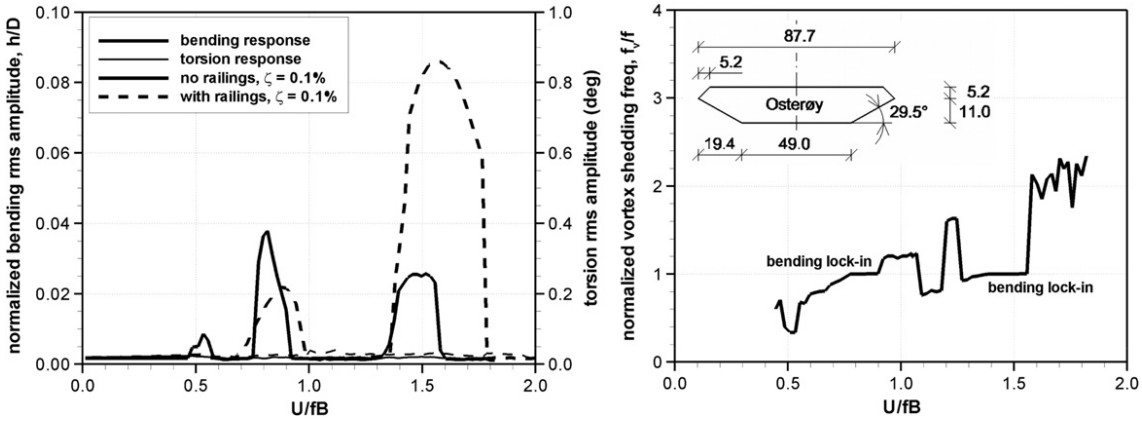


Figure 2.53: Response and f_s for a small scale model of the Østeroy bridge, with and without road furniture and at $\zeta = 0.1\%$, [75].

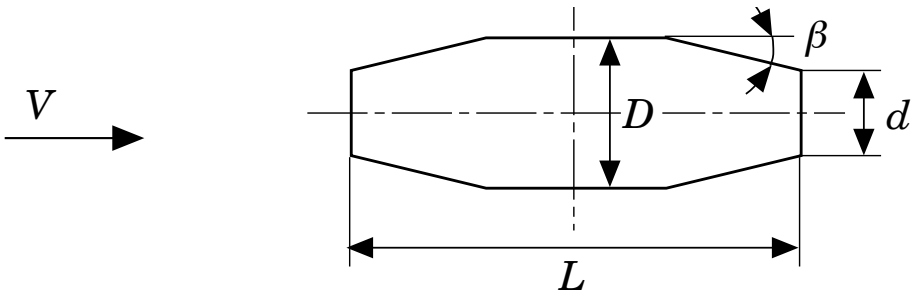


Figure 2.54: Octagonal prism model used by Chaix [76] to study the flow in towing tank experiments, undergoing forced oscillations, $\alpha = 0°$.

side of the wake, and pushing the formation of vortices into the far wake. The splitter plate was first investigated by Roshko [36] who experimented on the effect of a short and long splitter plate placed in different downstream positions in the wake of a circular cylinder in subcritical flow. The short splitter plate was of length $1.14D$ and when placed

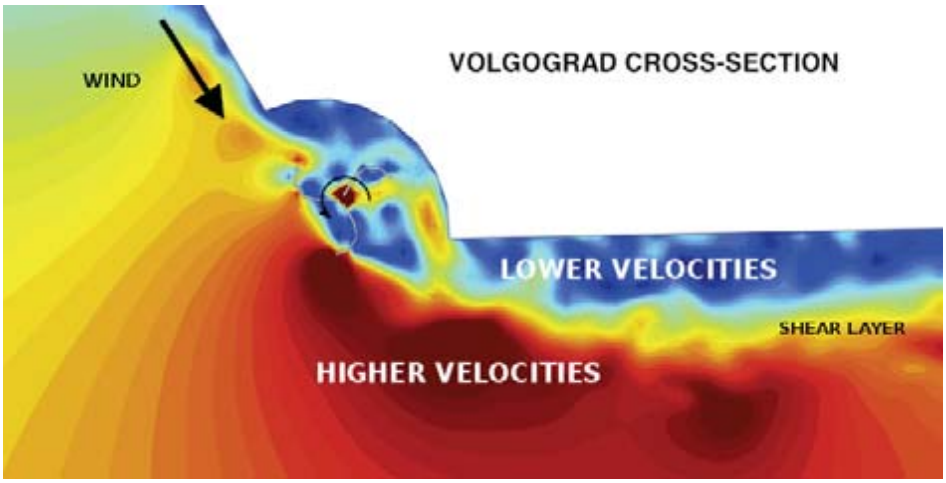


Figure 2.55: Savonius-type turbine placed in the leading-edge bottom corner of the Volgograd bridge deck section. Numerical simulations showed that the flow was altered relative to the base case, with lower amplitudes, [48].

directly behind the cylinder produced no reduction in vortex-shedding. As the plate was moved downstream, the vortex-shedding and base suction reduced until, at a distance of $2.75D$, the flow jumped back to the case of an isolated cylinder. The long splitter plate of length $5D$ produced a similar reduction in base suction to the short plate, but no velocity fluctuations were found in the wake, leading Roshko to conclude that shedding had been suppressed until the plate was at a distance $17D$ downstream. Bearman [78] determined an inversely proportional relationship between the vortex-formation length and base suction and confirmed the hypothesis that the shear layers cannot interact until the end of the splitter plate, producing weaker vortices far away from the body. Further work by Apelt and West [79] on splitter plates has shown that a length of at least $4D$ is required for suppression of shedding. Such long plates increase the surface area for pressure fluctuations, potentially exacerbating the effects of other flow instabilities.

Base bleed injects a flow of fluid between the shear layers, preventing interactions. Wood [80] experimented on a blunt-based elliptical body at $Re_D \approx 10^4$. The bleed rate, the ratio of the base bleed velocity to the free-stream velocity, was increased and an

increase in vortex-formation length and a reduction in the drag of 65% was observed. At bleed rates above 5% the shedding became irregular. Bearman [81] has shown that the vortex-shedding from a two-dimensional model similar to that used in Wood's experiments [80] can be significantly altered by base bleed. In this case, the base bleed flow is produced by a compressor and forced through a porous plastic material on the base of the model. Bearman found that increasing the bleed rate pushes the vortex-formation position into the far wake, and the near wake is completely vortex free. For the model and experimental conditions in Bearman's case, a base bleed velocity of approximately 17% of the free-stream velocity is required for this effect to occur. Comparison of the result of the base bleed with the splitter plate studies [78] shows the effects on vortex-formation length and base suction are similar and suggests the mitigation mechanisms are the same; pushing the shear layer roll up and vortex formation into the far wake. At some critical level of mitigation; splitter plate length or base bleed flow, the von Kármán street does not exist, instead there being two shear layers from each side of the body, which meet at some point in the far wake (or in the case of the splitter plate, the flow reattaches). At this point, the wake stabilises and tends towards the steady wake case (figure 2.56).

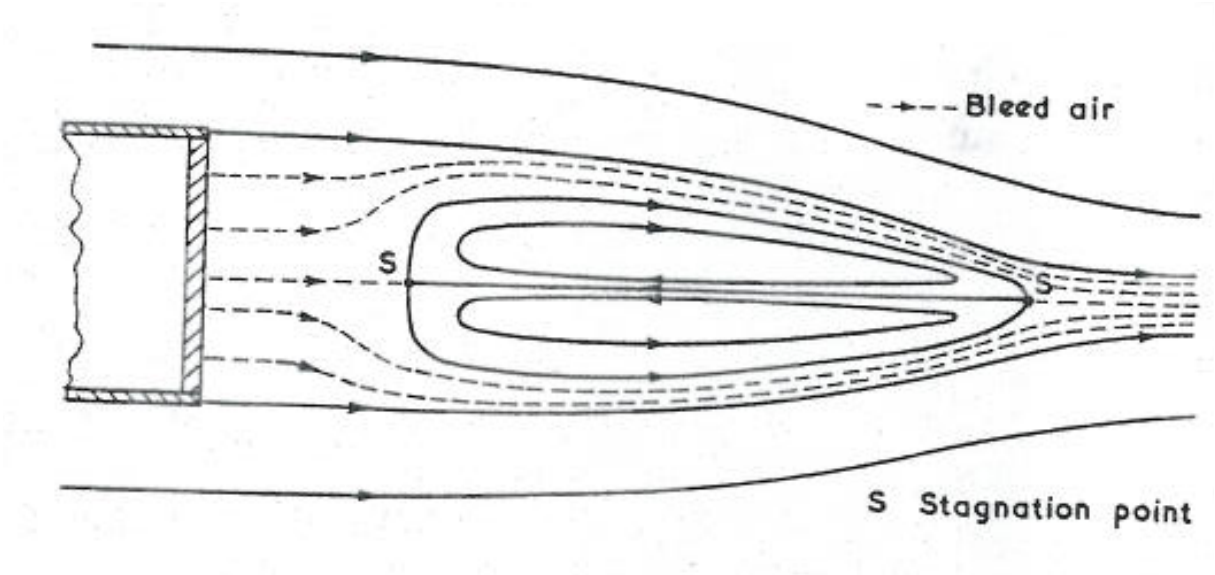


Figure 2.56: Steady wake flow with base bleed, [81].

The ILEV mechanism is a one-shear layer excitations and not the direct interaction of shear layers on opposite sides of a body. This mechanism is fundamentally different

to von Kármán street excitation and is not suppressed by a splitter plate placed in the wake. Figure 2.57 displays flow visualisation of an H-section, with and without a splitter plate in the near wake [82]. The shedding mechanism is ILEV and the vortex-formation at the leading edge, and convection along the body can be seen. The splitter plate does not destroy the vortex presence in the wake. Splitter plates can effectively suppress LEV and TEV mechanisms but not ILEV whose instability stems from the leading edge and the shear layer here. As many bridge models [51] have been shown to be initially excited by TEVS which triggers the motion-induced ILEV, it may be that splitter plates would effectively mitigate VIV by inhibiting TEVS.

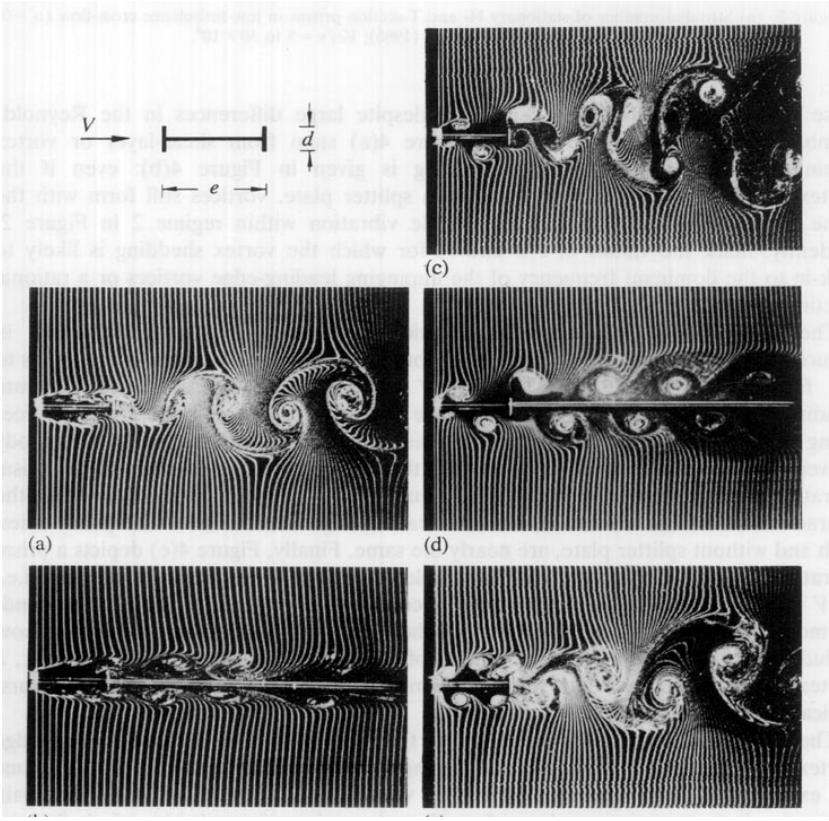


Figure 2.57: Flow visualisation of an H-section prism, $\alpha = 0°$, $B/D = 5$, $Re_D = 1200$. (a,b) stationary prism with and without a splitter plate; (c,d,e) prisms vibrating transversely with amplitude $y/d = 0.19$; (c) U_{nd}=8.65; (d) U_{nd}=8.65 with splitter plate; (e) U_{nd}=4.3, [82].

The vortex-suppression devices shown in figure 2.58 are passive three-dimensional ones. The three-dimensional geometric modifications vary along the spanwise direction, at the

point of separation or at the base (except for the helical strake (figure 2.58a)) and reduce the dominance of the two-dimensional shedding, resulting in reduced spanwise correlation of the wake. A three-dimensional wake will exert lower lift and drag forces on the body and will not enter lock-in.

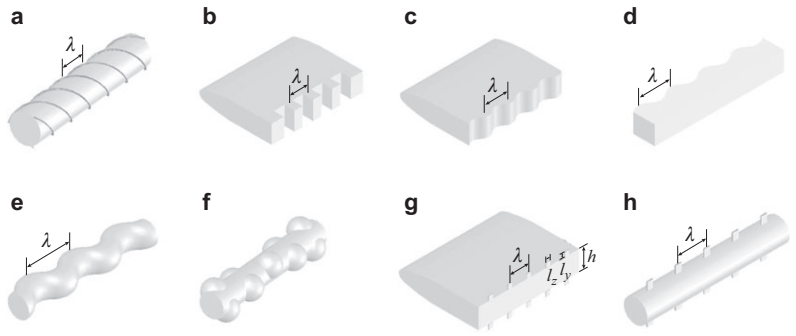


Figure 2.58: Passive control methods of decorrelating vortex-shedding by three-dimensional geometric modifications: (a) helical strake, (b) segmented trailing edge, (c) wavy trailing edge, (d) wavy stagnation face, (e) sinusoidal axis, (f) hemispherical bumps and (g,h) tabs, [83].

Investigations by Rodriguez [84] and Tombazis and Bearman [85] respectively, have shown that a segmented trailing edge, (figure 2.58b) and a wavy trailing edge, (figure 2.58c) on a blunt-based body introduces three-dimensionality into the wake and decorrelates the spanwise vortex-shedding.

Park *et al.* [86] performed wind tunnel experiments and numerical simulations on a blunt-based body with small tabs mounted on the upper and lower trailing edges (figure 2.58g) and varying the height, width and separation of the tabs. The effect of the tabs was to decorrelate the spanwise vortex-shedding and to push the von Kármán street further downstream. Yoon [87] found that tabs on a circular cylinder at the separation point (figure 2.58h) reduced the strength of the von Kármán vortex-shedding.

Helical strakes are protruding fins, placed around a circular cylinder in a helical pattern along the span and have been applied with success to large-scale structures, such as tall chimneys and sub-sea pipelines. The strakes reduce or suppress the oscillations by either preventing the spanwise correlation of the vortex-shedding or the three-dimensionality of

the separating flow introduced by the strakes could destroy regular vortex-shedding [88]. Typically, strakes have height $0.1D$. Applying such an arrangement of helical strakes to a bridge deck is obviously impractical, as the roadway must remain unobscured, and the additional steel contributes a significant additional dead load and material cost.

Bearman and Owen [89] performed experiments on a rectangular cylinder, with the front stagnation face exhibiting a spanwise waviness (figure 2.58d) and found that vortex-shedding was suppressed. Experiments on a circular cylinder with a sinusoidal axis (figure 2.58e) [90] have shown that above a certain level of waviness, the vortex-shedding is decorrelated along the span and that similar experiments on a circular cylinder with hemispherical bumps [90] (figure 2.58f) showed the vortex-shedding to be significantly weakened. On the fixed bodies the shedding could not be detected. For the elastically-mounted bodies, VIV amplitudes were present but reduced compared to the plain cylinder. Three-dimensional geometric disturbances have proven [89] [91] [92] to effectively reduce oscillating lift forces and drag forces (up to 30%) relative to equivalent nominally two-dimensional bodies.

El-Gammal *et al.* [93] performed wind tunnel experiments on a plate-girder section, B/D=10, with spanwise waviness at the leading trailing edges. The steepness of the wave, defined as the peak-to-peak wave height divided by the wavelength, had a significant effect on the response. The steepest wave (short wave) suppressed the VIV responses more than the more shallow wave (long wave) and the base case without waviness. The long wave reduced the peak amplitude by 50% relative to the base case, whereas the short wave effectively mitigated all response. The short wave attachments significantly reduced the fluctuating pressures at the trailing edge. There was a reduction in the strength of the ILEV attributed to the leading edge waviness which introduced three-dimensionality in the separation of the shear layers at the leading edge and rendered them less susceptible to roll-up into two-dimensional vortices. The trailing edge waviness is attributed to suppressing the von Kármán-type vortices shed at the trailing edge due to double shear layer instability. It is generally understood [91][92] that for waviness to be effective the wavelength needs to approximate the most unstable length scale naturally occurring in the undisturbed base case wake flow. El-Gammal *et al.* found that the short wave is much more effective at reducing ILEV strength and disrupting the von Kármán-

type wake.

It should be noted that when practically determining a counter-measure for VIV, the chosen measure should be assessed for the impact on the structural performance, additional whole-life cost and man-time, other aeroelastic instabilities and static aerodynamic effects, e.g. drag.

2.7 Synthesis

The flows around sharp-edged bodies, such as a box-girder and circular cylinders have similarities and differences. The main differences are the fixed separation at the sharp corners of the box, and lower sensitivity to Re_D, instead showing a greater dependance on the slenderness ratio, B/D.

Rectangles are shown to experience three modes of vortex-shedding that can excite VIV. Of these, ILEV and TEVS are observed on bodies of slenderness. The mode experienced depends on the slenderness, with ILEV modes only observed on stationary bodies at slenderness ratios up to ≈ 8 in high Re_D. However, on oscillating bodies, the leading edge acts to control the shedding and higher ILEV mode numbers can be measured. Even so, ILEV modes are observed on oscillating rectangles up to slenderness ratios ≈ 10.5. H-sections, modelling half-through bridges have been observed undergoing multiple instances of VIV, each instance associated with an ILEV shedding mode. The higher modes occur at lower wind speeds and were of lower amplitude, as has generally been observed for rectangular cylinders [38]. However, Naudascher and Wang [39] found that as the slenderness of a rectangle increases: a) the n=2 mode appears and then dominates, b) the oscillations reduce.

Box-girders are less well studied than rectangles. The reasonably slender sections are likely to experience two types of vortex-shedding excitation: ILEV and TEVS, with the mode depending on the slenderness ratio. The Storebælt bridge has been shown [51] to be excited by both the ILEV and TEVS mechanisms; the TEVS initially generates the motion-induced ILEV mechanism, which amplifies oscillations. The response and shedding modes of trapezoids, $B/D \geq 10$ has not been investigated experimentally. As the ILEV mechanism is expected to diminish with slenderness, it is of particular interest

to see if it is observed on this deck. The experiments in this thesis look at the behaviour of a slender box-girder model, $B/D = 11.2$ in VIV. This model, donated by BMT Fluid Mechanics was built for a commercial project investigating the aerodynamics of a tender design for the Humber Bridge. In chapter 5 the phenomenology of VIV for the slender deck is studied. In particular, similarities and differences to the less slender decks in the literature are discussed.

The ILEV and TEVS mechanisms require mitigations that target the formation of vortices at or near the leading edge and their convection down the body, and the vortex-shedding at the trailing edge respectively. The most common aerodynamic countermeasures used on a box-girder have been guide vanes and streamlined fairings. Guide vanes act to prevent or reduce separation when placed at the leading edge and trailing edge corners, instead accelerating the flow around the corner. Streamlined fairings have been shown to have a mixed effect. Sharp-edged trailing edges mitigate the TEVS more effectively than curved trailing edges. However, impinging vortex generation is enhanced by sharp edges at the leading edge, and it is the ILEV mechanism that contributed to maximum amplitudes for the Storebælt bridge [51]. The shape of triangular fairings has been shown to have a significant effect on VIV amplitudes [72] [75]. For a box-girder with handrails, a critical angle at the bottom knuckles of $\theta_B \approx 15°$ is found to give the minimum response [72] [75]. For a bare deck the critical angle is 20°. Numerical simulations [72] appear to indicate increased instability at lower values of θ_B when the tail moves low enough to allow the vortex formed at the bottom knuckle to be shed above the tail. When the tail position is fixed [75] a trapezoid also shows lower stability at shallower and steeper angles than the critical, although the physical mechanisms are not investigated or explained.

Experiments in Chapter 6 look at the impact of the fairing shape at both the leading edge and trailing edge. Of interest is whether changing the geometry of the bottom knuckle, (and fixing the nose position) affects the excitation mechanism and response in VIV. It is hoped these experiments can determine whether this slender trapezoid behaves similarly to the less slender Storebælt bridge [75], and explain any sensitivity to the geometry at the bottom knuckle.

Hysteresis has been observed for the Storebælt bridge, in wind tunnels tests and in

full scale [51]. Experiments in Chapter 7 look to see if hysteresis exists for this body, the mechanisms causing it and how it is characterised. Experiments bring the body stationary at each wind speed increment to assess the impact of body motion on VIV. Finally the impact of road furniture on the top surface of the deck, and the structural damping is characterised. It is well understood that damping acts to reduce amplitudes; a range of damping levels are investigated to understand the sensitivity and persistence of response. Research has shown that road furniture acts to enhance bending VIV and weaker torsional VIV [73], but there is no literature on the effects for a slender trapezoid.

The experiments described in the following chapters will address gaps in the knowledge of VIV, namely:

- the response of a very slender trapezoid, $B/D \geq 10$;
- the physical mechanisms and the mode of vortex-shedding driving the response;
- the sensitivity of both the response and physical mechanisms to the fairing shape at the leading and trailing edge. In particular the impact of the geometry at the bottom knuckle is investigated.;
- characterising the degree that hysteresis is present, if at all, for a very slender trapezoid in VIV;
- the impact of road furniture placed on the top surface on a very slender trapezoid;
- the sensitivity and persistence of response to structural damping.

Chapter 3

Methodology

3.1 Introduction

The approach in this investigation has been to conduct small-scale experiments in a wind tunnel. The experiments allow for clear observation of the behaviour of a trapezoidal box-girder through lock-in. As the VIV of a box-girder bridge deck has been largely unexplored, it is sensible to conduct the investigation experimentally, rather than through numerical simulations, to develop a clear and reliable understanding of the physics of the flow.

There are three common model forms for observing bridge aerodynamics. They are:

- Two-dimensional section models.
- Taut-strip models
- Full three-dimensional aeroelastic models

The section models are rigid models of a short length of bridge deck and are spring-mounted in a wind tunnel so that they oscillate in rigid-body modes corresponding to the elastic modes of a full length deck. Two-dimensional section models have been chosen in this investigation as they are the simplest geometry for which to observe VIV. The similarity of this model form to investigations of other cylinder sections [9, 31] allows the comparison of measurements.

Taut-strip models represent the scaled mass and external geometry of the full span of a bridge deck. Tensioned wires running through the model simulate the stiffness and dynamic characteristics of the deck. The model can vibrate in modes other than the fundamental, and is long enough to experience spanwise non-uniformity of flow, such as turbulence.

An aeroelastic model includes the full length of the bridge and all parts that affect the dynamic response, including bridge piers, cables and often the surrounding topography. Aeroelastic models accurately model the modal responses of the prototype by matching the distributions of mass, stiffness and structural damping. Aeroelastic models are large and require large wind tunnel test-sections. They are expensive to build and produce complex results.

The trapezoidal models in this investigation represent only the external geometry of a bridge deck, occasionally with the addition of road furniture. The aerodynamics of the towers and cables are not included. The rigid models were elastically-mounted within the wind tunnels, and allowed to oscillate freely in two degrees of freedom: heave and pitch. Measurements of the flow and response were taken.

This chapter describes the general approach taken to investigate vortex-induced motion of a trapezoidal box-girder. Section 3.2 describes the section models used, and section 3.4 describes the experimental set-up. The measurements made are discussed in section 3.6. Considerations of flow similarity, end effects and tunnel blockage are discussed. Many individual experiments were conducted in this investigation and this chapter aims to give an overview. The individual experiments will be described in later chapters.

Two wind tunnels were used to collect the data presented in this thesis. The $10' \times 5'$ wind tunnel in the Department of Aeronautics at Imperial College London was used for two experimental sessions. The final two experiments took place in the Aeronautical T5 wind tunnel at BMT Fluid Mechanics in Teddington. These are described in section 3.3.

3.2 Small-scale physical models

Five trapezoid sections were tested and are shown in figure 3.1. The models are all geometrically similar and vary only in the angle at the bottom knuckles and the length of

the inclined panels at the bottom knuckles (figure 3.2). This angle took values of 16°, 18°, 20°, 25° and 30°. The top surface and nose and tails position are identical for each model. These shapes were chosen as typical for long-span bridges (figure 3.3). Experiments on the Storebælt [75] found that $\theta_B = 19.7°$ was the most stable angle over the range 15° to 26° for the bare model. The θ_B values selected in this study rang either side of this critical angle. The same base model was used, with different leading edges and trailing edges. The leading and trailing edges were made from a foam, chosen for its low contribution to the total mass of the system, its stiffness and ease of manufacture.

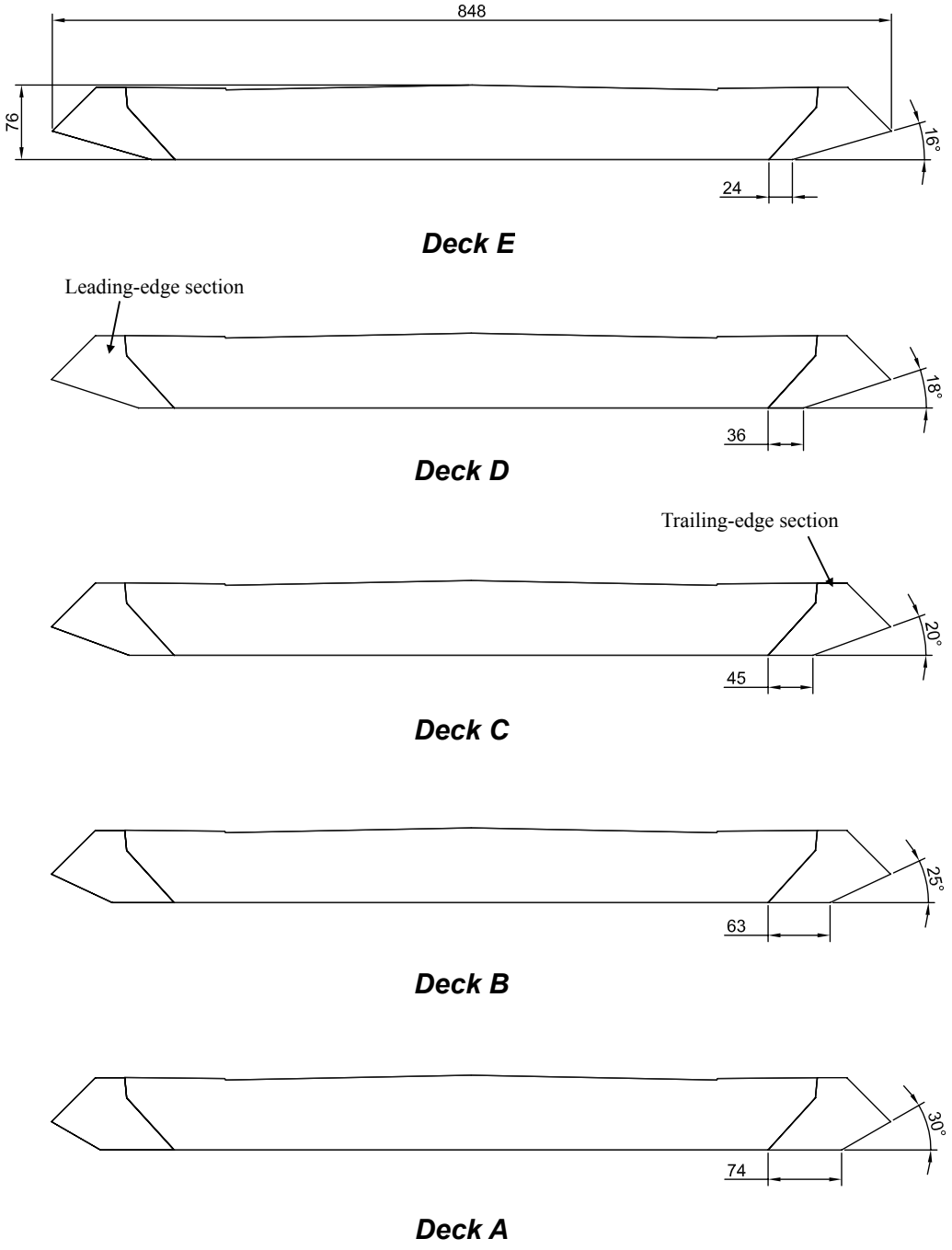
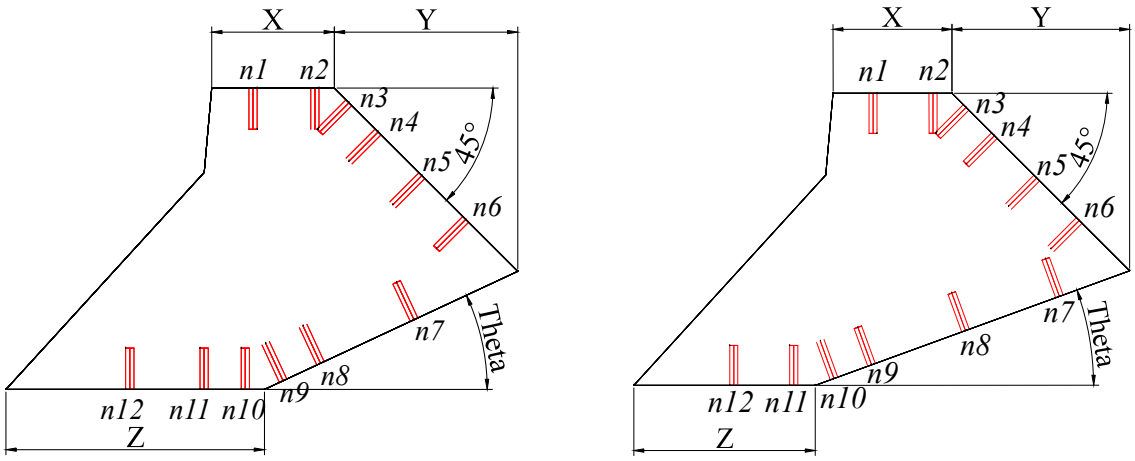


Figure 3.1: Two-dimensional bridge deck sections with varying angles between the extension of the bottom plate and the inclined lower plates. All dimensions shown are in mm.



(a) Fairing A, B

(b) Fairing C, D, E

Figure 3.2: Fairings A to E with pressure tappings shown. Nomenclature relates to a tap number in table 3.2

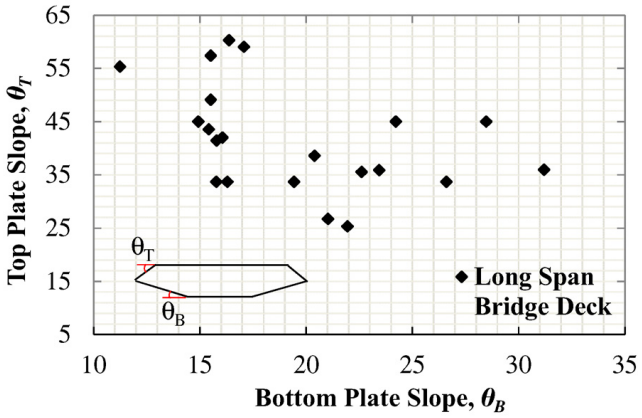


Figure 3.3: Top and bottom plate slopes of constructed box-girder bridge decks, compiled by Haque *et al*. [72]

Fairing	X	Y	Z	Theta
A	30	44	75	30°
B	30	44	63	25°
C	30	44	45	20°
D	30	44	36	18°
E	30	44	24	16°

Table 3.1: Dimensions of fairings A to E, all in mm.

The base model was a carbon-fibre model owned by BMT Fluid Mechanics. The model was built for a commercial project investigating the aerodynamics of a tender design for the Humber Bridge. All decks have the same aspect ratio, $B/D = 11.2$ where B is the overall deck width = 848 mm and $D = 76$ mm. Although a prototype does not exist, this represents an approximate scale of 1:50. The model is 2.74 m long, and designed to span the Aeronautical T5 tunnel with ends flush with the tunnel walls.

Pressure taps (figure 3.4 and figure 3.2) on the surface of the model were tapped directly into the carbon-fibre model. Table 3.2 gives the tap locations. Special leading and trailing edge sections of short length (100mm) were made from lightweight wood. These sections were positioned at at four spanwise locations: $0.3L, 0.44L, 0.51L$ and $0.81L$ from one end of the model. At $0.44L$ there are pressure taps uniformly around the section. The other sections have pressure taps only at the trailing edge.

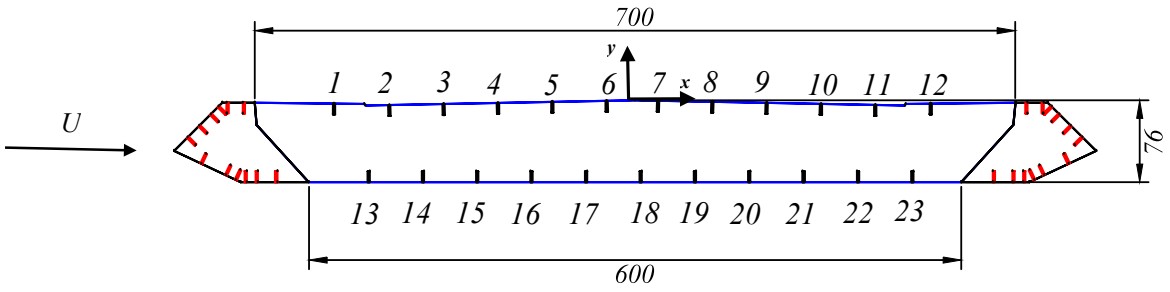


Figure 3.4: Pressure tap nomenclature on the base model, at a cross section $0.44L$ measured from the end on the model. Indicative leading edge and trailing edge is shown. The co-ordinate origin, referred to in table 3.2 is shown.

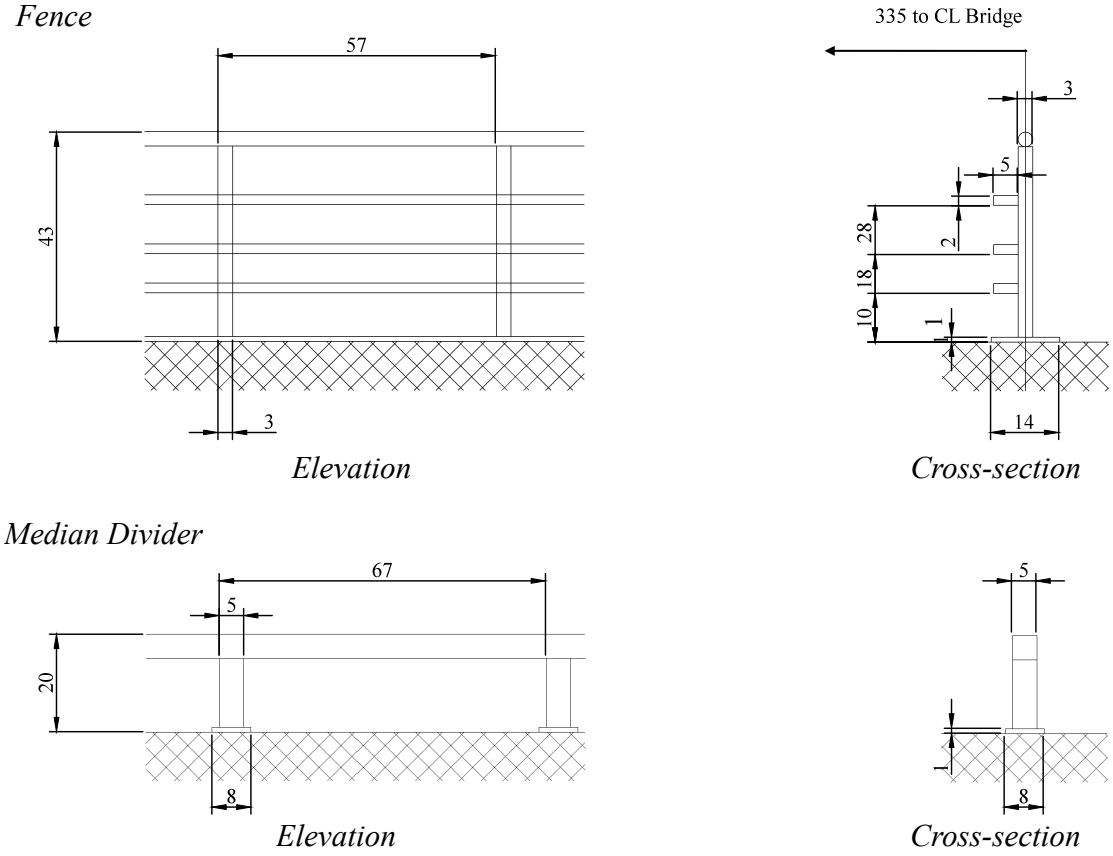


Figure 3.5: Road furniture. All dimensions shown are in mm.

Investigations on similar trapezoidal-sections have found a marked impact of road furniture on the vortex-induced response [75] . The addition of open railings and median dividers amplified heave responses and attenuated pitch responses. To determine the effect of road furniture on the trapezoid, some of the decks were tested with open railings and median dividers as shown in figure 3.5, and are approximately to scale for a prototype bridge.

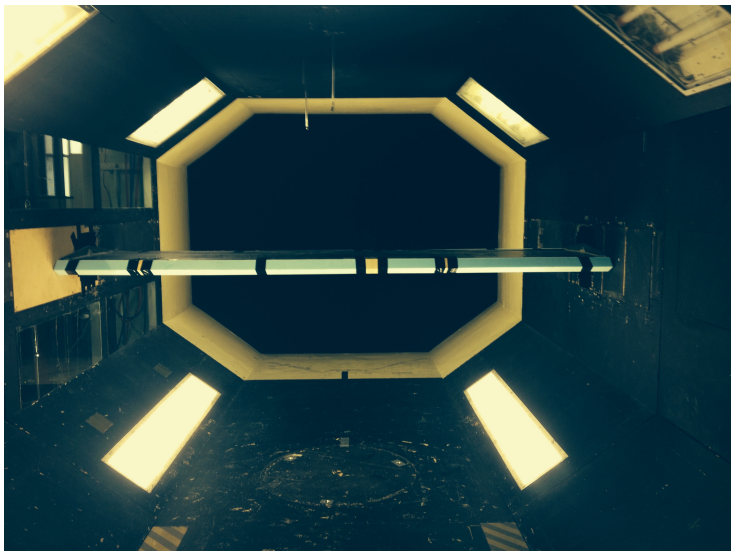


Figure 3.6: Looking downwind at the model mounted within the T5 tunnel at BMT Fluid Mechanics. The view is of the leading edge. The blue sections are foam and the shorter brown sections are made of wood and pressure-tapped.

		x	y	z			x	y	z
Base section	1	-272	-2	z_2	LE fairing A	n1	-360	-3	z_1,z_2,z_3,z_4
	2	-221	-2	z_2		n2	-375	-3	z_1,z_2,z_3,z_4
	3	-171	-1	z_2		n3	-384	-7	z_1,z_2,z_3,z_4
	4	-121	-1	z_2		n4	-391	-14	z_1,z_2,z_3,z_4
	5	-71	-1	z_2		n5	-401	-24	z_1,z_2,z_3,z_4
	6	-21	0	z_2		n6	-412	-34	z_1,z_2,z_3,z_4
	7	21	0	z_2		n7	-396	-63	z_1,z_2,z_3,z_4
	8	71	-1	z_2		n8	-388	-68	z_1,z_2,z_3,z_4
	9	121	-1	z_2		n9	-379	-73	z_1,z_2,z_3,z_4
	10	171	-1	z_2		n10	-365	-76	z_1,z_2,z_3,z_4
	11	221	-2	z_2		n11	-355	-76	z_1,z_2,z_3,z_4
	12	272	-2	z_2		n12	-345	-76	z_1,z_2,z_3,z_4
	13	-255	-76	z_2	TE fairing A	n1	360	-3	z_1,z_2,z_3,z_4
	14	-205	-76	z_2		n2	375	-3	z_1,z_2,z_3,z_4
	15	-155	-76	z_2		n3	384	-7	z_1,z_2,z_3,z_4
	16	-105	-76	z_2		n4	391	-14	z_1,z_2,z_3,z_4
	17	-55	-76	z_2		n5	401	-24	z_1,z_2,z_3,z_4
	18	-5	-76	z_2		n6	412	-34	z_1,z_2,z_3,z_4
	19	45	-76	z_2		n7	396	-63	z_1,z_2,z_3,z_4
	20	95	-76	z_2		n8	388	-68	z_1,z_2,z_3,z_4
	21	145	-76	z_2		n9	379	-73	z_1,z_2,z_3,z_4
	22	195	-76	z_2		n10	365	-76	z_1,z_2,z_3,z_4
	23	245	-76	z_2		n11	355	-76	z_1,z_2,z_3,z_4
						n12	345	-76	z_1,z_2,z_3,z_4

		x	y	z			x	y	z
LE fairing B	n1	-360	-3	z_1,z_2,z_3,z_4	LE fairing C	n1	-360	-3	z_1,z_2,z_3,z_4
	n2	-375	-3	z_1,z_2,z_3,z_4		n2	-375	-3	z_1,z_2,z_3,z_4
	n3	-384	-7	z_1,z_2,z_3,z_4		n3	-384	-7	z_1,z_2,z_3,z_4
	n4	-391	-14	z_1,z_2,z_3,z_4		n4	-391	-14	z_1,z_2,z_3,z_4
	n5	-401	-24	z_1,z_2,z_3,z_4		n5	-401	-24	z_1,z_2,z_3,z_4
	n6	-412	-34	z_1,z_2,z_3,z_4		n6	-412	-34	z_1,z_2,z_3,z_4
	n7	-399	-59	z_1,z_2,z_3,z_4		n7	-407	-53	z_1,z_2,z_3,z_4
	n8	-377	-69	z_1,z_2,z_3,z_4		n8	-383	-62	z_1,z_2,z_3,z_4
	n9	-368	-73	z_1,z_2,z_3,z_4		n9	-360	-70	z_1,z_2,z_3,z_4
	n10	-359	-76	z_1,z_2,z_3,z_4		n10	-350	-74	z_1,z_2,z_3,z_4
	n11	-349	-76	z_1,z_2,z_3,z_4		n11	-340	-76	z_1,z_2,z_3,z_4
	n12	-330	-76	z_1,z_2,z_3,z_4		n12	-325	-76	z_1,z_2,z_3,z_4
TE fairing B	n1	360	-3	z_1,z_2,z_3,z_4	TE fairing C	n1	360	-3	z_1,z_2,z_3,z_4
	n2	375	-3	z_1,z_2,z_3,z_4		n2	375	-3	z_1,z_2,z_3,z_4
	n3	384	-7	z_1,z_2,z_3,z_4		n3	384	-7	z_1,z_2,z_3,z_4
	n4	391	-14	z_1,z_2,z_3,z_4		n4	391	-14	z_1,z_2,z_3,z_4
	n5	401	-24	z_1,z_2,z_3,z_4		n5	401	-24	z_1,z_2,z_3,z_4
	n6	412	-34	z_1,z_2,z_3,z_4		n6	412	-34	z_1,z_2,z_3,z_4
	n7	399	-59	z_1,z_2,z_3,z_4		n7	407	-53	z_1,z_2,z_3,z_4
	n8	377	-69	z_1,z_2,z_3,z_4		n8	383	-62	z_1,z_2,z_3,z_4
	n9	368	-73	z_1,z_2,z_3,z_4		n9	360	-70	z_1,z_2,z_3,z_4
	n10	359	76	z_1,z_2,z_3,z_4		n10	350	-74	z_1,z_2,z_3,z_4
	n11	349	76	z_1,z_2,z_3,z_4		n11	340	-76	z_1,z_2,z_3,z_4
	n12	330	76	z_1,z_2,z_3,z_4		n12	325	-76	z_1,z_2,z_3,z_4

		x	y	z			x	y	z
LE fairing D	n1	-360	-3	z_1,z_2,z_3,z_4	TE fairing D	n1	360	-3	z_1,z_2,z_3,z_4
	n2	-375	-3	z_1,z_2,z_3,z_4		n2	375	-3	z_1,z_2,z_3,z_4
	n3	-384	-7	z_1,z_2,z_3,z_4		n3	384	-7	z_1,z_2,z_3,z_4
	n4	-391	-14	z_1,z_2,z_3,z_4		n4	391	-14	z_1,z_2,z_3,z_4
	n5	-401	-24	z_1,z_2,z_3,z_4		n5	401	-24	z_1,z_2,z_3,z_4
	n6	-412	-34	z_1,z_2,z_3,z_4		n6	412	-34	z_1,z_2,z_3,z_4
	n7	-398	-55	z_1,z_2,z_3,z_4		n7	398	-55	z_1,z_2,z_3,z_4
	n8	-374	-63	z_1,z_2,z_3,z_4		n8	374	-63	z_1,z_2,z_3,z_4
	n9	-350	-71	z_1,z_2,z_3,z_4		n9	350	-71	z_1,z_2,z_3,z_4
	n10	-341	-74	z_1,z_2,z_3,z_4		n10	341	-74	z_1,z_2,z_3,z_4
	n11	-330	-76	z_1,z_2,z_3,z_4		n11	330	-76	z_1,z_2,z_3,z_4
	n12	-315	-76	z_1,z_2,z_3,z_4		n12	315	-76	z_1,z_2,z_3,z_4

Table 3.2: Pressure tap locations on the variable leading edge (LE) and trailing edge (TE) fairings. $z_1 = 0.30L$, $z_2 = 0.44L$, $z_3 = 0.51L$, $z_4 = 0.81L$ indicate the four spanwise locations of the pressure taps. Pressure readings are not measured for Deck E. Where pressure measurements at locations on the decks are referenced in the body of this report, they are as follows: upwind top knuckle, n2; upwind bottom knuckle, n10 (fairings A, B) and n11 (fairings C, D and E); body, PT18 and PT6; downwind top knuckle, n3; downwind bottom knuckle, n10 (fairings A and B) and n10 (fairings C, D and E). All measurements to nearest mm.

3.3 Wind tunnels

3.3.1 $10' \times 5'$ wind tunnel

The $10' \times 5'$ wind tunnel is a low-speed closed-return tunnel. The model was placed in the downwind test section with dimensions 3.05 m×1.52 m×9 m, the contraction ratio is 3.41:1 and there is one honeycomb and one turbulence reducing screen. The streamwise turbulence intensity is $< 0.14\%$ measured at 25 ms^{-}1 [94] and there is uniform mean flow in the test section to $\pm 1\%$.

The $10' \times 5'$ tunnel has two direct-drive Leroy-Somer 106kW DC variable speed motors driven by a Mentor two drive system. The maximum wind speed for the empty tunnel is 40 ms^{-}1. A PID algorithm embedded in a LabView program (built by Antony Oxlade of the flow-control team) controls the voltage supplied to the motors to maintain constant tunnel speed. The wind speed was measured by a Furness FCO510 digital manometer sampling dynamic head from a reference Pitot tube placed upstream of the model, at the beginning of the test section. The manometer corrected for atmospheric pressure and temperature. The set-point error was assessed on two convergence criteria. For long transients, the error went through a first-order low-pass filter at 0.07 Hz. For short transients, a moving-average filter of 15 seconds was employed. Both errors were maintained to less than $\pm 0.2\%$.

3.3.2 Aeronautical T5 wind tunnel

This is a low-speed closed-return tunnel with turbulence grids. The test-section is octagonal with dimensions 2.7 m wide by 2.1 m high. The streamwise turbulence intensity is $< 0.21\%$ at 18 ms^{-}1. One of the most common uses of the tunnel is to investigate bridge deck aerodynamics and the dynamic rig with variable mass, stiffness and damping is set-up outside the tunnel.

The maximum wind speed for the empty tunnel is 60 ms^{-}1. The test section velocity was calibrated using a Betz manometer, which samples the dynamic head measured with a pitot tube placed at the beginning of the test section, and corrects for atmospheric pressure and temperature. The voltage to the motors was input using in-house software

instead of a LabView program. A calibration curve of voltage supplied to the motors and flow speed was determined. The wind speed measured at the beginning of the test section fluctuated within ±0.2% of the set speed.

For experiments in both tunnels, the tunnel velocity was incremented at either 0.06 ms^{-}1 or 0.12 ms^{-}1 through the range 0.92 ms^{-}1<U<6.4 ms^{-}1. After each increment the tunnel velocity was allowed to settle for 2 minutes before data acquisition.

3.3.3 Wind tunnel blockage correction

The solid geometry and wake of a model in the test section creates a blockage, which can cause errors in the measurements within the constrained flow when compared to unconstrained flow, e.g. for a full-scale bridge or experiments in a wind tunnel with lower blockage ratios. For these experiments the blockage is 5.4% in the $10' \times 5'$ wind tunnel and 4.5% in the T5 wind tunnel. Generally, when this value is less than 6% the effects of blockage are assumed small enough that the uncorrected measurements are valid. Correction methods are available to correct for the increase in dynamic pressure caused by blockage. Maskell [95] suggests a method for stationary bodies, based on measurements of separated flow around flat plates perpendicular to the flow. This correction is successful in correcting for constrained flow around circular, square and triangular cylinders. The validity of this correction method for a trapezoidal section has not be verified. Furthermore, there is insufficient information on correction methods for fluctuating pressure measurements and measurements on an oscillating body.

The $10' \times 5'$ tunnel has a rectangular test section with contoured walls upstream of the model location and the T5 tunnel had an octagonal test section. The corrections applied to each tunnel would therefore need to be different. As blockage is <6% none of the results stated in this investigation have been corrected for the effects of wind tunnel blockage. The effects of blockage on the VIV has not been investigated. Takeda and Kato [96] have shown a reduction in the amplitude of motion with increasing blockage.

3.4 Experimental set-up

3.4.1 Fixed body

For measurements with the body stationary, the deck was rigidly attached to the floor outside of the wind tunnel. The measurements allow investigation of the flow around the body held still. The angle of attack between flow direction and body inclination was fixed at 0^o.

3.4.2 Free Vibration

For measurements with the body freely oscillating, the model was suspended in a dynamic rig. The rig rigidly connects each end of the model to a set of four identical springs that allow heave and pitch motion. The rig is placed outside the wind tunnel at both ends and the view at one end is shown in figure 3.7. The system is rigid, except for the eight linear coil springs, which compress and extend to allow the motion. Dynamic properties of the system can be controlled by changing the springs, the lever arm between the point of rotation and the springs, and by adding mass to the rig. Taut sway wires were installed to fix the model in the streamwise direction.

3.4.3 End Plates

The length of the model was 2.74m, and designed to span the T5 tunnel, sitting flush with each wall. The $10' \times 5'$ tunnel is 3.05 m wide and with the model in position there was a 15 cm gap at each end. Studies on flows past circular cylinders [97], [98] have found that for length:diameter ratios ≥ 30, the mean and fluctuating pressures measured at the centre span are representative of those of a two-dimensional flow. Although the aspect ratio of this model satisfies this criterion, it was desired to increase the two-dimensionality of the flow, in order that measurements at other spanwise locations were representative of the approximately two-dimensional flow around the prototype. The spanwise correlation of shedding along the span is of interest in this study. End plates were placed flush with the model ends, spanning the full height of the tunnel, and $8.3D$ upstream and $16.5D$ downstream of the model. These were designed for another study of this model in the

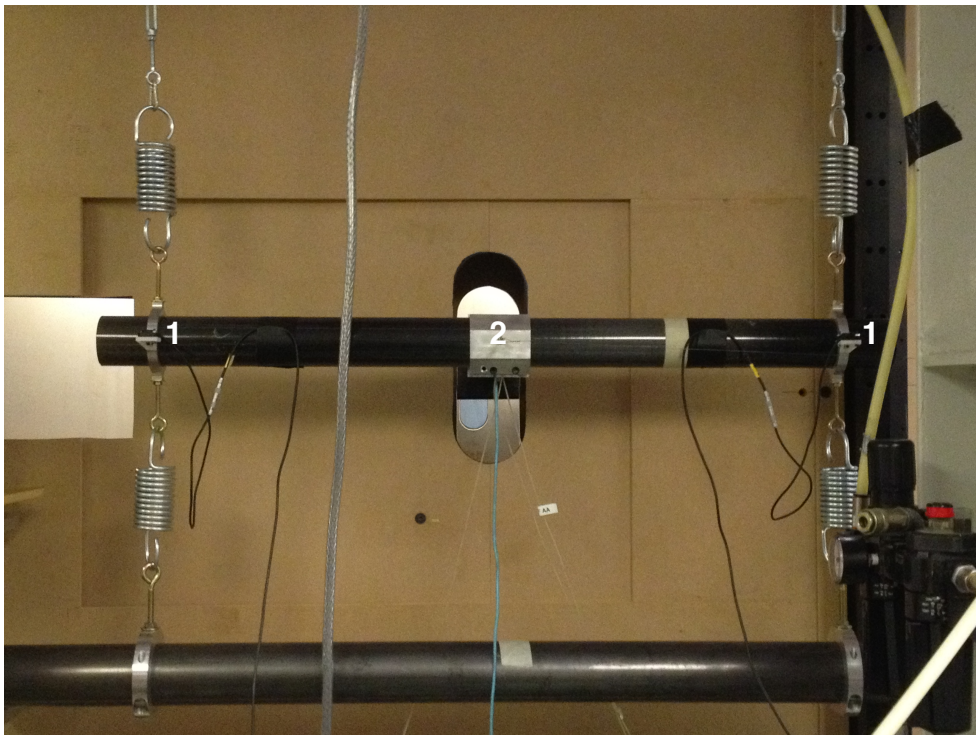


Figure 3.7: The view of the dynamic rig in the $10' \times 5'$ tunnel from one end of the model showing 1, the location of the accelerometers; 2, the suspension rig connection to the model. This set-up allows up and down motion in heave and rotational motion in pitch. The variable magnetic eddy-current damper is not shown in this picture.

$10' \times 5'$ tunnel /[99]. Each end plate had a rounded front face and sharp back face, designed to minimise separation and vortex-shedding from the wall.

3.4.4 Repeatability

Figure 3.9 compares the response of Deck B, measured in the $10' \times 5'$ tunnel with end plates, to the oscillations measured in the T5 tunnel, with the model ends flush with the tunnel walls, at the same Reynolds number and system damping, and show significantly different amplitudes; A_{max} measured in the $10' \times 5'$ tunnel is 36% of the value measured in the T5 tunnel. The onset critical velocities are similar

In section 3.3 it was discussed that increased blockage can reduce VIV amplitude. The

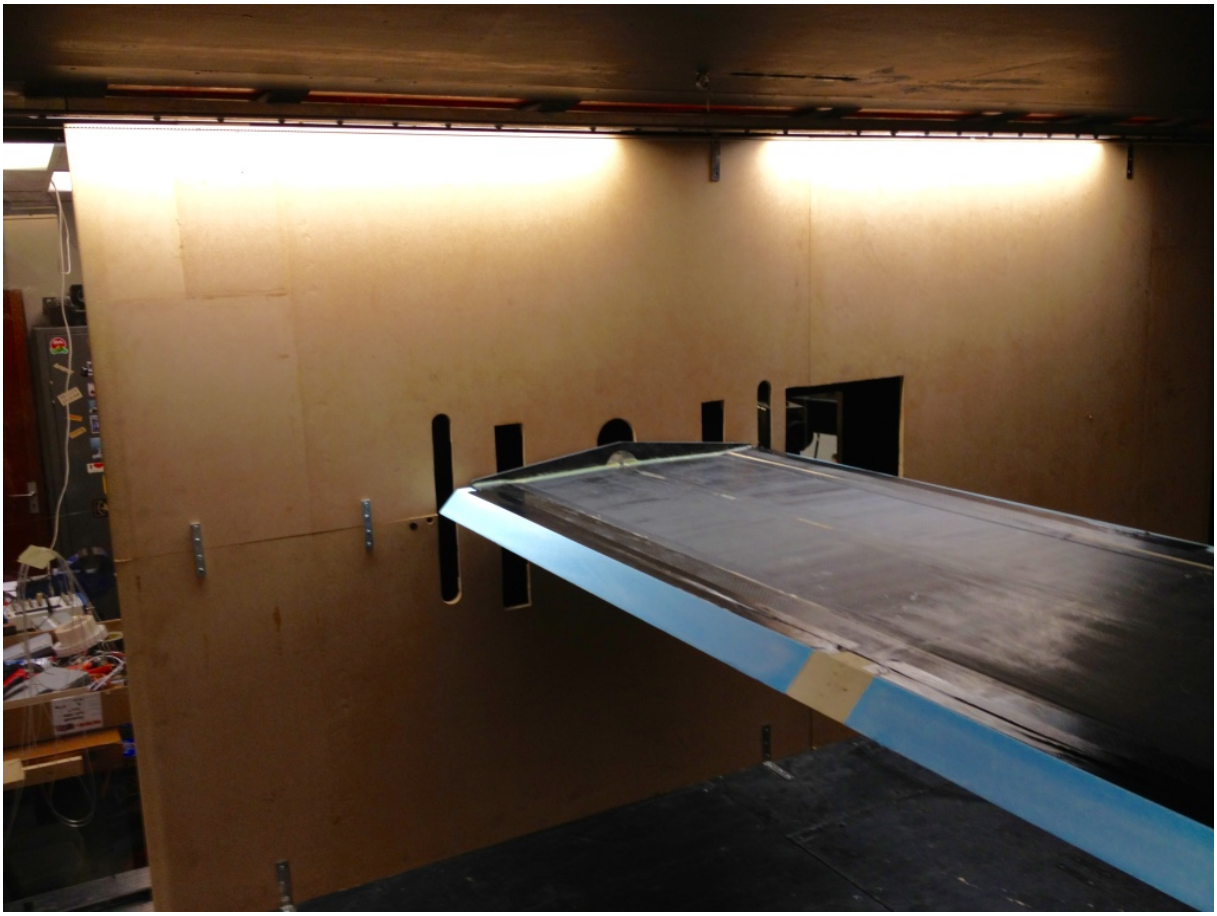


Figure 3.8: View of the end plate at one end of the model, mounted in the $10' \times 5'$ wind tunnel. The slots in the wall were made for a previous investigation and were sealed before the current experiments.

end plates increase the geometric blockage, but as the blockage remains below 6% it is not thought this effect should be significant. The major difference between the experiments is the presence of end plates and a gap at each end (between the tunnel and the walls) in the $10' \times 5'$ tunnel, whereas the model spans flush with the walls of the T5 tunnel. End effects due to free ends, end plates or interaction with tunnel boundary layers have been shown to affect the amplitude of response by modifying the shedding frequency, mean and fluctuating pressures and their spanwise correlation and the vortex formation length [100]. End effects and end-plate effects are dependent on the body shape, Re_D, aspect ratio $\frac{L}{D}$ and spanwise vortex-shedding structure [100]. There is little information on the effect of end plates on the flow around a trapezoid, but one may intuitively assess there will be some modification of the spanwise flow structure.

The set-up in the T5 tunnel approximates two-dimensional flow better, as the end plates in the $10' \times 5'$ tunnel increase the geometric three-dimensionality at the ends of the model. In the $10' \times 5'$ tunnel, the end plates are flush with the model, and the arm connecting the model to the rigid set-up outside the tunnel, passes through a gap of 145mm between the end plate and the tunnel walls. This additional geometry, and the air gap, add to the three-dimensionality of the geometry in the tunnel. This reduces the spanwise correlation of excitation force and therefore reduces the total synchronised force acting in lock-in, leading to the reduced response in the $10' \times 5'$ tunnel, seen in figure 3.9. Despite efforts to design-out wall shedding, the end walls may also produce vortices. In particular, the trailing vortices may increase the downwash of the wake at each end, reducing the component of lift perpendicular to the flow, thereby reducing amplitude, although these effects are not in the near wake, occurring $16.5D$ downstream of the tail and the interaction with the model wake is likely limited.

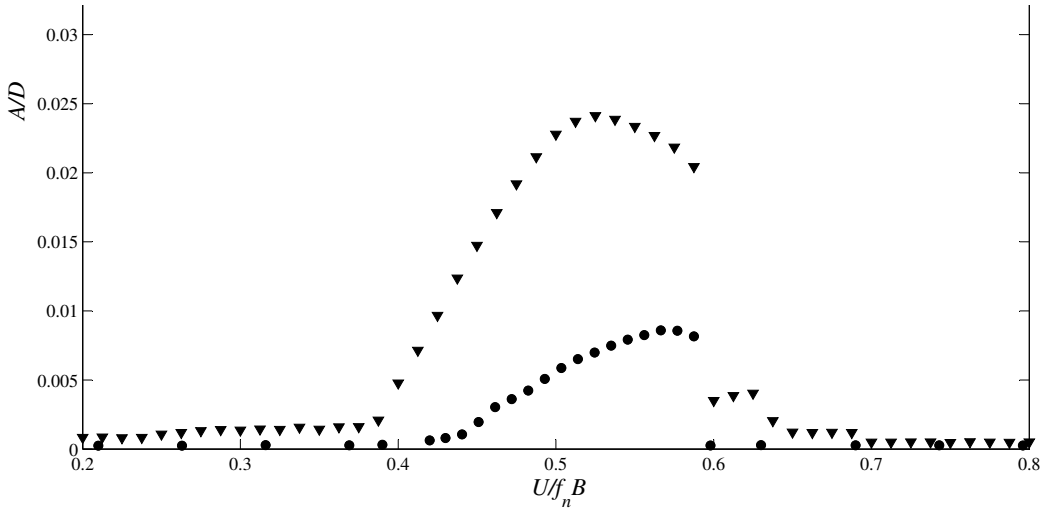


Figure 3.9: Heave response ◯, with end plates in the $10' \times 5'$ tunnel; ▽ with the model flush with the tunnel side walls in the T5 tunnel. These correspond to Run 2B↑ ψ and run 1B↑ φnDF respectively (see section 3.5.4 for nomenclature).

The significant impact of the end walls highlights the importance of three-dimensionality in experimental set-ups. A separate study is suggested, looking at the mechanisms of the wall impact. Ideally, models should be made to fit the tunnels they are tested in, without the need for end plates or gaps. This is especially the case where the behaviour is

dependant on the spanwise extent of the flow, as it is for VIV. In this study, the results are identified by a run ID (described in section 3.5.4) and compared only with results measured in the same tunnel. The sensitivities and trends are found to be consistent across both tunnels.

The other two differences in the experimental setup in the tunnels is the frequency ratio, f_{nt}/f_n and the turbulence intensity (see the next section). The frequency ratio is 2.04 in the T5 tunnel and 2.37 in the $10' \times 5'$ tunnel. f_n was set to match the previous experiments in the $10' \times 5'$ and f_{nt} set to the maximum achievable value, limited by the tunnel geometry. For given springs, the frequency can be increased by a larger horizontal separation of the spring connections to the rig. In the T5 tunnel, cast iron columns limited this separation. It was not intentional to set the frequency ratio to an integer. This can sometimes lead to coupled motion in both degrees-of-freedom. However, the responses in this study indicate there was no coupling, with heave and torsion occurring at separate wind speeds. Therefore, the frequency ratio does not appear to be the reason for the different responses across the tunnels.

It has been discussed that turbulence intensity has a significant impact on oscillation amplitude, with higher turbulence intensity resulting in reduced motion. This is discussed further in the next section, but as the intensities are low in both tunnels, the flow is essentially similar and smooth and is unlikely to be the cause of differences.

Given the different responses in the wind tunnels there are questions regarding the repeatability of the experiments and whether the results are sensitive to details other than those intended to be studied. A discussion of the differences in the the experimental set-ups indicates that the end walls are likely to be the cause of the reduced responses. Further work is required, with spanwise measurements close to the ends of the model to confirm this. In any case, several experiments were conducted in each tunnel and the findings consistent within each tunnel for both tunnels. Values are not compared across tunnels, instead trends are compared and found to agree. This satisfies the author that the trends are sensitive only to the details being studied and insensitive to the cause of tunnel differences.

3.4.5 Flow similarity

There will always be uncertainty in predicting full-scale behaviour using small-scale testing, due to the dissimilarity in modelling. The amplitude of motion measured in tests is rarely relied on to be an accurate prediction of the full-scale motion. Critical speeds for wind-induced phenomena are more reliable. Model tests are useful for comparison with other model tests, especially those with known prototype behaviour, to provide a parametric analysis.

The experiments in this investigation aim to characterise the behaviour of a trapezoidal box-girder in VIV. The small-scale experiments do not aim to model the behaviour of a specific prototype bridge, but the findings will be applicable to a wide range of realistic long-span bridges.

When modelling full-scale, three-dimensional wind-bridge interaction with small-scale, two-dimensional models, various similarity requirements are ideally satisfied. They are as follows:

1. Similarity of geometric shape and structural damping

2. Similarity of flow:

   Reynolds number, $Re_D = \frac{UD}{\upsilon}$

   Strouhal number, $St = \frac{f_s D}{2\pi U}$

   Turbulence intensity, $\frac{\sqrt{\bar{u^2}}}{U}$ and length scale

3. Similarity of structure:air parameters

   Non-dimensional mass, $m/\rho B^2$; and mass moment of inertia, $I/\rho B^4$

   Gravitational, Froude number, $Fr = \frac{U}{\sqrt{gL}}$

   Stiffness

There are limitations to the similarity that can be achieved. The Reynolds number of the prototype is $\approx 10^7$. In chapter 2, a rule of thumb was introduced; for $Re_D > 10,000$ the flow around sharp-edged bodies is insensitive to Re_D, but it was found that this does not apply for all trapezoids. The classification of a sharp-edged body may not include the

deck with shallow angles. Unfortunately, the Re_D range in this investigation could not be increased because of the low natural frequencies of the system, which are determined by the mass and springs. The mass was the minimum set by the deck and set-up and the spring stiffness the maximum determined by workability. Any stiffer and setting up the dynamic rig would have been prohibitively difficult. The Re_D range for this investigation is given in table 3.3 and is typical of similar investigations of deck aerodynamics [75].

Figure 3.10 shows the smoke visualisation of flow at the leading-edge corner of the stationary model at $Re_D = 1.3 \times 10^4$. The boundary layer appears to remain attached. The mean pressure distribution at this location shows a peak at the corner, which is amplified by oscillations, followed by a quick recovery, indicating no separation. Studies on some trapezoids, [17], have shown Re_D sensitivity of the flow, caused by separation at the leading-edge without reattachment along the body at low Re_D. For the Reynolds numbers in this investigation, this trapezoid does not exhibit the flow dissimilarity observed for the more squat section. This is not a surprise. Schewe and Larsen [17] showed a lack of similarity for the more squat spans of the Storebælt bridge but not for the wider suspended span.

The density and stiffness parameters can be adjusted by altering the mass, spring stiffness and rotational level arm. The mass, m and mass moment of inertia, I of the deck sections, including contributions from the suspension system were respectively: $m = 18.2$ kg/m and $I = 0.82$ kgm^2/m. With equivalent dimensionless values are $m/\rho B^2 = 20.7$ and $I/\rho B^4 = 1.3$. There is similarity with the values for the Storebælt suspension bridge, for which $m/\rho B^2 = 19.6$ but not for the moment of inertia, $I/\rho B^4 = 2.2$. As the results of these experiments are not to be used to calculate the rotational amplitudes of a prototype, this discrepancy will be kept in mind when comparing the response of the decks.

Turbulent scales in a wind tunnel are smaller than those observed in the atmospheric boundary layer and these parameters cannot be matched. Large-scale turbulence acts to reduce the spanwise correlation of shedding and causes the wind speed to fluctuate in and out of the critical range required to initiate VIV. The effect of turbulence length scale on the nature of motion-induced vortices such as the ILEV mode is important to consider. Saathoff and Melbourne [101] have shown that the larger length scales reduce the reattachment length at the upwind knuckle increasing the curvature of the shear



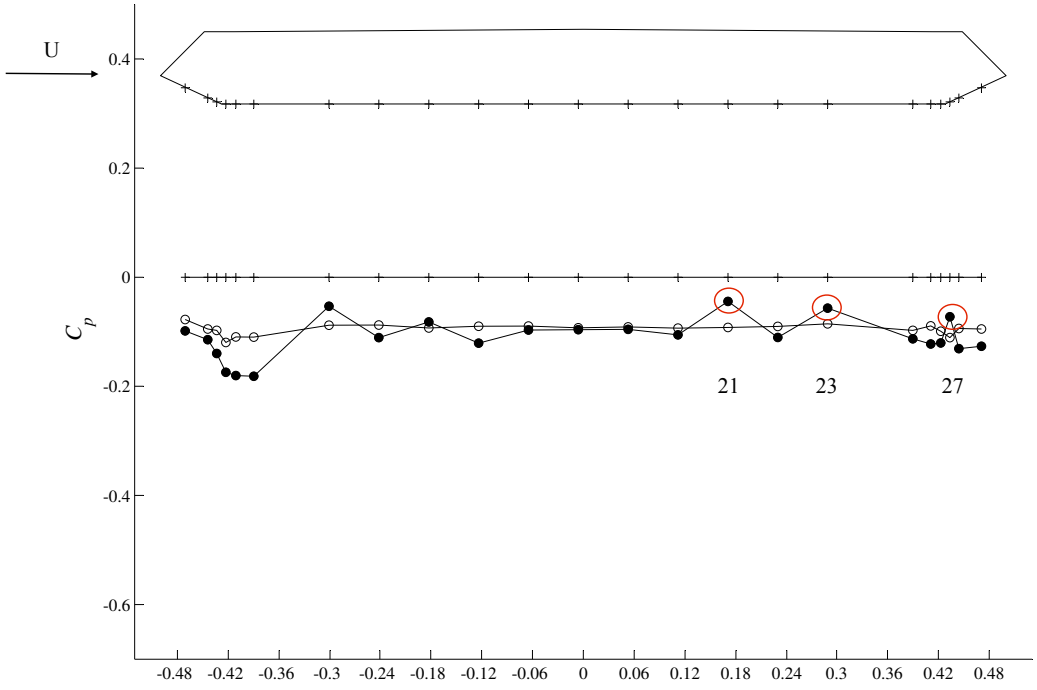


Figure 3.10: (a) Smoke visualisation at the leading edge and (b) distribution of mean pressure, C_p, measured on the bottom surface. Both at $Re_D = 1.3 \times 10^4$ with $\circ$, $A/D = 0$; $\bullet$, oscillating. This corresponds to run 1B↑ φnDF (see section 3.5.4 for nomenclature)

layer and increasing vorticity. It can be seen how a mismatch of length scales with the prototype may incorrectly model the contribution of ILEV mode excitation. Although the influence of turbulence cannot be examined satisfactorily, VIV is more pronounced at low turbulence intensities and tests carried out under these conditions provide a conservative assessment. The streamwise turbulence intensities are $I_u < 0.14\%$ (measured at 25 ms$^-$1) for the $10' \times 5'$ tunnel and $I_u < 0.21\%$ (measured at 18 ms$^-$1) for the T5 tunnel. At such

low intensities, it is expected that the effect of freestream turbulence is small.

		$10' \times 5'$	T5	
Spring stiffness	k	7190	7190	N/m
Effective spring stiffness	k_{eff}	57520	57520	N/m
System mass* (per unit length)	m	18.2	18.2	kg/m
Non-dimensional mass	$\frac{m}{\rho B^2}$	20.6	20.6	-
Mass inertia (per unit length)	I	0.83	0.83	kgm^2/m
Non-dimensional mass inertia	$\frac{I}{\rho B^4}$	1.31	1.31	-
Rotational lever arm	r	0.431	0.431	m
Heave frequency	f_n	5.2	5.4	Hz
Pitch frequency	f_{nt}	12.3	11.0	Hz
Reynolds number	Re_D	4.9×10^3-3.5×10^4	4.6×10^3-3.2×10^4	-
Turbulence intensity	I_u	$< 0.14\%$	$< 0.21\%$	

Table 3.3: The parameters of experimental set-up in this investigation. Body frequencies were measured from spectra of free vibrations in still air. *System mass includes contribution from dynamic rig.

3.5 General Experimental Procedure

3.5.1 Parameter Values

During the investigation of the vortex-induced behaviour of trapezoidal box-girders, experiments investigated the effect of various parameters. Experimental sessions carried out at different times of the year and in different tunnels resulted in different air temperatures. This affected the kinematic viscosity and Reynolds number. The maximum variation in Re_D was 10% between runs. Within a run, the temperature variation was very small and caused a variation in Re_D less than 1%.

The parameters investigated were trapezoidal shape, starting method, system damping and road furniture. The leading and trailing edges of the trapezoidal shapes were varied

between 16^o and 30^o, as described in section 3.2. The dependence on starting method described in section 3.5.3, and investigates the effect of initial condition of body motion, and hysteresis. Measurements were made with the model held stationary and allowed to freely vibrate at different structural damping values, as described in section 3.5.2. Small-scale model road furniture (figure 3.5) was added for some runs.

3.5.2 Varying the Structural Damping

The structural damping was controlled using a variable magnetic eddy-current (VMEC) damping system. The VMEC system is made up of four electromagnets and two copper conducting discs. Each disc oscillates between a pair of electromagnets placed at each end of the dynamic rig. The set-up at one end is shown in figure 3.11. The conducting discs were rigidly attached to the model and moved in unison.

The system works by the physical principle of electromagnetic induction. When the model is oscillating, the conducting discs oscillate with it. As each disc moves between a pair of electromagnets, they experience a changing magnetic flux and an induced voltage is generated in the discs. This leads to eddy currents in the disc, which have internal resistance to current and so heat is dissipated. Some of the energy in the fluid-structure system is dissipated as heat and the oscillations are opposed. The damping was controlled by varying the current supplied to the electro-magnet coil of the electromagnets.

Linear vibration theory proposes a damping coefficient that is directly proportional to the velocity of oscillations. The coefficient, C describes a viscous aerodynamic damping force that is synchronous and opposite in direction to the body motion. For a lightly damped system, $C < 2\sqrt{MK}$, the oscillations can be described by:

$$y = Y_0\sqrt{1 + (\frac{C}{2M\omega_C})^2}e^{-\frac{C}{2M}t}cos(\omega_C t - \phi_C) \tag{3.1}$$

where Y_0 is the position of the body at time, t=0 and ω_C and ϕ_C are the damping-altered natural frequency and phase shift respectively.

$$\omega_C = \sqrt{\omega_n^2 - (\frac{C}{2M})^2} \tag{3.2}$$

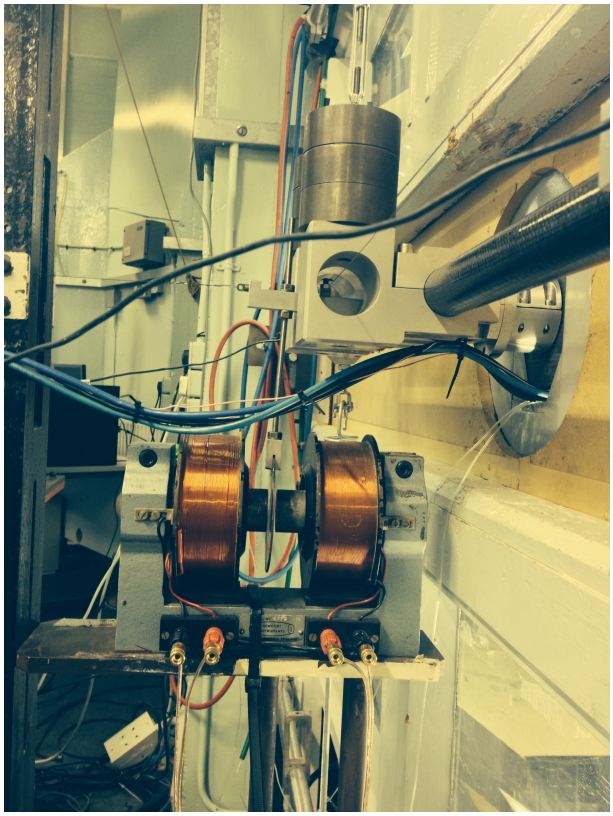


Figure 3.11: General view of the variable magnetic eddy-current (VMEC) damping system at one end of the dynamic rig. Another identical system is at the other end. The copper disc is rigidly connected to the model and moves with it, in between the two electromagnets.

$$\phi_C = tan^{-1}(\tfrac{C}{2M\omega_C}). \tag{3.3}$$

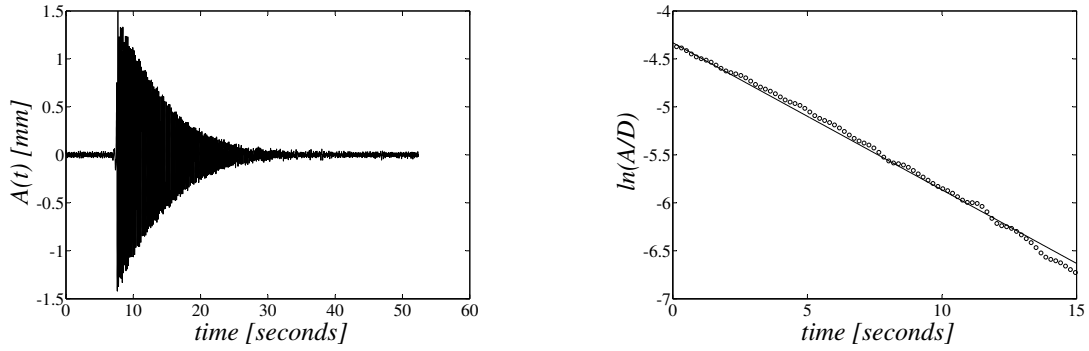
For the damping levels in this study, $\omega_C \approx \omega_n$ and ϕ_C is negligible. These values have not been corrected in this study. The time decaying amplitudes of motion can be expressed by simplifying equation (3.1) to give

$$A(t) = Y_0\sqrt{1 + (\tfrac{C}{2M\omega_C})^2}e^{-\frac{C}{2M}t}, \tag{3.4}$$

where the natural logarithm of decay amplitude:

$$\ln(A(t)) = \ln(Y_0\sqrt{1 + (\tfrac{C}{2M\omega_C})^2}) - \tfrac{C}{2M}t. \tag{3.5}$$

The structural damping was measured by perturbing the deck from its equilibrium



(a) (b)

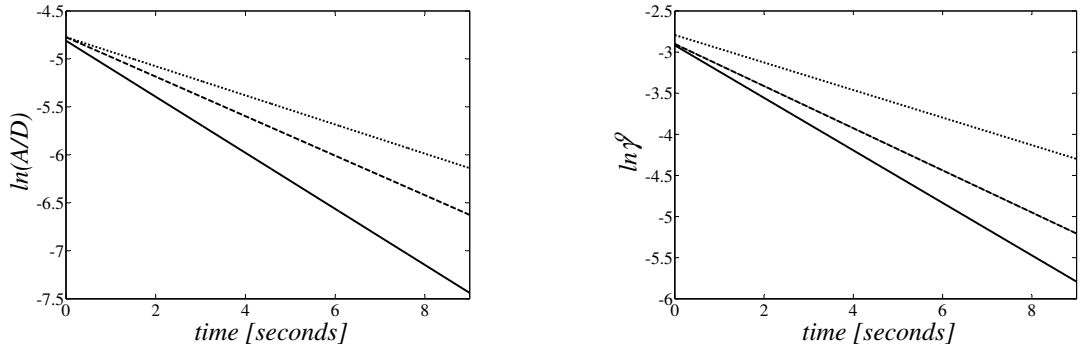
Figure 3.12: (a) sample of the time-decaying amplitude, measured by perturbing the deck to a position Y_0 and releasing in still air, and (b) the logarithmic amplitude, $\circ$ with a least squares linear curve fit, $-$.

position, in still air, and measuring the decay in amplitude. For most runs this was done by holding the model at Y_o using an electromagnet, which could be remotely turned off and released to give harmonic, decaying oscillations. The exception to this was for some runs in the $10' \times 5'$ wind tunnel, when the electromagnet had not yet been acquired. Here the model was forced by hand at f_n until harmonic motion was achieved and the forcing was removed. The decay in amplitude was then measured.

Equation 3.5 shows the logarithm of the decaying amplitude has a linear relationship with time, with a gradient $\frac{-C}{2M}$ that is proportional to the damping. A least-squares linear curve fit of the logarithmic amplitude was used to determine the gradient and calculate the damping. An example of this process is shown in figure 3.12. The linear nature of the data confirms the linear vibration for this experimental set-up for the range of velocities investigated. Table 3.4 describes the system damping for the experiments in this investigation and figure 3.13 shows the linear vibration for three of these values.

System damping	Tunnel	ζ_{heave}	ζ_{pitch}
φ	T5	0.5%	0.5%
ϖ	T5	0.5%	1.3%
χ	T5	1.0%	1.0%
ψ	$10' \times 5'$	0.7%	0.8%
$\varphi*$	$10' \times 5'$	0.5%	-

Table 3.4: Measured system damping in heave and pitch motion for experiments. $\varphi*$ was measured by forcing the model by hand at f_n until harmonic motion was achieved. The natural frequency in pitch was too high to oscillate by hand.



(a) (b)

Figure 3.13: Least-square fit of free-vibration decay for (a) heave and (b) pitch showing the linear relationship between the logarithm of the amplitude and time. −, χ;- - -,ψ; ...., φ.

ζ is defined so that $\zeta = 1$ denotes a critically damped system where no oscillations occur before motion is damped out. ζ is determined from the damping coefficient by $\zeta = C/2\sqrt{MK}$.

3.5.3 Starting method dependence

Various studies have shown hysteresis effects in the oscillation response of circular cylinders and D-section cylinders [9, 25]. The hysteresis is observed for bodies with branched amplitude response, in the transitions between the initial and lower branches. The initial conditions of each oscillation event at a given wind speed is important. The highest amplitudes of response were only achieved when the wind speed was increased in small increments. When the wind speed was reduced incrementally, or the body was released from rest at each ΔU, the amplitude response was reduced.

It was decided to determine if a trapezoid section also exhibits dependence on the initial conditions, by varying the initial conditions of each oscillation event. Three different starting methods were investigated. From a starting point with the body oscillating at a tunnel speed, U:

1. the tunnel speed was increased by a small increment $+\Delta U = 0.06$ or 0.12 ms^{-}1 with the model free to oscillate from its previous steady-state condition. This starting

method is referred to as ↑.

2. the tunnel speed was decreased by a small increment $-\Delta U = 0.06$ or 0.12 ms^{-}1 with the model free to oscillate from its previous steady-state condition. This starting method is referred to as ↓.

3. the tunnel speed was increased by a small increment $+\Delta U = 0.06$ or 0.12 ms^{-}1, 120 seconds waited, then the model released from rest. This starting method is referred to as ∧.

For all starting methods, the model is free to oscillate for 120 seconds to reach the steady-state condition.

3.5.4 Runs

Table 3.5 summarises the parameter values for each run. A "run" is used to refer to a complete test, in which the parameters are held constant, and measurements are made for a complete scan of tunnel speeds.

Run Name	Tunnel	Shape	Starting method	System damping	road furniture
e.g. 1A↑ φDF	T5:1	30^o :A	increased:↑	φ	with:DF
	$10' \times 5'$:2	25^o :B	decreased:↓	χ	without:nDF
		20^o :C	released:∧	ψ	
		18^o :D		φ^*	
		16^o :E		fixed:F	

Table 3.5: Nomenclature for experimental runs. The run name is based on a combination of numbers, letters and symbols, each referring to a parameter value.

For a given run in table 3.6, the tunnel speed was increased in increments by ΔU=0.06 or 0.12 ms^{-}1 through the range 0.92 ms^{-}1 $<U<$ 6.40 ms^{-}1. For each run, there are measurements at 51 to 96 tunnel speeds. The finer increments were used during the body oscillations and the coarser increments when there was no body motion.

After each increment in tunnel speed, initial transients were allowed to settle for two minutes before data recording began. This equated to approximately 650 oscillations in heave and 1300 oscillations in pitch. The data recording phase lasted two minutes and recorded the acceleration from two accelerometers mounted on the dynamic rig and the surface pressures at the pressure tap locations on the model. The next ΔU was implemented and the entire process was repeated for the complete range of tunnel speeds. The range of tunnel speeds was chosen to encompass VIV in heave and pitch. During a run, the data recording was remotely controlled by a LabView program. The LabView program sampled data from the accelerometers and transducers, via the transducer software MicroDaq Control Centre, to ensure that measurements of acceleration and pressure were simultaneous.

Run Name	Tunnel	Shape	Starting method	System damping	Road furniture
1A↑ ϖnDF	T5	30^o	increased	ϖ	without
1B↑ φDF	T5	25^o	increased	φ	with
1B↑ φnDF	T5	25^o	increased	φ	without
1B↓ φnDF	T5	25^o	decreased	φ	without
1B∧φnDF	T5	25^o	released	φ	without
1B↑ χnDF	T5	25^o	increased	χ	without
1B↓ χnDF	T5	25^o	decreased	χ	without
1B↑FDF	T5	25^o	increased	fixed	with
1B↑FnDF	T5	25^o	increased	fixed	without
1B↓FnDF	T5	25^o	decreased	fixed	without
1C↑ φDF	T5	20^o	increased	φ	with
1C↑ φnDF	T5	20^o	increased	φ	without
1C↓ φnDF	T5	20^o	decreased	φ	without
1D↑ ϖnDF	T5	18^o	increased	ϖ	without
2A↑ φnDF	$10' \times 5'$	30^o	increased	φ*	without
2B↑ φnDF	$10' \times 5'$	25^o	increased	φ*	without
2B↑ ψnDF	$10' \times 5'$	25^o	increased	ψ	without
2B↓ ψnDF	$10' \times 5'$	25^o	decreased	ψ	without
2B↑FnDF	$10' \times 5'$	25^o	increased	fixed	without
2B↓FnDF	$10' \times 5'$	25^o	decreased	fixed	without
2C↑ φnDF	$10' \times 5'$	20^o	increased	φ*	without
2C↑ ψnDF	$10' \times 5'$	20^o	increased	ψ	without
2C↓ ψnDF	$10' \times 5'$	20^o	decreased	ψ	without
2D↑ φnDF	$10' \times 5'$	18^o	increased	φ*	without
2E↑ φnDF	$10' \times 5'$	16^o	increased	φ*	without

*only applicable to damping in heave motion. Pitch motion not measured.

Table 3.6: Nomenclature and parameter values for all runs in this investigation.

3.6 Measurements

3.6.1 Accelerometers

The motion of the deck was measured by two Kistler K-Beam 8305B10M2 accelerometers placed on the dynamic rig, as shown in figure 3.14. Care was taken to place the accelerometers symmetrically and horizontally. The dynamic rig moves rigidly and in phase with the model. Placement on the rig allows the accelerometers to measure the motion of the model from outside the tunnel and not impact on the flow around the model.

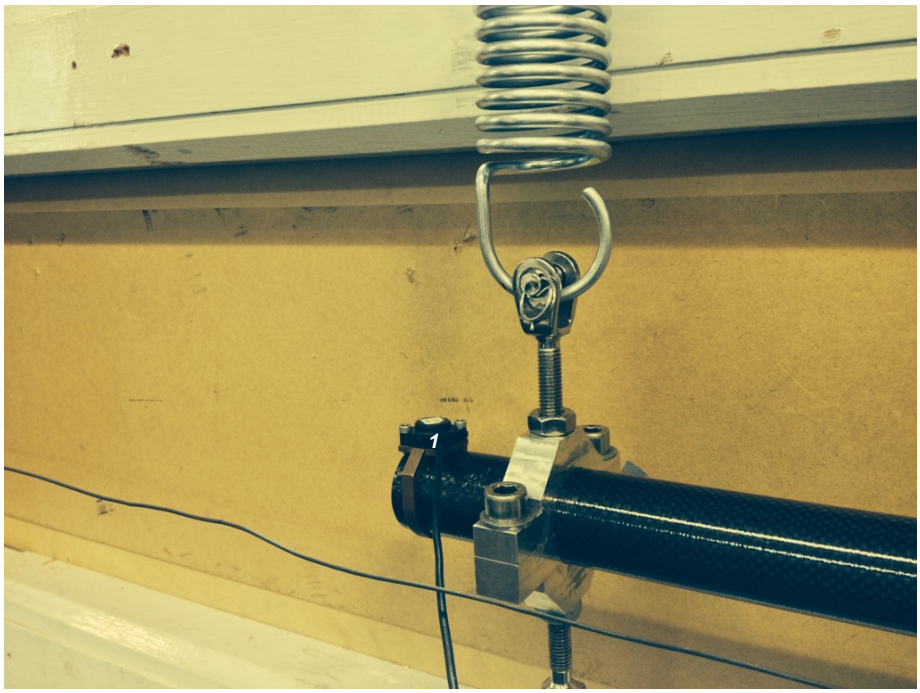


Figure 3.14: View of one accelerometer (1) in position on the dynamic rig.

The accelerations were sampled at 300 Hz for two minutes. The voltages were converted to acceleration using the unique calibration determined for each accelerometer. The voltage magnitude depends linearly on the acceleration. The acceleration recorded took account of the effect of gravity.

3.6.2 Pressure scanners

The pressure was measured at 64 taps on the surface of the model; 47 taps were distributed around a cross-section $0.44L$ along the span, and 17 taps distributed at the trailing-edge

at spanwise locations at $0.3L$, $0.51L$ and $0.81L$ measured from one end of the model. The spanwise taps were placed at the same chordwise locations to allow correlations of shedding to be determined.

The 64 pressure tappings were connected to two Chell microDAQs. The microDAQs are complete pressure scanning systems, containing a PSI ESP pressure scanner. Each microDAQ had 32 pressure diaphragms and for these experiments, two microDAQs were run in parallel using the Chell microDAQX software. microDAQX includes a built-in Control Centre to allow multiple microDAQs to be controlled from a central point, with the possibility of all data acquisitions being combined into one log file. The benefits of using two 32-channel scanners via Control Centre rather than one 64-channel scanner, is the increased acquisition speed and the shorter length of tubing required to connect all the surface taps to the scanners. The microDAQs were triggered with a TTL signal to synchronise measurements of pressure and acceleration. When a microDAQ receives a positive edge, it will generate a set of measurements for all 32 channels.

The microDAQs were mounted on foam pads within the hollow internal area of the model to minimise the length of tubing required. All taps were connected to a microDAQ via 750 mm lengths of 1 mm i.d. portex tubing. This length was the minimum required. The effect of tubing on the measured pressure is discussed in Chapter 4.

Chapter 4

Analyses

4.1 Introduction

Acceleration and pressure data were gathered in the experiments described in chapter 3. In this chapter, the analysis methods employed to process the data are described. The accelerometer data is used to provide vertical and angular displacement and the pressure data is presented as non-dimensional coefficients, phase angles and spanwise correlations. The mathematical definitions of the coefficients, correlations and spectra are included.

The approach in this study has been to conduct small-scale physical experiments in a wind tunnel. The long span of the model and the distance between pressure taps on the surface of the model and the DAQ units collecting the data, resulted in 750mm lengths of tubing to connect taps to the DAQ. A description of how the tubes modify the measured signal and the correction employed follows. The pressures are integrated to give aerodynamic forces. The motion-generated component is significant for a body with long chord-wise extent, B, as is the case here. A correction method is described.

4.2 Acceleration measurements

Measurements from the accelerometers were used to calculate heave acceleration and angular acceleration (pitch) using LabView software. The heave acceleration was calculated as an average of the measurements from the two accelerometers. The pitch accelerations

was calculated using measurements from the two accelerometers and their separation distance. Details of the measurement parameters are given in table 4.1.

Table 4.1: Acceleration measurement parameters

Sampling frequency, f_s	300 Hz
Sampling time	120 s
Sampling length	36000
Accelerometer full scale range	$\pm 10g$
Accelerometer resolution	$1.5 \times 10^{-3}g$

The measured acceleration was integrated twice to give displacements. Before integration, the signal was low-pass filtered at the Nyquist frequency, 150Hz, and high-pass filtered at 2.5 Hz to remove the low frequency components that are disproportionately amplified during the integration. The r.m.s. accelerations during lock-in are affected by less than 0.25% by the high-pass filter. A 5th-order Butterworth filter was used for its maximally flat response in the passband and the filter was applied in both the forwards and backwards direction in time, resulting in no phase distortion to the acceleration.

The displacements are presented as dimensionless r.m.s. vertical displacement, A/D and angular displacement, γ. The oscillation frequency, f_y was determined as the dominant peak in the acceleration spectra.

4.3 Pressure measurements

Each microDAQ outputs data over ethernet to a PXI via a cable which runs through the model and exits the wind tunnel via the suspension system. The microDAQX software was used to zero the scanners before each run in still air. On powering on, the MicroDAQs carry out a real-time temperature calibration, which was completed before data measurements began.

The pressure measurements were processed to give time-averaged pressure and fluctuating pressure. The pressure measurements are presented as pressure coefficients, C_p:

$$C_p = \frac{p - p_\infty}{0.5\rho U^2} \tag{4.1}$$

where p is the measured pressure and p_∞ is the ambient pressure, measured at a pitot tube placed in the wind tunnel at the same stream-wise location as the deck. The coefficient is non-dimensional by the free-stream dynamic pressure. The pressures were integrated to give aerodynamic forces.

$$C_L = \frac{F_L}{\frac{1}{2}\rho U^2 B} \tag{4.2}$$

$$C_M = \frac{F_M}{\frac{1}{2}\rho U^2 B^2} \tag{4.3}$$

where C_L and F_L are the lift coefficient and force respectively, and C_M and F_M are the moment coefficient and force respectively.

The shedding frequency, f_s was determined from the fluctuating pressure signal measured at the bottom downwind knuckle, where a coherent vortex is expected to form. Details of the pressure measurements are shown in table 4.2.

Table 4.2: Pressure measurement parameters

Sampling frequency, f_s	300 Hz
Sampling time	120 s
Sampling length	36000
Microdaq full-scale range	$\pm$1000 Pa
Microdaq resolution pressure	3.1×10^{-2} Pa
Frequency resolution	8.3×10^{-3} Hz

As mentioned in the chapter 3, the pressure measurements were not corrected for the effect of geometric blockage. The microDAQs were corrected for the small instrumentation delay of 50×10^{-6} s per channel, generated by reading the channels on each scanner in series. The maximum error was 1×10^{-3} s, equivalent to a phase shift of 2.5° for a pressure signal at f_y.

4.3.1 Tubing effects

Tubing connected the pressure taps in the model surface to the transducer. The tubing can modify the measured pressure in three ways:

- Attenuation at frequencies above a critical cut-off frequency
- Phase shifts at frequencies above another, different critical cut-off frequency.
- Amplification at the oscillation frequency, f_y.

The attenuation and phase shift of the pressure signal is dependent on the tubing type, length and internal diameter. Rigas [102] carried out calibrations for the same portex tubing and ESP system, but with 1.5 m long lengths; double the tubing here. The transfer function, describing how the tubing of the Rigas system, modifies the pressure signal, is shown in figure 4.1. The cut-off is quite rounded and the critical frequency refers to the -3 dB cut-off, which is 18 Hz. Non-zero phase shifts occur for frequencies greater than 2 Hz. This transfer function can be estimated by a complex number, $H(s = i\omega)$:

$$H(s = i\omega) = \frac{1}{1+i\frac{\omega}{\omega_H}} \tag{4.4}$$

where ω_H is the resonant frequency of a Helmoltz resonator, made up of the cavity-orifice system of the ESP cavity and connected tubing.

$$\omega_H = \sqrt{\frac{3\pi r^2 c^2}{4lv}} \tag{4.5}$$

where r is the radius of the tubing, c is the speed of sound in air, l is the length of the portex tubing and v is the volume of the cavity.

The magnitude of the transfer function $|H(s = i\omega)|$ is used to calculate the gain of the tubing system, defined as:

$$Gain = 20log_{10}|H(s = i\omega)| = \frac{1}{\sqrt{1+(\frac{\omega}{\omega_H})^2}} \tag{4.6}$$

The phase shift induced by the tubing is the argument of the transfer function:

$$Angle = \angle H(s = i\omega) = \tan^{-1}(\frac{\omega}{\omega_H}) \tag{4.7}$$

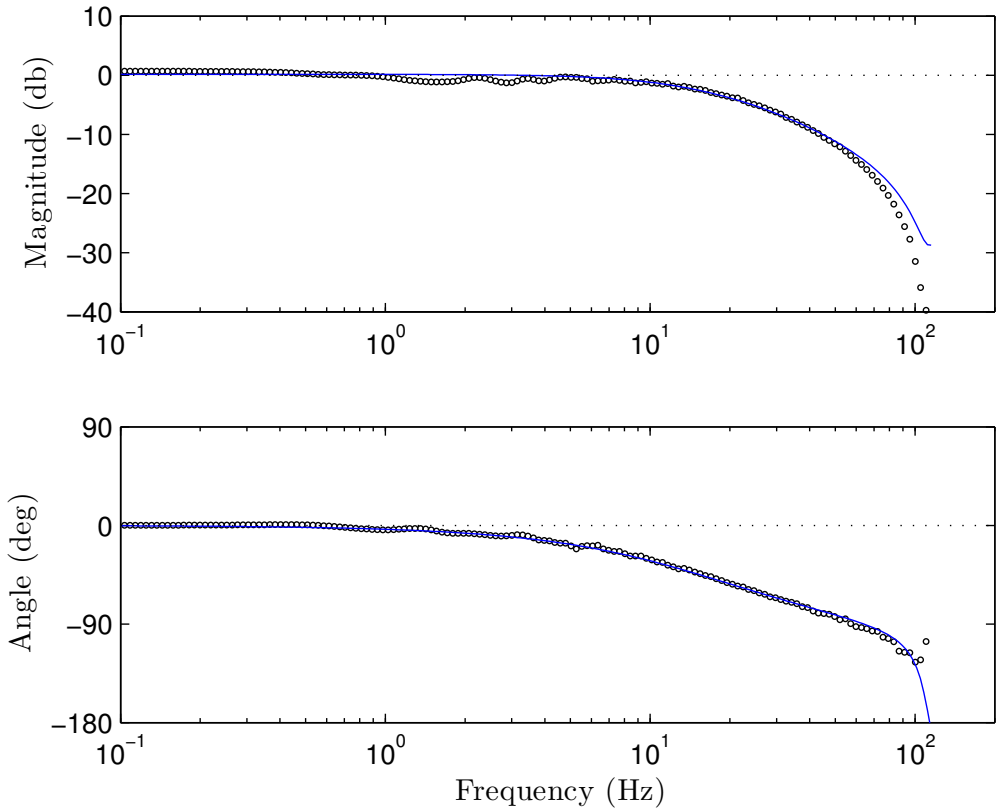


Figure 4.1: Frequency response of the pressure measurement system, with 1.5 m lengths of 1 mm i.d. portex tubing connected to an ESP with a discrete first order filter fit (line), [102].

Equation 4.6 and equation 4.7 are approximations that show good agreement with the measurements by Rigas on the system in figure 4.1.

An estimation of the attenuation and phase shift of the same system with 750 mm lengths of tubing, can be made. The Bode plots are shown in figure 4.2. The calculated -3 dB cut-off frequency is 25.5 Hz which is above the frequencies of interest in this work, $f_n \leq 5.4$ Hz and $f_{nt} \leq 12.3$ Hz. The maximum error in amplitudes are 2% at f_n and 8% at f_{nt}. Therefore no correction for attenuation of the pressure is enforced. There are predicted phase shifts at f_n and f_{nt} of $-12°$ and $-23°$ respectively. These are applied to all pressure measurements.

Bearman & Currie [11] discuss how tubing leads to an amplification of the pressure signal at the oscillation frequency, if the model experiences any acceleration along a line

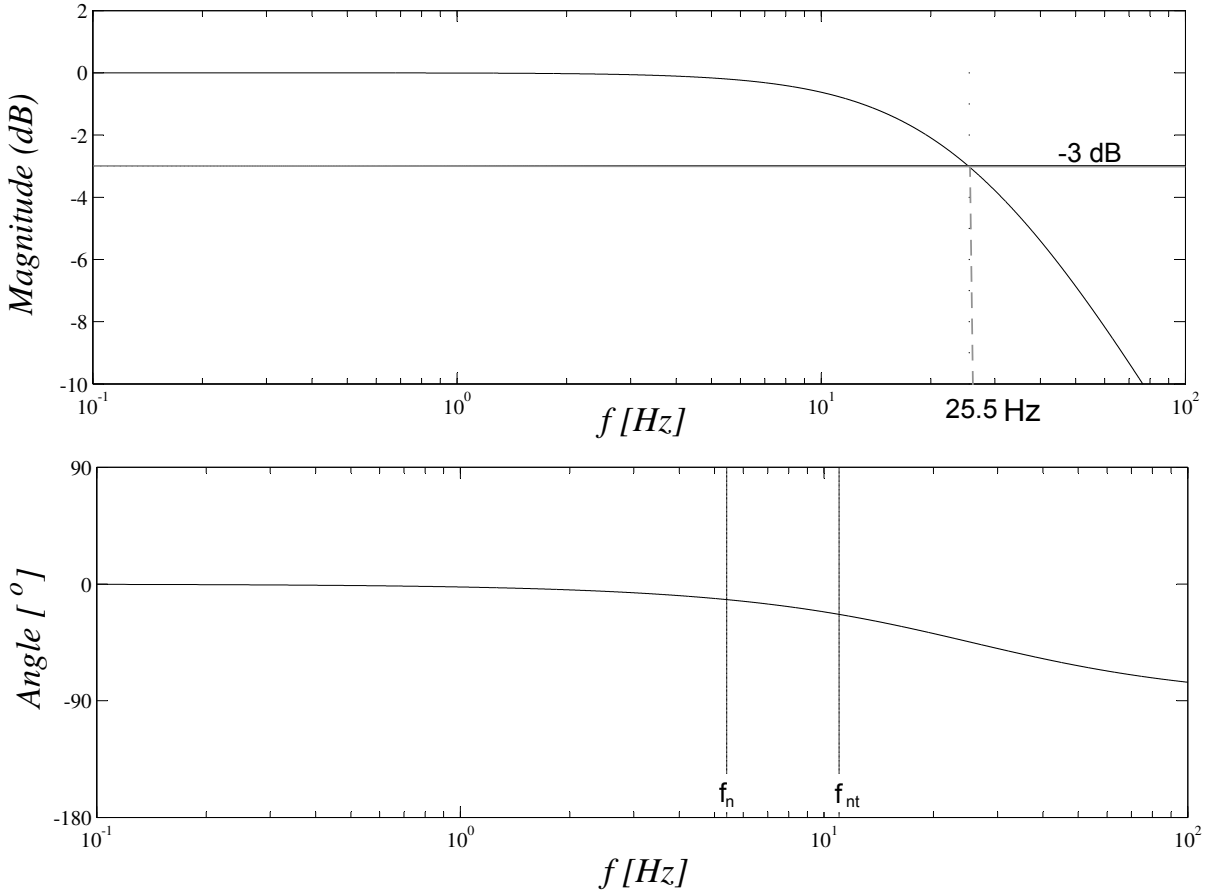


Figure 4.2: Bode plots of frequency response of the pressure measurement system with 750 mm lengths of portex tubing, modified from figure 4.1 and equations 4.6 and 4.7.

connecting the transducer to the pressure tap. Bearman & Currie [11] propose an r.m.s. pressure coefficient $C'_{pA}(f_y)$ to account for this,

$$C'_{pA}(f_y) = 4\sqrt{2\pi^2}\frac{A}{D}\frac{h}{D}(\frac{f_n D}{U})^2, \tag{4.8}$$

where h is the distance between the transducer and the pressure tap in line with the direction of acceleration. Measurements of C'_p can be corrected for the effect of tube length by using equation:

$$C'_p = (C'_{pA}(f_y)^2 + {C'_{pm}}^2 - 2C'_{pA}(f_y)C'_{pT}(f_o)cos\beta)^{\frac{1}{2}}, \tag{4.9}$$

where C'_{pm} is the measured fluctuating pressure coefficient, $C'_{pT}(f_y)$ is the r.m.s. of the measured fluctuating pressure coefficient at the oscillation frequency and β is the angle

by which the measured suction leads the displacement. The correction is only necessary when there is body motion.

Measured phase angles, β are affected by the acceleration effect, $C'_{pA}(f_y)$. The corrected phase angle, ϕ can be calculated from the relation:

$$\phi = arctan(\frac{C'_{pT}(f_y)sin\beta}{C'_{pT}(f_y)cos\beta - C'_{pA}(f_y)}). \tag{4.10}$$

The maximum effect in pressure for these experiments is 1.6% in amplitude and a 0.9° phase shift. These are negligible errors and none of the pressure measurements in this work have been corrected for this effect.

4.3.2 Theodorsen forces

When the bridge deck is in motion, induced by the flow, it also experiences a lift force and moment generated by the body motion. Measurements of the pressure on the body, L_{total} will include a motion-generated component, that is not associated with the von Kármán vortex wake. The forces are calculated from integration of the cross-sectional pressures:

$$F_{L,total} = -\int_{-b}^{b}(p_u - p_l)dx \tag{4.11}$$

where b is the half-chord ($\frac{B}{2}$), p_u and p_l are the measured pressures for the upper and lower surfaces respectively, and x is the co-ordinate in the chord-wise direction.

Theodorsen's theory [103] for a flat plate and thin aerofoils gives the solution of the motion-generated forces and moments on a thin body in heave and/or pitching motion in a potential flow with a thin wake. In VIV, the body motion captures the shedding frequency; the vortex excitation and the motion-generated forces have the same frequency. Distinguishing the force components is important to understand how the vortex excitation changes through lock-in. As there is a similarity between streamlined bridge decks and thin aerofoils, the Theodorsen theory can be used, with limitations, to remove the direct motion-generated pressures and forces from the measured pressures and forces in this investigation.

The main limitations stem from the assumptions of the body and flow used to derive Theodorsen's theory. The body in this investigation differs in shape to a thin aerofoil of

flat plate, has thickness and camber. The impact of steady effects such as camber and thickness will be a constant bias to the mean measurements. However, we are primarily interested in the fluctuations about the mean caused by the unsteady vortex-shedding and these steady biases are not concerning. Where the deviations of shape from a flat plate exist, particularly at the knuckles, the theory will be less adequate at approximating the motion-generated effects. Additionally, the flow has viscosity and is separated, with a substantial wake, whereas Theodorsen's theory is based on unseparated and irrotational flow. Separation ahead of the tail affects the Kutta condition and hence the accuracy of Theodorsen's theory to approximate the motion-generated effects. Notwithstanding these limitations in applying the theory to the trapezoid, as the motion-generated component is substantial, there is merit in estimating and removing it.

Theodorsen describes two components of the motion-generated force: the non-circulatory component, $F_{L,NC}$ (equation 4.12) and the circulatory component, $F_{L,circ}$ (equation 4.13), that linearly superpose:

$$F_{L,NC} = -\rho b^2(\pi\ddot{h} + \pi U\dot{\gamma}) \tag{4.12}$$

where $\ddot{h}$ is heave acceleration and $\dot{\gamma}$ is pitch velocity.

$$F_{L,circ} = -2\pi\rho bUC(U\gamma + \dot{h} + 0.5b) \tag{4.13}$$

Where C is Theodorsen's function; a filter which attenuates the lift force depending on the value of the reduced frequency of oscillation, k.

$$k = \frac{\omega_y b}{U} \tag{4.14}$$

For this work, k is very large, ≈ 6 and $C(k) \approx 0.50$. The apparent mass dominates.

Both components are two-dimensional along the span and directly proportional to the amplitude of motion. The non-circulatory component contributes to the added mass term, which describes the energy to displace the volume of air around the model as it oscillates. This reduces the resonant frequency (but only by a little in air) and opposes the motion of the body. As the bridge deck has a large chord, B, the volume of air displaced and therefore the non-circulatory component is substantial. Added mass of a

flat plate in heave is equal to a circular cylinder of air, with the same diameter as the plate's chord. The circulatory component is in phase with the body velocity, and gives the damping component of the motion-generated force. The circulatory component modifies the inviscid potential model to satisfy the Kutta condition that the stagnation point at the rear of the body be found at the tail, and takes account of the local effect of viscosity which causes this.

In the case of the bridge deck in this investigation, the non-circulatory component is much larger than the circulatory component, and makes up 85% of the total motion-generated forcing. Sharp corners will have more effect on circulatory than non-circulatory components as they promote separations which interfere with the Kutta condition with a thick wake and generate "virtual" thickness and camber effects which will be time-dependent and will therefore also contaminate the unsteady forces. This component has not been removed from the total measured forces, with the understanding that it will increase in a fixed proportion with body motion.

$$L_{VIV} = L_{total} - (L_{NC} + L_{circ}) \tag{4.15}$$

In this work, the measured forces have had the non-circulatory motion-generated component removed. Individual pressure measurements have not had motion-generated components removed. These components are based on potential flow around an aerofoil, and the error in applying to the decks in this study, stemming from the separated flow and difference in shape, varies around the cross-section. A more complex correction method for the amplitude and phase at each tap location is required. It is deemed misrepresentative to compare values of the C'_p distribution with varying degrees of error at different positions in the cross-section. Where figures present C'_p at more than one cross-sectional location, it is thought more representative to present the measured pressure coefficient and explain the limits for interpretation. Comparison of the cross-sectional pressure distribution is made with other studies, where the motion-induced forces are generally small and are not removed. The exception to this is where pressures are presented at the same cross-section location, where the error is unknown, but constant. This is the case for the spanwise correlations. For these measurements, only the non-circulatory component is removed, as the circulatory component is hard to predict at the sharp-edged trailing edge

of the trapezoid. The circulatory component will increase in a fixed proportion with body motion and this is kept in mind when looking at results.

4.4 Spanwise Pressure Correlation

The spanwise correlation of the fluctuating pressure, at the trailing edge corner is made using a two-point cross-correlation and performed for every combination of pressure tapping points. For earlier experiments, there were three spanwise tapping points on the line, giving four correlation coefficients, $R_{(p',z)}$. In later experiments, pressure taps were added giving four tapping points on the line and seven correlation coefficients, $R_{(p',z)}$.

$$R_{(p',z)} = \frac{\sum_n (p_{zA}(t) - \bar{p_{zA}})(p_{zB}(t) - \bar{p_{zB}})}{\sqrt{\sum_n (p_{zA}(t) - \bar{p_{zA}}) \sum_n (p_{zB}(t) - \bar{p_{zB}})}} \tag{4.16}$$

where p_{zA} and p_{zB} are pressure time-series measured at pressure tappings A and B, and z is the separation distance.

The correlation length L_R is given by:

$$L_R = \int_0^\infty R_{(p',z)} dz \tag{4.17}$$

4.5 Pressure Spectra

In chapters 5, 6 and 7 the displacement and pressure data are sometimes presented in terms of the power spectral density, PSD, $\Phi(f)$. The PSD describes the power present in a signal, as a function of frequency, per unit frequency. Welch's method is used to estimate the PSD. Using the example of a fluctuating pressure signal, $p'(t)$, Welch's method:

- splits the sample into L segments, of length M, each overlapping by D points. For the analysis in this study D=50%
- a window function, $w(t)$ is applied to each segment
- the discrete fourier transform, DFT is performed on each windowed segment:

$$X_l(f) = \sum_{t=1}^{t=M} p'(t)w(t)e^{-i2\pi ft} \tag{4.18}$$

- the modified periodogram value is calculated :

$$P_l(f) = \frac{1}{W} \mid X_l(f) \mid^2 \tag{4.19}$$

where W is a normalisation factor:

$$W = \sum_{t=1}^{t=M} w^2(t) \tag{4.20}$$

- the Welch estimate of the PSD averages the periodogram values over all the segments at each frequency:

$$\Phi(f) = \frac{1}{L} \sum_{l=1}^{l=L} P_l(f) \tag{4.21}$$

The PSD is presented in spectra as $\Phi(f)$ and premultiplied spectra, $f\Phi(f)$, presented on semi-log plot. If the only consideration is finding the peaks, there is no need to premultiply. The area under the premultiplied curve and the ordinate is proportional to the power of the signal [104].

$$\int_0^\infty \Phi(f)df = \overline{p'(t)^2} \tag{4.22}$$

$$\int_{-\infty}^\infty f\Phi(f)d(logf) = \overline{p'(t)^2} \tag{4.23}$$

4.6 Conclusion

This concludes detail on the general analysis methods. The next three chapters describe the findings from the experiments carried out as described in chapter 3. Chapter 5 presents

the behaviour of Deck B, with a typical fairing shape, and determines the mechanisms of the slender trapezoid in VIV. Chapter 6 looks at the sensitivity to fairing shape, in particular to the bottom knuckle angle and position, with dramatic results. Chapter 7 describes the impact of starting condition (in terms of body and flow), road furniture and damping on the behaviour in VIV.

Chapter 5

Vortex-induced vibration of a trapezoidal box-girder

5.1 Introduction

There is significant literature on the VIV of low aspect-ratio bodies, such as circular and square cylinders. The nature of VIV differs depending on the cross-section shape. A stationary square cylinder appears less stable than a stationary circular cylinder, but the fluid-structure interaction through lock-in amplifies the shedding of the circular cylinder to a much greater degree.

There is less literature on the behaviour of high aspect-ratio bodies in VIV. Although slender rectangles have been studied, the behaviour of trapezoids has been limited mostly to commercial tests on bridge decks with slenderness in the range $6 \leq B/D \leq 10$. In chapter 3 it was discussed that trapezoids are excited to VIV by three mechanisms; LEVS, ILEV and TEVS, dependant on the aspect ratio, B/D. Experiments in this chapter are carried out on Deck B, shown in figure 5.1. Deck B has an angle at the leading and trailing edge corners of 25°. The Storebælt bridge is one of the most extensively studied box-girders [51], [75], [53]. The similarities between the Storebælt bridge and the experiments by Larsen and Wall [75] and Terres-Nicoli and Kopp [51], and Deck B allows a comparison of the measurements. The principal similarities and differences are summarised in Table 5.1. Results for the Storebælt studies can be seen in figures 2.47 and 2.29.

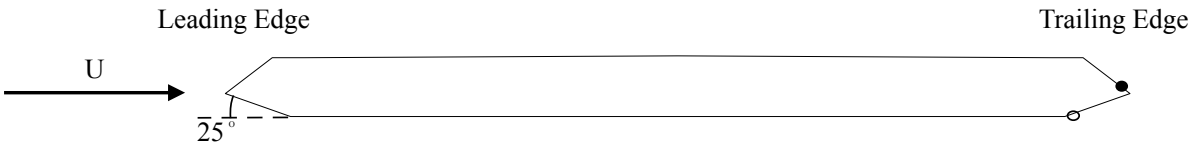


Figure 5.1: Deck B, $B/D = 11.2$, with a 25° angle at the leading and trailing edges. Labels indicate the location of measurements; • base: pressure, C_{pb}; ∘, trailing edge: fluctuating pressure, C'_p, shedding frequency, f_s and spanwise correlations, $R_{p',z}$.

	Storebælt		Deck B	
	[75]	[51]	Run 1B↑ φnDF	Run 2B↑ ψnDF
Deck	single box-girder	"	single box-girder	"
Shape	trapezoid	"	trapezoid	"
B/D	7.8	"	11.2	"
θ_T	26^o	"	45^o	"
θ_B	27^o	"	25^o	"
$\frac{f_n}{f_{nt}}$	1.78	na	2.04	2.30
$\frac{m}{\rho B^2}$	22.1	na	20.6	"
$\frac{I}{\rho B^4}$	2.46	na	1.31	"
Re_D	$0.3 - 4.0 \times 10^4$	$0.9 - 6.0 \times 10^4$	$0.5 - 3.2 \times 10^4$	$0.5 - 3.5 \times 10^4$
I_u	$< 0.8\%$	$< 0.5\%$	$< 0.21\%$	$< 0.14\%$
ζ	0.1%-0.2%	0.3%	0.5%	0.7% heave, 0.8% torsion

Table 5.1: A comparison of the Storebælt main span and the experiments of Larsen and Wall [75] and Terres-Nicoli and Kopp [51] and Deck B in this investigation.

Deck B is a similar shape to the Storebælt deck, but significantly more slender. The angles at the bottom knuckles are similar but different at the top knuckles. In terms of comparing the experiments; the Reynolds numbers are very similar with the experiments of Terres-Nicoli and Kopp [51] the highest. The damping levels are higher in this study (0.5% was the minimum damping with the VMEC system off) and the turbulence levels smaller, although the studies on the Storebælt are in smooth flow.

The Storebælt model has been observed to experience multiple instances of lock-in within a range of continuous wind speeds ($0.1 \leq U(f_nB) \leq 1.6$), for both heave and pitch, as shown in figure 2.47. One of these lock-in instances involved significant frequency shifting from $f_s = 2.5f_n$ down to f_n, a phenomenon not observed elsewhere in the literature. Multiple instances of lock-in were observed in the same study for the Osteroy bridge (figure 2.53) and are indicative of ILEV shedding in multiple modes.Terres-Nicoli and Kopp [51] show a bending peak is excited by TEVS and motion-generated ILEV, n=2.

In this chapter, it is hoped to assess the phenomenology of VIV for Deck B by looking at measurements of the flow and response for run 1B↑ φnDF and run 2B↑ ψnDF, made with the body stationary and freely oscillating, to describe the effects of lock-in. The location of measurements are shown in figure 5.1. Pressure measurements around the trapezoidal section were measured at a cross-section at $0.44L$, where L is the span of the model, presented as pressure coefficients. The pressures in this section include the motion-generated component. An approximation of the motion generated component is removed from the lift force, and examples of the total and VIV-generated components are presented later in this chapter. The approximation is described in more detail in Chapter 4.

In particular the mechanism of VIV excitation is investigated by looking at fluctuating pressures on the body. Very little is known about the excitation of a trapezoid at this slenderness. As Deck B is very slender, it is expected to undergo VIV, excited by TEVS. Very slender rectangles, $B/D \gtrsim 10.5$ have been shown to be only experience TEVS [44]. This may excite motion-generated ILEV, as it has for a wind-tunnel model of the Storebælt [51]. The large number of wavelengths required for ILEV excitation of this slender body renders the feedback sensitive to perturbations and less likely to occur in practice than

for a less slender body. However, high modes of ILEV vortex generation, up to n=4 have been observed on rectangular cylinders (figure 2.27). The ILEV mechanism is expected to diminish with slenderness, as it does for rectangular bodies [38]. It is of interest the extent to which ILEV plays a role in the VIV of this slender box-girder.

5.2 Results

The vortex-shedding frequency, f_s, identified from spectra of the fluctuating pressure recorded at the trailing edge, normalised by the natural frequency in heave, f_n is shown plotted in figure 5.2 for run 1B↑ φnDF. The shedding frequency is captured at lock-in by the body frequency for one instance in heave ($0.39 \leq U/(f_n B) \leq 0.59$) and one instance in pitch ($0.76 \leq U/(f_n B) \leq 1.25$). The shedding frequency for the stationary body is plotted on the same graph for comparison. For both instances of lock-in, the resonant point (the flow speed at which f_s for a stationary body is equal to f_n) occurs at the onset of lock-in, similar to observations of the Storebælt deck [75] and circular cylinders [9]. Figure 5.3 plots the same measurements for run 2B↑ ψnDF, where lock-in exists for $0.49 \leq U/(f_n B) \leq 0.56$ in heave and $0.89 \leq U/(f_n B) \leq 1.35$ in pitch. The higher onset critical velocity for pitch is due to the higher natural frequency in run 2B↑ ψnDF. The Strouhal number for the stationary body is 0.24, calculated using a least-squares linear curve fit. This is similar to $St \approx 0.22$ measured by Schewe and Larson [17] for a model of the Storebælt approach span, B/D=3.7, at Reynolds number: $4 \times 10^5 < Re_D < 4 \times 10^6$ (two orders of magnitude higher than those in these experiments). Measurements on a model of the Storebælt main span [75] (figure 2.47) at similar Re_D to this study show a much higher shedding frequency; $St \approx 0.32$.

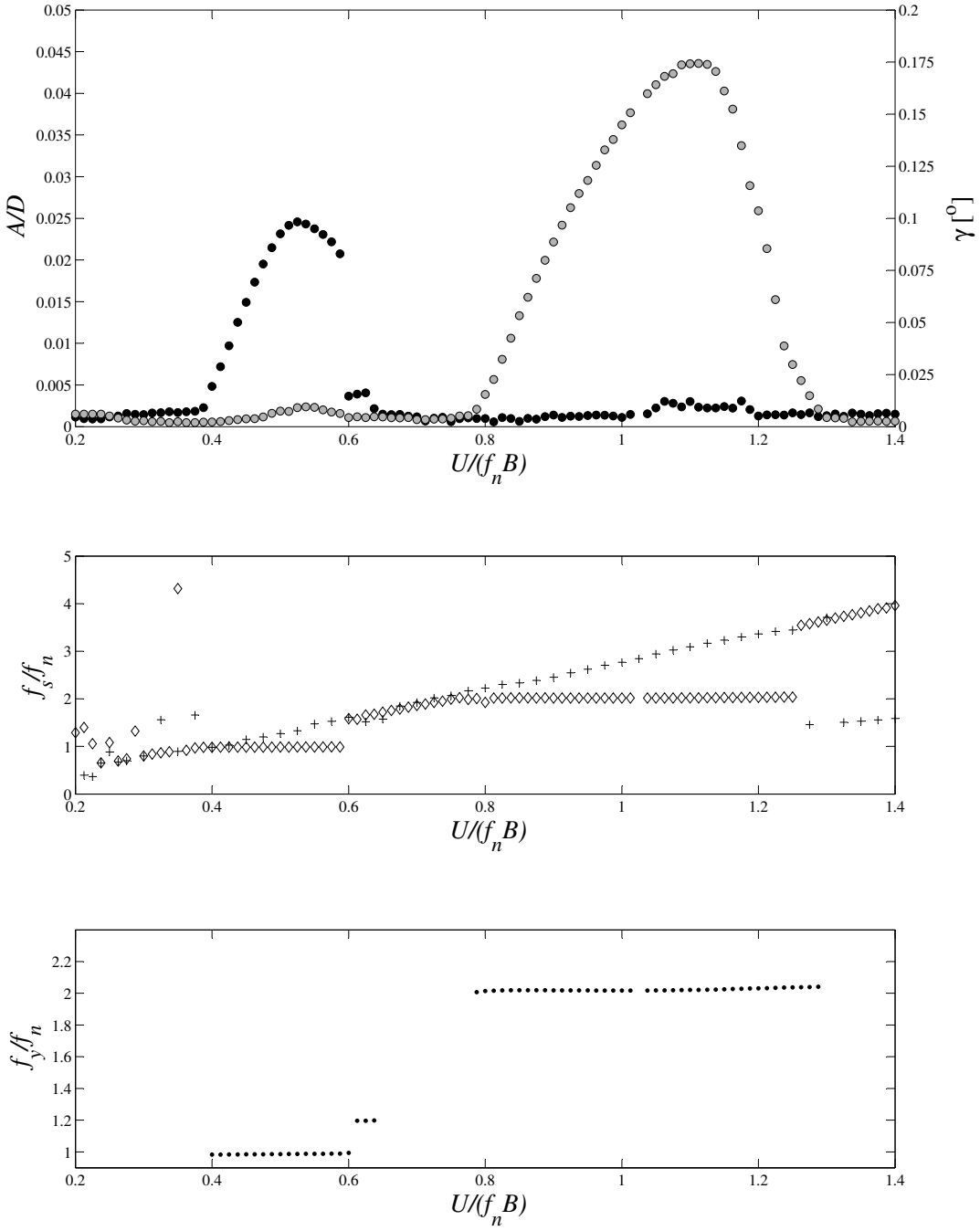


Figure 5.2: Run 1B↑ φnDF: •, rms displacement in heave A/D; •, torsion γ; +, vortex-shedding frequency, f_s of the stationary body; and ◊, elastically-mounted body; ·, body frequency, f_y.

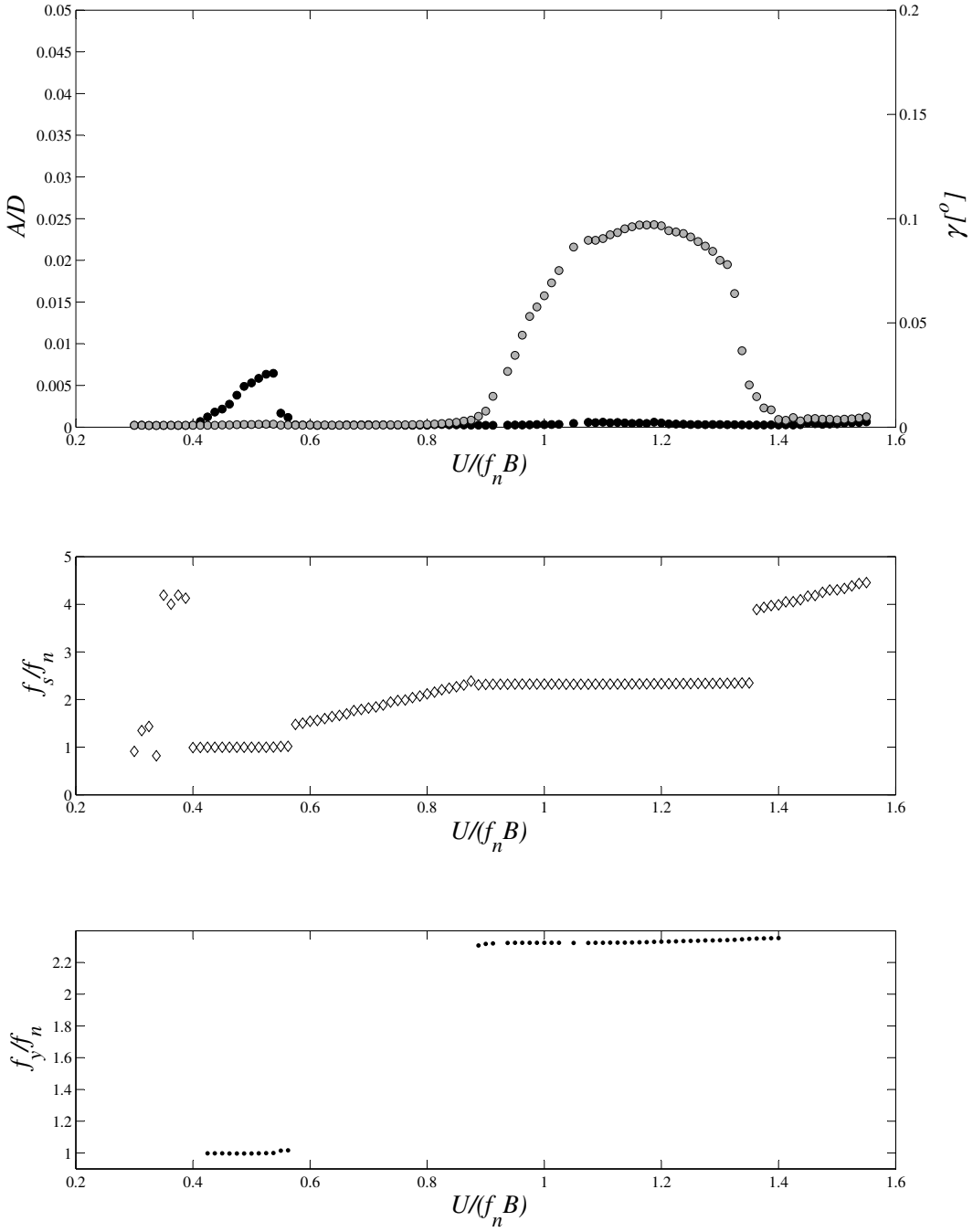


Figure 5.3: Run 2B↑ ψnDF: •, rms displacement in heave A/D; •, torsion γ; ◊, vortex-shedding frequency, f_s of the elastically-mounted body; ·, body frequency, f_y.

The lock-in is accompanied by body motion. The body displacement is shown plotted against non-dimensional velocity, $U/(f_nB)$ in figure 5.2 and figure 5.3, where γ is the angle through which the body rotates, relative to the horizontal. The maximum amplitudes are $2.4\%D$ and 0.18° for run 1B↑ φnDF and $0.6\%D$ and 0.10° for run 2B↑ ψnDF. The apparent heave response in figure 5.2 at $0.6 \leq U(f_nB) \leq 0.64$ is another rigid body motion; roll, where the body rotates about a pivot at the mid-span. The accelerometers placed at only one end of this set-up, record a vertical heaving motion. Analysis of the forces acting on the body indicates very little motion-generated component close to the mid-span, that grows with proximity to the model ends. This agrees with what would be expected for roll motion; larger amplitude motion further from the mid-span pivot will generate larger motion-generated pressures at f_y. The spring support system allows roll to occur, and this has been observed on the same deck, in another study, tested in the $10' \times 5'$ wind tunnel [99].

In figure 5.3, all the response $0.40 \leq U(f_nB) \leq 0.56$ is heave, with no roll present. Two distinct sets of heave response exist, separated by a discontinuity. The heave response displays an initial branch and lower branch, as termed by Govardhan and Williamson [24] to describe the discontinuous response of a circular cylinder: the initial branch describes the displacement response from the onset of motion at low wind speeds and up to A_{max}, the lower branch refers to the response at higher wind speeds and smaller amplitudes. The branched heave response observed here has been seen for wind-tunnel tests of the Storebælt section in figure 2.29, a plate girder section [93] and the numerical simulations of a rectangular cylinder, [10]. It is difficult to tell whether the responses of the Storebælt model in figure 2.47 are discontinuous. The data points are not plotted at a sufficiently high resolution of wind speeds to be certain. In figure 5.2 and figure 5.3 the amplitudes of the torsional rotation show a smooth progression throughout lock-in. The amplitude response is slightly asymmetrical, with γ_{max} occurring at a higher wind speed than the mid-point of the range of capture. The range of capture is ≈ 3 times larger for pitch compared to heave.

The body frequency, f_y was determined from spectra of the oscillations recorded by the accelerometers. f_y normalised by f_n is plotted in figure 5.2 and figure 5.3. The roll frequency at $\approx 1.2f_n$ can be seen in figure 5.2.

Figure 5.4 and figure 5.6 show the distribution of time-averaged pressure, C_p around a cross-section of the model when stationary and oscillating at A_{max}/D. Figure 5.5 and figure 5.7 show the distribution of C_p at maximum pitch, γ_{max}. For a stationary body, $C_p = 1$ at the front stagnation point. The geometry of the sharp corner and the leading edge prohibited positioning of a pressure tap at the stagnation point. The front face of the model experiences positive pressures, with the rest of the body in suction. C_p reached maximum suction at the leading edge corners, identifying the extreme surface curvature. At higher wind speeds these peaks are stronger on the stationary body . The region downwind of these peaks displays an adverse pressure gradient, indicating the flow separates in this region. This indicates separation bubbles at the leading edge, both at the top (tap n2 to tap 1) and the bottom (tap n7 to tap 13), of significant length $\approx 2D$.

In chapter 2, the Re_D dependence of a trapezoid was described for $Re_D < 4 \times 10^5$, caused by flow separating at the upwind bottom kncukle and controlling shedding. The mean pressure distribution in these experiments indicates no persistent separation at the leading edge.

In figure 5.4 to figure 5.7, circles highlight pressure taps that measure unexpected values. These three taps read more positive pressures than is expected from measurements at adjacent taps. The resolution of measurements of C_p is 9×10^{-3} at A_{max} and 2×10^{-3} at γ_{max}. With the model stationary, the taps read as expected and similar to adjacent taps. In still flow before the run, readings indicated no error or positive offset. When the model is elastically mounted, for all flow speeds, the circled taps in run 1B↑ φnDF read more positive pressures than adjacent taps. These measurements should therefore be treated with caution. Mounting the model, or the oscillations during the free runs, may have caused the portex tubing inside the model connecting the surface taps to the DAQs to become squashed, kinked or blocked. Tap 12 in run 2B↑ ψnDF shows zero values for all wind speeds, indicating a fault with the tap.

The impact of oscillations on the pressure distribution varies between the wind tunnels. In Chapter 3, the difference in response between the $10' \times 5'$ wind tunnel and the T5 wind tunnel is discussed further. It is not known what causes this difference, although it is likely related to the presence of end plates in the $10' \times 5'$ which increase three-dimensionality. The pressure distributions for the stationary bodies are similar, except the suction peaks

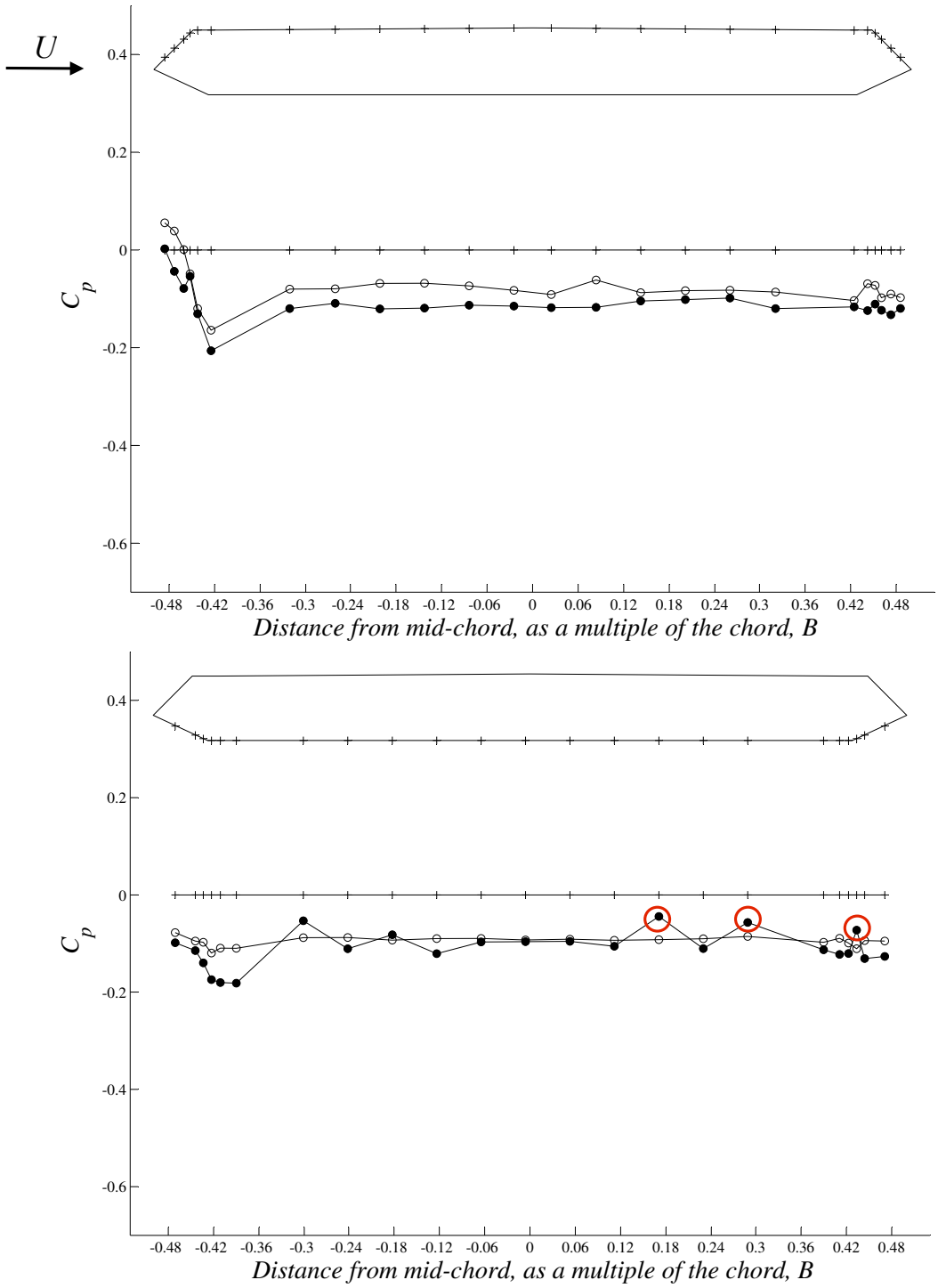


Figure 5.4: Run 1B↑ φnDF: distribution of mean pressure, C_p at $U/(f_n B) = 0.53$ at a cross-section at $0.44L$. $\circ, A/D = 0$, $\bullet$ $A_{max}/D = 2.4\%$. Pressure tap locations are indicated, +. Pressure taps giving erroneous results are circled in red.

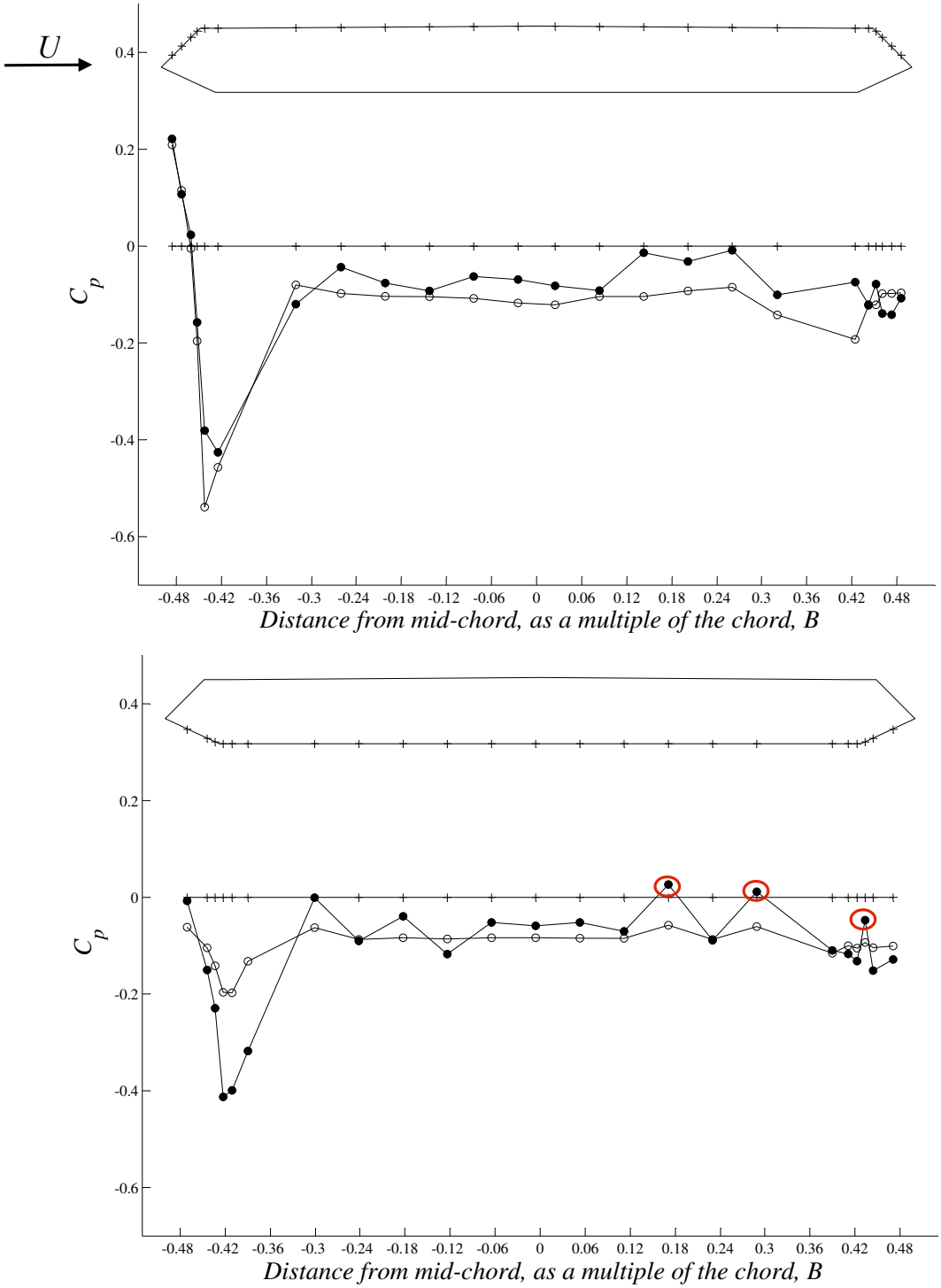


Figure 5.5: Run 1B↑ φnDF: distribution of mean pressure, C_p at $U/(f_n B) = 1.11$ at a cross-section at $0.44L$. $\circ, \gamma = 0°$, $\bullet$ $\gamma_{max} = 0.18°$. Pressure tap locations are indicated, $+$. Pressure taps giving erroneous results are circled in red.

at the leading edge are much stronger for run 2B↑ ψnDF. The impact of oscillations also differs. For both runs, the oscillations do not appear to change the locations of separation and reattachment on the body. The flow appears to separate at the upwind knuckles, reattaching further downstream.

Figure 5.8 plots the mean pressure, measured at the knuckles of the stationary model. It is evident that the separation at the top upwind knuckle is Re_D dependent up to $\approx 3 \times 10^4$ At higher wind speeds the suction increases. The separation at the bottom upwind knuckle is sensitive to a lesser degree. The trailing edge separation is independent of Re_D for the range investigated in this study. The pressure distribution graphs also indicate that the separation bubble at the leading edge displays Re_D sensitivity, whilst the pressures in other locations do not. A possible reason for Re_D differences is a change in the separation and reattachment of flow around the body. However, the C_p distribution in figure 5.4 to figure 5.7 show the leading edge peaks return to low suctions rapidly, indicating that the separated flow does not persist beyond the leading edge. Indeed, the length of the separation bubbles at the leading edge appears to remain constant with Re_D, although the suction increases significantly.

Figure 5.9 plots base pressure, C_{pb} against non-dimensional velocity for the stationary and oscillating model. The base suction is increased by oscillations, with two peaks coinciding with the body displacement in heave and pitch. A discontinuity in C_{pb} occurs at the trnasition from heave oscillations to roll oscillations. The strongest suction through heave lock-in does not coincide with A_{max} but instead the suctions continues to increase with wind speed through lock-in and plateaus at $U/(f_n B) = 0.56$. The peak in C_{pb} for pitch lock-in coincides with γ_{max} and reduces with increasing wind speed. Equation (2.12) was introduced in Chapter 2 and relates the vorticity in the wake, to the base pressure. Davies [33] assumed the entrainment, α was unaffected by oscillations when describing the effect of lock-in on vorticity shed from a D-cylinder. Applying the same assumption here, the vortex-strength shed from the trailing edge at lock-in for the trapezoidal section is amplified by 3% and 3% over the stationary case, in heave and pitch respectively. The small size of this increase, adds importance to the assumption of constant entrainment.

At high wind speeds, when no motion or lock-in is observed, C_{pb} increases continuously with flow speed to twice the stationary body value at the maximum wind speed

investigated, instead of taking the stationary body values. The only difference between the stationary body and the elastically-mounted body with no oscillation, is the ability of the deck to take an angle of incidence to the flow. The centroid of the mean lift force is upstream of the mid-chord and can act to rotate the body. The set-up in these experiments is not able to measure steady changes in the angle of incidence (the accelerometers only measure motion about a mean), and so this hypothesis is not confirmed.

Fluctuating pressures measured on the stationary and elastically-mounted model are presented in figure 5.10 to figure 5.12 as pressure coefficients, C'_p. Distribution of fluctuating pressure around the model through heave lock-in is shown in figure 5.10. The effect of oscillation through the lock-in range is to increase the fluctuating pressure. The largest pressures exist at maximum amplitude. At the resonant point: $U/(f_nB) = 0.39$, C'_p values are slightly increased relative to the stationary model. Interestingly, the fluctuating pressure is larger at $A/D = 1.5\%, U/(f_nB) = 0.45$ than at $A/D = 2.1\%, U/(f_nB) = 0.59$, despite the amplitudes. The effect of oscillation is smallest at the front of the deck, growing over the body. Peaks at the trailing edge identify sharp increases in fluctuating pressure, possibly due to shedding.

Figure 5.11 plots the Reynolds sensitivity of the fluctuating pressure measured at the upwind and downwind knuckles of the stationary model. C'_p measured at the knuckles displays Re_D dependence, with fluctuations increasing with wind speed. The downwind knuckles display the greatest sensitivity, especially at the bottom. As wind speed increases, it appears shedding from the trailing edge is strengthened.

The fluctuating pressures measured at the base and trailing edge (shown in figure 5.12) are similar in shape. C'_p values peak at A_{max} and have a similar shape to the displacement response graphs in figure 5.2. In pitch, C'_p values peak before γ_{max} and the peak in mean base pressure, shown in figure 5.9. The peak in C'_{pb} is at a lower wind speed than the peak at the trailing edge. The amplification over the stationary case is greatest in heave, especially at the trailing edge. In pitch, the pressure amplitudes are very similar in the two locations.

The fluctuating pressures measured at the surface of the body, along a line coinciding with the downwind bottom knuckle were correlated to give coefficients, $R_{p',z}$. The analysis is described in chapter 4. Results for the heaving body, plotted in figure 5.13 show how the

correlation varies with spanwise separation distance (z/D) and increments of oscillation. The pressures in figure 5.13a have had the motion-generated component removed, as an estimate of the von Kármán-generated force, whereas in figure 5.13b includes the fully two-dimensional motion-generated component. When included, this component leads to much higher apparent correlations, even at small amplitudes. As explained in Chapter 4, the calculation of the motion-generated component is based on unseparated, potential flow and will include an error for the separated flow around Deck B. In particular the effect of motion on circulation around Deck B has been ignored, as this component is particularly affected by unseparated flow. However, the jump up in correlation in figure 5.13a from $A = 0.2\%D$ to $0.5\%D$ is not proportional, and suggests the pressures nearly completely represent the vortex shedding component, since the direct effect of motion in circulation around the deck will only change in a manner that is a fixed proportion of amplitude. To the author's knowledge, the spanwise correlation of only the vortex-shedding component for a bridge deck, has not been previously presented.

When the body is stationary, the flow is highly three-dimensional. The correlation length is approximately $2.3D$. This is a measure of the area under the correlated portion of figure 5.13; that part at smaller separation where $R_{p',z}$ reduces linearly. Oscillation significantly increases the spanwise correlation of surface pressure above the stationary case. Small increases in amplitude, early on in lock-in, result in large increases in correlation along the span. There is a consistently high level of correlation for the full separation distance investigated: $20D$ for amplitudes above 0.8%.

Through heave lock-in, the vortex-shedding is very sensitive to oscillations and a large increase in spanwise correlation is observed above a threshold amplitude of $0.002D$. Comparisons with correlations of oscillating circular cylinders, calculated from the total measured pressure, is reasonable, as the scale of the motion-generated forces for this low aspect ratio, (B/D) body is much smaller. For the circular cylinder, the motion-generated forces are generally proportional to D^2 as opposed to the bridge deck, whose forces scale with B^2. The threshold amplitude of $0.002D$ for the bridge is an order of magnitude smaller than the threshold amplitude for a circular cylinder [23], suggesting the trapezoid is more sensitive to increases in correlation through lock-in. This is probably due to the presence of the sharp corners, which define the separation point.

At low amplitude oscillations, the correlation coefficients do not monotonically decrease with separation distance. The correlation coefficients have not been calculated for the same single reference pressure, and this inhomogeniety in the flow is thought to be caused by three-dimensional effects, including the end conditions.

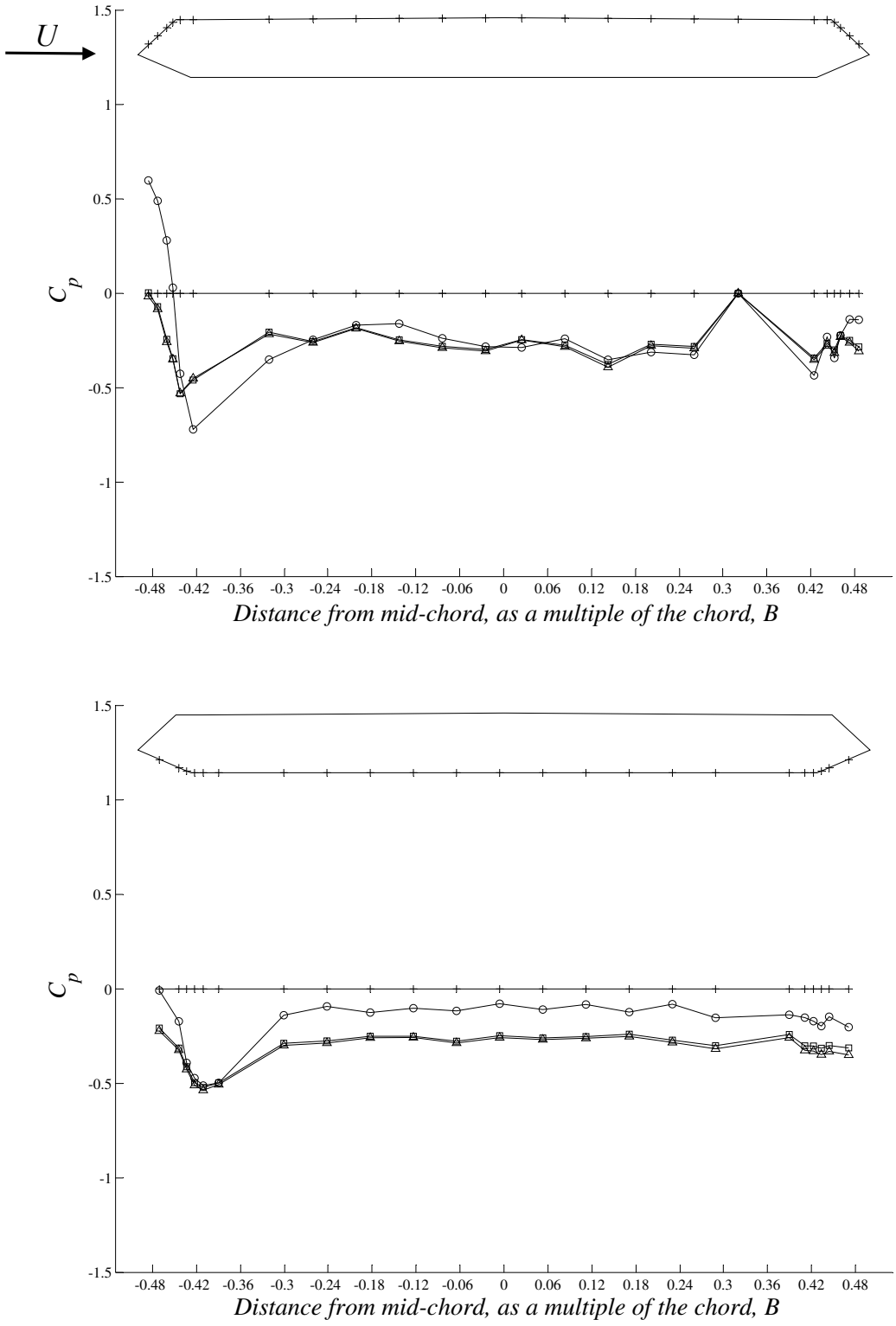


Figure 5.6: Run 2B↑ ψnDF: distribution of mean pressure, C_p at $U/(f_n B) = 0.54$, at a cross-section at $0.44L$. $\circ, A/D = 0$; $\square$ $A_{max}/D = 0.6\%$ $U/(f_n B) = 0.55$, $\triangle$. Pressure tap locations are indicated, $+$. Pressure taps giving erroneous results are circled in red.

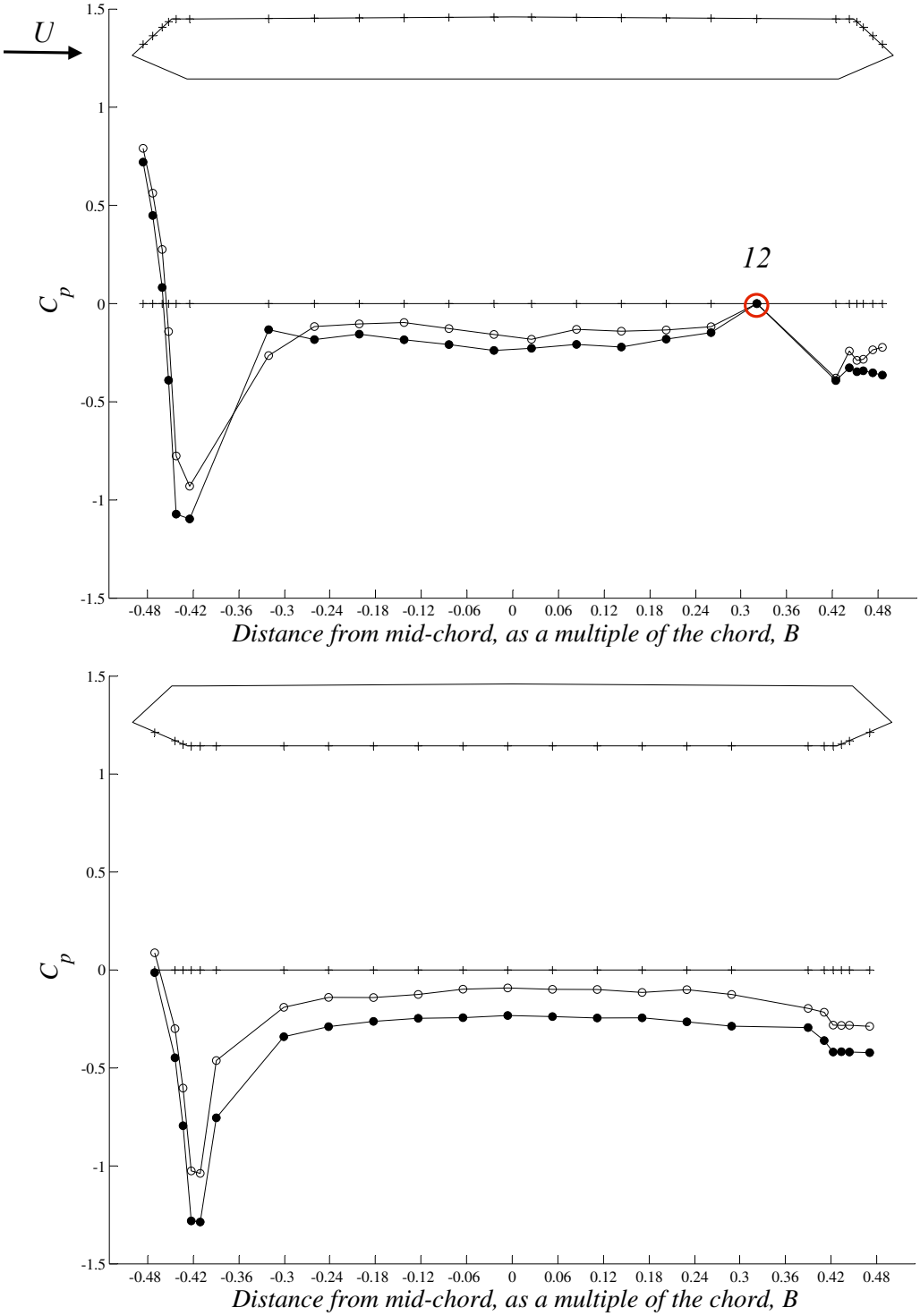


Figure 5.7: Run 2B↑ ψnDF: distribution of mean pressure, C_p at $U/(f_n B) = 1.18$ at a cross-section at $0.44L$. $\circ, \gamma = 0°$, $\bullet$ $\gamma_{max} = 0.1°$. Pressure tap locations are indicated, $+$. Pressure taps giving erroneous results are circled in red.

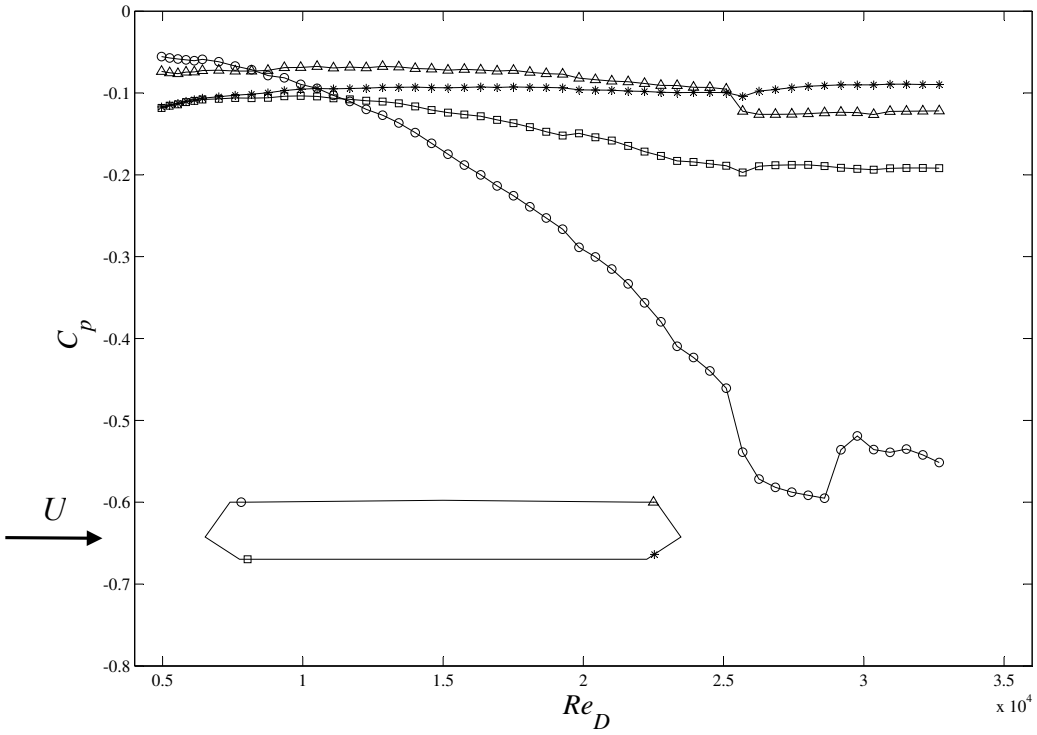


Figure 5.8: Run 1B↑ φnDF: effect of Re_D on mean pressure, C_p for the stationary deck measured at $\bigcirc, \square$, the leading edge; $\bullet$, trailing edge.

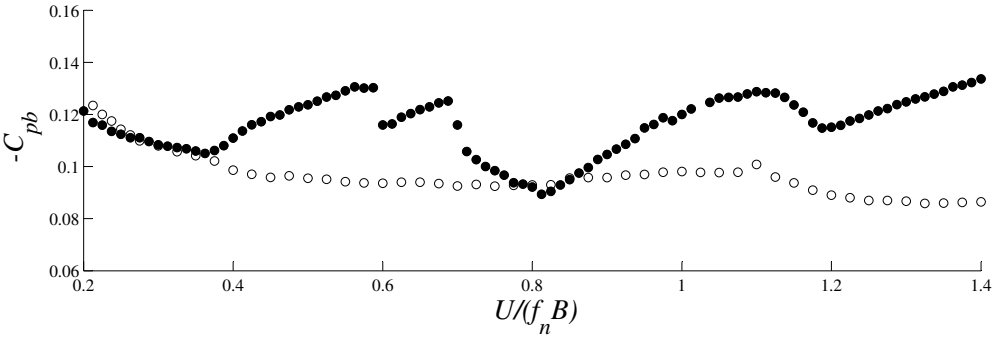


Figure 5.9: Run 1B↑ φnDF: base pressure, $-C_{pb}$, $\bigcirc$, $A/D = 0$; $\bullet$, elastically-mounted.

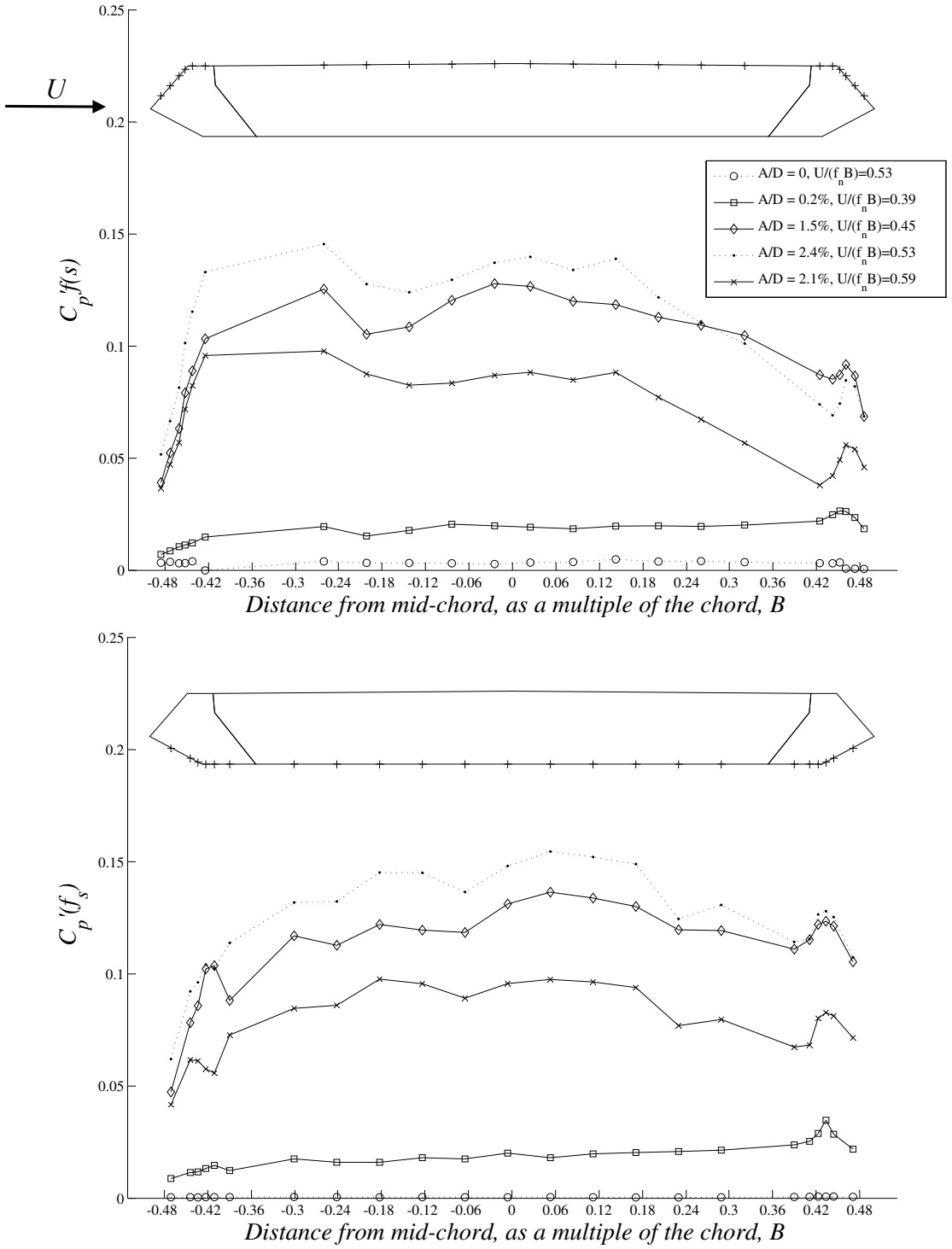


Figure 5.10: Run 1B↑ φnDF: the effect of oscillations on the rms fluctuating pressure, C'_p, bandpass filtered $+/-0.5$Hz f_s, at a cross-section at $0.44L$. $+$, pressure taps on the cross-section.

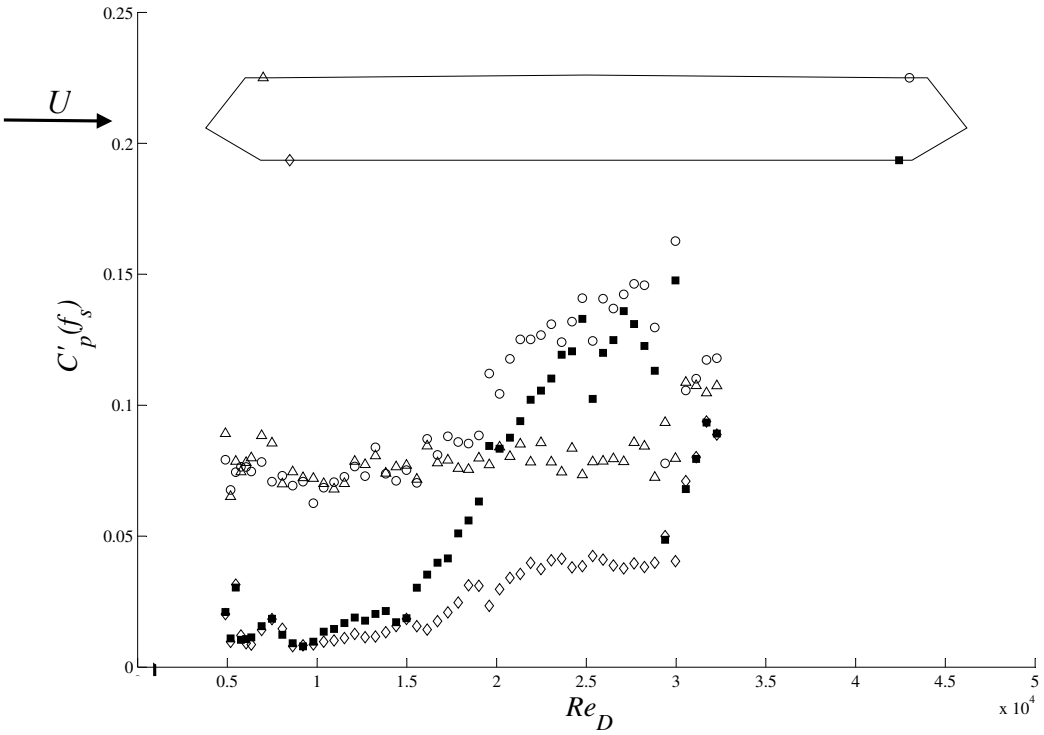
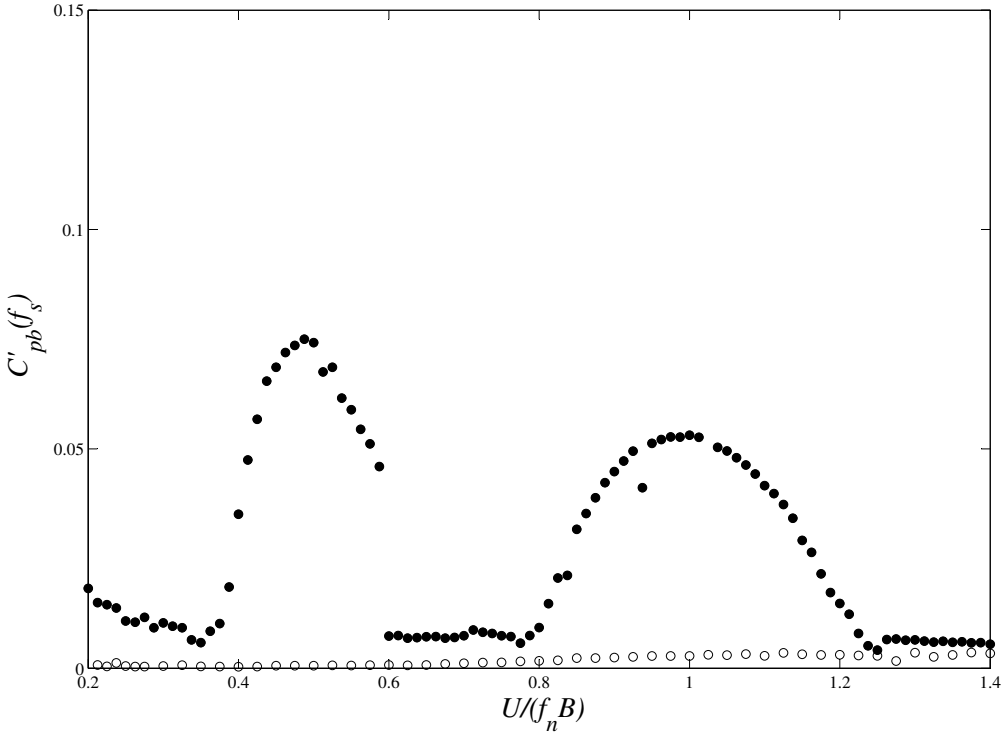
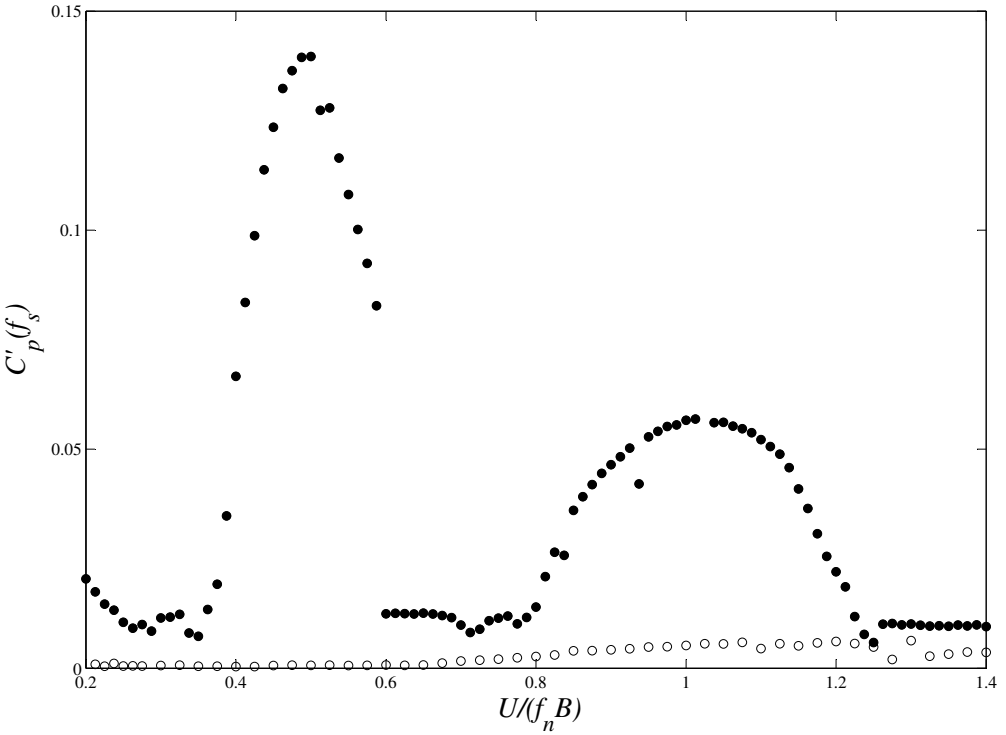


Figure 5.11: Run 1B↑ φnDF: effect of Re_D on r.m.s fluctuating pressure, C'_p for the stationary deck, $\triangle, \Diamond$, measured at the leading edge; $\bullet$, trailing edge.

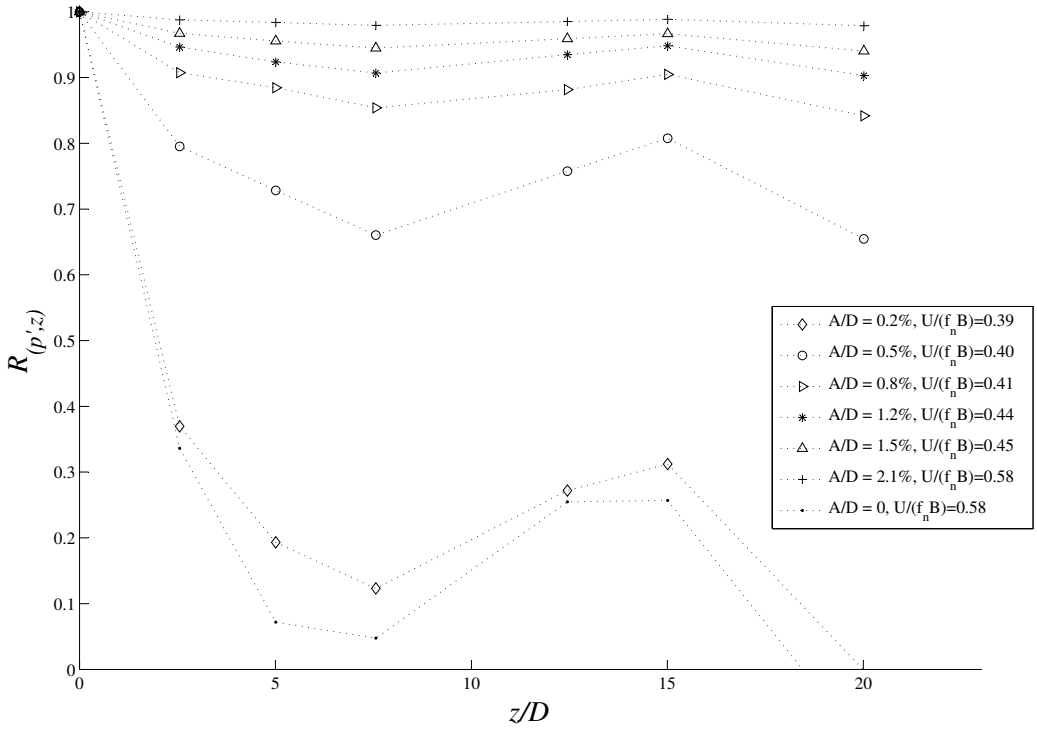


(a) Base

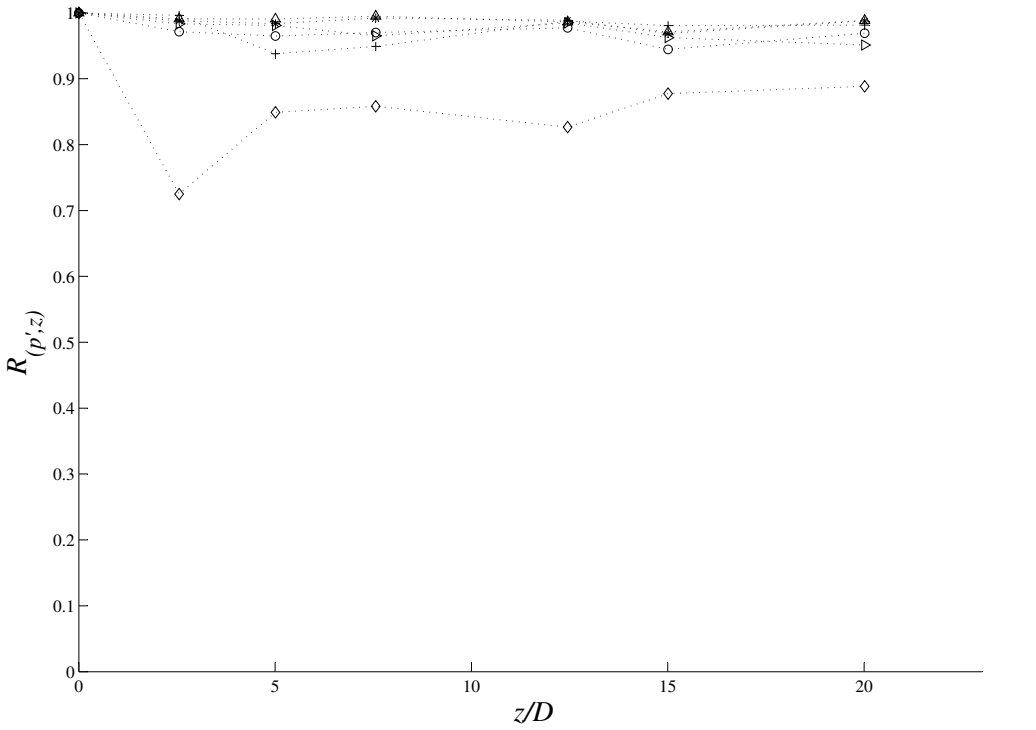


(b) Trailing edge

Figure 5.12: Run 1B↑ φnDF: rms fluctuating pressure, C'_p measured at (a) the base and (b) trailing edge. ◯, $A/D = 0$; •, elastically-mounted.



(a) Without motion-generated component



(b) Including motion-generated component

Figure 5.13: Run 1B↑ φnDF: correlation of surface pressures, $R_{p',z}$, measured at the bottom downwind knuckle, versus spanwise separation, z/D for the stationary and oscillating body, with (a) motion-generated component removed; (b) with motion-generated component included.

5.3 Heave response: Initial branch and lower branch

Deck B experienced a single instance of lock-in for heave and pitch each, over the range of wind speeds considered, unlike the Storebælt section (figure 2.52) and Østeroy section (figure 2.53), which both experienced lock-in multiple times for both degrees-of-freedom over a similar range of wind speeds. Both models were elastically-mounted with a structural damping, lower than these experiments. It may be that at lower damping levels, Deck B would also experience multiple lock-in events.

The heave response in figure 5.3 is "branched". There are two distinct parts to the response; an initial branch which includes responses starting at the onset velocity and reaching A_{max}, and the lower branch, which includes the response at higher wind speeds. There is a discontinuity in the amplitude between the branches. Figure 5.14 shows the responses on both branches. An incremental change in wind speed causes a significant change in amplitude. The response on the initial branch is characterised by periodic, sinusoidal oscillations. The peaks are consistently of similar amplitude, characterised by low peak factors ≤ 2, where the peak factor is the peak value of the acceleration divided by the rms value (the acceleration signal being filtered above 50Hz to remove the contribution of main AC power). The response on the lower branch gets progressively noisier with increasing wind speed. There is a breakdown of the organised motion resulting in peak factors ≥ 3. There is a distinct difference at the transition between branches, with the peak factor jumping from 1.95 on the initial branch, $U/(f_nB) = 0.54$ to 3 on the lower branch, $U/(f_nB) = 0.55$.

The mean pressure distribution, shown in figure 5.6 does not change significantly at the transition, suggesting the flow around the body in terms of separation and reattachment is similar. The fluctuating pressure does show change however. On the initial branch, spectra are flat with a single sharp peak at f_n. On the lower branch, this peak persists (figure 5.15). There is however a broadband peak at the trailing edge pressure taps that corresponds to the fixed body shedding. The presence of this fixed body frequency suggests desynchronisation of the shedding on the lower branch. With increasing wind speed this desynchronisation increases until lock-in is lost completely. Therefore it can be said the lower branch is associated with intermittent lock-in and desynchronisation. As

well as intermittent lock-in, the lower branch displays much lower spanwise correlation of fluctuating pressure (figure 5.17), measured at the bottom downwind knuckle.

The stationary bodies exhibit TEVS as the only apparent vortex excitation. The spectra of pressure in figure 5.17 show peaks only at the trailing edge. Spectra upwind are flat. When Deck B begins to oscillate in heave the only peaks in spectra are at f_n. This is the case throughout heave for run 1B↑ φnDF and for the initial branch of run 2B↑ ψnDF. It appears that TEVS at $St = 0.24$ is the driver for heave oscillations. This excited motion at $U/(f_n B) = 0.40$, leading to periodic, large amplitude oscillations. For run 2B↑ ψnDF the shedding becomes desynchronised over a short range of wind speeds at the upper end of the range of capture, with shedding switching between the body frequency and fixed body shedding.

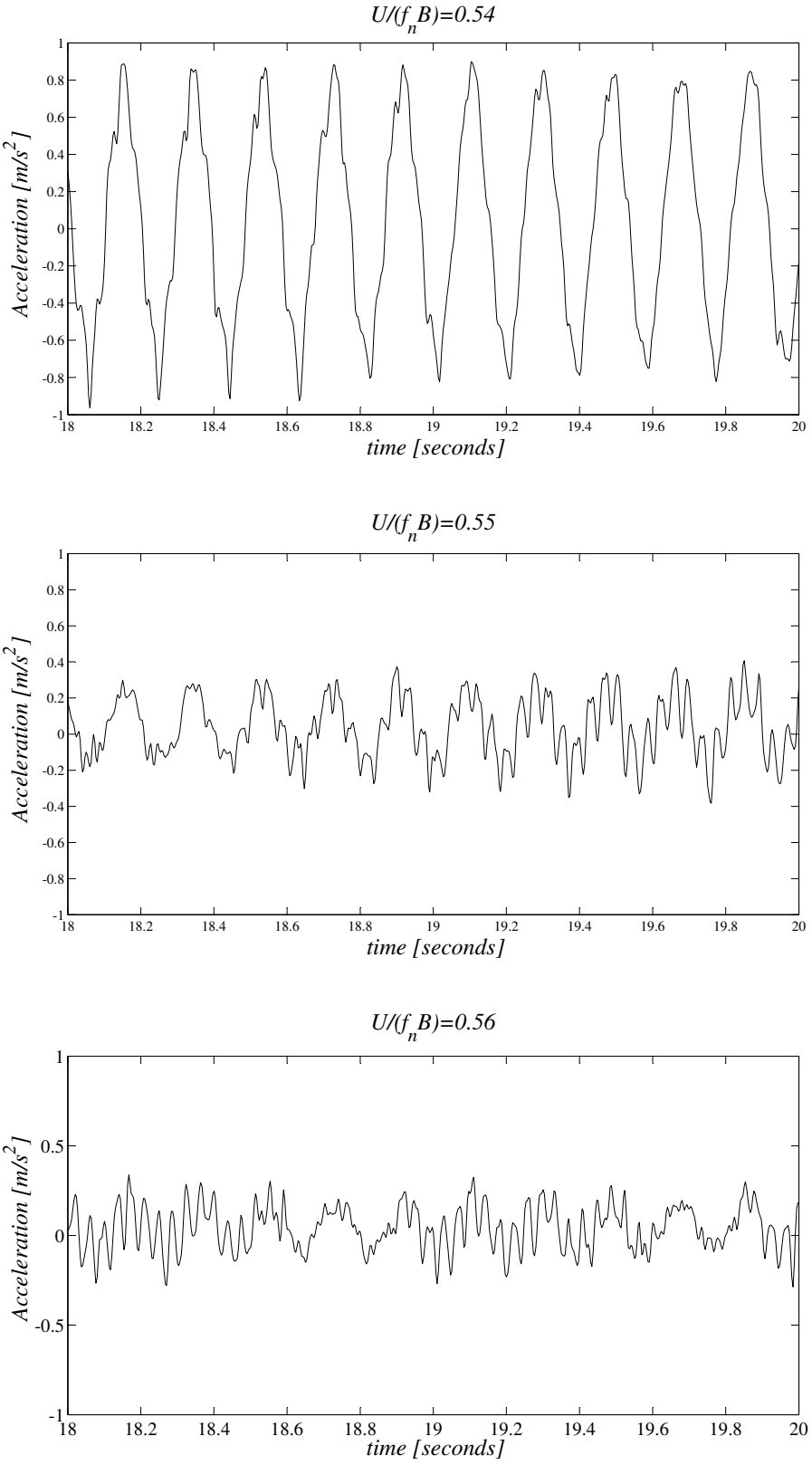
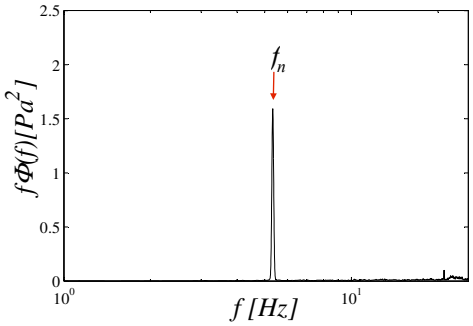


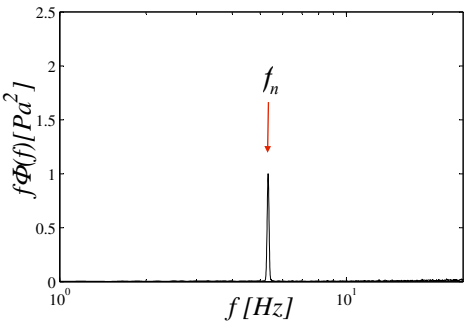
Figure 5.14: Run 2B↑ ψnDF: Acceleration measured on the initial branch and lower branch of heave lock-in.

Bottom surface

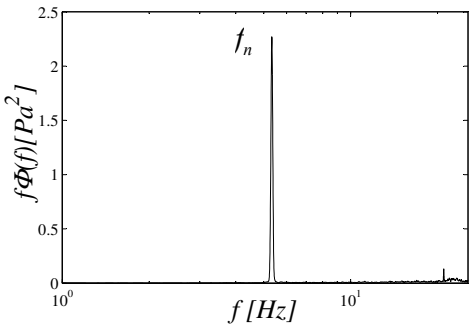
Top surface .

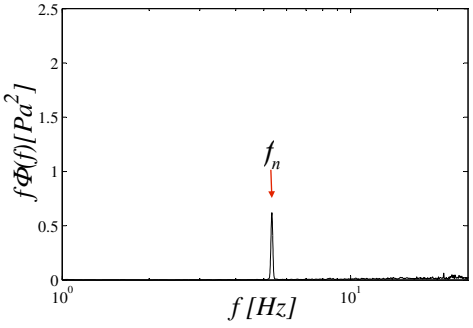
Upwind knuckles .



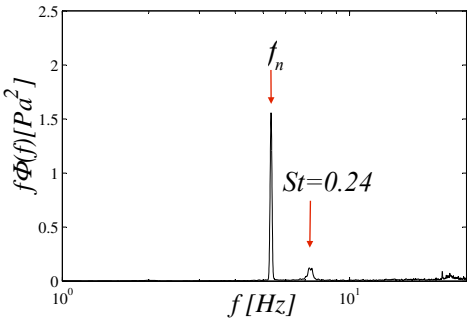


Body .





Bottom knuckles .



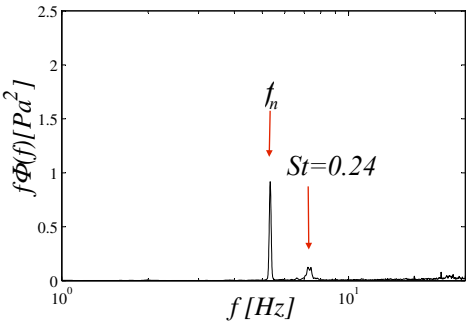


Figure 5.15: Run 2B↑ ψnDF: Premultiplied spectra at select pressure taps at a cross-section at $0.44L$ at $U/(f_nB)$=0.55 on the lower branch of heave. Peaks at the body frequency are evident, as well as a broadband peak at the stationary body frequency, $St = 0.24$ found at the downwind knuckles.

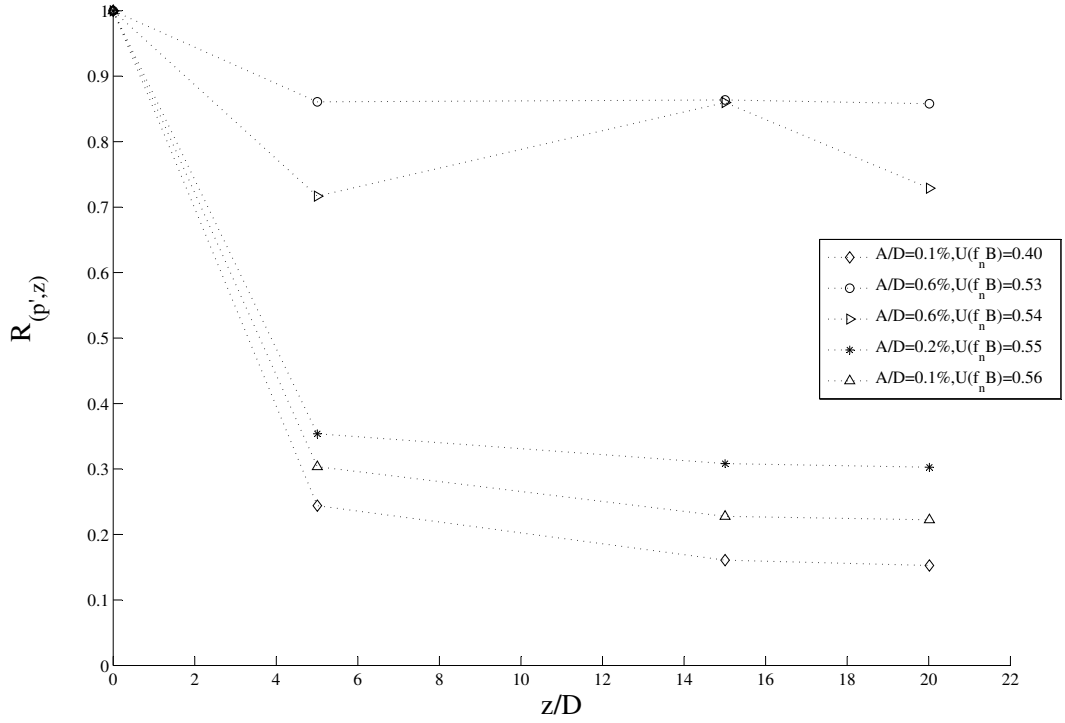
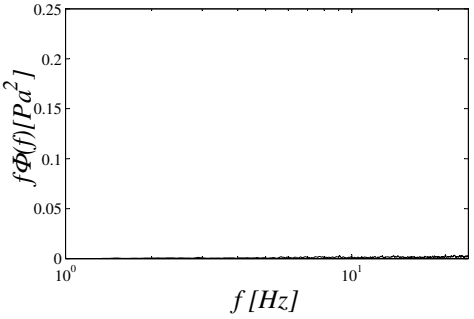
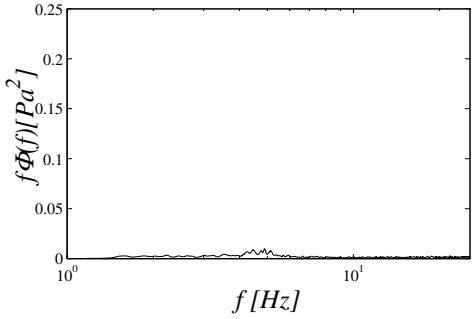


Figure 5.16: Run 2B↑ ψnDF: correlation of surface pressures on the initial and lower branches of heave lock-in, measured on a line at the trailing edge versus spanwise separation, z/D.

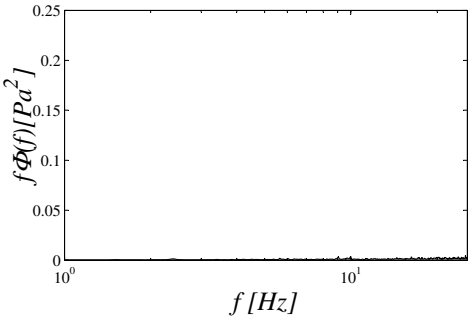
Bottom surface Top surface .

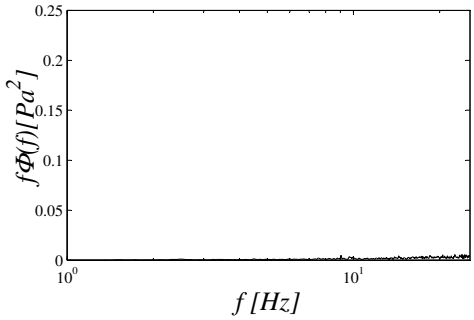
Upwind knuckles .



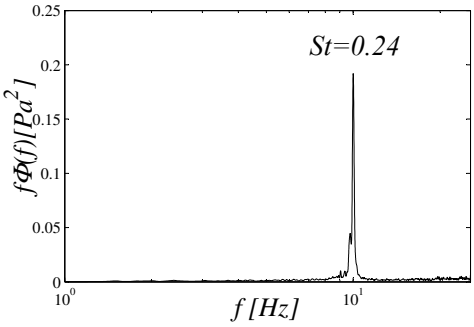


Body .





Bottom knuckles .



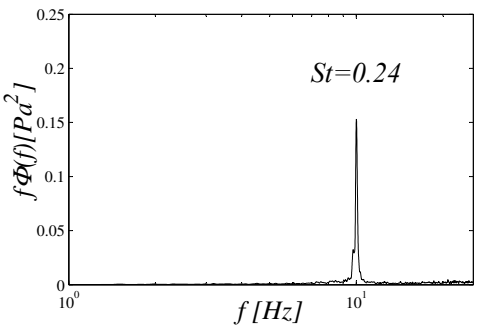


Figure 5.17: Run 1B↑ φnDF: Premultiplied spectra at select pressure taps at a cross-section $0.44L$ at $U/(f_nB)$=0.69 for the stationary body. Peaks at the downwind knuckles are evident, at $St \approx 0.24$.

Figure 5.18 plots the phase angle, ϕ through heave lock-in, based on the estimation of the VIV-generated lift force, calculated as described in Chapter 4. The acceleration and pressure measurements were triggered so that readings were simultaneous and could be compared to determine a phase angle that the lift led the displacement. The lift force was calculated from the integration of the surface pressures and taken to act perpendicular to the bridge axis (in the y direction). The rms values were calculated. Figure 5.19 shows the components of the lift force at A_{max}. The lift coefficients, $C'_L(f_s)$ are filtered to the shedding frequency, f_s. The non-circulatory component is substantial in amplitude because B is significant; rms $C'_{L,NC} \approx 0.13$ and is in phase with the body displacement.

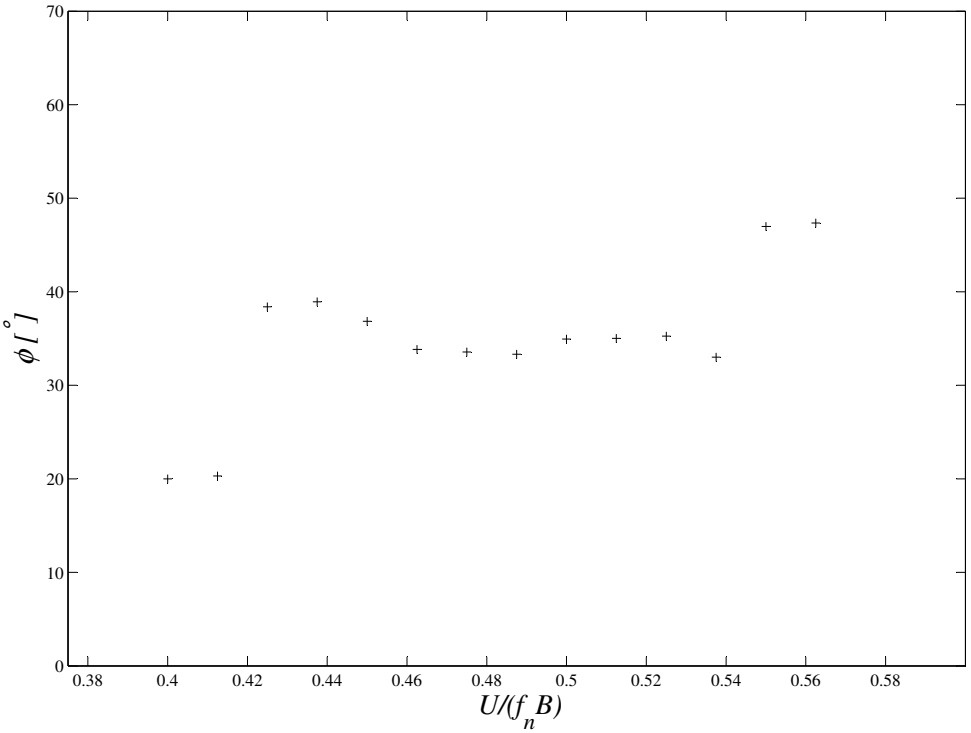
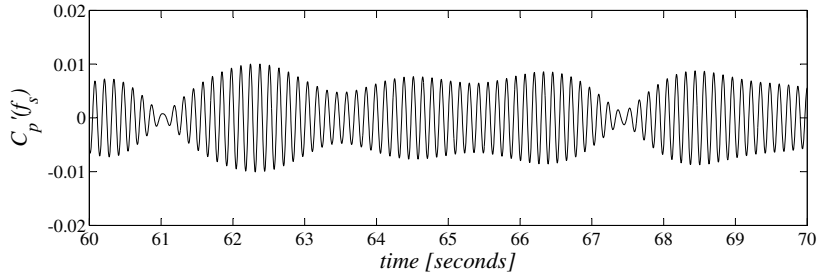
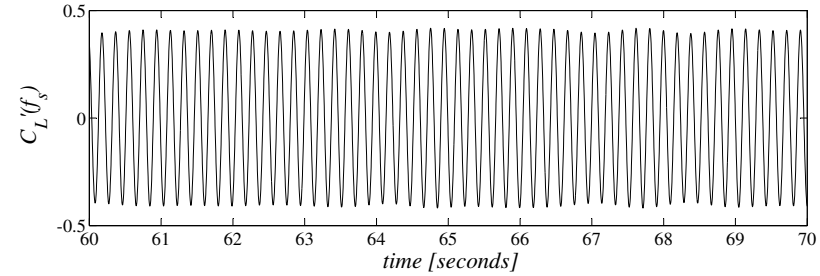


Figure 5.18: Run 2B↑ ψnDF: +, phase angle, ϕ between the lift force generated by VIV and body displacement, through heave lock-in.

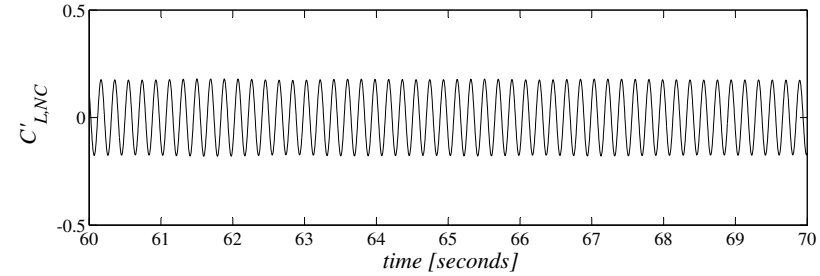
Removing the motion-generated component results in a VIV lift of smaller amplitude than the measured lift. There is significant amplitude modulation of the lift at the shedding frequency, when the body is stationary. Oscillations remove the modulations and increase the peak-to-peak amplitudes by more than a factor of ten. Through lock-in, the



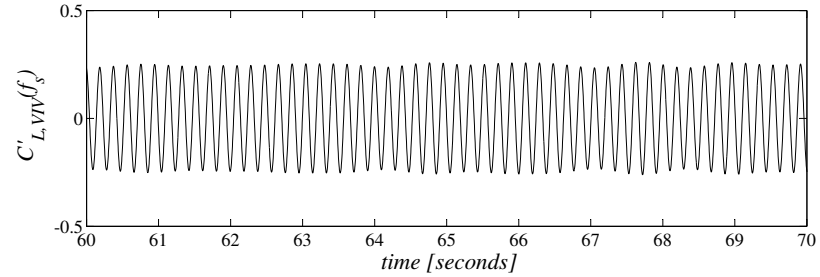
(a)



(b) rms $C_L'(f_s) = 0.29$



(c) rms $C'_{L,NC}(f_s) = 0.13$



(d) rms $C'_{L,VIV}(f_s) = 0.18$

Figure 5.19: Run 2B↑ ψnDF: time series of fluctuating lift at the shedding frequency, f_s for (a) the stationary body; (b)A_{max} for the elastically-mounted body as measured; (c) an estimate of the motion-generated component; (d) with motion-generated component removed. All measurements at $U/(f_n B)$=0.54. Note y-axis scales differ.

shedding becomes stronger and more organised.

The phase angle shows a small increase through lock-in. There appears to be two positive jumps; the first early in lock-in, at $U/(f_nB) = 0.43, (\phi = 20^\circ$ to $38^\circ)$ and the second at the transition from the initial branch to the lower branch, at $U/(f_nB) = 0.55, (\phi = 33^\circ$ to $47^\circ)$. All values fall within the range $0^\circ \leq \phi \leq 180^\circ$, indicative of self-excitation. The phase jumps indicate changes in the timing of shedding, and increase the component of lift force that excites motion, $C'_L sin\phi$, plotted in figure 5.20. $C'_L sin\phi$ increases through lock-in, up to a maximum at A_{max}, with a significant jump down at the lower branch. The phase increase at the lower branch increases the proportion of C'_L that contributes to excitation, but not sufficiently to offset the drop in lift amplitude.

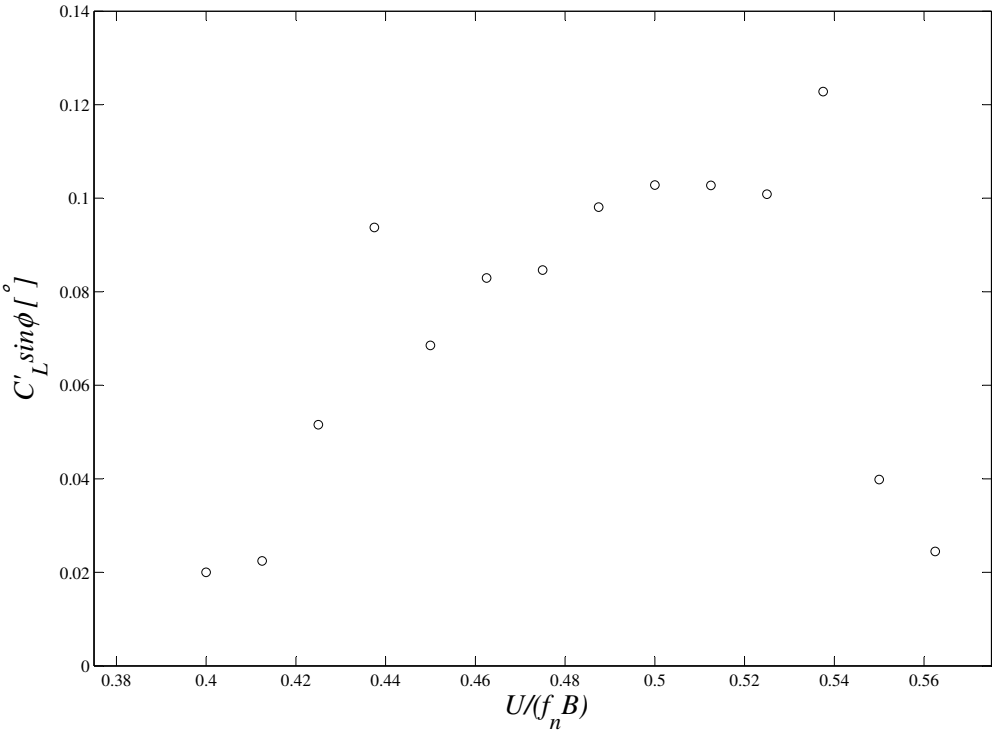


Figure 5.20: Run 2B↑ ψnDF: The variation of the component of rms lift force in phase with the body velocity, $C'_L sin\phi$ through heave lock-in.

Typically, the phase angle of most cylinders in lock-in behaves as shown in figure 2.9, with jumps up to more positive values. For the trapezoid, ϕ also increases through lock-in, from approximately 20° to 45°. The literature on the phase of VIV for trapezoids is very

limited, and this author found no comparison. The component of the lift force in phase with the body velocity, $C_L sin\phi$, excites oscillations, therefore values of $0° < \phi < 180°$ sustain oscillations, while values outside this range damp them out. Figure 5.20 plots $C_L sin\phi$ through heave lock-in. It can be seen that there is a trend of increasing excitation force through lock-in, which drops suddenly at the onset of desynchronisation.

5.4 Pitch response: leading edge and trailing edge modes

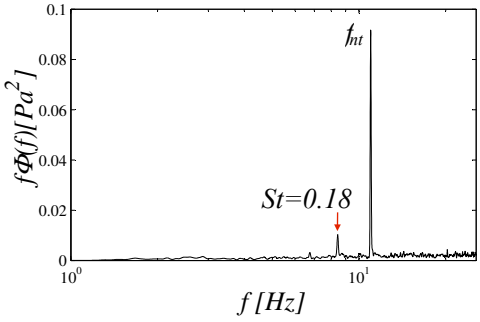
At the onset critical velocity for pitch, three peaks are present in the spectra (figure 5.21) around the $0.44L$ cross-section:

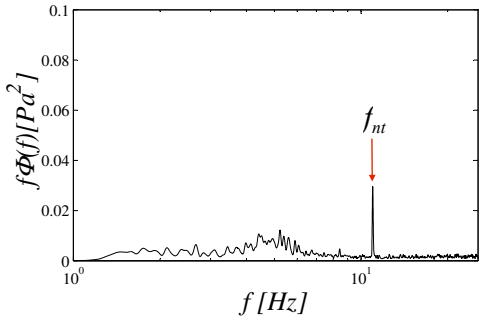
- A peak at the natural frequency, f_{nt} is present everywhere. This is expected to be mostly motion-generated.
- At the bottom upwind knuckle, a peak at $St = 0.18$ is present. It is postulated that this is an ILEV mode as it is not present at the downwind knuckles and corresponds to the frequency expected for the n=3 mode. The spectra on both surfaces of the body also indicate this frequency, suggesting the leading edge vortices are convecting downwind.
- At the downwind knuckle, a peak at $St = 0.24$ is observed. This is likely TEVS as it is present only at the trailing edge, and agrees with the frequency of shedding observed at lower wind speeds.

Bottom surface

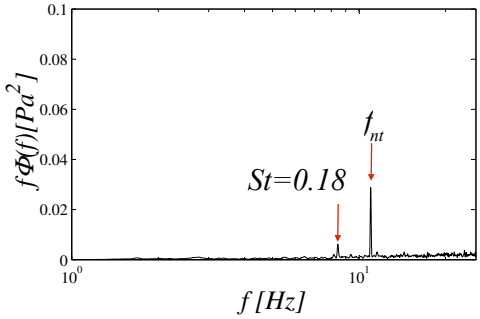
Top surface

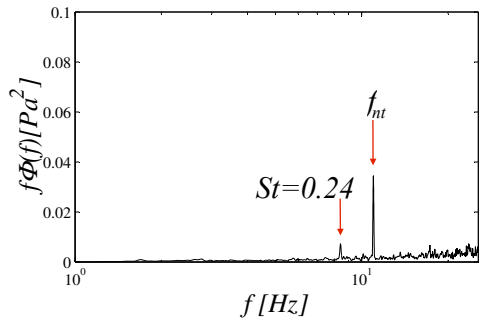
Upwind knuckles



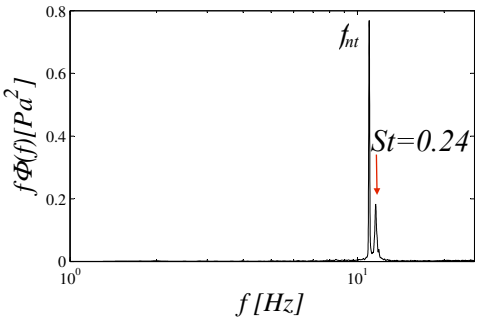


Body





Downwind knuckles



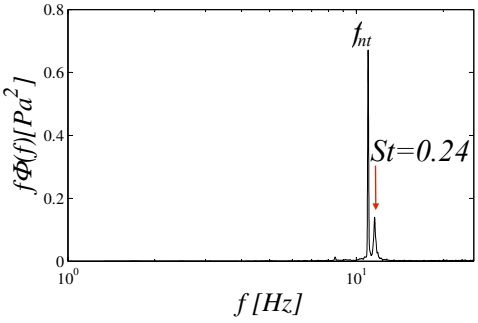
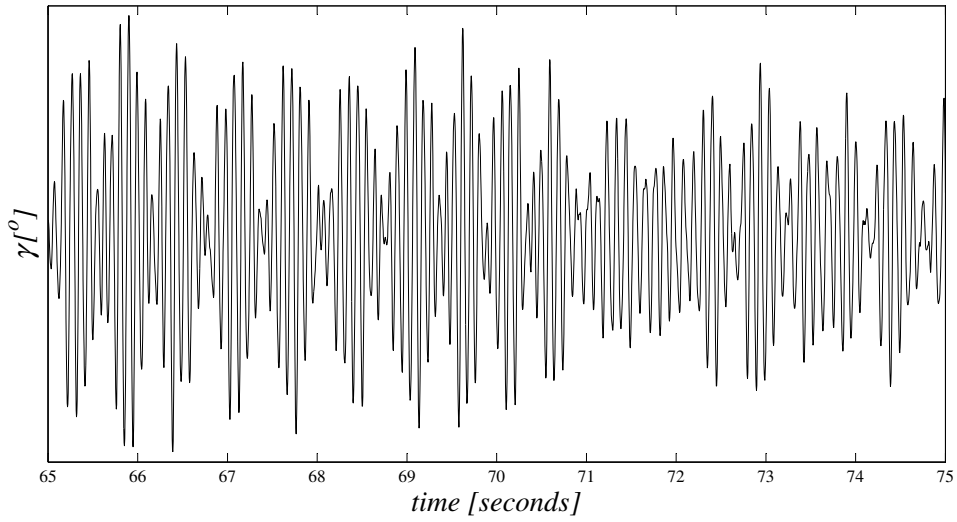


Figure 5.21: Run 1B↑ φnDF: Premultiplied spectra at select pressure taps at a cross-section at $0.44L$ at the onset critical velocity for ptich $U/(f_nB)$=0.79. Three peaks are evident at various locations on the body.

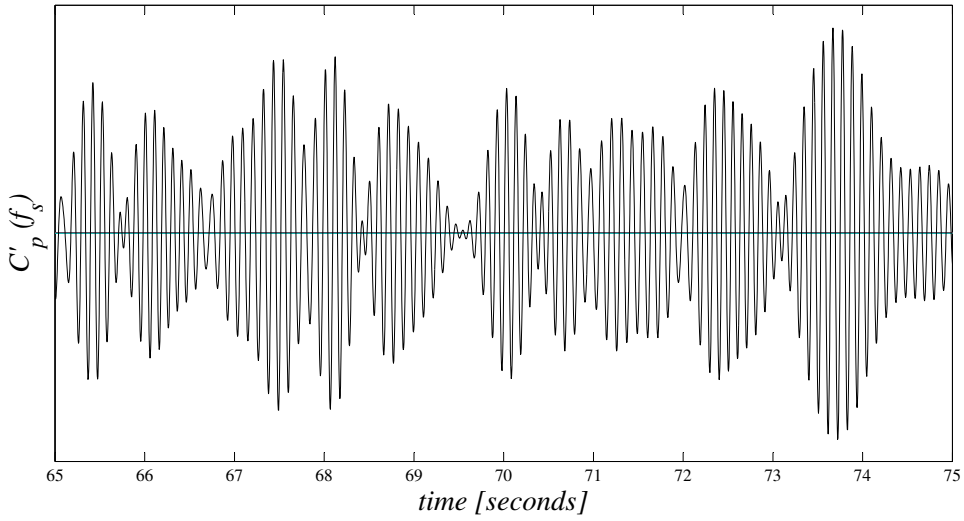
As the wind speed increases and oscillations grow, the only peak in spectra are f_{nt}. There are some similarities with Terres-Nicoli and Kopp [51] who observed leading edge fluctuations on a small scale model of the Storebaelt at the onset of both heave and torsion oscillations. These leading edge fluctuations were not present on the stationary body and were attributed to a motion-generated ILEV n=2 mode.

The higher modes of ILEV excitation are not often observed. Generally ILEV is not observed on very slender bodies and instead TEVS dominates. A notable exception is the H-beam ($B/D = 5$) tested by Schewe [45] which displayed ILEV modes of significant amplitude up to n=5 in bending and n=6 in pitch (figure 2.28). Naudascher and Wang [39] discovered that as rectangles became more slender, the second mode of ILEV excitation for vertical oscillations appeared and then dominated. Extrapolation would suggest that as the slenderness increased beyond the maximum tested, $B/D = 8$, that even higher modes of ILEV would appear and dominate. Here, for this very slender trapezoid, it appears that TEVS dominates and initiates the pitch motion, but a high ILEV mode is amplified by motion of the leading edge.

At wind speeds at the start and finish of the pitch response region, an amplitude modulation is observed. The modulation indicates a beating phenomenon. The frequency of the modulation is irregular and very small, less than 0.5 Hz. The amplitude modulation disappears at wind speeds further within the range of capture, where large amplitude, organised oscillations persist. Beating is not associated with heave lock-in. Figure 5.22 plots the oscillation amplitude and pressure fluctuations measured at the trailing edge at $U/(f_n B) = 0.78$. Beating has been observed for circular cylinders and Feng [9] hypothesised that it is caused by (i) the shedding trying to catch up with the body frequency, (ii) and uncorrelated shedding. Figure 5.23 shows that there is almost no correlation of shedding along the span. When the speed is increased incrementally, the correlation starts to increase rapidly, and beating is no longer observed in the body motion. Beating occurs for those wind speeds that are locked-in but where motion is below the threshold required for spanwise correlation.



(a) Peak factor =2.9



(b) Peak factor =2.9

Figure 5.22: Run 1B↑ φnDF: time series of (a) body displacement displaying beating amplitude modulations and (b) fluctuating pressure measured at the bottom downwind knuckle at $U/f_nB = 0.78$.

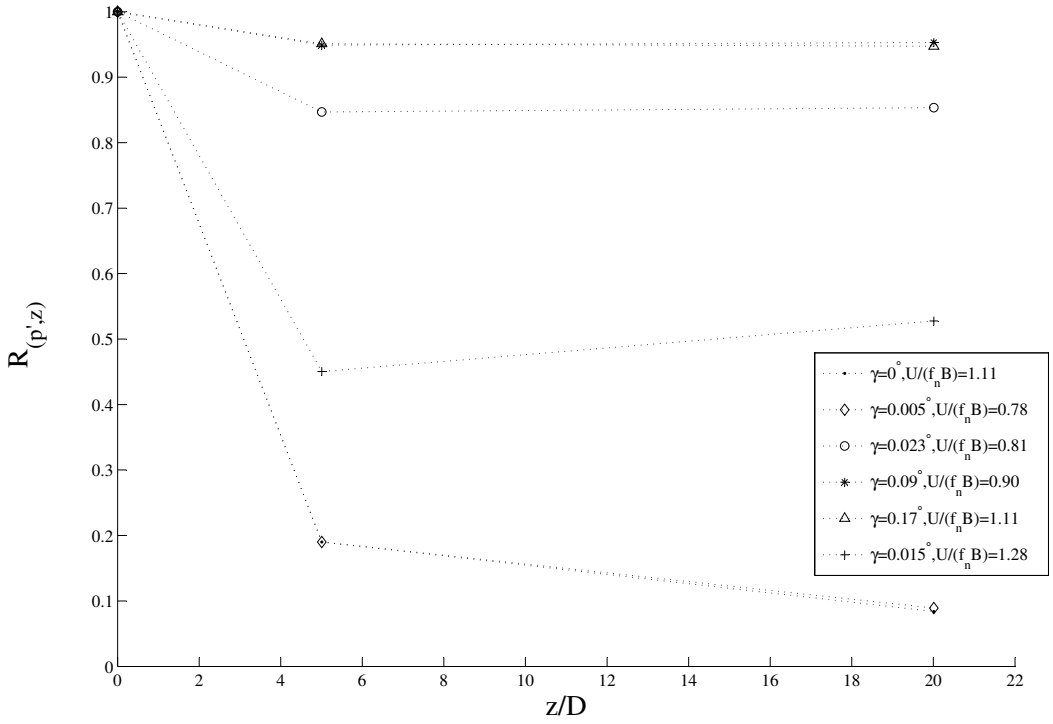


Figure 5.23: Run 1B↑ φnDF: Correlation of surface pressures, measured on a line at the trailing edge (figure 5.1) throughout pitch lock-in, versus spanwise separation, z/D.

5.5 Conclusion

A slender trapezoid experiences lock-in at speeds where the trailing edge vortex-shedding approaches a natural frequency. The shedding frequency is captured by the body frequency and is accompanied by oscillations in heave and pitch, and organised shedding with a significant increase in spanwise correlation and excitation force. An incremental increase in wind speed, far from the resonant point, results in desynchronisation. This leads to another type of response, at lower amplitudes, here termed the lower branch.

The heave displacement response can consist of an initial branch and a lower branch. Branched responses have been observed for circular and D-section cylinders before [9] and possibly for other trapezoids [51] [75] although the literature is not clear. For circular and D-section cylinders, each branch is characterised by a different shedding mode; 2S or 2P. Here, the branches indicate the limits of desynchronisation.

The heave response is excited by TEVS only. This is unsurprising for such a slender trapezoid. Slender rectangles, $B/D \gtrsim 10.5$ exhibit TEVS only [44]. However, other less slender trapezoids such as the Storebælt, are excited by a combination of TEVS and ILEV modes, and this trapezoid behaves differently in heave. This difference may have an impact on the amplitudes and appropriate models to predict these, as well as mitigation measures. It appears that leading edge mitigation will not have any direct impact on the heave of this trapezoid.

The pitch of the slender trapezoid did display a combined excitation. Both TEVS and ILEV mode n=3 were observed at the onset of oscillations. It is apparent that the TEVS initiates the small leading edge motion required to strengthen the ILEV mode. This is in agreements with findings for the Storebælt bridge [51] where an n=2 mode was observed. It is unsurprising that a higher mode of shedding is observed in these experiments, as the mode number for a given wind speed is expected to increase with slenderness. It has been shown that the higher modes of ILEV generate smaller amplitudes [38] [45] but other studies have refuted this and show that the higher modes can dominate the response of very slender rectangles [39]. It is of interest to see if at higher wind speeds other ILEV modes appear and how the amplitudes compare. This is important in predicting the response of this trapezoid in VIV.

The behaviour of this slender bridge deck section in VIV has similarities and differences with other less slender decks. The pitch response appears very similar in excitation mechanism to the Storebælt bridge [51]. In contrast, the heave response is excited by only the TEVS mechanism.

Chapter 6

The effect of the shape of trapezoidal box-girders on vortex-induced vibration

6.1 Introduction

This chapter examines the effect of varying the shape of a slender box-girder on the VIV, using the experimental set-up and small-scale models described in chapter 3. The focus is on the vortex excitation and the response. The current work varies the bottom topography of the box-girder, specifically the angle at the bottom knuckles, θ_B and the position of the knuckles relative to the nose and tail. The top surface, and nose/tail position are identical for all the models. The impact on VIV of these shape changes for a very slender trapezoid has never been studied. Studies on the behaviour of less slender box-girders, namely the Storebælt bridge by Larsen and Walls [75] and a generic rectangular section with fairings (B/D=5) by Haque *et al.* [72] are referred to for comparison. The experiments were run; steadily increasing the flow speed in the wind tunnel, and the acceleration and pressure measured.

Haque *et al.* [72] found that varying θ_B results in a critical value where steeper and shallower angles were less stable, as long as the tail was low enough at very shallow θ_B to allow the bottom trailing edge vortex to be shed on the upper part of the base. The

behaviour was governed by trailing edge separation and tail location. Larose and Larsen [7] assert that it is vortices that are shed from the bottom knuckle that dominate the response of a trapezoid as the dead air region below the tail is larger than that above, allowing the vortex below the nose to grow more. Therefore, it is hypothesised that as θ_B is reduced, separation will also reduce (as Larsen and Wall [75] observed) and the previously dominant bottom vortex in the near wake is pushed to the far wake, where its effects on the body are weaker.

Here it is predicted that the heave will be particularly affected as it is only purely by TEVS, and will be very sensitive to changes in the strength of shedding at the trailing edge, whereas the pitch motion relies additionally on the ILEV mode. As the ILEV mode appears to be generated by motion of the leading edge, generated by the TEVS, there may be a more complex relationship with θ_B. It is expected that at some critically shallow angle, TEVS is so weakened that there may be insufficient amplification of the ILEV mode and pitch oscillations will not be observed. As the tail location is fixed for all models in this investigation, the vortex forming at the downwind lower knuckle is expected to shed in the same vertical location relative to the tail and angles shallower than a critically stable θ_B would also be stable.

It is found that changing the bottom topography of leading edge and trailing edge fairings significantly changes the response in VIV.The deck with $\theta_B = 20°$ displayed much reduced response without lock-in. The effect is more pronounced for lower values of θ_B (and associated long inclined panels) where the heave response disappears and the pitch response is reduced. For $\theta_B \geq 25°$ heave VIV is driven by strong TEVS. For $\theta_B \leq 20°$ the TEVS is weakened and it is postulated insufficient to generate heave VIV.

Varying θ_B has a significant impact on the leading edge frequency and the TEVS strength of pitch. This combination of effects results in Deck C displaying no lock-in for the range of wind speeds investigated. Decks D and E display lock-in, significant and organised pitch oscillations, with amplitudes greatest for Deck E. This is a surprising result, as it was expected the trapezoid would become more stable the more streamlined it became. The critically stable $\theta_B = 20°$ is appreciably larger than that found for the less slender rectangle with fairings [72] but agrees with that found for the Storebælt bridge [75].

The range of free-stream velocities is $0.20 \leq U/(f_n B) \leq 1.64$. θ_B took values of 16°, 18°, 20°, 25° and 30°. The values were chosen as the data revealed Deck C was critically stable, and there was interest in how stability varied with shallower angles affected the VIV. $\theta_B \leq 16°$ was not tested as a trend in response became clear: with reducing angle below 20° amplitudes were growing.

6.2 Results

Only accelerometer data was measured for the five runs listed below. The conditions for all runs are described in table 3.6.

- Run 2A↑ φnDF
- Run 2B↑ φnDF
- Run 2C↑ φnDF
- Run 2D↑ φnDF
- Run 2E↑ φnDF

Figure 6.1 plots the response of the five models. Deck A is most responsive in VIV, exhibiting one instance of heave motion and one instance of pitch motion over the wind speed range investigated (figure 6.1). The heave motion is observed over the range $0.40 \leq U/(f_n B) \leq 0.53$, with $A_{max}/D = 1.0\%$. The vertical acceleration observed over the range $0.72 < U/f_n B < 0.82$, is likely to be roll, which is not constrained in this experimental set-up. We cannot definitively determine the mode of vertical acceleration as accelerometers are placed at one end of the model and no pressure data is available for these runs. Figure 6.2 shows the oscillations are at $\approx \sqrt{3} f_n$, that expected for the roll mode with auniform spanwise distribution of mass.

The heave responses for decks A and B do not exhibit branching; there is a continuous increase in amplitudes with increasing wind speed up to a maximum, and soon after a sudden loss of any oscillations. The torsional response for Deck A and Deck B is similar: a gradual increase up to $\gamma_{max} = 0.19°$ and $\gamma_{max} = 0.18°$ respectively. The response is

asymmetrical with γ_{max} occuring at a higher wind speed than the mid-point. At the onset of torsional response, f_y increases with slightly wind speed and reaches a plateau at the natural torsional frequency (figure 6.2). The frequency of oscillations are at the natural frequencies, f_n in heave and f_{nt} in torsion.

Decks C, D and E do not exhibit any heave response in the wind speed range investigated. Deck C in particular shows an almost zero response for all flow speeds. At a single flow speed ($U/(f_nB) = 0.79$) a very small torsional response is measured, made up of beating, with a peak factor of 3.3. The time trace in figure 6.3, shows the modulated amplitude indicative of beating. The frequency of the beating modulation is irregular, varying between 0.2 and 0.5 Hz. There are no other oscillations observed, making Deck C the most stable model tested.

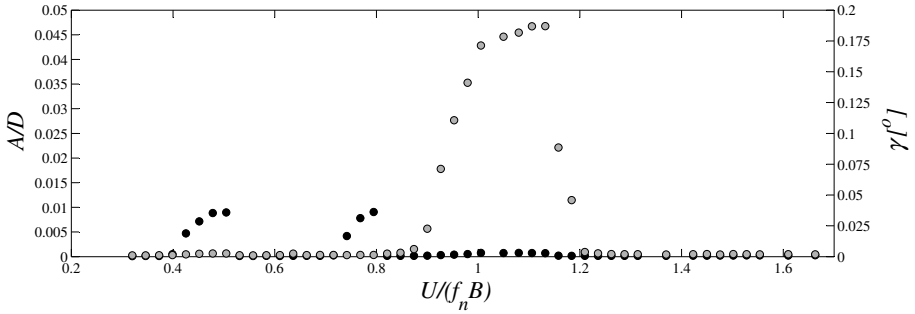
It was hypothesised that reducing the angle at the bottom downwind knuckle would reduce the shear layer separation and therefore VIV response. It is intuitive that a critical angle exists, at or below which VIV responsiveness stays at a minimum. Here, the critical angle (of those tested) is 20° at which there is an almost zero response. However reducing the angle further to 18° results in a significant increase in pitch response (figure 6.1d), oscillations are of constant significant amplitude; $\gamma_{max} = 0.06°$ through the range $0.77 < U/(f_nB) < 0.89$.

The shallowest angle tested is 16°, which has a similar response to the 18° section. Figure 6.1e shows torsional oscillations at $\gamma_{max} = 0.08°$ (over the range $0.74 \leq U/(f_nB) \leq 0.84$).

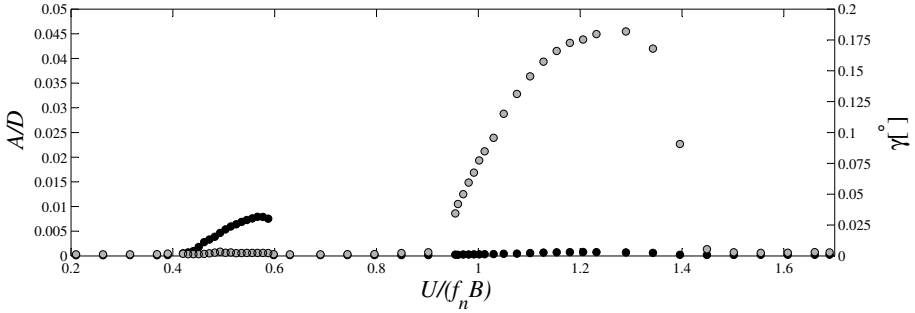
Two further runs: Run 2B↑ ψnDF and Run 2C↑ ψnDF were carried out at the higher damping level. Accelerometer and pressure data was measured. The response in run 2B↑ ψnDF (figure 5.3) was discussed in chapter 5. The heave response displays an initial branch and lower branch, unlike Run 2B↑ φnDF in figure 6.1. The initial branch is associated with strong lock-in, driven by TEVS. The lower branch marks the beginning of desynchronisation.

Run 2C↑ ψnDF results in very low responses once again (figure 6.4). The only response is a small torsional rotation consisting of beating. At the maximum rms amplitude, the peak factor is 3.8, indicating significant amplitude modulation. A higher resolution of tunnel speed (compared to run 2C↑ φnDF) indicate a range of wind speeds, $0.76 \leq$

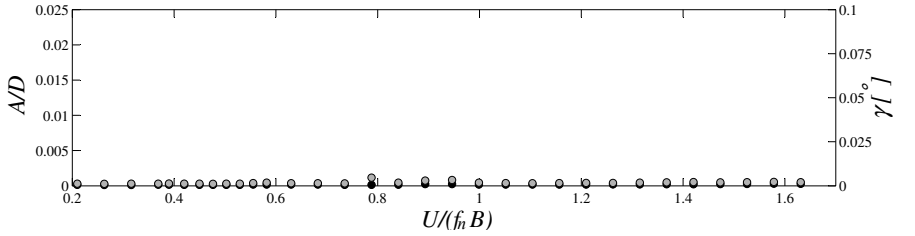
$U/(f_n B) \leq 0.84$ in which a torsional beating response is observed. The oscillations are not accompanied by lock-in, and the shedding frequency increases linearly, as it would for the stationary model.



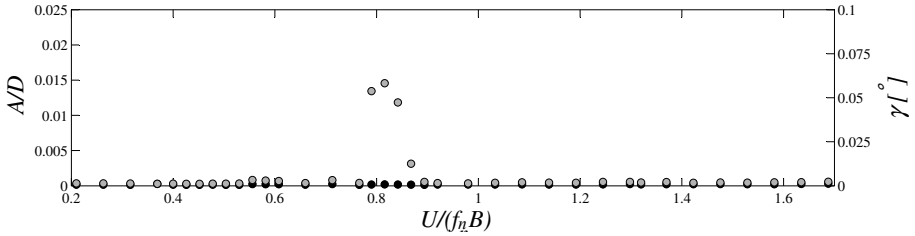
(a) Deck A: $\theta_B = 30°$



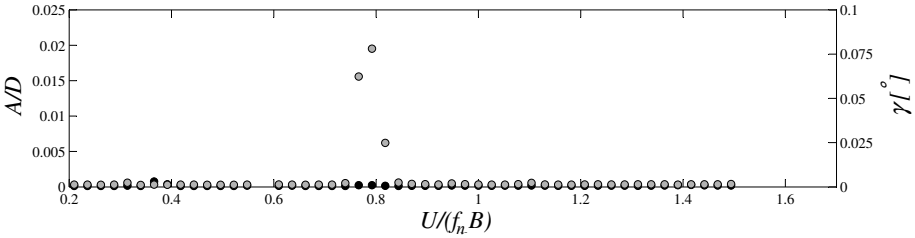
(b) Deck B: $\theta_B = 25°$



(c) Deck C: $\theta_B = 20°$

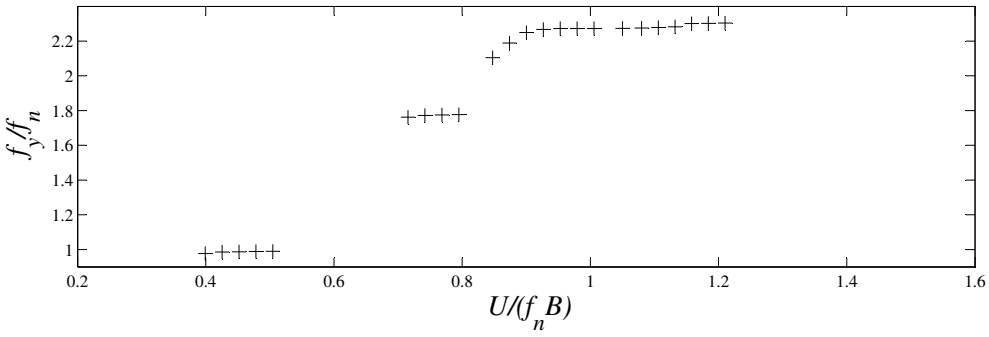


(d) Deck D: $\theta_B = 18°$

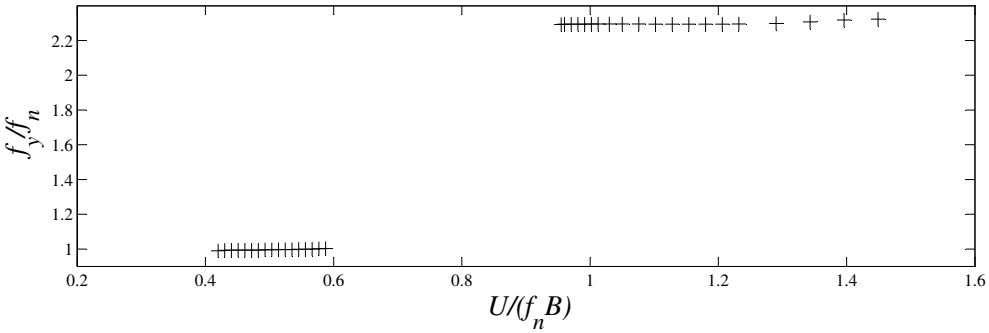


(e) Deck E: $\theta_B = 16°$

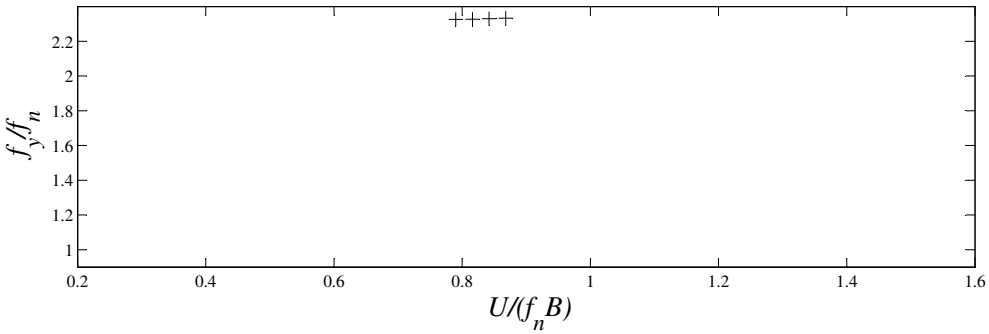
Figure 6.1: Run 2X↑ φnDF (where X = A - E): •, rms displacement in heave A/D; •, torsion γ;



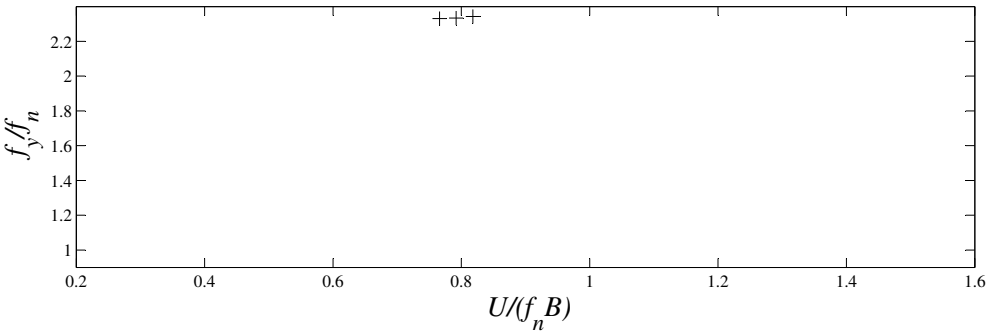
(a) Deck A: $\theta_B = 30°$



(b) Deck B: $\theta_B = 25°$



(c) Deck D: $\theta_B = 18°$



(d) Deck E: $\theta_B = 16°$

Figure 6.2: Run 2X↑ φnDF (where X = A - E): +, Body frequency, f_y. $f_{nt} = 2.3f_n$. Deck C did not experience periodic oscillations and has been omitted.

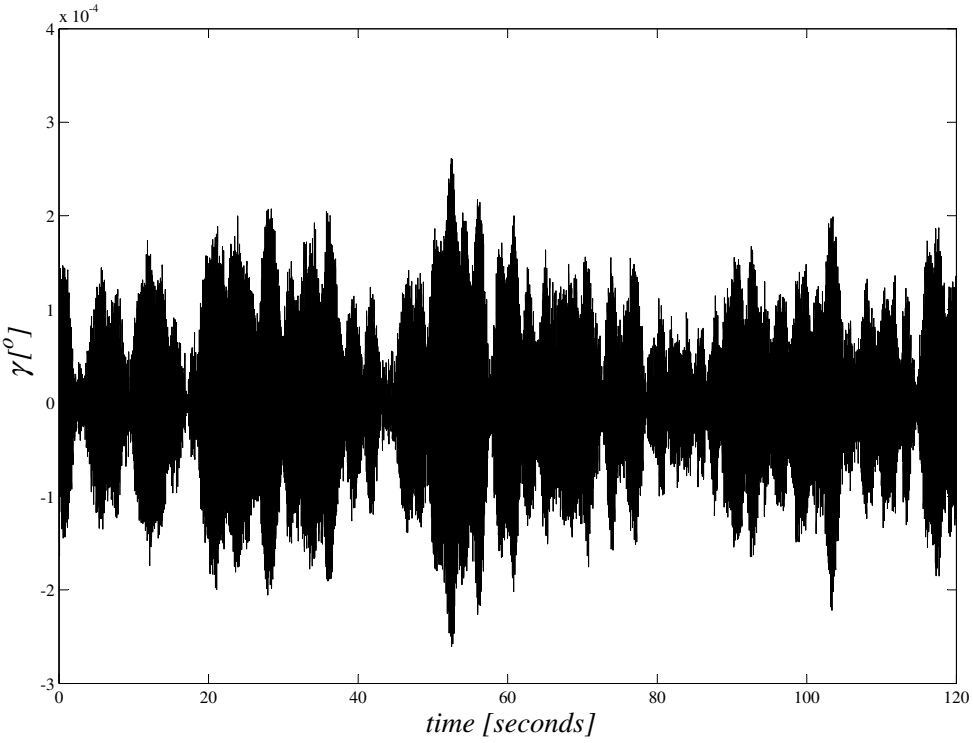


Figure 6.3: Run 2C↑ φnDF: torsional response, γ° at $U/(f_n B) = 0.79$. The beating is defined as amplitude modulation of the signal, such that peaks vary significantly in amplitude. The peak factor is 3.3.

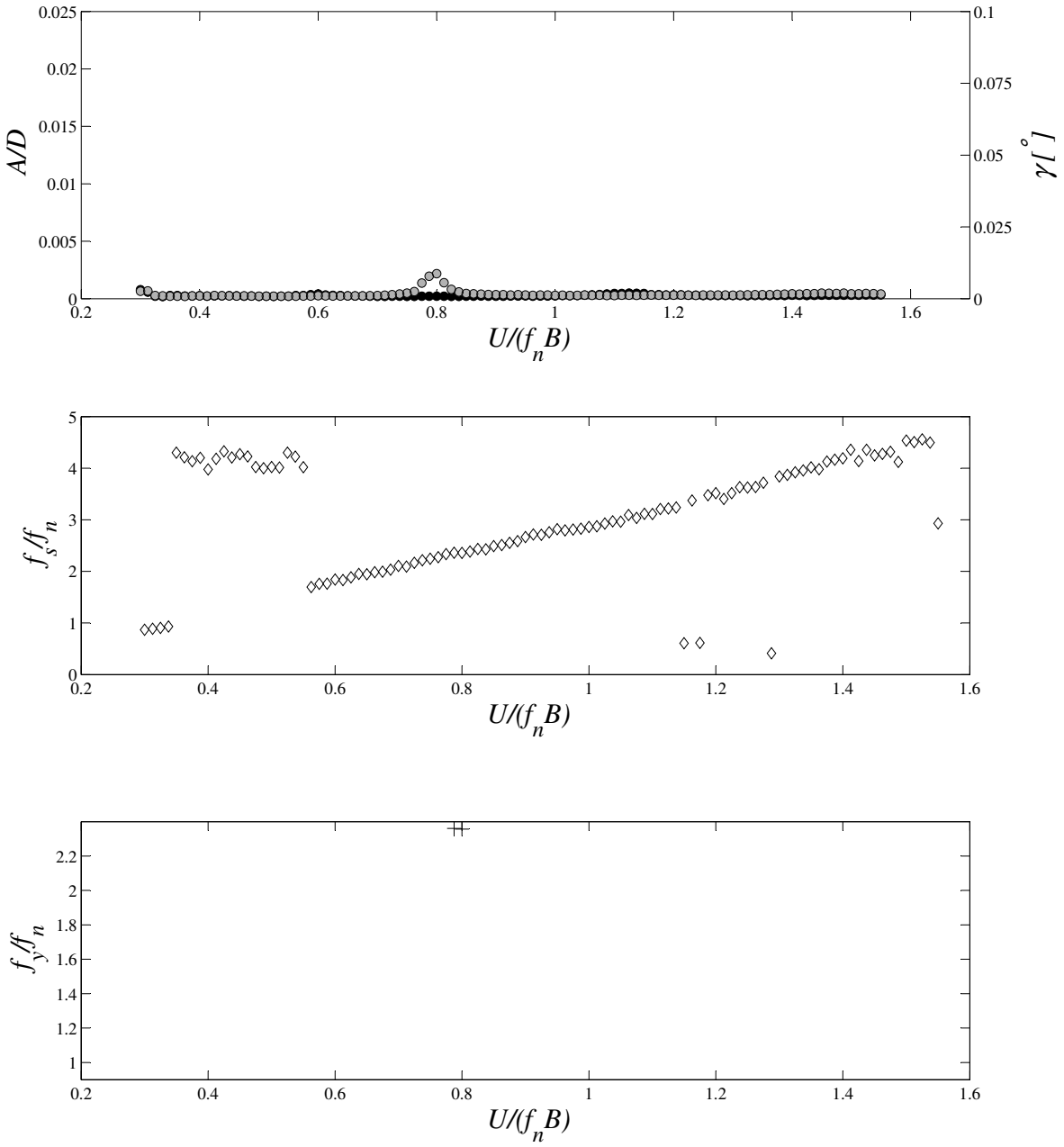


Figure 6.4: Run 2C↑ ψnDF: •, rms displacement in heave A/D; •, torsion γ; ◊, vortex-shedding frequency, f_s of the elastically-mounted body; ·, body frequency, f_y. $f_{nt} = 2.3 f_n$

The vortex-shedding frequency, f_s, identified from spectra of the pressure fluctuation recorded at the trailing edge corner, as shown in figure 5.1. For a range of wind speeds, $0.35 \leq U/(f_n B) \leq 0.55$, f_s is much higher than is predicted for a stationary body with a linear Strouhal relationship. These wind speeds coincide with the range of capture for heave lock-in for Deck A and Deck B. The dominant shedding is so much greater than the natural frequency at these wind speeds, which may explain why lock-in and associated oscillations are not observed. The organisation of the TEVS mode appears to improve with increasing wind speed.

In the T5 tunnel, four runs: Run 1B↑ φnDF and Run 1C↑ φnDF and at a different damping level: Run 1A↑ ϖnDF and Run 1D↑ ϖnDF were investigated. Accelerometer and pressure data was measured. One instance each of significant amplitude heave and pitch oscillations were observed, with associated lock-in. In the T5 tunnel, figure 6.5 shows Deck C is unresponsive in heave over the wind speed range tested and only exhibits beating in pitch for a small range of wind speeds. This agrees with results from the $10' \times 5'$ tunnel (figure 6.1 and figure 6.4). The beating is not associated with lock-in.

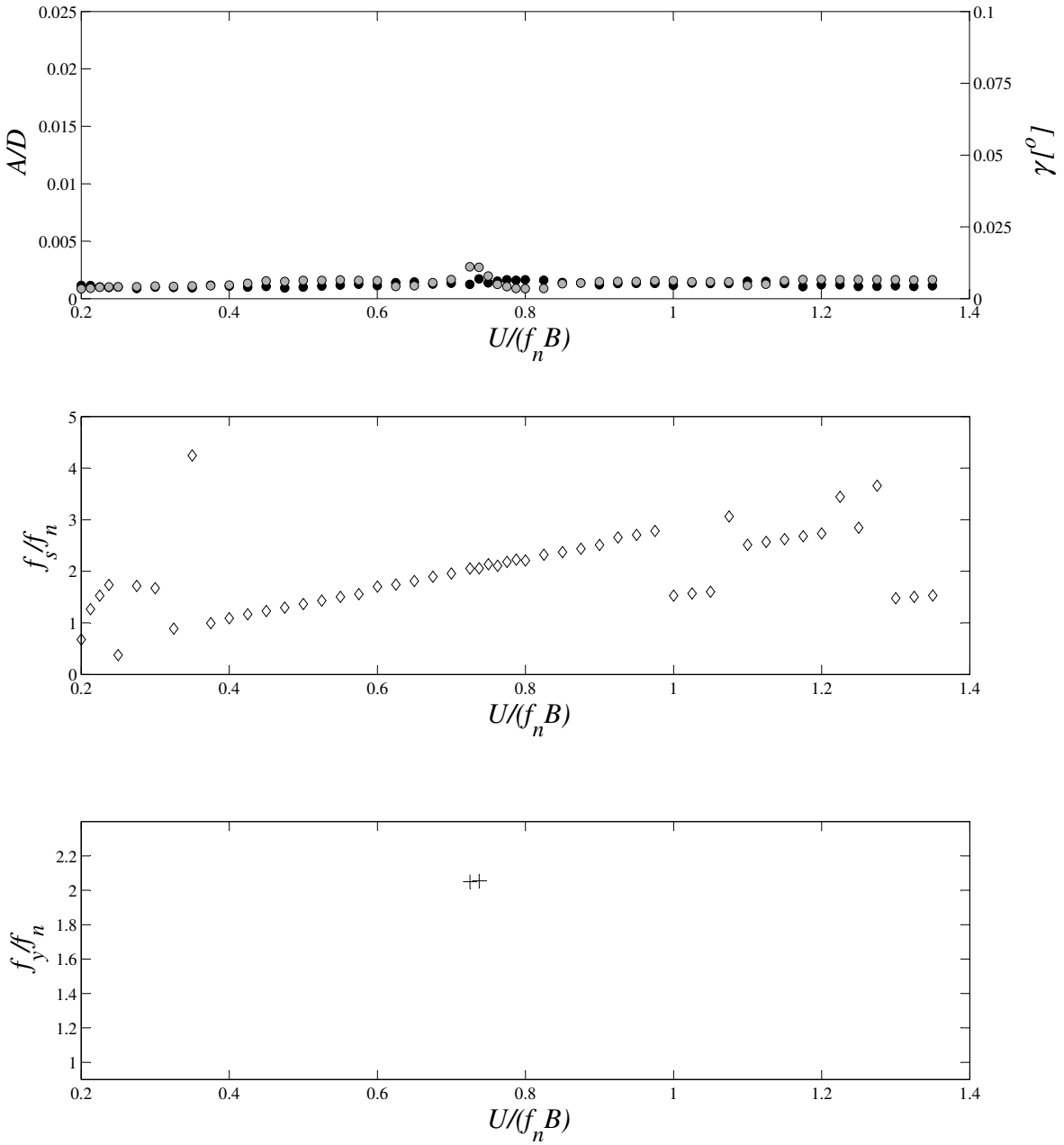


Figure 6.5: Run 1C↑ φnDF: •, rms displacement in heave A/D; •, torsion γ; ◊, vortex-shedding frequency, f_s of the elastically-mounted body; ·, body frequency, f_y. $f_{nt} = 2.0 f_n$

Figure 6.6 shows the response of Deck A in run 1A↑ ϖnDF where there is a single instance of heave lock-in. The heave response smoothly progresses with wind speed, with increasing amplitudes beyond the onset velocity up to $A_{max}/D = 2.6\%$, shortly after dropping out of any oscillations and suddenly losing lock-in (i.e. the transitional desynchronisation of run Run 2C↑ ψnDF is not observed). The pitch response is smooth, with an asymmetry resulting in $\gamma_{max} = 0.06^{\circ}$ at a wind speed past the mid-range of capture. At the onset of pitch lock-in, the body frequency is at the natural frequency in pitch, and increases throughout lock-in. The increase in f_y is quickest during early lock-in. This trend has been observed for all the models in both tunnels.

The response of Deck D in the T5 tunnel (run 1D↑ ϖnDF) is similar to the $10' \times 5'$ tunnel (figure 6.7). There is a large amplitude pitch response at $0.65 \leq U/(f_n B) \leq 0.76$ with associated lock-in.

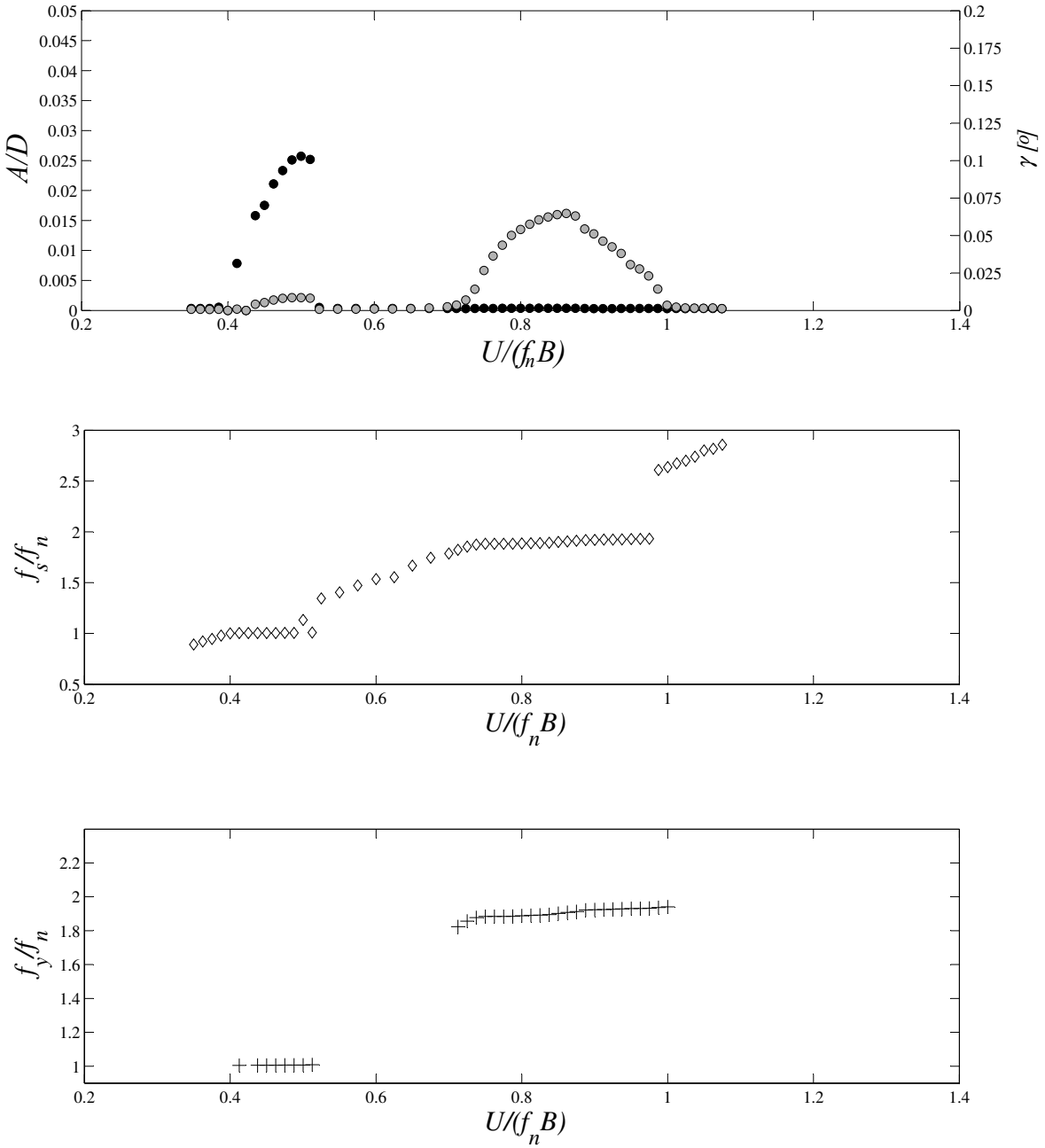


Figure 6.6: Run 1A↑ ϖnDF: •, rms displacement in heave A/D; •, torsion γ; $\Diamond$, vortex-shedding frequency, f_s of the elastically-mounted body; $\cdot$, body frequency, f_y. $f_{nt} = 2.0 f_n$

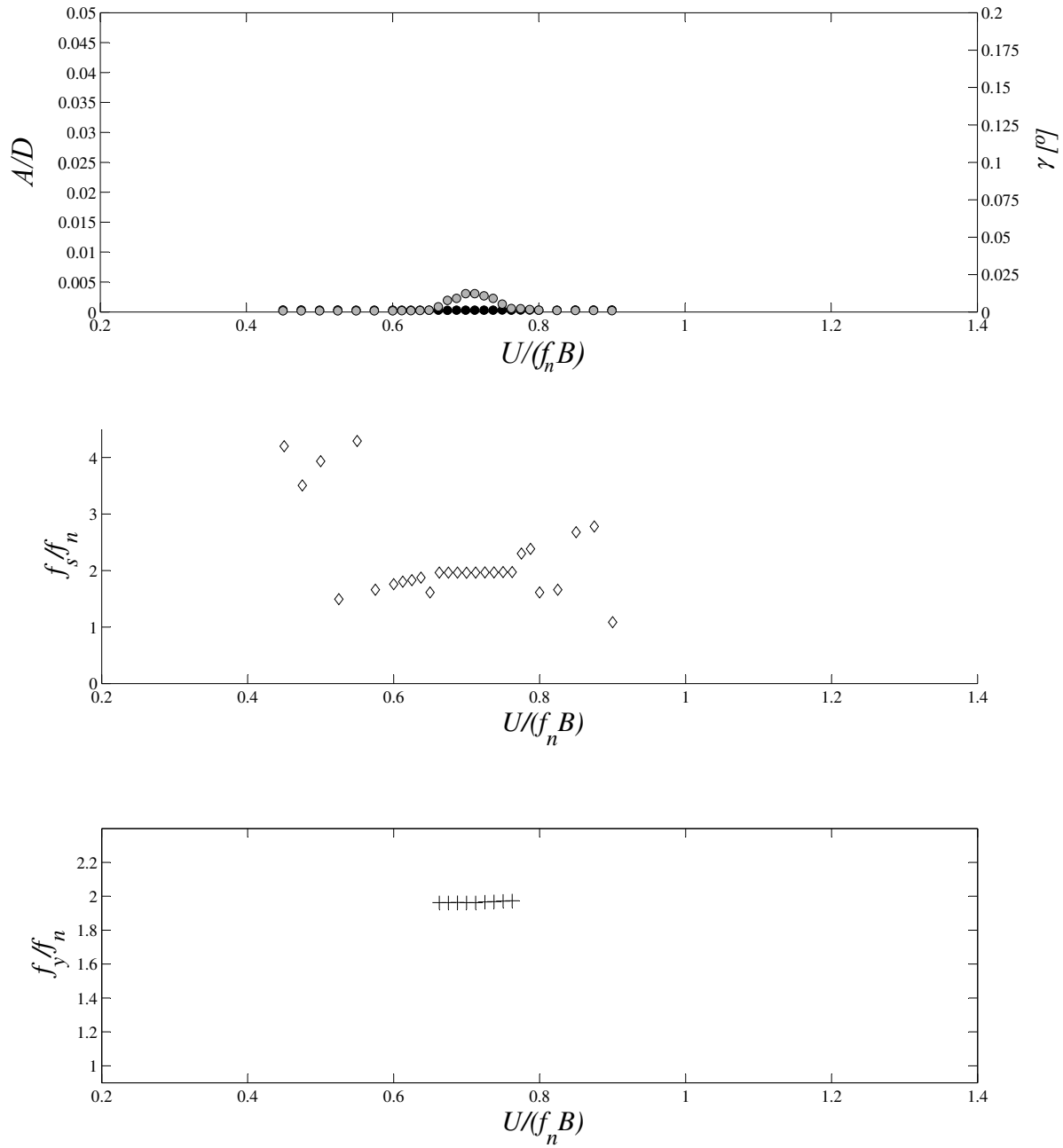


Figure 6.7: Run 1D↑ ϖnDF: •, rms displacement in heave A/D; •, torsion γ; ◊, vortex-shedding frequency, f_s of the elastically-mounted body; ·, body frequency, f_y. $f_{nt} = 2.0 f_n$

6.3 Discussion

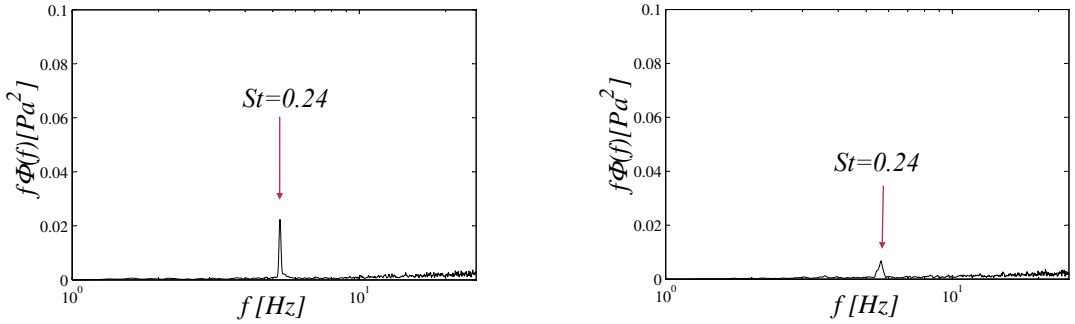
The bottom topography of the fairings has a significant effect on the behaviour of the trapezoid in VIV. Of the five models tested, Deck C, with a 20° angle at the bottom knuckles is the least responsive. All other decks exhibited an increased response in heave and/or pitch for the wind speeds investigated. Deck C did not exhibit lock-in and only a pitch beating response that was small in amplitude, highly modulated and did not persist over a significant range of wind speeds. Beating responses are observed for all the models at the onset and end of pitch. This is an amplitude modulation, which is irregular and at very low frequencies, < 0.5Hz. For most of the models, the amplitude modulation disappears at wind speeds further within the range of capture, where large amplitude, organised oscillations take over. However, for Deck C, this beating never develops into large amplitude, organised angular displacement, and instead persists for a small range of wind speeds.

6.3.1 Heave response with different fairings

Only Deck A and Deck B exhibit any kind of heave VIV. Decks C, D and E do not. In chapter 5 it was determined the TEVS drives for the heave response of Deck B. Pressures on the stationary and oscillating body showed strong fluctuations at the downwind knuckles that increase linearly with wind speed. Pressures on the stationary Deck A show strong fluctuations at the downwind knuckles that increase linearly in frequency with wind speed, indicating TEVS as the driver for this body too. in order to understand why TEVS does not excite vertical oscillations of decks C, D and E, the pressure at the trailing edge is examined. Comparing the stationary Deck B and Deck C at $U/(f_n B) = 0.38$ (figure 6.8) (just before the onset of oscillations for the elastically-mounted Deck B in figure 6.8) indicates that TEVS is much weaker and more broadband for Deck C. The shallow angle, θ_B or the position of the trailing edge, moved further back from the tail that has reduced the TEVS.

Deck B, $C'_M = 0.01$ Deck C, $C'_M = 0.009$.

Top downwind knuckle



Bottom downwind knuckle

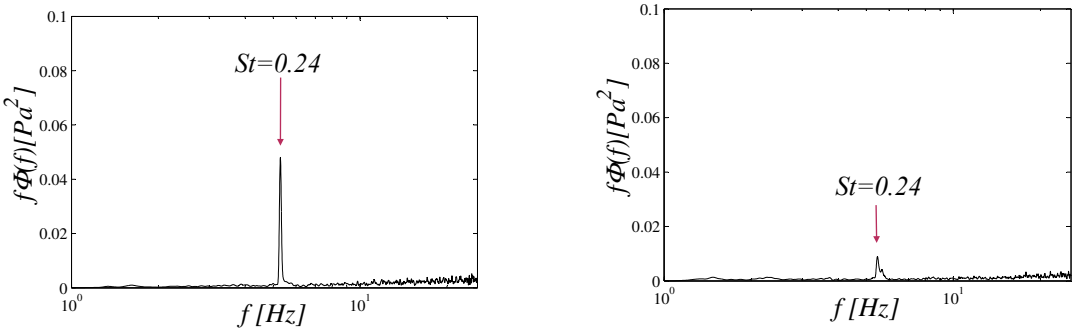


Figure 6.8: Run 1B↑ φnDF (left) and Run 1C↑ φnDF (right): Premultiplied spectra at the downwind knuckles, at a cross-section at 0.44L and $U/(f_n B)$=0.38 for the stationary body. The TEVS mode appears stronger and more organised for Deck B. C'_M is calculated as described in chapter 4.

It is postulated that the shallow angle reduces separation at the lower knuckle and reduces the TEVS mechanism responsible for the heave oscillations. Larsen and Wall [75] have shown that reduced separation of the Storebælt deck at $\theta_B = 14.7°$ results in a delay of vortex roll-up further from the body. This leads to a reduction in the lift force felt by the body. Here, the rms moment coefficient (defined in chapter 4) is 0.01 for Deck B and 10% less for Deck C. As TEVS is still present on Deck C, it is postulated that al lower damping levels, Deck C may display vertical oscillations. At low wind speeds Deck D does not display any apparent organised shedding on the stationary body - spectra in figure 6.9 are flat. It is expected that Deck D will not exhibit vertical VIV at these wind speeds, even at very low damping levels, unless excited in motion by some other mechanism initially, e.g. turbulent buffeting, that can control the vortex-shedding. Both decks may experience vertical oscillations at higher wind speeds, where it is shown later that TEVS grows.

Top downwind knuckle Bottom downwind knuckle .

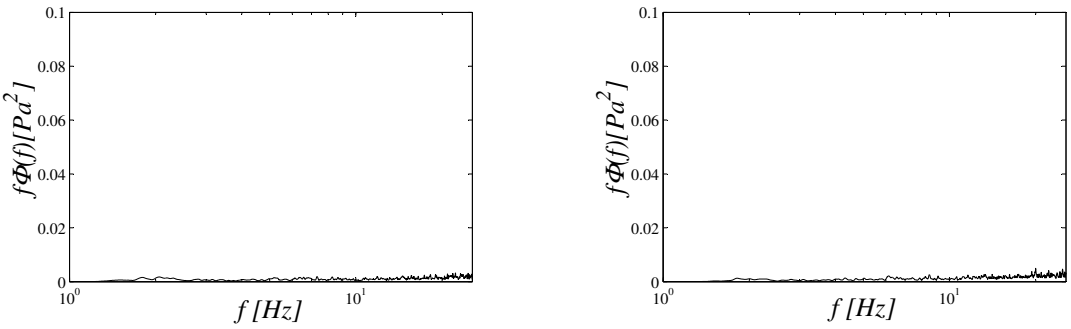


Figure 6.9: Run 1D↑nDF: Premultiplied spectra at the downwind knuckles, at a cross-section at 0.44L and $U/(f_nB)$=0.45 on the stationary body. No trailing edge shedding mode is apparent.

TEVS is a shear layer interaction, involving shear layers on the top and bottom of the trapezoid interacting in the wake. By changing only the bottom topography, the top shear layer is initially unaffected. It is only through interaction with the bottom shear layer that the TEVS is modified sufficiently so that Deck C and Deck D are stable. For a rectangular section with symmetric fairings the flow will be equally sensitive to the

top and bottom angles. Larose and Larsen [7] suggest that the vortex below the tail is dominant for a trapezoid as the backwards position of the knuckle on the bottom creates space for the vortex to grow. In figure 6.8 the pressures indicate more power at the TEVS frequency at the bottom knuckle. This agrees with the findings of Larose and Larsen [7] and suggests that the vertical VIV would be more sensitive to changes in θ_B than θ_T. The interaction of top and botto vortices mean that weakening the bottom vortices will weaken the top vortices and vice versa. Further work is required to understand the sensitivity of TEVS on trapezoids to both θ_T and θ_B at the downwind knuckles.

6.3.2 Pitch response with different fairings

ILEV is not a shear layer interaction. The top vortices are not directly affected by the bottom vortex generation, although they are strengthened by leading edge motion, which may be affected by strong shed vortices from the bottom of the body. Deck C is the most stable model, exhibiting only a beating response over a very short range of wind speeds. The pressure distributions in figure 6.10, around Deck B and Deck C at the resonant velocity indicate that it is not a difference in the global separation and reattachment that is the cause of the drastic difference in response. The pitch response of Deck B was shown in chapter 5 to be excited by a combination of trailing edge and leading edge modes. The leading edge mode corresponds to the frequency expected for the third mode of ILEV. It was not measurable on the stationary body, indicating it is a motion-generated form of excitation, probably amplified by the TEVS-generated oscillations. We have seen that the TEVS is less organised and of lower power for Deck C than Deck B. Interestingly, the change of shape at the trailing edge fairing results in the shedding appearing less significant than the top (figure 6.11) suggesting the effects of the bottom vortex in the body have weakened. As the body begins to beat, a small peak at $St = 0.13$ emerges in the leading edge spectra. This frequency can be seen convecting along the body. At larger response amplitudes the only frequency present in spectra is the natural frequency. The frequency, $St = 0.13$ corresponds with the n=2 mode of ILEV (based on equation 2.15) and is different to the mode seen for Deck B in chapter 5.

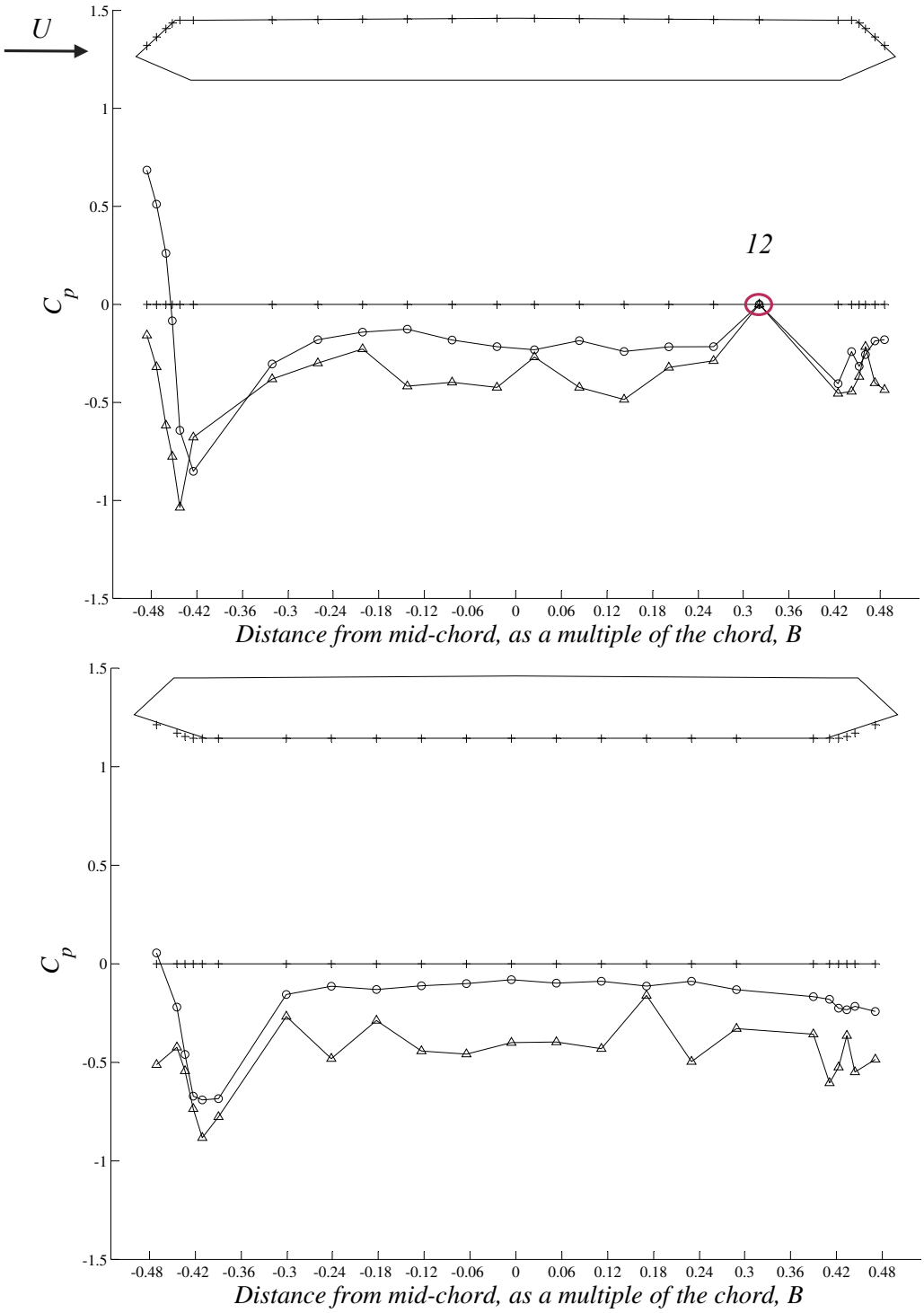
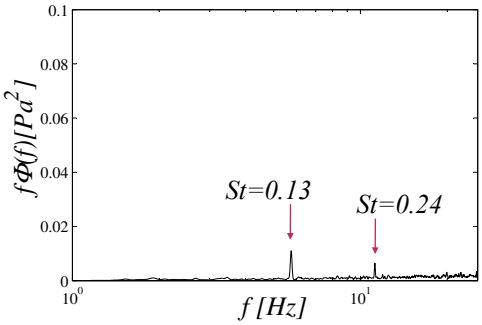


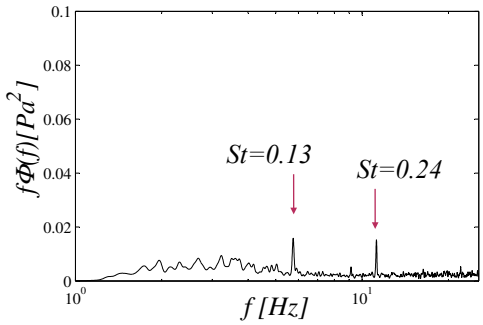
Figure 6.10: Distribution of mean pressure, C_p at a cross-section at 0.44L at the resonant wind speed for pitch. ∘, Run 2B↑ ψnDF at $U/(f_nB) = 0.79$; △, Run 2C↑ ψnDF at $U/(f_nB) = 0.70$. Pressure tap locations are indicated, +. Pressure taps giving erroneous results are circled in red.

Bottom surface

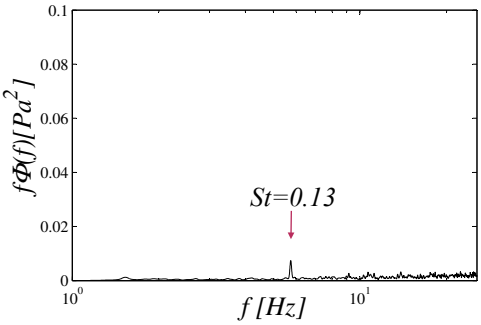
Top surface .

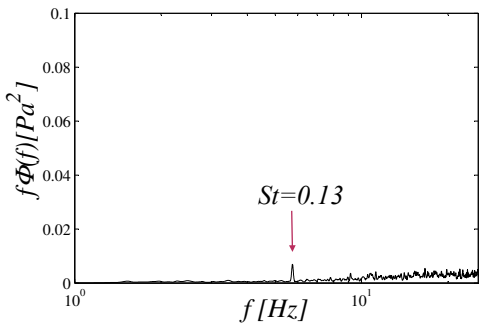
Upwind knuckles .



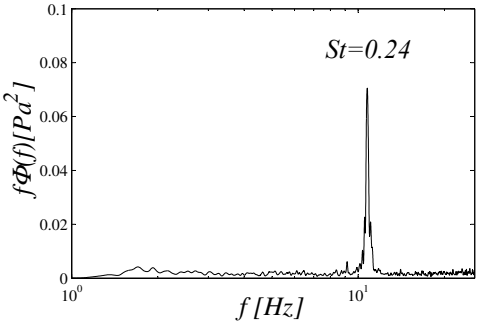


Body .





Bottom knuckles .



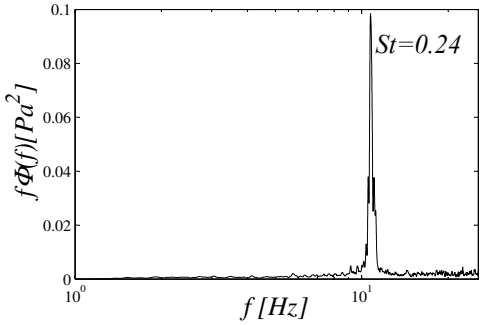


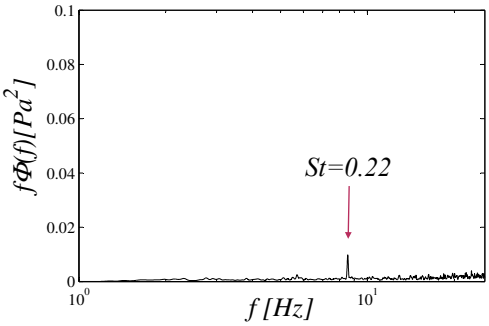
Figure 6.11: Run 1C↑ φnDF: Premultiplied spectra at select pressure taps, at a cross-section at 0.44L at $U/(f_n B)$=0.70 the resonant velocity for pitch beating. A peak at the leading edge has frequency $St = 0.13$ and a the strong peak at the trailing edge has frequency $St = 0.24$.

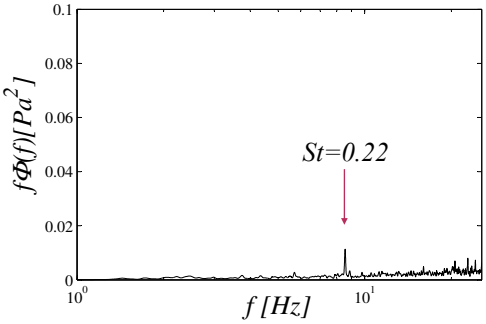
As Deck D does not have measurable TEVS when stationary, unlike Deck C, it is interesting that it experiences large amplitude pitch VIV. This suggests TEVS does not play a primary role in the pitch VIV of this body. Figure 6.12 shows that the oscillations amplify the TEVS, which appears but is broadband A leading edge mode is observed at $St = 0.22$, corresponding with the frequency for an n=4 ILEV mode. It is postulated that the TEVS of Deck D, although weak, is sufficient to generate some body motion when $f_s = f_{nt}$. It has been shown that only very small vibrations are required to generate ILEV [50]. This motion generates the leading edge mode. Terres-Nicoli and Kopp [51] postulate the ILEV modes are responsible for growing the body motion. As the most significant difference between the leading edge shedding on the decks in this study is the frequency, it is postulated that the higher modes of shedding, n=3 and n=4 are better at amplifying oscillations of this trapezoid. Whilst the n=3 and n=4 modes generate significant oscillations and lock-in, the n=2 mode does not. Investigation of the large amplitude pitch oscillations for Deck A determines a leading edge mode at $St = 0.22$. This agrees with the assertion that the higher modes of shedding amplify the motion more. Both decks A and D experience the $St = 0.22$ leading edge frequency, but deck A has much larger amplitude oscillations. As the TEVS may be controlled by oscillations at St_{TEVS}, and contribute to the excitation, there is a sensitivity to TEVS beyond the initial motion required to activate ILEV. It is postulated that the stronger TEVS at the sharp bottom downwind knuckle acts to grow the amplitudes more than the weaker TEVS of Deck D. Spectra of Deck D show peaks at $St = 0.25$ are strongest at the knuckle, suggesting the separation point have not moved downwind.

Bottom surface

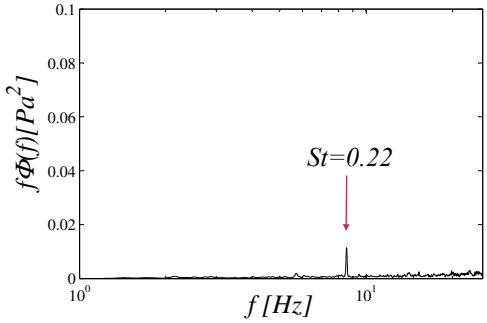
Top surface

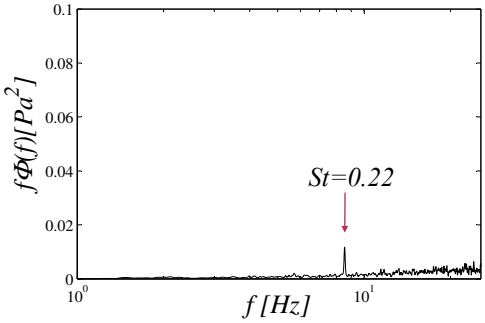
Upwind knuckles



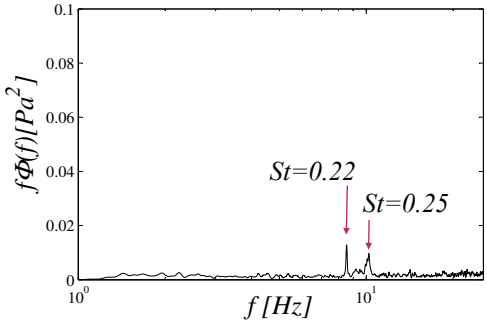


Body





Bottom knuckles



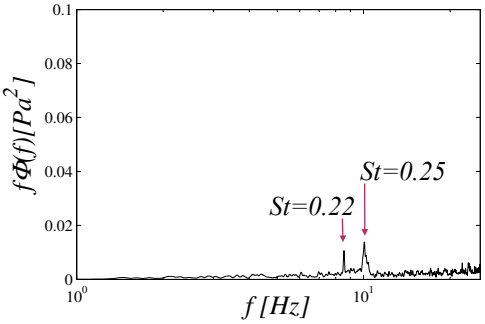


Figure 6.12: Run 1D↑ φnDF: Premultiplied spectra at select pressure taps, at a cross-section at 0.44L at $U/(f_n B) = 0.65$, the resonant velocity for pitch. A peak at the leading edge has frequency $St = 0.22$, and broadband peaks at the trailing edge (and strongest at the knuckle) have frequency $St = 0.25$.

The literature suggests that modes higher than n=2 are rarely observed on prisms. A Storebælt model [51] experienced n=2 excitation for heave and pitch. However, the aspect ratio of the Storebælt ($B/D = 7.8$) is significantly smaller than the models in this study ($B/D = 11.2$). Indeed, Naudascher and Wang [39] found that increasing the aspect ratio of rectangles up to 8, shifted the dominant ILEV mode from 1 to 2. It may be that had they looked at higher ratios the dominant excitation mode would further increase to 3 and 4, as seen for this trapezoid. Additionally, modes up to n=5 in bending and n=6 in torsion have been observed on H-sections [45] (figure 2.28).

It is clear that changing the bottom topography of the leading fairing has an effect on the leading edge mode. It is not clear what causes this difference; whether it is the change in angle, θ_B or the increased length of the upwind panel that means the shear layer is more developed. Further work is needed to understand the driver of the mode change.

Table 6.1 below gives a summary of St measured for different decks for different runs. The Strouhal number, St appear constant for all angles, $/theta_B$ over the range $\theta_B = 18°$ to 30°. St is calculated using a least-squares linear curve fit to the shedding frequency measured at the trailing edge bottom knuckle. Where pressure data on the stationary decks is not available, a best fit is made of the elastically-mounted models at wind speeds with no measured motion, where $A/D = \gamma = 0$.

	2X↑ ψnDF	1X↑nDF
Deck A	-	0.24^{em}
Deck B	0.24	0.24^{em}
Deck C	0.24	0.24^{em}
Deck D	-	0.25^{em}

Table 6.1: Strouhal numbers, St calculated from the shedding frequency, f_s (measured at the downwind knuckle) relationship with wind speed. ^{em} denotes where St was calculated from measurements of the elastically-mounted deck, when $A/D = \gamma = 0$.

Experiments by Larsen and Wall [75] on the bare deck of the Storebælt main span (figure 2.49) indicate agreement with the results here: $\theta_B = 19.7°$ was more stable than the steeper or shallower angles in both heave and pitch. This is in contrast to the decks with road furniture, where $\theta_B = 14.7°$ is more stable. No investigation of the shedding mode or explanation for this critical angle is given by Larsen and Wall. The models are varied in a similar way to the models in this investigation; the nose and tail locations are fixed, and the location of the knuckles are varied to change the angle, θ_B.

6.4 Conclusion

It is clear that modifying the bottom topography of the fairings significantly impacts heave and pitch VIV. The heave VIV for this slender trapezoid is driven by TEVS, and is strengthened at steep angles at the bottom knuckles. At $\theta_B \leq 20°$ the TEVS is reduced in strength and organisation, resulting in no observable heave oscillations. For Deck D, TEVS is not observed at low wind speeds on the stationary deck. Although the shedding is weakened, it is expected that heave oscillations for Deck C would be observed at lower damping levels. The lowest damping level in this study is 0/5% rel-to-crit; the lowest achievable for this set-up. As the heave is caused by TEVS, modifying the trailing edge fairing is an effective way to mitigate response. By changing only the bottom knuckle location and angle, heave is seen to be completely mitigated at angles $\leq 20°$ at $\zeta = 0.5\%$. It is postulated that the shallow angle reduces separation and coherent vortex formation in the near wake.

The pitch lock-in involves a combinations of leading edge and trailing edge excitation modes. The leading edge mode number varies with the fairings, either because of θ_B or because of the longer inclined panel and more developed shear layer approaching the upwind knuckle. Decks A and D both experience large amplitude pitch oscillations excited by a leading edge mode. Deck B has similar oscillations, excited by an n=3 mode. Deck C does not experience lock-in, beating oscillations in pitch are observed, and shedding corresponds with an n=2 mode. It appears that for this very slender trapezoid, higher modes of ILEV are observed than for less slender trapezoids [51], and that these higher modes dominate. The amplitude of response is a function of the ILEV mode, with the

higher modes; n=3 and n=4 exciting larger amplitude motion than the n=2 mode. It is postulated that the TEVS does not primarily drive the pitch response. It is required to generate small amplitude motion that excites the motion-generated ILEV modes. It is postulated that both the TEVS and ILEV mode contribute to the maximum amplitude, as the main difference between decks A and D appears to be the strength of TEVS Generally, higher ILEV modes and strong TEVS generate large amplitude oscillations (as for Deck A and B). Further work is required to confirm the presence of the vortex modes visually, the n=2 mode will display 2 vortices on the top and bottom each, the n=3 mode 3, and so on.

Deck C is the most stable model tested. The shallow angle at the downwind knuckle appears to limit TEVS and heave oscillations at $\zeta = 0.5\%$ $\theta_B = 20°$ is stable, although at lower damping levels this may not be the case. Long-span bridges can have very low structural damping, and the critical angle, below which bending is not observed is likely to reduce with damping. The pitch oscillations for the very slender trapezoid here is mitigated by weak TEVS and a low mode number for impinging vortices. Comparisons with measurements on less slender bridges [75] indicate generally higher leading edge modes. in this study the higher modes are more effective at amplifying motion. This is similar to the trend seen in rectangular cylinders [39]. Further work is required to understand the relationship between the slenderness, leading edge mode and response.

Deck C here has $\theta_B = 20°$, which agrees with the critically stable angle for the Storebælt bare deck [75], despite the difference in slenderness. The Storebælt bridge has been shown to also be excited by a combination of TEVS and ILEV. As the pitch is triggered by TEVS and then amplified by motion-generated ILEV, both fairing geometries impact the response. It appears there is greater sensitivity to the ILEV mode number, but that the strength of TEVS also plays an important role in amplifying the ILEV shedding.

Chapter 7

Hysteresis, damping and road furniture

7.1 Hysteresis

7.1.1 Introduction

Hysteresis has not been extensively investigated for trapezoids. It was observed in the full-scale Storebælt bridge, and in wind tunnel tests for both the heave and torsion responses (figure 2.29 [51]). The sign of the wind speed increment changes A_{max} and the range of wind speeds for which a response is observed, but the onset critical wind speed is unchanged. Hysteresis is a common theme in VIV and has been observed for circular and D-section cylinders [9] (figures 2.8 to 2.10). Only those responses exhibiting branches, with different excitation mechanisms for each branch displayed the damping. Smooth responses, with only one excitation mechanism did not exhibit hysteresis. Williamson and Roshko [30] explain the hysteresis of circular cylinders is caused by two possible modes of shedding, 2S and 2P, over a range of wind speeds. The 2S mode excites the initial branch and the 2P mode the lower branch. The prevailing mode and associated response is dependent on the history of the flow. Negative wind speed increments extend the lower branch and reduce A_{max}, but the onset critical velocity is constant.

Run 2B↑ ψnDF exhibited a branched heave response, with the initial branch characterised by strong TEVS locked into the body, and the lower branch experiencing desyn-

chronisation. The desynchronised region represents a different kind of excitation mode, split over two forcing frequencies and it is expected that the mode at a given wind speed will be sensitive to the sign of the wind speed increment.

To determine if the trapezoid in this study exhibits this dependence on the initial conditions, three different starting methods were investigated. These methods are described in Chapter 3 and are summarised here:

1. the tunnel speed is increased by a small increment with the model free to oscillate from its previous steady-state condition, $\uparrow$.

2. the tunnel speed is decreased by a small increment with the model free to oscillate from its previous steady-state condition, $\downarrow$.

3. the tunnel speed was increased by a small increment, 120 seconds waited, after which the model released from rest, $\wedge$.

Deck B and Deck C are investigated. For all the runs, all measurements are taken 120 seconds after the steps above are carried out.

7.1.2 Results

Comparisons of run 1B$\uparrow$ φnDF and run 1B$\wedge\varphi$nDF in figure 7.1 indicate a significant effect of starting method on the heave response. The response for run 1B$\wedge\varphi$nDF is much lower in amplitude, with a narrower response range. The response for $U/(f_nB) \geq 0.60$ is roll. No roll is observed when the body is brought still at each increment. Owen *et al*. [90] find that it takes a long time for the build up of large amplitude response after the vortex-shedding has occurred. Bringing the body to stationary alters the motion and flow, as VIV is an interaction of body and flow. It may be surmised that a lag time of 120 seconds between the body being released and taking measurements is not sufficient for the flow-structure interaction to converge with the continuously increasing wind speed case. However, the responses at all wind speeds for both runs is steady and sinusoidal, indicating that the build up time is much longer than 120 seconds for the model, or that steady state amplitudes are limited by the starting method, for any build-up time. There is clearly a difference in excitation force. Pressure measurements indicate that

both responses are driven by TEVS of similar strength. It may be that a difference in the phase angle (that the forcing leads the response) results in a reduction of the component of TEVS that excites motion for the body released from rest. In figure 5.18 the phase angle (with the model free to oscillate from its previous steady-state condition) is seen to increase through heave lock-in, with a jump early in the lock-in. This jump leads to an increase in the component of shedding exciting motion. Phase information is not available for run 1B$\wedge\varphi$nDF. Further work is required to understand what is limiting amplitudes for the body released from rest.

Figure 7.2 shows that when the sign of wind speed increment changes, there is almost no difference in the response at a given wind speed. This suggests that small differences in the starting body motion (and flow) are insufficient to generate hysteresis, but when the body is brought to rest the difference is large. Further work is required to understand the difference in the excitation mode, not observed in this study.

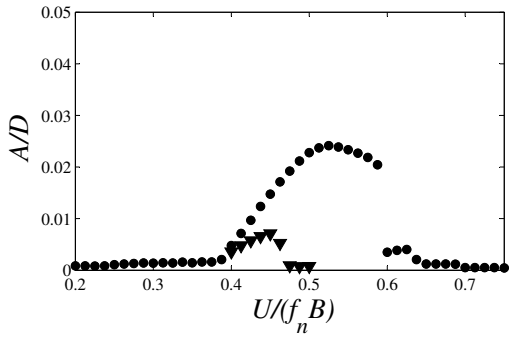


Figure 7.1: rms displacement in heave A/D, for • the wind speed increased incrementally (run 1B↑ φnDF), and ▼ from rest (run 1B$\wedge\varphi$nDF).

In figure 7.2, the only difference for wind speed increment is the later part of the heave response, at high wind speeds. A lower branch, characterised by desynchronisation exists for a single wind speed when the speed is increased incrementally, and is not observed when the wind speed is decreased incrementally. The desynchronised regime is sensitive to the previous state of body and flow. Consider approaching from lower wind speeds, the body is in lock-in with large amplitude oscillations. Far from the resonant point, the lock-in is gradually lost (especially when ΔU is small) and desychronised shedding

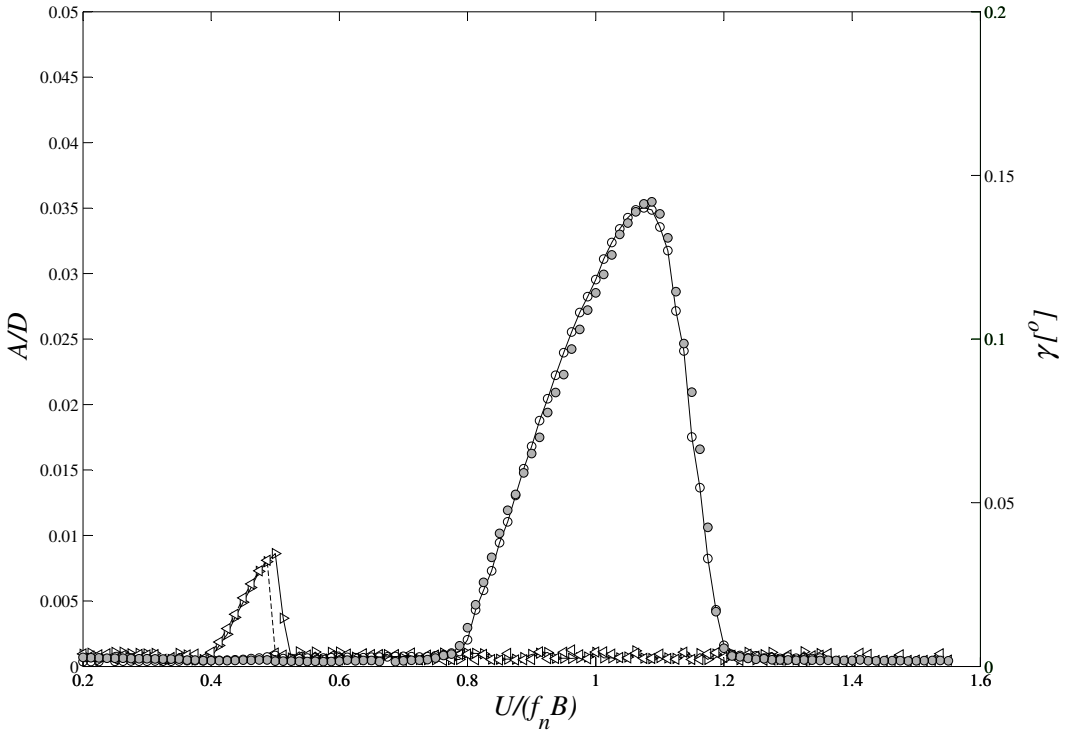


Figure 7.2: Hysteresis observed for Deck B: Run 1B↑ χnDF $\triangleright$, rms displacement in heave A/D; $\bullet$, torsion γ; Run 1B↓ χnDF $\triangleleft$, rms displacement in heave A/D; $\circ$, torsion γ.

is observed intermittently, and amplitude reduce, but are non-zero. If instead, this wind speed is approached from higher values, the body is stationary with fixed body shedding. Lock-in involves a significant jump down in shedding frequency and there is not sufficient energy in the system, so far from the resonant point to initiate oscillations of lock-in. Body motion does not happen until the body is able to fully lock-in. The rest of the response appears insensitive to wind speed increment. Hysteresis is only evident at the discontinuity of the fully locked-in regime and desynchronised regime and is unaffected by small changes in flow and body motion history.

Hysteresis is also observed for the beating response of Deck C in figure 7.3. With decreasing wind speed the response is zero. When the wind speed is gradually increased, a beating response without lock-in is observed over a small range of wind speeds. The TEVS and ILEV on the stationary bodies appear unaffected by increment direction and the difference in response is not understood.

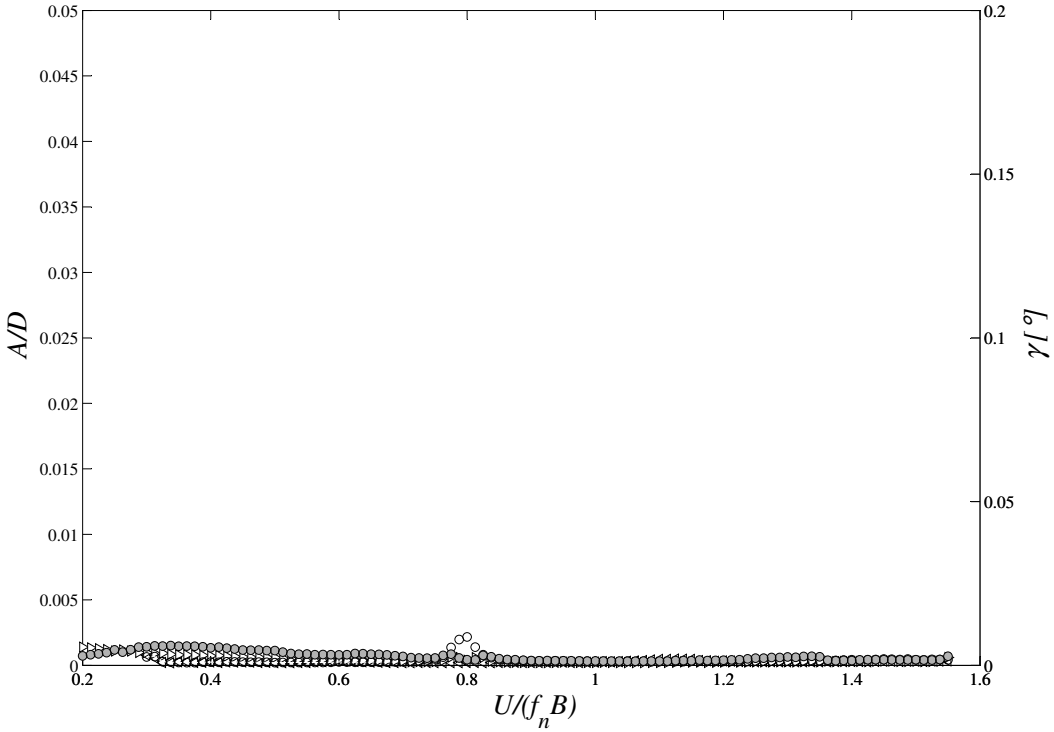


Figure 7.3: Hysteresis observed for Deck C: run 2C↑ φnDF $\triangleright$, rms displacement in heave A/D; $\circ$, torsion γ; run 2C↓ φnDF $\triangleleft$, rms displacement in heave A/D; $\bullet$, torsion γ.

7.1.3 Conclusions

Experiments show hysteresis is observed for Deck B and Deck C, in a similar manner to the Storebælt bridge, both experiments and full-scale measurements [51]. For Deck B this is limited to the desynchronised regime/lower branch. For negative wind speed increment no desynchronisation is observed. The response on the initial branch and in pitch are unaffected. The desynchronised regime is characterised by partial lock-in of the TEVS and intermittent shedding at the fixed body frequency. It is postulated that the desynchronised regime can only be entered in from a state of lock-in and associated large amplitude oscillations. The stationary state does not posses the energy to jump into partial lock-in/desynchronisation. The small amplitude beating response of Deck C is mitigated when the wind speed is decreased.

When the model is brought to rest before each wind speed increment, the response is significantly reduced; A_{max} is reduced by 70%. This shows that the response is strongly dependent on initial conditions of body motion history, more so than wind speed. The impact of bringing the body to rest is much greater than the sign of the wind speed increment. This is important in the prediction of amplitudes in the design stage. Large amplitude oscillations may result from the initial motion from another flow excitation such as turbulent buffeting, which may push the deck into a less stable body-flow interaction. Exploration of the pressure data does not reveal any difference in the shedding modes, frequencies or intensities. More information on the flow around the body is required to better understand why amplitudes are limited when the body is released from still.

7.2 Damping

7.2.1 Introduction

Damping acts to produce waste energy in a system and reduce oscillations. By observation of equation 2.4, damping will act to reduce the amplitude of oscillations of a bridge deck. The manner in which it does is less well understood than for circular and D-section cylinders. Wind tunnel experiments on the Storebælt bridge [51] shows a similar behaviour with damping to the circular cylinder (figure 2.29). Experiments on circular cylinders [9] have shown that runs at different damping levels share the same rising side of heave response and break off to different maxima (figure 2.9). For the Storebælt, the onset critical velocity is constant for a range of damping values, with the maximum response and range of capture reduced at higher damping levels. Experiments by Larsen and Wall [75] agree. It is therefore expected that this trapezoid will behave in a similar manner.

The effect of damping for Deck B is investigated using the experimental set-up described in chapter 3. Two cases are presented, comparing runs with the same conditions, differing only in damping.

7.2.2 Results

Run 1B↑ φnDF: $\zeta_{heave} = 0.5\%$ and $\zeta_{pitch} = 0.5\%$
Run 1B↑ χnDF: $\zeta_{heave} = 1.0\%$ and $\zeta_{pitch} = 1.0\%$

Figure 7.4 shows the response in heave and pitch is significantly affected by the damping. When ζ_{heave} is doubled, the maximum heave response, A_{max}/D is reduced from 2.4% to 0.9% and the range of capture approximately halved. γ_{max} is less affected and reduces from 0.17° to 0.14° and the range of capture is reduced by 20% only. It is interesting that the pitch and heave are not equally affected, and is thought to be because of the differing mechanisms exciting each response. In chapter 5 it was found that the heave response is driven by TEVS and the pitch response is a combination of TEVS and motion-generated ILEV. The responses share the same onset velocity, but diverge to different maxima, and come to a still at lower wind speeds. This is similar to what has been observed for the Storebælt bridge [51] [75]; the responses share an onset critical velocity, but the range

of capture and maximum response are reduced. At the higher damping level, A_{max} and γ_{max} are shifted to lower wind speeds.

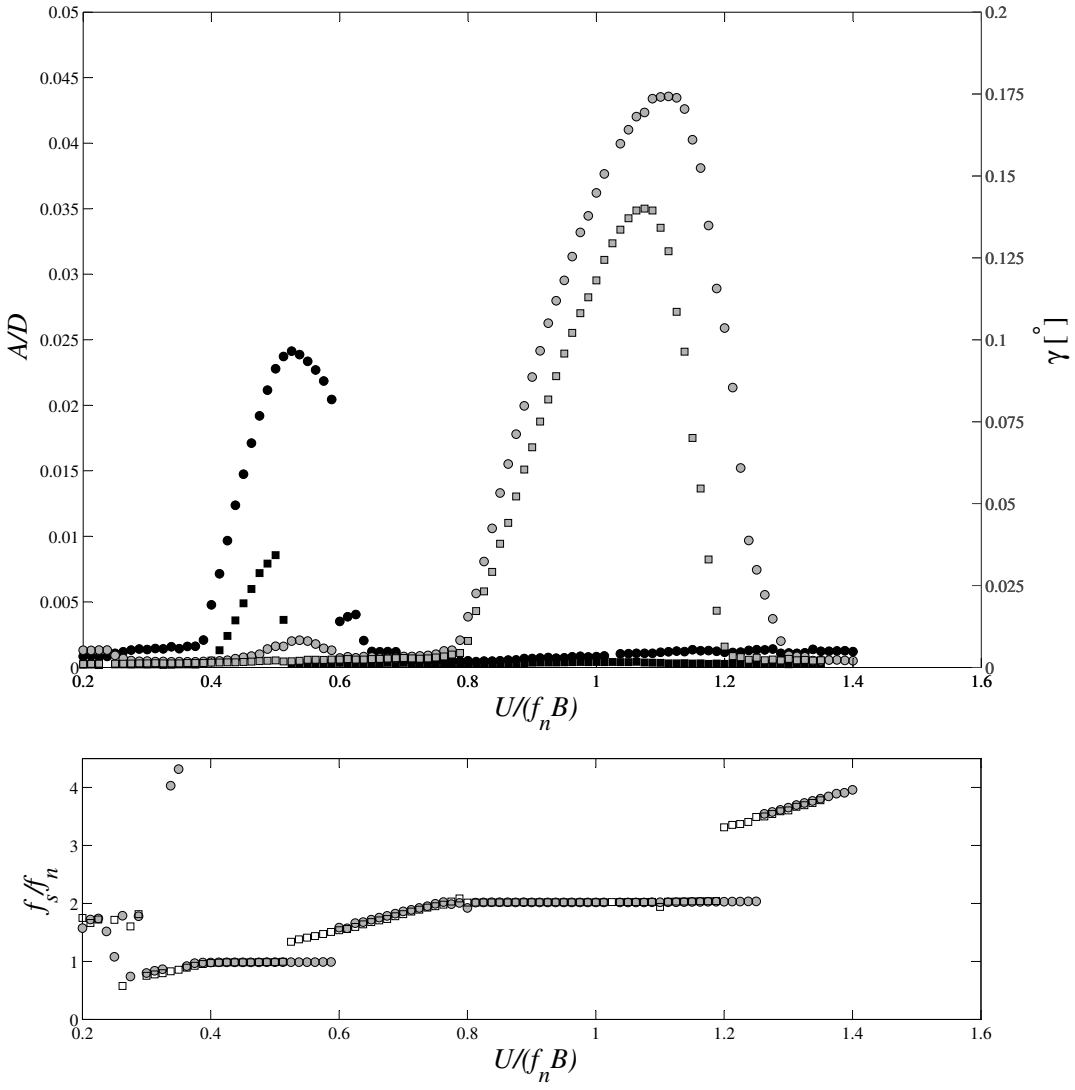


Figure 7.4: Run 1B↑ φnDF and run 1B↑ χnDF: rms displacement in heave A/D, •, $\zeta_{heave} = 0.5\%$; ■, $\zeta_{heave} = 1.0\%$; torsion γ, • ,$\zeta_{heave} = 0.5\%$; □, $\zeta_{pitch} = 1.0\%$. At high wind speeds, $0.60 \leq U/(f_n B) \leq 0.64$ the response seen for Run 1B↑ φnDF is roll.

Run 2B↑ φnDF: $\zeta_{heave} = 0.5\%$

Run 2B↑ ψnDF: $\zeta_{heave} = 0.7\%$

Only the heave response is compared for these two runs, as ζ_{pitch} was not measured for run 2B↑ φnDF. This smaller difference in damping has a similar effect on the response, as shown in figure 7.5. A_{max}/D is reduced from 0.9% to 0.6% and shifted to lower

wind speeds. Both responses start at the same onset critical velocity. The range of response is reduced by 13%. The higher damping level has a clearly defined, non-zero lower branch, characterised by desynchronisation. The desynchronised responses become large amplitude oscillations when the damping is reduced.

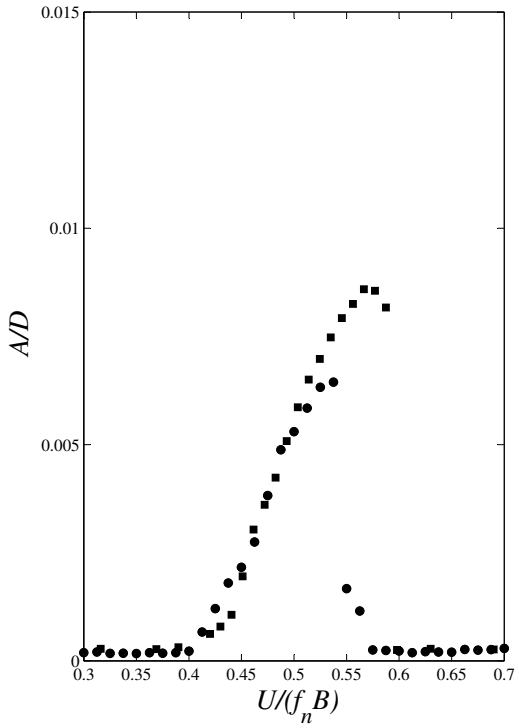


Figure 7.5: Run 2B↑ φnDF and run 2B↑ ψnDF: rms displacement in heave A/D, ■, $\zeta_{heave} = 0.5\%$; •, $\zeta_{heave} = 0.7\%$.

The damping acts to reduce the VIV amplitudes in two ways. For a given excitation force, the amount of excitation energy is dissipated through other means, heat for example. This reduces the amplitudes of an oscillating body which is known to impact the interaction of fluid and body; lower amplitudes lead to reduced lock-in effects, which in turn do not amplify oscillations as much as they would at larger amplitudes. This explains why desynchronisation is seen at higher damping levels, when at lower damping levels lock-in is observed. As the interaction is non-linear, it is not expected that the effect of damping is linear, i.e. the effect varies through lock-in.

7.2.3 Conclusions

The trapezoid behaves similarly to the Storebælt deck and a circular cylinder. The behaviour with damping with increasing wind speed increment, can be summarised as:

1. a reduction in amplitudes
2. a reduction in the range of wind speeds for which lock-in and response are observed
3. a shift of maximum response to lower wind speeds
4. all damping levels share the onset critical velocity and rising side of response

The heave response is more sensitive than the pitch to damping. It is postulated that the excitation mechanism; TEVS is more sensitive to damping than the ILEV mechanism.

A Scruton diagram based on the results in this section, is presented in figure 7.6. Whether amplitudes are dependant on the product of mass and damping, or on each parameter independently is not conclusive in the literature. The Scruton diagram shows the stability of the models through heave lock-in, displaying how the maximum response and the region of capture vary with damping. These are presented as a function of the Scruton number, Sc, which is also known as the mass-damping parameter. For experiments in air, the non-dimensionless mass, $m/\rho d^2$, is very low and Sc varies only as ζ changes. The impact of increasing the damping is to reduce A_{max} and reduce the range of capture.

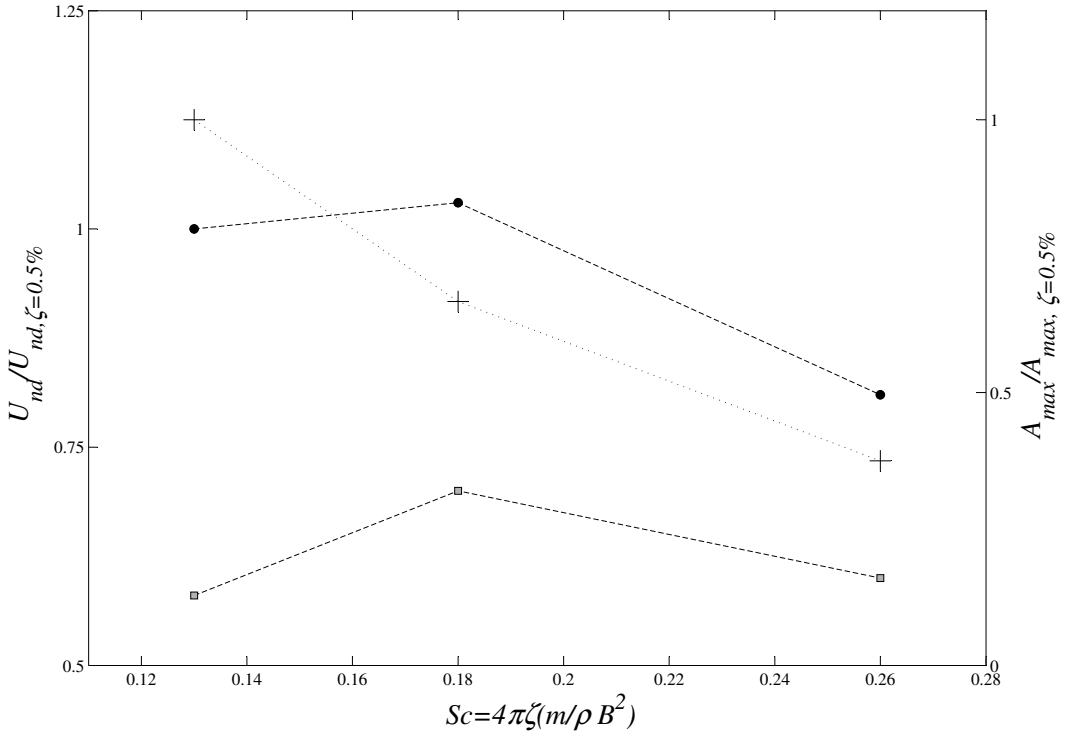


Figure 7.6: Scruton diagram for Deck B. the region of capture: □, minimum wind speed, • maximum wind speed; +, A/D_{max}. The results have been normalised based on the result for $\zeta_{heave} = 0.5\%$. The Scruton number, Sc, varies only with damping, ζ

7.3 Road Furniture

7.3.1 Introduction

In chapter 6 it was seen that a small change at the leading edge and trailing edge of a trapezoid can affect the flow excitation and response in VIV. Open railings and a median divider, as described in Chapter 3 (figure 3.5), representing typical road furniture often found on road bridges, were added to the top surface of Deck B and Deck C. The impact is drastically different for heave and pitch responses; the heave is completely mitigated, whilst the pitch is amplified. In chapter 5 the heave response of Deck B was shown to be excited by strong TEVS. Organised shedding is not observed on the stationary body with road furniture at low wind speeds. It is postulated that the addition of road furniture disrupts the TEVS. At higher wind speeds, the TEVS is sufficient to generate the motion required to trigger growth of the leading edge shedding mode and oscillations, but only at higher wind speeds than the bare deck.

The results in this section are contrary to the existing literature. Kobayashi *et al.* [73] found that railings placed on a rectangular body with outriggers enhanced the heave motion. The torsional response was sometimes mitigated and sometimes enhanced, depending on the depth and height above deck of the single horizontal rail. Corriols and Morgenthal [48] find that railings enhance vertical oscillations and mitigate torsional excitation in their numerical simulations of a bridge deck. Larsen and Wall [75] carry out experiments on the Storebælt bridge and find that the largest bending peak is amplified, while the smaller two are reduced. The torsional response is generally mitigated. No explanation is given for the different results. There is limited literature on this subject, and the varying results across experiments o different models emphasises the need for further work in this area.

7.3.2 Results

Figure 7.7 shows the response for Deck B, where the addition of road furniture completely removes the heave response. The pitch lock-in remains, with γ_{max} increased from 0.17° for the bare deck to 0.19°, and the range of capture is shifted to higher wind speeds than for

the bare deck. Comparison should be made to the equivalent run without deck furniture in figure 5.2. At lower wind speeds, the shedding frequency, f_s in figure 7.7, measured at the bottom downwind knuckle is scattered and does not follow the linear Strouhal relationship, observed for Run 1B↑ φnDF. Figure 7.8 shows the effect on a stationary Deck B is similar.

The addition of road furniture disrupts the strong TEVS observed on the bare deck. Spectra of the pressure in figure 7.9, measured at the downwind knuckles, show no organised shedding at the resonant velocity for heave oscillation of the bare deck. TEVS is an interaction of the top and bottom shear layers in the near wake. The road furniture disrupts the interaction and the formation of coherent vortices at the trailing edge is mitigated. Deck B is excited to VIV oscillations by TEVS. The addition of deck furniture mitigates the heave response by disrupting the TEVS.

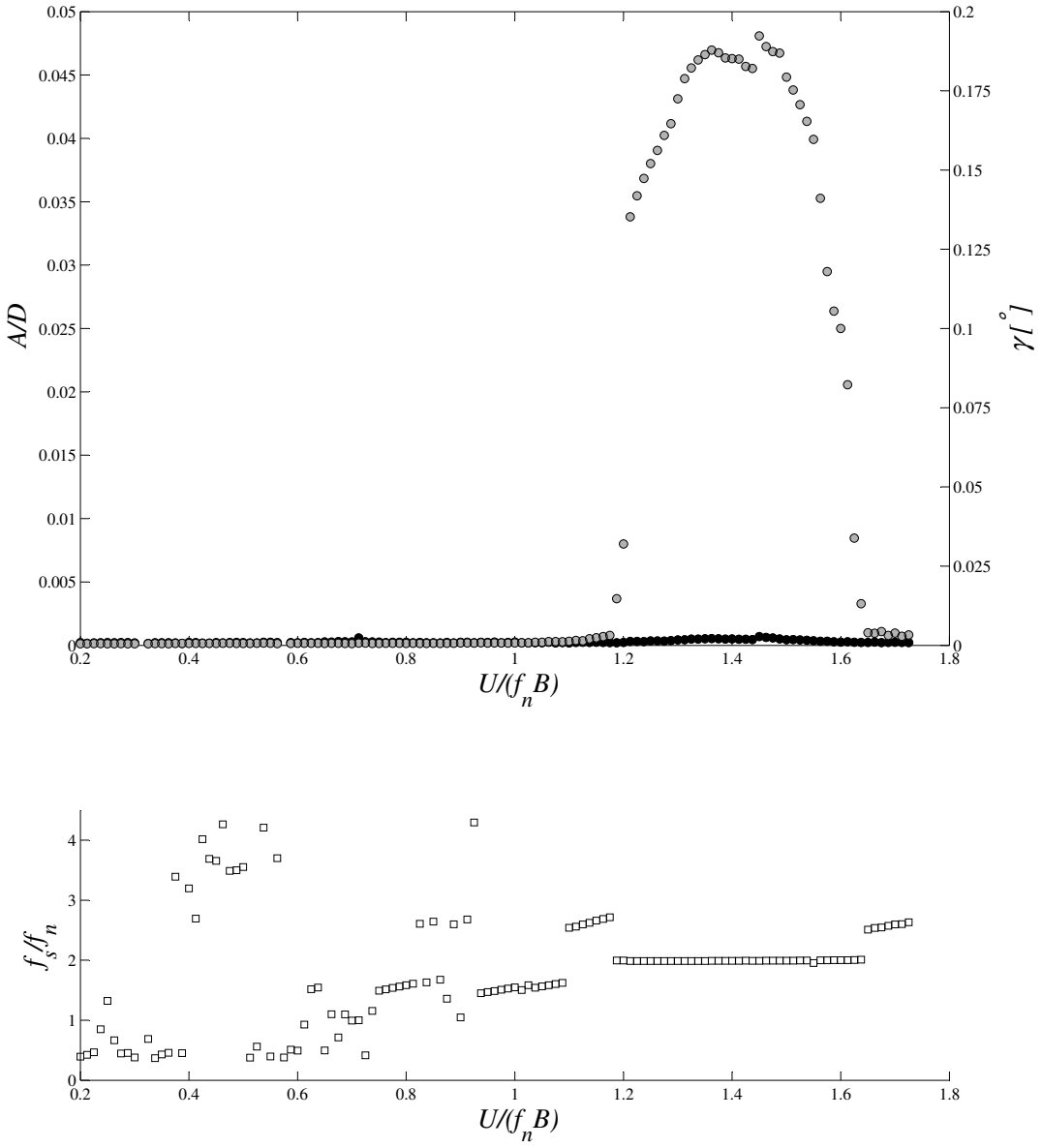


Figure 7.7: Run 1B↑ φDF: •, rms displacement in heave A/D; •, torsion γ; ◊, vortex-shedding frequency, f_s of the elastically-mounted body. Comparison should be made to the equivalent run for the bare deck in figure 5.2.

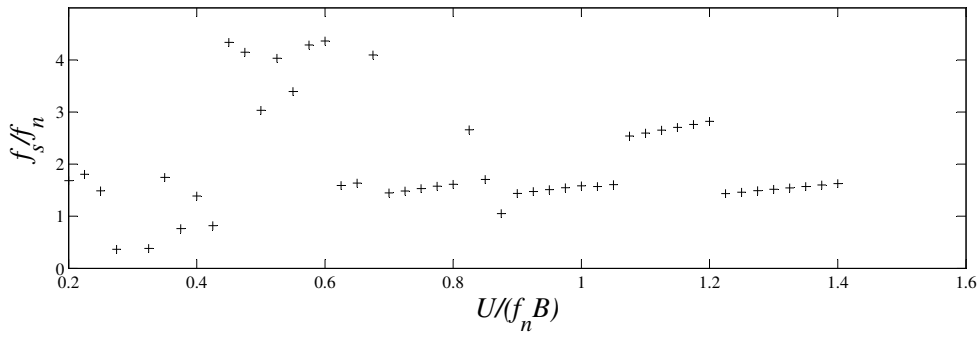
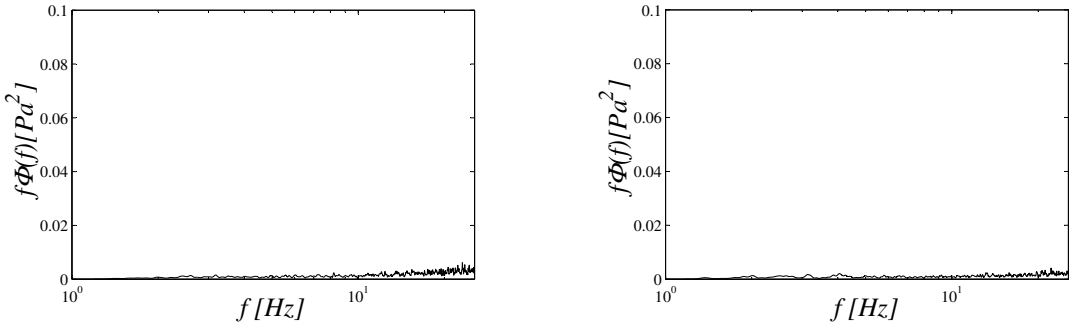


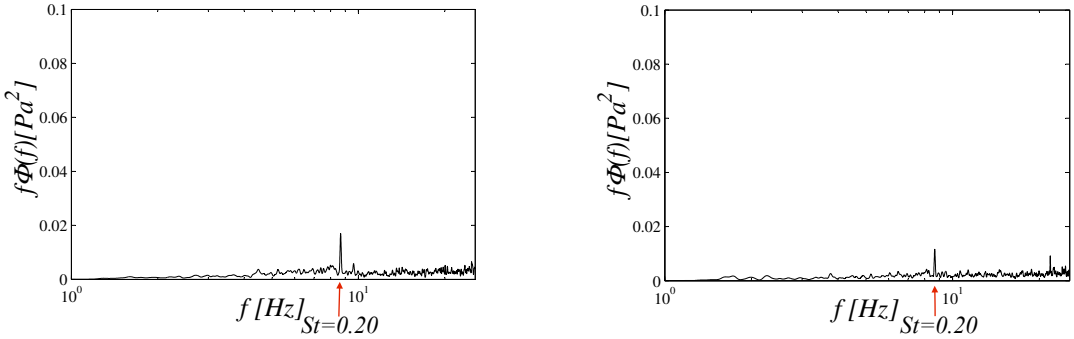
Figure 7.8: Run 1B↑DF: +, vortex-shedding frequency, f_s, measured on the stationary deck with open railings and a median divider.

Bottom knuckle Top knuckle .

$U/(f_nB) = 0.40$.



$U/(f_nB) = 0.80$.



$U/(f_nB) = 1.13$.

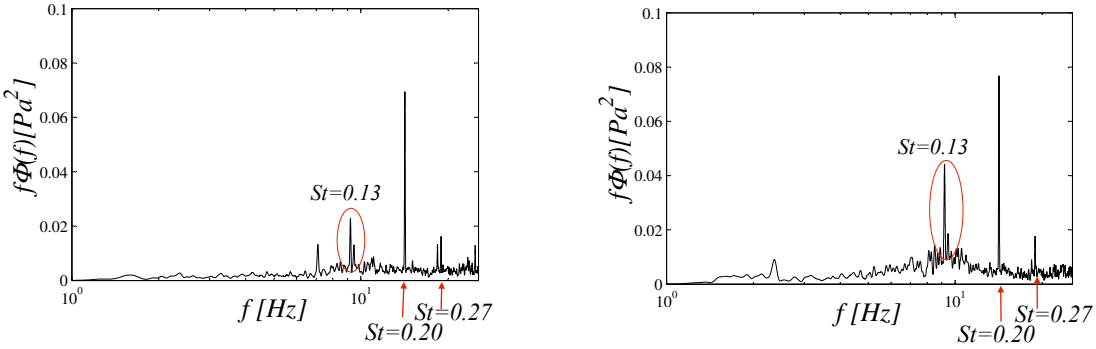


Figure 7.9: Run 1B↑ φDF: Pressure spectra measured at the downwind knuckle for the stationary model with deck furniture. $St = 0.27$ corresponds with the TEVS and $St = 0.20$ with an ILEV mode, n=3.

At the resonant velocity for pitch oscillations of the bare deck, $U/(f_n B) = 0.80$ the TEVS is still not observable on the deck with road furniture (figure 7.9). The only peak present on the body is the ILEV mode n=3, around the cross-section. This mode was observed for the bare deck combined with TEVS. The absence of any coherent trailing edge shedding, with road furniture may explain the lack of response at this wind speed. It has been postulated that TEVS initiates the small amplitude motion required to amplify the leading edge shedding and grow oscillations.

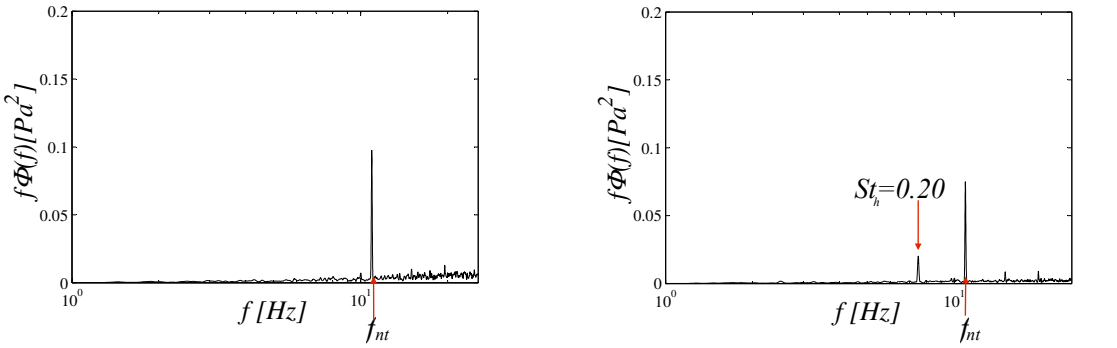
As the wind speed increases further the TEVS, at $St = 0.27$ is observed at the down-wind knuckles. There are also several other peaks present in the spectra in figure 7.9. The TEVS and n=3ILEV mode are observed on the bare deck. One peak is not observed on the bare deck, at St (based on the depth of the deck)= 0.13 which appears to be generated by the road furniture. It is not understood how the railings interact with the formation and shedding of vortices from the deck.

A large pitch response is observed at $U/(f_n B) = 1.19$. At this wind speed the effect of the road furniture on the TEVS is reduced (figure 7.7). Again, the spectra (figure 7.10) have additional peaks with the road furniture. This is unsurprising as it is thought the railings will act similarly to a turbulence grid and break up large coherent vortices into smaller, high frequency components, and that shedding from the railings themselves will occur.

Bottom knuckles

Top knuckles

Upwind



Downwind

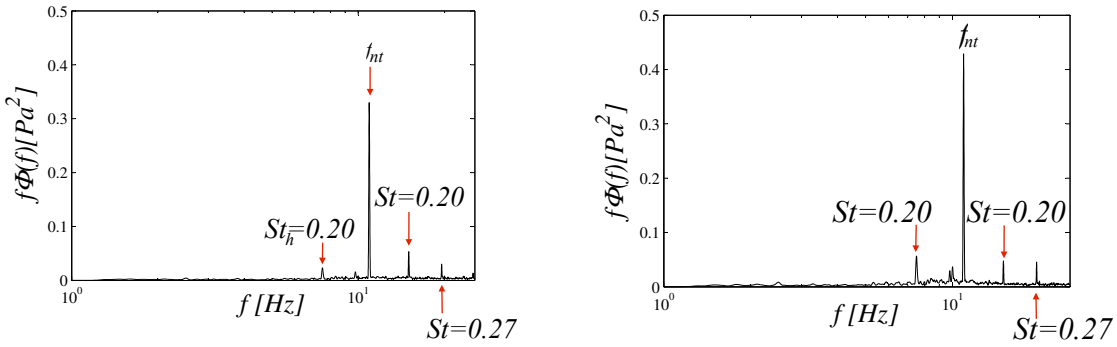


Figure 7.10: Run 1B↑ φDF: Pressure spectra measured at the downwind knuckle at $U/(f_n B) = 1.19$ for the stationary model with deck furniture. $St = 0.27$ labels the TEVS, $St = 0.20$ and $St_h = 0.20$ the n=3 ILEV mode and a $\frac{1}{2}$ harmonic respectively.

The addition of road furniture removes the beating response of Deck C in figure 7.11. Comparison should be made to run 1C↑ φnDF in figure 6.5. Again, the shedding does not follow a linear relationship at low wind speeds, but appears to become more organised at $U/(f_n B) \geq 0.75$.

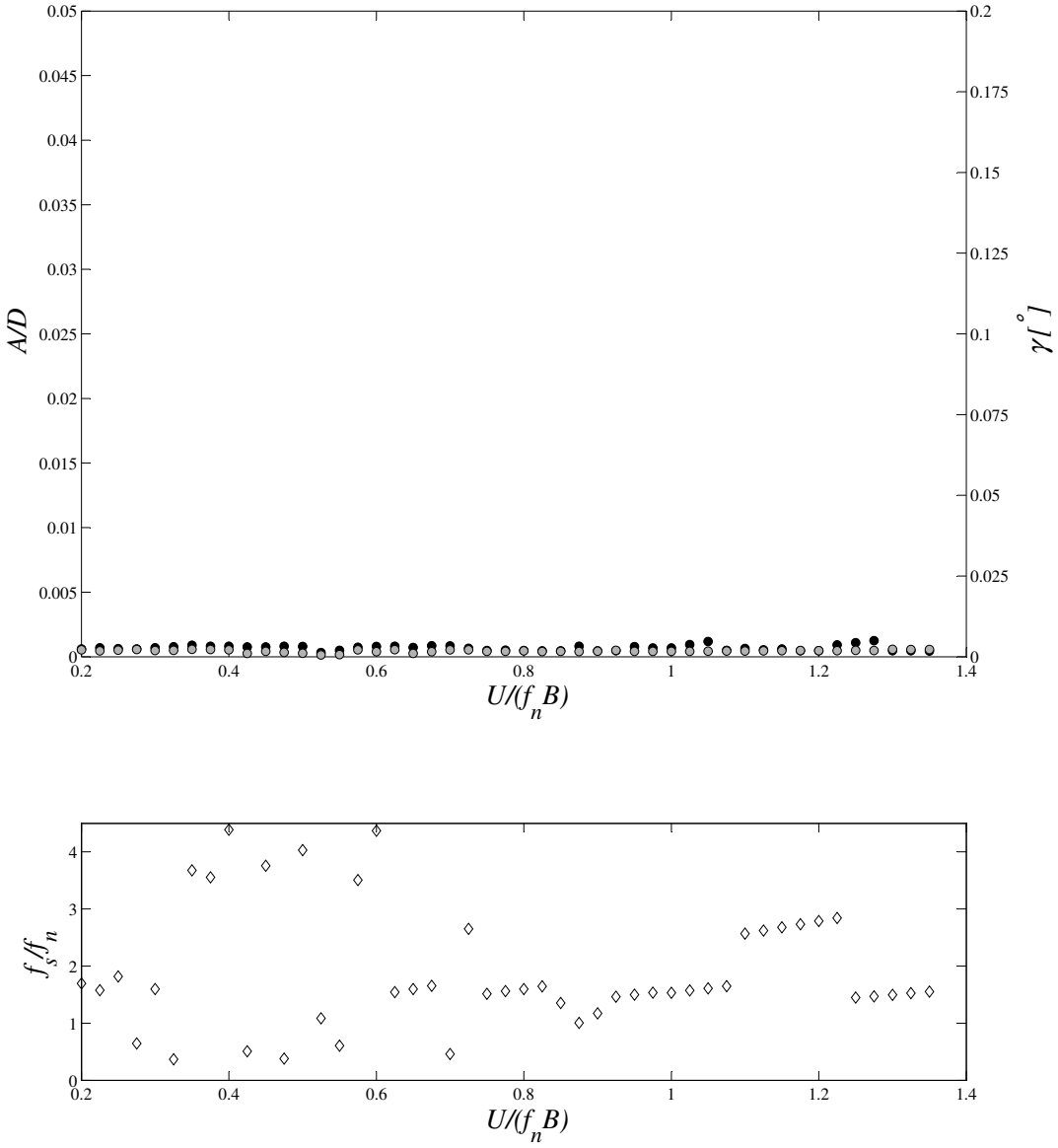


Figure 7.11: Run 1C↑ φDF: •, rms displacement in heave A/D; •, torsion γ; ◊, vortex-shedding frequency, f_s of the elastically-mounted body, measured at the down-wind knuckle. Comparison should be made to run 1C↑ φnDF in figure 6.5

7.3.3 Conclusion

Road furniture appears to disrupt the von Kármán vortex-shedding from the trailing edge. This effect is greatest at low wind speeds, where the TEVS is not observable. As the regular and organised shedding of a von Kármán wake is required for heave lock-in of this trapezoid, this explains why the addition of road furniture mitigates the heave response.

Interestingly, the presence of road furniture amplifies the pitch response. The TEVS becomes more organised and stronger at increasing wind speeds. It is postulated that pitch oscillations cannot occur at lower wind speeds, as the TEVS required to initiate motion is too weak. This acts to push the onset critical velocity to higher wind speeds. Practically this is a mitigation of sorts, as the likelihood of reaching higher wind speeds is generally smaller than the likelihood of smaller wind speeds. It is postulated that where the response is excited by TEVS, this can only happen at high wind speeds, where the effects of road furniture on trailing edge shedding are minimised. As the ILEV mode is amplified by the TEVS action to vibrate the leading edge, the mitigation of the TEVS is an indirect mitigation of the ILEV mode.

The findings in this section run contrary to observations on other trapezoids. Generally, the vertical response is observed to be amplified whilst the pitch response mitigated [75][48].

Further work is required to understand how the furniture disrupts the TEVS, ideally through flow visualisation of the trailing edge. It is of interest to parameterise the railings for this trapezoid, in order to understand the sensitivity to depth and height of horizontal railings. Also of interest is whether the upwind or downwind railing, or the combined effects of both cause the difference in response. It should be noted that there are likely scale effects associated with modelling the railings at small scale. The model $Re_D \approx 700$, compared to the full-scale $\approx 10^5$.

Chapter 8

Conclusions and recommendations for further work

8.1 Conclusions

The VIV of a slender box-girder bridge deck has been investigated in this thesis. The main aim of this study has been to develop an understanding of the mechanisms of VIV and lock-in for a very slender box-girder. This research is believed to be the first to examine experimentally, the behaviour of a trapezoid with slenderness, $B/D \geq 10$. The majority of previous research has focused on less slender decks, often without explaining the physics. These have often been commercial studies, focused on the response and mitigation measures. The response and excitation mechanisms have been found to differ to less slender trapezoids, and this is discussed later in this chapter. As this is the first study into such a slender section, simplifications were necessary to develop an understanding of the basic fluid-structure interaction, and the complexity of real-life situations sets limitations on the findings of this work. This provides scope for future investigations of the VIV of very slender decks (see section 8.2).

This research is motivated by the absence of any experimental study into the VIV of very slender box-girders. As mentioned in chapter 2, the behaviour of trapezoids, particularly the VIV excitation mechanism, is expected to depend strongly on the slenderness ratio B/D. Developing an understanding of the behaviour and underlying mechanisms

of such a slender bridge deck section is a necessary step in improving the resilience of designs to VIV. VIV causes fatigue damage as well as reducing the value a bridge can provide to society, through closures during oscillations and tarnishing of the perception of the bridge. As bridge spans continue to get longer and lighter, through structural and material advances, it is becoming increasingly important that understanding of the aerodynamics does not hinder progress.

The approach taken in this study has been experimental. Small-scale physical models representing the deck geometry were placed in wind tunnels, providing approximate dynamical similarity with the full-scale prototype where possible. This allowed accurate predictions to be made from the results of the experiments, within the constraints of assumptions made in the modelling process.

The major findings of this investigation are now outlined:

1. The heave response is shown to be excited by TEVS (section 5.3). This is in contrast to less slender decks that are excited by a combination of TEVS and ILEV mechanisms [51]. This will have an impact on appropriate mitigations measures, and potentially predicted amplitudes. The response can comprise an initial branch and a lower branch, the former characterised by lock-in and organised shedding, and the latter by desynchronisation of shedding at the trailing edge, and lower amplitudes.

2. The shape of the leading edge and trailing edge fairings has a dramatic effect on the response of the trapezoid. In particular the angle at the bottom knuckles and the length of the inclined panels determine the stability in VIV (section 6.2). The heave VIV, driven by TEVS, is reduced at shallow θ_B. It is postulated that shallow angles at the trailing edge reduce the separation and formation of the normally dominant, bottom coherent vortex.

3. The pitch response is excited by a combination of TEVS and ILEV mechanisms. Combined mechanisms are also observed for less slender decks [51] (section 5.4).

4. The ILEV mode number is sensitive to the fairing shape, specifically the angle

at the bottom knuckle, θ_B and the length of the inclined panel at the knuckle (section 6.3). Higher modes, n=3 and n=4 are observed for $\theta_B = 30°, 25°, 18°$ and result in larger amplitudes than the n=2 mode, observed for $\theta_B = 20°$. Both the ILEV and TEVS contribute to the amplitude of pitch response.

5. Hysteresis is observed at the lower branch of the heave response, characterised by the intermittent desynchronisation of TEVS (section 7.1). When the wind speed is gradually decreased and the body free to oscillate, the desynchronised regime is not observed. It is postulated that the desynchronised regime can only be entered from a state of lock-in and associated large amplitude oscillations. The impacts of the body motion history is found to be much greater than the sign of the wind speed increment.

6. The behaviour of this slender trapezoid with varying damping is similar to less slender trapezoids; amplitudes and the range of wind speeds for which lock-in and response are observed are reduced (section 7.2). The pitch response is less sensitive than the heave response. It is postulated that the cause is that the ILEV mode is less sensitive to damping than the TEVS mode.

7. Open railings and median divider act to mitigate the response at low wind speeds through the disruption of TEVS (section 7.3). It is only at higher wind speeds, that the TEVS grows sufficiently to excite pitch motion. No heave motion for the deck with railings was observed in this study. This finding is contrary to other literature [48][75] where heave response tends to be amplified and pitch mitigated.

It is well known that the aerodynamic behaviour and VIV response of bridge decks is sensitive to minor changes in geometry affecting separation, reattachment and shedding but there is limited understanding of how these changes affect the mechanisms of excitation of a slender trapezoid. To the author's knowledge, this is first study to explain the sensitivity of the ILEV mode frequency as the driver for the drastic change in pitch response and the presence of a critical geometry at the bottom knuckle. It is also the first study (to the best of the author's knowledge) to demonstrate the excitation of the heave and pitch mode to be different.

These findings lead to the following design recommendations for very slender box-girders, such as the model in this work:

- the heave mode is excited by TEVS and may be mitigated by modifications at the trailing edge. The pitch response is less sensitive to mitigation of the TEVS and is most likely best mitigated by disrupting the ILEV mode at the leading edge. Disrupting the TEVS acts to increase the onset critical velocity for pitch oscillations;

- there is great sensitivity to the angle at and location of the bottom knuckles. As the top topography of a bridge deck is often constrained by roadway requirements, this gives great scope to mitigate VIV with minimal disruption to the bridge use. A critical angle appears to exist where response is a minimum,. Further work is required to confirm the mechanisms and causes for these differences. In the meantime, it is recommended that designs parameterise the bottom knuckle location and angle in wind tunnel tests, in order top optimise stability in VIV;

- as the body motion history plays a bigger role in amplitudes than the wind speed history, it may be that if the body is forced in a large initial amplitude by another flow phenomenon e.g. turbulent buffeting or a strong gust, the resulting VIV amplitudes would be greater than the free case, often tested in wind tunnels. It is recommended that wind tunnel testing of designs should consider an reasonable initial amplitude of oscillations in determining VIV response;

- the heave response for this slender trapezoid appears very sensitive to damping, more so than the heave. Overestimation of damping is common in design, as it is notoriously difficult to predict. It is recommended that the response with the lowest reasonable structural damping for the prototype be used to predict response;

- the use of necessary road furniture may be an effective tool to mitigate responses (although the literature suggests the impact is body-shape dependant). Road furniture has been shown to have a dramatic effect on response, and should be incorporated in wind tunnel testing of the permanent case. However, bare model testing for the construction stage should be considered, as the amplitudes of the bare deck are larger at lower wind speeds and may govern.

8.2 Limitations and future work

The physical models used in this study are a much simplified version of the full-scale prototype. The main geometric features of a box-girder bridge deck were retained, but the three-dimensionality of the geometry (including towers, cables and pylons) and the topography (including orography and buildings) was not modelled. In particular, the turbulence length scales have not been matched, as almost always the case for wind tunnel studies. The vertical inclination was not investigated in this study and the wind was assumed to flow horizontally and perpendicular to the longitudinal axis of the deck; a highly idealised case. The literature shows there is a sensitivity to the vertical inclination of wind, relative to the deck.

Some of the measurements in this work have been presented as estimates of the VIV-generated component. Theodorsen's theory for calculating the pressure field around a thin aerofoil has been used to calculate and remove the motion-generated component. Using thin aerofoil theory to calculate values for the trapezoid introduces error, greatest where the geometry of the bodies diverge. Theodorsen's theory is based on potential, unseparated flow, which is not the case for the separated flow around the trapezoid. The literature on other bridge decks does not mention the removal of the motion-generated component to estimate the VIV-generated component only.

Further research is needed to fully understand the different mechanisms of flow excitation in heave and pitch lock-in, to confirm what has been suggested, and to uncover further information. In particular, visualisations of the velocity field particle image velocimetry, PIV and computational fluid dynamics, CFD around the body and in the near wake will be useful to identify the mechanisms. Sensitivity to θ_B, the starting body amplitude and road furniture has been found. Velocity fields will help to identify how the mechanisms are altered by these parameters. A greater resolution of θ_B could be tested and the road furniture parameterised further in terms of number of railings, railing height above deck and railing depth. The range of wind speeds tested here is $0.20 \leq U/(f_n B) \leq 1.6$. This range could be extended to higher wind speeds in order to identify if lower ILEV modes are present for the slender trapezoid.

An extensive experimental study could look at parametrising the slenderness ratio of

this deck to identify how and at which values the excitation mechanisms change, as it has been done for rectangular cylinder (figure 2.27). Based on this, a theoretical framework could be developed to determine the behaviour of trapezoids based on slenderness and excitation mechanisms.

Experimental and computation work into the behaviour of a full long-span bridge, with realistic topography could develop once the two-dimensional deck -section behaviour is understood. In-field studies could be conducted to validate the small-scale experiments.

Bibliography

[1] C. Rhodes, "Infrastructure policy briefing paper," *House of Commons Library*, no. 06594, May 2016.

[2] "The investment plan for europe," *European Commission State of Play*, May 2016.

[3] M. Witkowska and J. Hald, *DK Eyewitness Travel Guide Denmark*. Dorling Kindersley Limited, London, 2005.

[4] V. Khatri, *101 Wonders of the World: Natural and Man-made*. Pustak Mahal, Delhi, 2012.

[5] J. Gimsing and C. T. Georgalus, *Cable-supported bridges: concept and design*. John Wiley and Sons, Ltd, 1997.

[6] T. Dinescu and C. Radulescu, *Slip form techniques*. Abacus Press, 1984.

[7] G. Larose and A. Larsen, "Dynamic wind effects on suspension and cable-stayed bridges," *Journal of Sound and Vibration*, vol. 334, pp. 2–28, 2015.

[8] R. Blevins, *Flow-Induced Vibration*. Van Nostrand Reinhold New York, 1990.

[9] C. Feng, "The measurement of vortex-induced effects in flow past stationary and oscillating circular and d-section cylinders," Master's thesis, University of British Columbia, Vancouver, 1968.

[10] S. Daniels, I. Castro, and X. Zheng-Tong, "Numerical analysis of freestream turbulence effects on the vortex-induced vibrations of a rectangular cylinder," *Journal of Wind Engineering and Industrial Aerodynamics*, vol. 153, pp. 13–25, 2016.

[11] P. Bearman and I. Currie, "Pressure-fluctuation measurements on an oscillating circular cylinder," *Journal of Fluid Mechanics*, vol. 91, pp. 661–677, 1979.

[12] A. Larsen, "Aerodynamic aspects of the final design of the 1624 m suspension bridge across the great belt," *Journal of Wind Engineering and Industrial Aerodynamics*, vol. 48, pp. 261–285, 1993.

[13] J. Lienhard, *Synopsis of Lift, Drag and Vortex Frequency Data for Rigid andular Cylinders*. Washington State University, College of Engineering, Research Division Bulletin 300, 1966.

[14] A. Larsen, "Advances in aeroelastic analyses of suspension and cable-stayed bridges," *Journal of Wind Engineering and Industrial Aerodynamics*, vol. 74-76, pp. 73–90, 1998.

[15] G. Larose and A. Auteuil, "On the Reynolds number sensitivity of the aerodynamics of bluff bodies with sharp edges," *Journal of Wind Engineering and Industrial Aerodynamics*, vol. 94, pp. 365–376, 2006.

[16] L. Prandtl and O. Tietjens, *Applied Hydro and Aeromechanics*. McGraw-Hill, New York, 1934.

[17] G. Schewe and A. Larsen, "Reynolds number effects in the flow around a bluff bridge deck cross section," *Journal of Wind Engineering and Industrial Aerodynamics*, vol. 74-76, pp. 829–838, 1998.

[18] G. Schewe, "Reynolds number effects in flow around more-or-less bluff bodies," *Journal of Wind Engineering and Industrial Aerodynamics*, vol. 89, pp. 1267–1289, 2001.

[19] BSI, *Eurocode 1. Actions on structures. General actions, wind actions, EN 1991-1-4*. British Standards Institution, London, 2005.

[20] S. Komatsu and S. Kobayashi, "Vortex-induced oscillations of bluff cylinders," *Journal of Wind Engineering and Industrial Aerodynamics*, vol. 6, pp. 335–362, 1980.

[21] B. J. Vickery and R. I. Basu, "Across-wind vibrations of structures of circular cross-section. part i. development of a mathematical model for two-dimensional conditions,"

[22] C. Scruton, "On the wind-excited oscillations of stacks, towers and masts," *Int. Conf. Wind Effects on Buildings and Structures, Teddington, London*, no. HMSO, pp. 798–836, 1963.

[23] P. Bearman, "Vortex shedding from oscillating bluff bodies," *Annual Review of Fluid Mechanics*, vol. 16, pp. 195–222, 1984.

[24] R. Govardhan and C. Williamson, "Modes of vortex formation and frequency response of a freely vibrating cylinder," *J. Fluids Mech.*, vol. 420, pp. 85–130, 2000.

[25] D. Brika and A. Laneville, "Vortex-induced vibrations of a long flexible circular cylinder," *J. Fluids Mech.*, vol. 250, pp. 481–508, 1993.

[26] J. Smith, "An experimental study of the aeroelastic instability of rectangular cylinders," Master's thesis, University of British Columbia, Vancouver, 1962.

[27] C. Scruton, *An Introduction to wind effects on structures*. Oxford University Press, 1966.

[28] M. Zradkovich, "Scruton number: A proposal," *Journal of Wind Engineering and Industrial Aerodynamics*, vol. 10, pp. 263–265, 1982.

[29] M. Paidoussis, S. Price, and E. de Langre, *Fluid-Structure Interactions, Cross-Flow Induced Instabilities*. Cambridge Unversity Press, 2011.

[30] C. Williamson and A. Roshko, "Vortex formation in the wake of an oscillating cylinder," *Journal of Fluids and Structures*, vol. 2, pp. 85–130, 1988.

[31] P. Bearman and E. Obasaju, "An experimental study of pressure fluctuations on fixed an oscillating square-section cylinders," *Journal of Fluid Mechanics*, vol. 119, pp. 297–321, 1982.

[32] O. Griffin and G. Koopmann, "The vortex-excited lift and reaction forces on resonantly vibrating cylinders," *Journal of Sound and Vibration*, vol. 54, pp. 435–448, 1977.

[33] M. Davies, "A comparison of the wake structure of a stationary and oscillating bluff body, using a conditional averaging technique," *Journal of Fluid Mechanics*, vol. 75, pp. 209–231, 1975.

[34] O. Griffin and S. Ramberg, "On vortex strength and drag in bluff-body wakes," *Journal of Fluid Mechanics*, vol. 69, pp. 721–728, 1975.

[35] O. Griffin and S. Ramberg, "The vortex-street wakes of vibrating cylinders," *Journal of Fluid Mechanics*, vol. 66, pp. 553–576, 1974.

[36] A. Roshko, "On the drag and shedding frequency of two-dimensional bluff bodies," *NACA tech. note 3169*, 1954.

[37] P. Bearman and M. Davies, "The flow about oscillating bluff structures," *Proceedings of the International Conference on Wind Effects on Buildings and Structures*, vol. 4th edition, pp. 285–295, 1977.

[38] N. Shiraishi and M. Matsumoto, "On classification of vortex-induced oscillation and its application for bridge structures," *Journal of Wind Engineering and Industrial Aerodynamics*, vol. 14, pp. 419–430, 1983.

[39] E. Naudascher and Y. Wang, "Flow-induced vibrations of prismatic bodies and grids of prisms," *Journal of Fluids and Structures*, vol. 7, pp. 341–373, 1993.

[40] M. Matsumoto, "Vortex shedding of bluff bodies: a review," *Journal of Fluids and Structures*, vol. 13, pp. 791–811, 1999.

[41] W. Zhang, Z. Wie, Y. Yang, and Y. Ge, "Comparison and analysis of vortex induced vibration for twin-box bridge sections based on experiments in different reynolds numbers," *Journal of Tongji University (Natural Science)*, vol. 36, pp. 6–11, 2008.

[42] Y. Nakamura and T. Mizota, "Unsteady lifts and wakes of oscillating rectangular prisms," *Journal of the Engineering Mechanics Division*, vol. 101, pp. 855–871, 1975.

[43] G. Toebes and P. Eagelson, "Hydroelastic vibrations of flat plates related to trailing edge geometry," *Journal of Basic Engineering*, 1961.

[44] R. Parker and M. Welsh, "The effect of sound on flow over bluff bodes," *International Journal of Heat and Fluid Flow*, vol. 4/87/81, pp. 113–127, 1983.

[45] G. Schewe, "Nonlinear flow induced resonances of a h-shaped section.," *Journal of Fluids and Structures*, vol. 3, pp. 327–348, 1989.

[46] Y. Nakamura, Y. Ohya, and H. Tsuruta, "Experiments on vortex shedding from flat plates with square leading and trailing edges," *Journal of Fluid Mechanics*, vol. 222, pp. 437–447, 1991.

[47] D. Nguyen and E. Naudascher, "Vibration of beams and trashracks in parallel and inclined flows," *Journal of Hydraulic Engineering*, vol. 117, pp. 1056–1076, 1991.

[48] A. Corriols and G. Morgenthal, "Computational analysis of viv observed on existing bridges," *The Seventh International Colloquium on Bluff Body Aerodynamics and Applications BBAA7*, 2012.

[49] A. Stokes and M. Welsh, "Flow-resonant sound interaction in a duct containing a plate; ii:square leading edge," *Journal of Sound and Vibration*, vol. 104, pp. 55–73, 1986.

[50] D. Rockwell and E. Naudascher, *Flow-Induced Vibrations: An Engineering Guide*. Courier Corporation, 2005.

[51] J. Terrés Nícoli and G. Kopp, "Mechanisms of the vertical vortex induced vibration of the storebaelt bridge," *11th Americas Conference on Wind Engineering San Juan, Puerto Rico*, 2009.

[52] M. Matsumoto, T. Yagi, H. Tamaki, and T. Tsubota, "Vortex-indcued vibration and its effect on torsional flutter instability in the case of b/d=4 rectangular cylinder," *Journal of Wind Engineering and Industrial Aerodynamics*, vol. 96, pp. 971–983, 2008.

[53] A. Larsen, S. Esdahl, J. Anderson, and T. Vejrum, "Storebaelt suspension bridge - vortex shedding excitation and mitigation by guide vanes," *Journal of Wind Engineering and Industrial Aerodynamics*, vol. 8, pp. 283–296, 2000.

[54] H. Li, S. Laima, Z. Qiagqiang, N. Li, and L. Zhiqiang, "Field monitoring and validation of vortex-induced vibrations," *Journal of Wind Engineering and Industrial Aerodynamics*, vol. 124, pp. 54–67, 2014.

[55] O. Flamand, F. De Oliveira, A. Stathopoulos-Vlamis, and P. Papanikolas, "Conditions for occurrence of vortex shedding on a large cable stayed bridge: Full scale data from monitoring system," *Journal of Wind Engineering and Industrial Aerodynamics*, vol. 135, pp. 163–169, 2014.

[56] I. J. Smith, "Wind induced dynamic response of the wye bridge," *Engineering Structures*, vol. 2, no. 4, pp. 202–208, 1980.

[57] R. L. Wardlaw, "Cable supported bridges under wind actions," *Proceedings of seminar on cable-stayed bridges: recent developments and their future*, no. 4, pp. 213–234, 1991.

[58] A. R. Burden, "Japanese cable-stayed bridge design," *Proceedings of the Institute of Civil Engineers*, vol. 90(1), pp. 1021–1051, 1990.

[59] J. Owen, A. Vann, and J. Davis, "The prototype testing of kessock bridge: response to vortex shedding," *Journal of Wind Engineering and Industrial Aerodynamics*, vol. 60, pp. 91–108, 1996.

[60] T. Wu and A. Kareem, "An overview of vortex-induced vibration (viv) of bridge decks," *Frontiers of Structural and Civil Engineering*, vol. 4, pp. 335–347, 2012.

[61] M. Matsumoto, N. Shiraishi, S. Stoyanoff, and T. Yagi, "Mechanism of, and turbulence effect on vortex-induced oscillations for bridge box-girders," *Journal of Wind Engineering and Industrial Aerodynamics*, vol. 49, pp. 467–476, 1993.

[62] V. Jones and J. Howells, "Suspension bridges," in *ICE manual of bridge engineering* (G. Parke and N. Hewson, eds.), London: Thomas Telford, 2008.

[63] C. Meinhardt, D. Newland, J. Talbot, and D. Taylor, "Vibration performance of london's millennium footbridge," *24th International Congress on Sound and Vibration, London*, pp. 2453–2460, 2017.

[64] C. Ostenfeld, A. Frandsen, and G. Haas, "Model tests for the superstructure of the motorway bridge across Littlebælt," *Bygningsstatiske Meddelelser*, vol. 41, 1970.

[65] A. Larsen, M. Savage, A. Lafreniere, M. Hui, and S. Larsen, "Investigation of vortex response of a twin box bridge section at high and low Reynolds numbers," *Journal of Wind Engineering and Industrial Aerodynamics*, vol. 96, pp. 934–944, 2008.

[66] E. Szechenyi and H. Loiseau, "Mesures aéroélastique et dynamiques sur la pont de saint-nazaire," *Communication and general reports for 6 and 7 June 1978, Association Francaise des Pont et Charpentes*, 1978.

[67] T. N. Okubo, N. Nanta, and K. Yokoyama, "Improvement of wind stability of cable-stayed girder bridges," *Proceedings of the fourth international conference on wind effects*, 1977.

[68] J. H. G. Macdonald, P. A. Irwin, and M. S. Fletcher, "Vortex-induced vibrations of the second severn crossing cable-stayed bridge - full-scale and wind tunnel measurements," *Proceedings of the Institution of Civil Engineers*, vol. 2, pp. 123–134, 2001.

[69] J. H. G. Macdonald, P. A. Irwin, and M. S. Fletcher, "Discussion: Vortex-induced vibrations of the second severn crossing cable-stayed bridge - full-scale and wind tunnel measurements," *Proceedings of the Institution of Civil Engineers*, vol. 3, pp. 332–333, 2003.

[70] S. M. G. Irwin, P. A. and R. L. Wardlaw, "A wind tunnel investigation of a steel design for the st johns river bridge, jacksonville, florida.," *National Research Council Canada, Ottawa*, no. 220, 1978.

[71] Y. Sakai, K. Ogawa, H. Shimodoi, and T. Saitoh, "An experimental study on aerodynamic improvements for edge girder bridges," *Journal of Wind Engineering and Industrial Aerodynamics*, vol. 49, pp. 459–466, 1993.

[72] N. Haque, H. Katsuchi, H. Yamada, and M. Nishio, "Investigation of edge fairing shaping effects on aerodynamic response of long-span bridge deck by unsteady rans," *Archives of Civil and Mechanical Engineering*, vol. 16, pp. 888–900, 2016.

[73] F. Nagai, E. Utsunomiya, E. Yoshioka, A. Ikeuchi, and H. Kobayashi, "Effects of handrails on separated shear flow and vortex-induced oscillation," *Journal of Wind Engineering and Industrial Aerodynamics*, vol. 69-71, pp. 819–827, 1997.

[74] M. Sarwar and T. Ishihara, "Numerical study on suppression of vortex-induced vibrations of box girder bridge section by aerodynamic countermeasures," *Journal of Wind Engineering and Industrial Aerodynamics*, vol. 98, pp. 701–711, 2008.

[75] A. Larsen and A. Wall, "Shaping of bridge box girders to avoid vortex shedding response," *Journal of Wind Engineering and Industrial Aerodynamics*, vol. 104-106, pp. 159–165, 2012.

[76] B. Chaix, "Effets d'interference entre moulinets hydrometriques, supports et parois lors de mesures de debits," Master's thesis, Swiss Federal Institute of Technology Lausanne, Juris Verlag Zurich, Switzerland, 1972.

[77] Y. Fujino and Y. Yoshida, "Wind-induced vibration and control of trans-tokyo bay crossing bridge," *Journal of Structural Engineering, ASCE*, vol. 128, pp. 1012–1025, 2002.

[78] P. Bearman, "Investigation of the flow behind a two-dimensional model with a blunt trailing edge and fitted with splitter plates," *Journal of Fluid Mechanics*, vol. 21, pp. 241–255, 1965.

[79] C. Apelt and G. West, "The effects of wake splitter plates on bluff-body flow in the range 10^4<R<5×10^4. part 2," *Journal of Fluid Mechanics*, vol. 71, pp. 145–160, 1975.

[80] C. Wood, "Visualisation of an incompressible flow with base bleed," *J. Fluid Mech.*, vol. 29, pp. 259–272, 1967.

[81] P. Bearman, "The effect of base bleed on the flow behind a two-dimensional model with a blunt trailing edge," *Aeronautical Quarterly*, vol. 18, pp. 207–2524, 1967.

[82] E. Naudascher and M. Nakashima, "Vortex excitation of prisms with elongated rectangular h and t cross-sections," *Journal of Fluid Mechanics*, vol. 163, pp. 149–169, 1986.

[83] H. Choi, W.-P. Jeon, and K. Jinsung, "Control of flow over a bluff body," *Annu. Rev. Fluid Mech.*, vol. 40, pp. 113–139, 2008.

[84] O. Rodriguez, "Base drag reduction by the control of three-dimensional unsteady vortical structures," *Exp. Fluids*, vol. 11, pp. 218–226, 1991.

[85] N. Tombazis and P. Bearman, "A study of three-dimensional aspects of vortex shedding from a bluff body with a mild geometric disturbance," *Journal of Fluid Mechanics*, vol. 330, pp. 85–112, 1997.

[86] H. Park, D. Lee, W.-P. Jeon, S. Hahn, and J. Kim, "Drag reduction in low over a two-dimensional bluff body with a blunt trailing edge using a new passive device," *J. Fluids Mech.*, vol. 563, pp. 389–414, 2006.

[87] J. Yoon, "Control of flow over a circular cylinder using wake disrupter," Master's thesis, Seoul National University, Korea, 2005.

[88] P. Bearman and M. Brankovic, "Experimental studies of passive control of vortex-induced vibration," *European Journal of Mechanics B/Fluids*, vol. 23, pp. 9–15, 2004.

[89] P. Bearman and J. Owen, "Reduction of bluff-body drag and suppression of vortex shedding by the introduction of wavy separation lines," *J. Fluids Struct.*, vol. 12, pp. 123–130, 1998.

[90] J. Owen, P. Bearman, and A. Szewczyk, "Passive control of viv with drag reduction," *J. Fluids Struct.*, vol. 15, pp. 597–605, 2001.

[91] R. Darekar and S. Sherwin, "Flow past a square-section cylinde rwith a wavy stagnation face," *Journal of Fluid Mechanics*, vol. 426, pp. 263–295, 2001.

[92] A. Dobre, H. Hangan, and B. Vickery, "Wake control based on spanwise sinsoidal perturbation," *AIAA J.*, vol. 44, pp. 485–492, 2005.

[93] M. El-Gammal, H. Hangan, and P. King, "Control of vortex shedding-induced effects in a sectional bridge model by spanwise perturbation method," *Journal of Wind Engineering*, vol. 95, pp. 663–678, 2007.

[94] T. Saeed, J. Morrison, and M. Mughal, "Roughness effects on swept-wing cross-flow transition in moderate free-stream turbuence," *Proceedings of the International Council of the Aeronautical Sciences*, 2014.

[95] E. Maskell, "A theory of blockage effects on bluff bodies and stalled wing in a closed wind tunnel," *Aeronautical Research Council Reports and Memoranda*, vol. No 3400, 1965.

[96] K. Takeda and M. Kato, "Wind tunnel blockage effects on drag coefficient and wind-induced vibration," *Journal of Wind Engineering and Industrial Aerodynamics*, vol. 41-44, no. 2, pp. 897–908, 1992.

[97] T. Fox and G. West, "On the use of end plates with circular cylinders," *Experiments in Fluids*, vol. 9, no. 4, pp. 237–239, 1990.

[98] G. West and C. Apelt, "The effects of tunnel blockage and aspect ratio on the mean flow past a circular cylinder with reynolds number between10^4 and 10^5," *Journal of Fluid Mechanics*, vol. 114, pp. 361–377, 1978.

[99] X. Xhao, K. Gouder, J. Graham, and D. Limebeer, "Buffet loading dynamic response and aerodynamic control of a suspension bridge in a turbulent wind," *Journal of Fluids and Structures*, vol. 62, pp. 384–412, 2016.

[100] S. Szepessy and P. Bearman, "Aspect ratio and end pate effects on vortex shedding from a circular cylinder," *Journal of Fluid Mechanics*, vol. 234, pp. 191–217, 1992.

[101] P. Saathoff and W. Melbourne, "Effects of free stream turbulence on surface pressure fluctuations in a separation bubble," *Journal of Fluid Mechanics*, vol. 337, pp. 1–24, 1992.

[102] G. Rigas, *Modelling of turbulent wakes.* PhD thesis, Imperial College of London, 2014.

[103] T. Theodorsen, "General theory of aerodynamic instability and the mechanism of flutter," *NACA tech. note 496*, 1934.

[104] A. Perry, "Turbulence modelling using coherent structures in wakes, plane mixing layers and wall turbulence," *Perspectives in Turbulence Studies: International Symposium DFVLR Research Center*, pp. 115–153, 1987.